# Innovative design of polarizing matrices for the early detection of cancer by MRI

Matthieu Cavailles

## To cite this version:

Matthieu Cavailles. Innovative design of polarizing matrices for the early detection of cancer by MRI. Other. Université de Lyon, 2018. English. NNT : 2018LYSE1204 . tel-02022867

HAL Id: tel-02022867
https://theses.hal.science/tel-02022867

Submitted on 18 Feb 2019

**HAL** is a multi-disciplinary open access archive for the deposit and dissemination of scientific research documents, whether they are published or not. The documents may come from teaching and research institutions in France or abroad, or from public or private research centers.

L'archive ouverte pluridisciplinaire **HAL**, est destinée au dépôt et à la diffusion de documents scientifiques de niveau recherche, publiés ou non, émanant des établissements d'enseignement et de recherche français ou étrangers, des laboratoires publics ou privés.

N°d'ordre NNT : 2018LYSE1204

# THESE de DOCTORAT DE L'UNIVERSITE DE LYON

opérée au sein de
**l'Université Claude Bernard Lyon 1**

**Ecole Doctorale de Chimie de Lyon** N°206

**Spécialité Chimie**

Soutenue publiquement le 16 Octobre 2018, par :

## Matthieu CAVAILLES

# Design innovant de matrices polarisantes pour le diagnostic précoce du cancer par IRM

Devant le jury composé de :

**M. Christian HILTY**, Professeur à l'Université du Texas (A&M) : Rapporteur
**M. Ahmad MEHDI**, Professeur à l'Université de Montpellier (UM) : Rapporteur

**Mme Bénédicte ELENA-HERRMANN**, Chargée de recherche CNRS à l'Institut pour l'Avancée des Biosciences (IAB), Grenoble : Examinatrice
**M. Stéphane PAROLA**, Professeur à l'Université de Lyon 1 (UCBL), Lyon : Examinateur
**M. Sami JANNIN**, Professeur à l'Université de Lyon 1 (UCBL) : Examinateur

**Mme Chloé THIEULEUX**, Directrice de recherche CNRS au Laboratoire de Chimie, Catalyse, Polymères et Procédés (LC2P2), Lyon : Directrice de thèse

# UNIVERSITE CLAUDE BERNARD - LYON 1

| | |
|---|---|
| **Président de l'Université** | **M. le Professeur Frédéric FLEURY** |
| Président du Conseil Académique | M. le Professeur Hamda BEN HADID |
| Vice-président du Conseil d'Administration | M. le Professeur Didier REVEL |
| Vice-président du Conseil Formation et Vie Universitaire | M. le Professeur Philippe CHEVALIER |
| Vice-président de la Commission Recherche | M. Fabrice VALLÉE |
| Directrice Générale des Services | Mme Dominique MARCHAND |

## *COMPOSANTES SANTE*

| | |
|---|---|
| Faculté de Médecine Lyon Est – Claude Bernard | Directeur : M. le Professeur G.RODE |
| Faculté de Médecine et de Maïeutique Lyon Sud – Charles Mérieux | Directeur : Mme la Professeure C. BURILLON |
| Faculté d'Odontologie | Directeur : M. le Professeur D. BOURGEOIS |
| Institut des Sciences Pharmaceutiques et Biologiques | Directeur : Mme la Professeure C. VINCIGUERRA |
| Institut des Sciences et Techniques de la Réadaptation | Directeur : M. X. PERROT |
| Département de formation et Centre de Recherche en Biologie Humaine | Directeur : Mme la Professeure A-M. SCHOTT |

## *COMPOSANTES ET DEPARTEMENTS DE SCIENCES ET TECHNOLOGIE*

| | |
|---|---|
| Faculté des Sciences et Technologies | Directeur : M. F. DE MARCHI |
| Département Biologie | Directeur : M. le Professeur F. THEVENARD |
| Département Chimie Biochimie | Directeur : Mme C. FELIX |
| Département GEP | Directeur : M. Hassan HAMMOURI |
| Département Informatique | Directeur : M. le Professeur S. AKKOUCHE |
| Département Mathématiques | Directeur : M. le Professeur G. TOMANOV |
| Département Mécanique | Directeur : M. le Professeur H. BEN HADID |
| Département Physique | Directeur : M. le Professeur J-C PLENET |
| UFR Sciences et Techniques des Activités Physiques et Sportives | Directeur : M. Y.VANPOULLE |
| Observatoire des Sciences de l'Univers de Lyon | Directeur : M. B. GUIDERDONI |
| Polytech Lyon | Directeur : M. le Professeur E.PERRIN |
| Ecole Supérieure de Chimie Physique Electronique | Directeur : M. G. PIGNAULT |
| Institut Universitaire de Technologie de Lyon 1 | Directeur : M. le Professeur C. VITON |
| Ecole Supérieure du Professorat et de l'Education | Directeur : M. le Professeur A. MOUGNIOTTE |
| Institut de Science Financière et d'Assurances | Directeur : M. N. LEBOISNE |

# Remerciements

Cette thèse est le reflet de trois années de travail menées au Laboratoire de Chimie, Catalyse, Polymères et Procédés (LC2P2) avec la participation de nombreuses personnes.

Je souhaite premièrement remercier Mr Christian Hilty, Mr Mehdi Ahmad, Mme Bénédicte Elena-Herrmann, Mr Stéphane Parola et Mr Sami Jannin pour avoir accepté de faire partie de mon jury de thèse.

Merci à Chloé Thieuleux pour son encadrement pendant les trois années de ma thèse. Je te remercie pour les critiques constructives et tes conseils avisés. Je tiens également à remercier David Baudouin avec qui j'ai eu plaisir à travailler au début de ce projet. Ton implication dans le projet a été très appréciable.

Je remercie l'ensemble des membres de l'EPFL : Aurélien Bornet, Mathieu Baudin, Basile Vuichoud, Jonas Milani, Geoffrey Bodenhausen et Sami Jannin. Ils m'ont toujours accueilli avec enthousiasme et se sont montrés disponibles pour l'ensemble de notre collaboration. Je tiens plus particulièrement à souligner l'implication d'Aurélien, Basile et Mathieu qui ont réalisé les mesures de polarisation (souvent sur des longues journées intenses …) sans s'y limiter.

J'exprime ma gratitude à Stéphane Parola et Frédéric Chaput pour m'avoir accueilli dans leur équipe à l'ENS Lyon. Merci également à Mateusz Odziomek pour son expertise sur les aérogels et xérogels.

Mon expérience d'enseignement dans le département de chimie-biochimie à l'Université Claude Bernard Lyon 1 a aussi été très enrichissante. Je tiens donc à remercier l'ensemble des enseignants-chercheurs avec qui j'ai pu travailler et pour qui la pédagogie est aussi importante que leurs propres projets scientifiques.

Mon doctorat n'aurait été complet sans les formations proposées par l'école doctorale de chimie. Je remercie donc l'ensemble des intervenants et bien sûr l'organisation de l'école doctorale de chimie de Lyon pour mettre à disposition de telles formations qui viennent compléter notre bagage scientifique. J'ai particulièrement apprécié cette ouverture professionnelle qui a largement orienté ma décision d'effectuer mon projet de thèse à Lyon.

Je suis également reconnaissant envers tous mes collègues : Clément, Iurii, Marc, Matilde, Medet, Pooja, Ravi, Sébastien, Tapish, Tin, Vittoria et Walid (en espérant n'avoir oublié personne) pour tous les bons moments passés ensemble. Votre soutien moral et nos discussions scientifiques a fortement contribué à l'aboutissement de cette thèse.

Un grand merci aux Toulousains qui ont toujours été là même avec quelques kilomètres d'écart.

Merci à famille, mes parents, ma sœur et mon frère de m'avoir toujours soutenu et encouragé durant toutes mes études.

Mes derniers remerciements et pas des moindres vont à Laure qui m'a également soutenu et encouragé dans toutes mes décisions. L'ensemble de ce travail n'aurait pas pu voir le jour sans ta patience, ton enthousiasme et ta bienveillance. Pour tout cela, je te remercie mille fois !

# Résumé

La résonance magnétique nucléaire (RMN) est une technique non-destructive qui permet d'identifier la structure des molécules avec précision. Depuis les années 50, elle a connu un essor considérable avec des améliorations aussi bien au niveau des séquences de pulses qu'au niveau de son instrumentation. En effet, une large gamme d'expérience est aujourd'hui disponible permettant des analyses en 2 dimensions alors qu'il n'était possible d'analyser auparavant qu'un seul noyau à la fois. En ce qui concerne les spectromètres RMN, il est possible aujourd'hui d'effectuer en recherche des analyses de très haute précision sur des appareils allant jusqu'au gigaHz. Des nouvelles technologies sont aussi disponibles pour réduire au maximum les bruits parasites. En parallèle, d'autres systèmes visant à augmenter l'intensité des signaux par augmentation de la polarisation n'ont cessé de croître. On compte parmi elles la méthode dite « brute-force », le pompage optique, la Para-Hydrogen Induced Polarization (PHIP) ou encore la Polarisation Dynamique Nucléaire (PDN).

Dans le cadre de ce projet de thèse, nous nous sommes intéressés à la PDN qui est une technique d'hyperpolarisation permettant de polariser des échantillons liquides à très basse température (1-4 K). La procédure habituelle nécessite de mélanger l'échantillon avec un « agent glaçant » et des radicaux dans des proportions bien contrôlées. Cet « agent glaçant » est un solvant tel que le glycerol ou le DMSO. Il permet d'éviter l'agrégation des radicaux et des molécules d'intérêt lors du processus de refroidissement de l'échantillon et de conserver une répartition homogène et aléatoire des radicaux dans la solution. Ces espèces paramagnétiques utilisées pour ces expériences sont classées en deux grandes familles que sont les nitroxides et les trityls. Parmi les nitroxides, le 2,2,6,6-tetramethylpiperidine-1-oxyl connu aussi sous le nom de TEMPO est communément utilisé pour polariser les atomes d'hydrogène des molécules cibles. Les radicaux trityl sont eux généralement employés pour polariser les atomes de carbone des molécules d'intérêt. D'autres types de radicaux sont aussi en cours de développement de manière à optimiser la polarisation.

Après avoir préparé cet échantillon, il est placé dans un réceptacle qui est lui-même introduit dans le polariseur. Les micro-ondes sont déclenchées pour transférer la haute polarisation des électrons aux espèces cibles ce qui permet d'augmenter l'intensité de leurs signaux RMN. Avec ce type de formulation, on observe des polarisations élevées par

exemple autour de P = 90 % pour des espèces protonées en présence de radicaux TEMPO. Bien que de telles valeurs soient obtenues, une fois que l'échantillon est retiré du polariseur, l'ensemble des espèces relaxent très rapidement vers leur état d'équilibre gommant ainsi toute amélioration obtenue par polarisation.

En 2003, la PDN connait une révolution grâce à une avancée scientifique mise au point par Ardenkjaer-Larsen et al.. Connecté au sommet du polariseur, ils installent un tunnel relié à un spectromètre RMN permettant de transférer l'échantillon hyperpolarisé à température ambiante dans un tube RMN. Une amélioration considérable du rapport signal sur bruit d'un facteur de plus de 10 000 est observée pour la première fois à l'état liquide. Depuis cette prouesse, de nombreuses équipes de recherche améliorent le système de dissolution afin de réduire le temps de transfert et d'optimiser la séparation entre les radicaux et les échantillons. Les espèces paramagnétiques provoquent la relaxation des noyaux ce qui conduit à une perte considérable de la polarisation. On peut également citer une autre amélioration développée par Milani et al. qui consiste en l'élaboration d'un tunnel magnétique permettant une exposition continue et minimale à un champ magnétique même lors de l'étape de dissolution. De cette manière, une plus grande polarisation est maintenue et mesurée après dissolution dans le spectromètre RMN. Une version commerciale du polariseur connue sous le nom de SPINlab® est même disponible à la vente chez GE Healthcare.

Suite à ces nombreux changements, de nouvelles applications telles que le suivi d'intermédiaires réactionnels ou le suivi métabolique par IRM ont fait leur apparition. Un exemple récurrent en d-PDN est l'étude de la transformation du pyruvate en lactate. En effet, l'effet Warburg est défini comme une surconsommation de glucose chez les patients atteints de cancer, avec une transformation de celui-ci en pyruvate puis en lactate. A contrario, un organisme sain transforme le pyruvate par l'intermédiaire des mitochondries en $CO_2$ et en énergie.

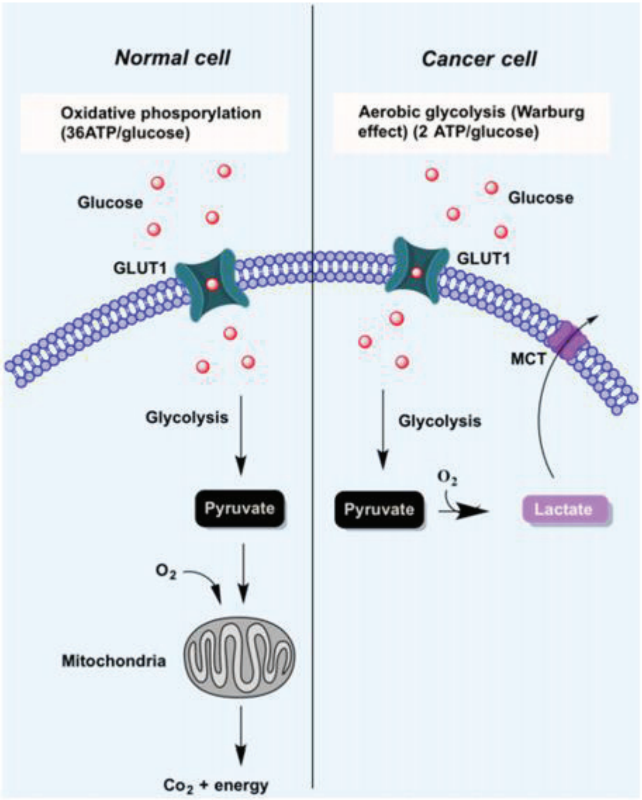

*Figure 1: Représentation schématique de la glycolyse et transformation du pyruvate en différents produits selon l'état des cellules : normales ou cancéreuses.*

Le diagnostic du cancer et son évolution pourront donc être suivis par injection au patient d'un bolus de pyruvate hyperpolarisé lors d'un examen IRM ; la présence de lactate permettant la détection du cancer ou d'en étudier son évolution. Cependant, la préparation de l'échantillon nécessite l'utilisation d'espèces paramagnétiques potentiellement toxiques d'autant plus sur des organismes affaiblis par la maladie.

Suite à ces observations, nous avons développé, par procédé sol-gel, différentes matrices polarisantes nommées HYPSO pour HYbrid Polarizing SOlids. Ces silices mésoporeuses sont hautement poreuses et présentent de grandes surfaces spécifiques ainsi que de grands volumes poreux. Des espèces paramagnétiques y sont liées de manière covalente grâce à la mise au point et au contrôle d'une synthèse multi-étape robuste. Les matériaux fonctionnalisés présentent les caractéristiques nécessaires pour être utilisés en d-PDN telles que de grands volumes poreux ou l'absence d'interaction avec les micro-ondes. De plus, l'immobilisation des radicaux sur ce type de support a permis de s'affranchir de l'utilisation « d'agent glaçant » puisque ces derniers sont répartis de manière homogène et aléatoire à la surface des matériaux.

Dans un premier temps, l'immobilisation de radicaux TEMPO a été réalisée sur un solide mésoporeux organisé connu sous le nom de SBA-15. Ce type de matériau présente un arrangement hexagonal de son réseau poreux qui est constitué de longs canaux parallèles.

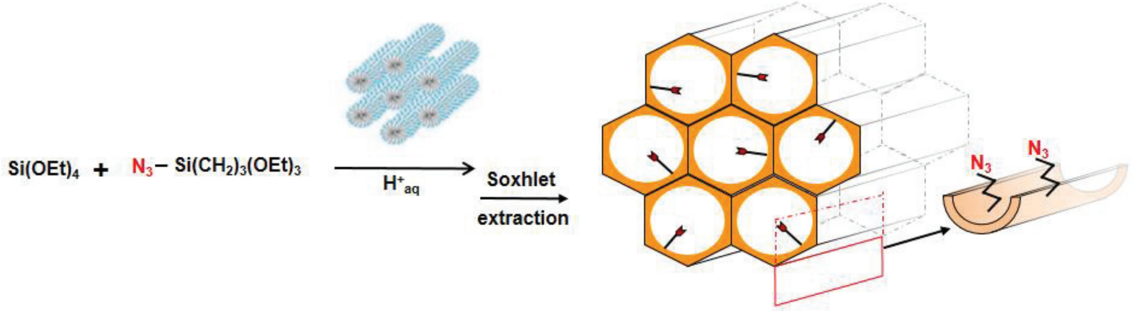

*Figure 2: Incorporation directe des fragments azido dans une structure de type SBA-15.*

Ces matériaux sont tout d'abord imprégnés avec une solution de référence composée d'un mélange $H_2O$ : $D_2O$ (2 : 8) puis introduits dans le polariseur PDN à basse température (1-4 K). Le transfert de polarisation des électrons aux protons effectué par l'irradiation micro-onde a révélé une polarisation maximale P ($^1H$) = 50 % pour $B_0$ = 6.7 T et T = 1.2 K.

En comparaison et basé sur le même schéma de synthèse, des radicaux TEMPO ont été immobilisés sur des matériaux mésoporeux organisés de type SBA-16. Ces matériaux affichent une porosité de type cubique 3D avec des cavités interconnectées par des canaux.

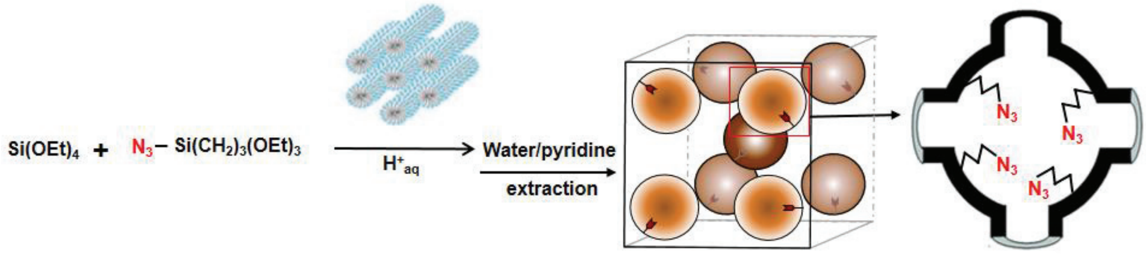

*Figure 3: Incorporation directe des fragments azido dans une structure de type SBA-16.*

Après imprégnation de ces nouveaux matériaux avec une solution contenant un mélange $H_2O$ : $D_2O$ (2 : 8), une polarisation maximale P ($^1H$) = 63 % a été mesurée pour un champ magnétique de $B_0$ = 6.7 T et une température de T = 1.2 K. Cette différence de polarisation avec les matériaux de type SBA-15 a été expliquée par l'influence de la matrice de silice. L'architecture de cette dernière qui présente une porosité interconnectée dans les 3 dimensions de l'espace favorise la diffusion de la polarisation au sein même de la matrice. En complément, une solution à 3M [1-$^{13}$C] d'acétate de sodium a été imprégnée dans la matrice de silice et une expérience de polarisation croisée a permis de transférer la polarisation des protons aux carbones. Dans ce même polariseur, une polarisation P ($^{13}$C) = 36 % a été mesurée et la valeur obtenue peut être expliquée par une perte de polarisation lors du transfert réalisé par CP ainsi que des différences chimiques entre les deux solutions.

Il est important de noter l'efficacité de ces matrices qui fournissent des polarisations tout à fait convenables avec des avantages considérables.

Dans un second temps, une étude de l'influence de la taille des pores à granulométrie constante a été réalisée sur des sphères de silice non structurées. Puis une étude de la taille des grains avec un diamètre poreux fixe de 6 nm. Afin d'obtenir des résultats comparables, des concentrations équivalentes de radicaux TEMPO ont été immobilisés à la surface de ces billes.

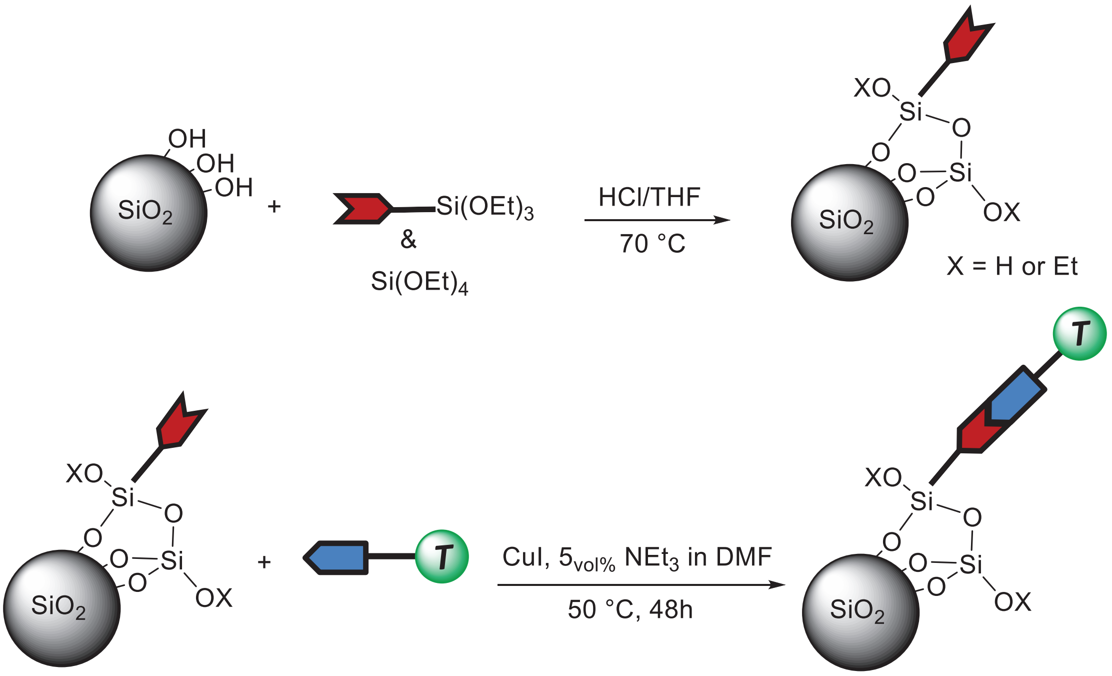

*Figure 4: Synthetic procedure allowing to prepare the HYPSO 5 through the incorporation of the TEMPO radicals into a silica layer.*

Les échantillons avec un diamètre poreux de 6 nm et une granulométrie comprise entre 250 µm et 500 µm ont permis premièrement d'améliorer la filtration des solides et deuxièmement de faciliter l'expulsion du liquide hyperpolarisé. Une polarisation record de P ($^1$H) = 99 % (± 5 %) a été enregistré sur ces même matériaux après imprégnation d'un mélange $H_2O$ : $D_2O$ (2 : 8). Ce résultat surpasse même les polarisations proton utilisant la formulation de base dépourvue de matrice polarisante qui jusqu'à ce jour fournissaient de meilleures polarisations. Après un transfert de la polarisation des protons aux carbones pour notre solution de référence à 3M [1-$^{13}$C] d'acétate de sodium, une augmentation de la polarisation jusqu'à P ($^{13}$C) = 51 % a été mesurée témoignant encore de l'efficacité de ces nouvelles matrices polarisantes.

En tant que preuve de concept, des images IRM utilisant les matériaux HYPSOs comme matrices polarisantes ont été obtenues par hyperpolarisation d'une solution d'acétate de sodium de référence. Cette solution hyperpolarisée a été injectée dans un phantom qui consiste en un tube RMN muni d'un capillaire remplie avec du $D_2O$. Par l'intermédiaire d'une séquence FLASH et d'une sonde à gradient triple, une tranche de ce tube a été imagée. Ceci est la première image IRM témoignant du potentiel des matrices HYPSOs.

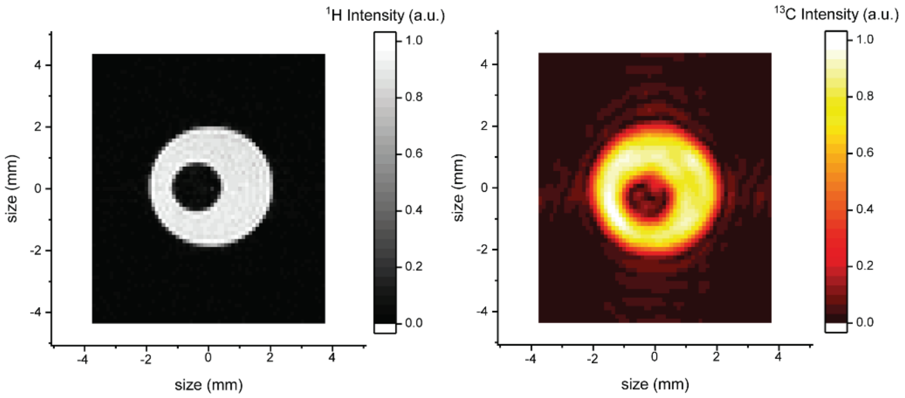

*Figure 5: Images IRM d'une section d'un tube RMN contenant un capillaire remplie avec du $D_2O$ après utilisation d'une matrice polarisante HYPSO pour hyperpolariser le liquide.*

Enfin, nous nous sommes intéressés à une toute nouvelle formulation basée sur l'incorporation de radicaux TEMPO dans des xérogels de silice. Au lieu d'être sous forme de poudre, ces échantillons sont des monolithes de silice avec des textures similaires à celles des matériaux utilisés précédemment. Les premiers résultats affichent de bonnes polarisations avec la capacité d’utiliser un même monolithe pour polariser différents liquides.

# Table of contents

## Chapter 4 : Hybrid polarizing solids based on silica xerogels....181

# List of abbreviations

| | |
|---|---|
| AIBN | Asobisisobutyronitrile |
| ALTADENA | Adiabatic Longitudinal Transfer After Dissociation Engenders Net Alignment |
| APTES | 3-aminopropyltriethoxysilane |
| BET | Brunauer-Emmett-Teller |
| BDPA | Bis(Diphenylene)-2-Phenyl-Allyl |
| CP | Cross-Polarization |
| CTM | Cooperative Templating mechanism |
| CuAAC | Copper(I)-Catalyzed Alkyne-Azide Cycloaddition |
| D-DNP | Dissolution-Dynamic Nuclear Polarization |
| DCCI | N,N'-dicyclohexyldicarbodiimide |
| DMF | Diméthylformamide |
| DNP | Dynamic Nuclear Polarization |
| DQ | Double Quantum |
| DRIFT | Diffuse Reflectance Infrared Fourier Transform |
| EDTA | Ethylenediaminetetraacetic acid |
| EMAAm | N-ethyl-N-methylacrylamide |
| EPR | Electron Paramagnetic Resonance |
| $^{18}$F-FDG | $^{18}$F-Fluorodeoxyglucose |
| HEPES | (4-(2-hydroxyethyl)-1-piperazineethanesulfonic acid) |
| HPLC | High Pressure Liquid Chromatography |
| HRTEM | High Resolution Transmission Electron Tomography |
| HYPSO | Hybrid Polarizing Solid |
| IUPAC | International Union of Pure and Applied Chemistry |
| MABP | 4-mehtacryloyloxybenzophenone |
| MAS | Magic Angle Spinning |
| MCM | Mobil Composition of Matter |
| MEOP | Metastable Exchange Optical Pumping |
| MMA | Methacrylic acid |
| MOF | Metal Organic Framework |
| MRI | Magnetic Resonance Imaging |

| | |
|---|---|
| NMR | Nuclear Magnetic Resonance |
| OX063 | Trityl radical |
| P123 | Pluronic P123 |
| PASADENA | Para-hydrogen and Synthesis Allow Dramatically Enhanced Nuclear Alignment |
| PET | Positron Emission Tomography |
| PFTFA | Pentafluorophenyltrifluoroacetate |
| PHIP | Para-Hydrogen Induced Polarization |
| PO | Propylene Oxide |
| PTFE | Polytetrafluoroethylene |
| SABRE | Signal Amplification By Reversible Exchange |
| SAXS | Small Angle X-ray Scattering |
| SBA | Santa Barbara Amorphous |
| SEOP | Spin Exchange Optical Pumping |
| SFC | Supercritical Fluid Chromatography |
| TBAB | Tetra-n-Butylammonium Bromide |
| TEOS | Tetraethyl orthosilicate |
| TEM | Transmission Electron Microscopy |
| TEMPO | 2,2,6,6-Tetramethylpiperidine-1-oxyl |
| TEMPOL | 4-hydroxy-TEMPO |
| TMOS | Tetramethyl orthosilicate |
| TPSA | 4-trimethoxysilyl-1,2,5,6-tetrahydrophtalic anhydride acid |
| TRIS | (2-amino-2-hydroxymethyl-1,3-propandiol) |
| ZQ | Zero Quantum |

# - General introduction -

# Introduction

The goal of this PhD project was to explore a new formulation of solid samples that could be advantageously used as hyperpolarizing matrices for dissolution Dynamic Nuclear Polarization (d-DNP). DNP is used to hyperpolarize NMR active nuclei of molecules by transferring the high polarization of electrons (present in stable organic radicals) at low temperatures (1-4 K) to the surrounding targeted nuclei. In many cases, the use of a glass forming agent is also required to insure the homogeneous dispersion of the radicals and the molecules of interest in the frozen liquid. However, the presence of organic radical species and glass forming agent may be detrimental for biological applications and the glass forming agent can disturb the NMR analysis by recovering the NMR peaks. Therefore, we aim here at developing new solid polarizing matrices by sol-gel process allowing to fix the aforementioned issues. These solid matrices are denoted HYPSO for HYbrid Polarizing SOlids and are composed of a silica framework where TEMPO radicals are covalently linked and homogenously distributed into the porosity. Different types of HYPSO (HYPSO 2, 3 and 5) will be prepared and the impact of these modifications on the polarization values will be studied.

**Chapter 1** will present the different ways to hyperpolarize molecules with a peculiar interest direct towards dynamic nuclear polarization. The mechanisms: solid effect, cross-effect and thermal mixing that are responsible of the polarization transfer are presented and explained in detail. Finally, the various systems used in the past as polarizing matrices will be reviewed.

**Chapter 2** will illustrate the methodologies to immobilize TEMPO radicals on ordered mesoporous silica materials and the preparation of polarizing matrices based on SBA-15 and SBA-16 frameworks (HYPSO 2 and HYPSO 3). The characterization of these materials will be presented as well as the polarization values obtained after hyperpolarization of a benchmark solution of $H_2O$:$D_2O$ and a 3M [1-$^{13}$C] sodium acetate solution.

**Chapter 3** will show the influence of the pore size and the particle size of post-functionalized silica beads with TEMPO radicals on the polarization performances. The influence of these two parameters on the polarization values is discussed taking into account that large silica particles will ease the filtration process. Then, the first MRI pictures using HYPSO as polarizing matrix will be shown.

**Chapter 4** will describe the preparation of two types of hybrid silica xerogels obtained through a one-pot synthesis or a post-functionalization method.  The preliminary results using such types of materials will be presented and the possibility to reuse them will also be investigated.

Finally, general conclusions and potential perspectives using these polarizing matrices will be provided at the end of this manuscript.

# Chapter 1: General concepts and bibliography

# I. Hyperpolarization methods as a tool to improve the NMR sensitivity

The nuclear magnetic resonance phenomenon is based on the specific property of the nuclei having a spin S different from 0 to be influenced by a magnetic field. To understand this phenomenon, we will consider a system with a spin S= ½ which turns out to be the typical case of the proton. After applying a magnetic field $B_0$, Figure 1 represents schematically the so-called Zeeman Effect which splits the energy level in two other levels commonly denoted as α and β.

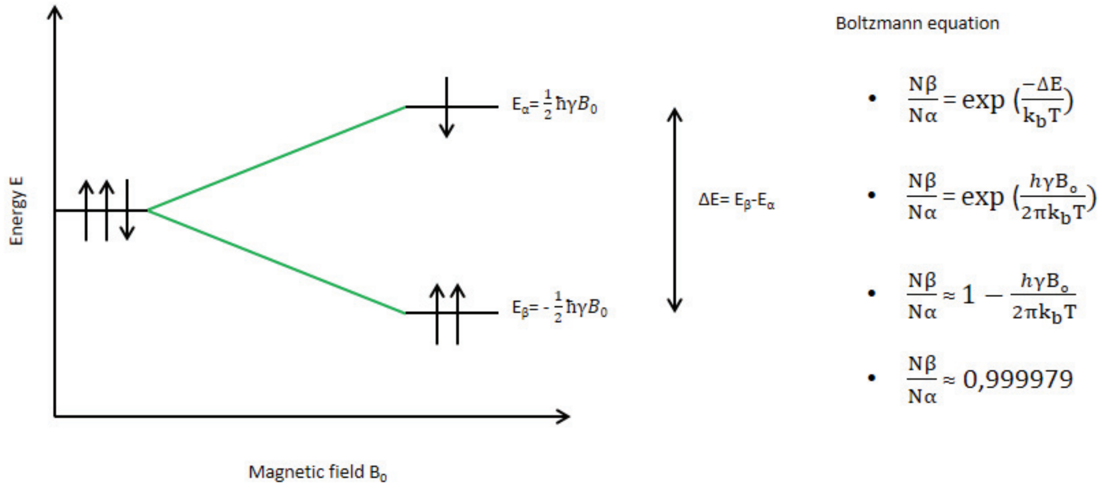

*Figure 1: Representation of the Zeeman Effect for a spin system S= ½ and the Boltzmann equation at $B_0$ = 3 T and T = 298 K.*

The energy difference between both levels is directly related to the nature of the nucleus and the strength of the magnetic field. One can also notice the population distribution where a higher number of spin nuclei is located in the lower energy level. This population difference follows the statistical Boltzmann distribution as calculated on the right of Figure 1. In addition to the magnetic field, a brief radio-frequency field is applied and lead, once stopped, to the relaxation of the nuclear spin system by emitting a signal responsible of the NMR phenomenon.

This method was largely used in analytical chemistry to precisely characterize the structure of molecules but also in biochemistry, in physics and in medicine with the magnetic resonance imaging (MRI). However, despite the wealth of information provided by nuclear magnetic resonance spectroscopy, the lack of sensitivity arising from the method itself requires long analysis times or results on really low signal intensities. To compensate this lack of sensitivity several hyperpolarization techniques were developed such as brute force method, optical pumping, Para-Hydrogen Induced Polarization (PHIP) and Dynamic Nuclear Polarization (DNP).

In the next section, the different hyperpolarization techniques are presented with particular emphasis on DNP, which has been used as efficient tool to polarize liquid samples.

## A. Hyperpolarization using brute-force

The brute-force method is based on a pure instrumental development to decrease the temperature and increase the strength of the magnetic field in order to enhance the polarization. Using this method, the hyperpolarization of a sample consists in submitting it to a strong magnetic field and very low temperatures without other additives. Then, the sample is dissolved and analyzed by NMR at room temperature to quantify the polarization enhancement. Brute-force method has led to the hyperpolarization of different metabolites such as [1-$^{13}$C] pyruvic acid,[5] [1-$^{13}$C] sodium lactate[5] or [1-$^{13}$C] acetic acid[5], the observation of the lungs through the hyperpolarization of $^{129}$Xe[6] and more recently to the possibility to transport a hyperpolarized sample far from the polarizer.[7] Despite the wide range of applications, cutting-edge technologies are required to reach high magnetic field and low temperature curbing thus the development of this technique (around $B_0$ = 14 T and temperature ranging from 4 K to 100 mK).

## B. Hyperpolarization using optical pumping

Optical pumping has been developed for the first time by A. Kastler who received the Nobel Prize in 1966. His work described the possibility to modify the population of the energy levels using a polarized light. Then, hyperpolarized noble gas were produced using two strategies which are known as: Spin Exchange Optical Pumping (SEOP) and Metastable Exchange Optical Pumping (MEOP). SEOP method is divided in two steps, which the first consists in using a polarized light to optically pump the electronic spins of an alkali metal such as rubidium. The second step allows transferring the polarization of the rubidium to the noble gases such as the $^{3}$He and $^{129}$Xe by collision. This process can take a few minutes to few hours. The MEOP technique is generally used only for $^{3}$He and produces a metastable state at low pressure allowing to polarize samples in few seconds.

## C. Hyperpolarization using para-hydrogen induced polarization

The PHIP technique uses the property of the dihydrogen molecule, which has two spin isomers. Indeed, at room temperature, the dihydrogen is composed of 75% of ortho-hydrogen (parallel spins and triplet state) and 25% of para-hydrogen (antiparallel spins and singlet state). At low temperature, it is possible to produce para-hydrogen which will be inserted (hydrogenation through PASADENA or ALTADENA methods) to an unsaturated precursor leading to the rupture of the magnetic symmetry of the protons. Unfortunately, this technique is limited to unsaturated molecules. An alternative version known as SABRE for Signal Amplification By Reversible Exchange allows to exchange the labile protons of a complex with para-hydrogen protons to hyperpolarize molecules.

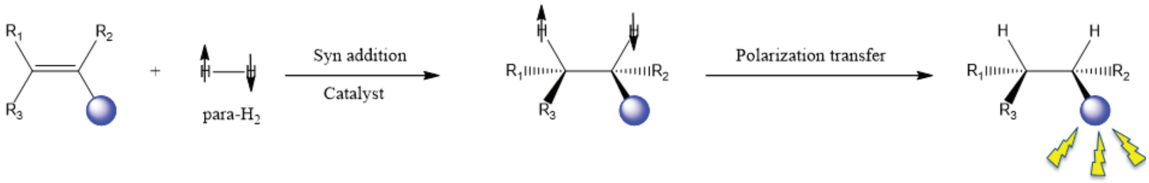

*Figure 2: Schematic representation of a syn-addition of para-$H_2$ resulting in the polarization of a target molecule.*

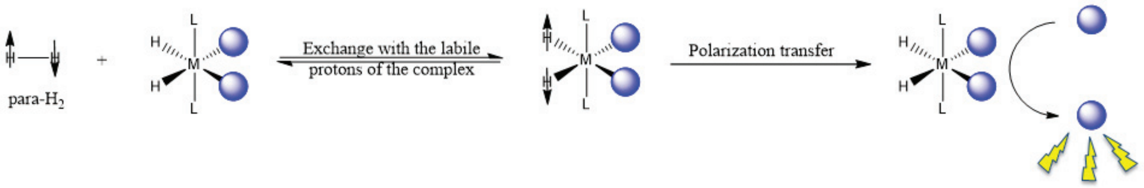

*Figure 3: Schematic representation of the SABRE method where the labile protons of a complex are exchanged with the para-$H_2$ and resulting to the polarization of a target molecule.*

## D. Hyperpolarization using dynamic nuclear polarization

“ - *A. Overhauser has predicted that the saturation of the conduction electrons should simultaneously increase the population difference between the nuclear Zeeman levels by a factor of several thousand and has proposed this as a method of polarizing nuclear spins* “

This quotation comes from the report of T. R. Carver and C. P. Slitcher[8] entitled “Polarization of Nuclear Spins in Metals” where they have shown for the first time the polarization of lithium metal based on the prediction of A. Overhauser. They have placed 5 $cm^3$ of lithium dispersed in oil in a static magnetic field and observed the signal arising from the polarization of lithium.

This so-called polarization is described in DNP but also for the other hyperpolarization methods by the following equation:

$$P = \left(\frac{n_\alpha - n_\beta}{n_\alpha + n_\beta}\right) \quad \text{with } \left(\frac{n_\alpha}{n_\beta}\right) = \exp\left(\frac{-\Delta E}{k_B\,T}\right) \quad \text{and } \Delta E = E_\beta - E_\alpha = \gamma\hbar B_0$$

$$P = \tanh\left(\frac{\Delta E}{4\pi k_B\,T}\right) = \tanh\left(\frac{\gamma\hbar B_0}{4\pi k_B\,T}\right) \qquad \textit{equation 1}$$

$\Delta E$: Energy difference between the levels α and β.

$\gamma$: gyromagnetic ratio

$k_B$ : Boltzmann constant

$h$: Planck constant

$T$ : Temperature of the system

$B_0$: Strength of the magnetic field

As mentioned in equation 1, the increase of polarization could be realized by increasing the magnetic field or decreasing the temperature (the other factors being constants). However, even by using a relative strong magnetic field and low temperatures, a maximum proton polarization $P(^1H) = 0.004$ % was calculated (Table 1).

*Table 1: Polarization of different nuclei with a magnetic field of $B_0 = 11.75$ T (500 MHz for protons) and T = 300 K.*

| Nuclei | Polarization (%) | Magnetic field (T) |
|---|---|---|
| $^1$**H** | 0.004 | 11.75 |
| $^{13}$**C** | 0.001 | 11.75 |
| $^{15}$**N** | 0.0004 | 11.75 |

The electrons have a gyromagnetic ratio 660 times larger than the protons which display the higher polarization at low temperature with a relatively strong magnetic field. The electrons could thus be efficiently polarized at low temperature and used to transfer their high polarization to other nuclei. Figure 4 confirms the high polarization of the electrons at $B_0 = 6.7$ T which can reach a theoretical maximum polarization of $P(e^-) = 100$ % at low temperatures (ca. 1 K).

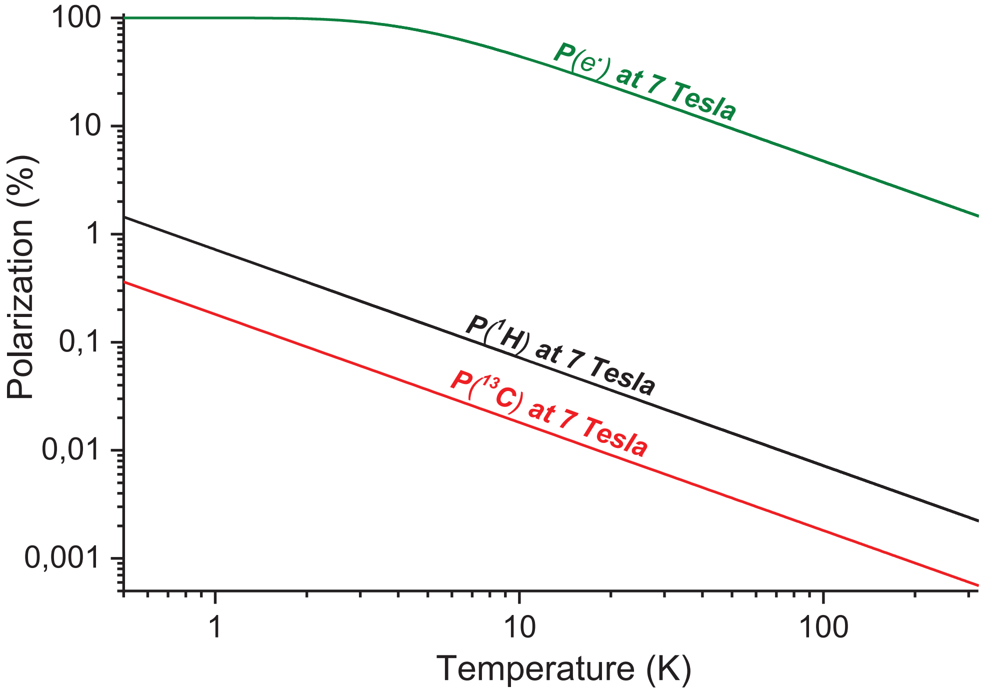

*Figure 4: Polarization values as a function of the temperature for $^1H$, $^{13}C$ and electron.*

Dynamic nuclear polarization is thus taking advantage of the high polarization of the electrons at low temperature to polarize surrounding nuclei through a polarization transfer that can be achieved by the application of a microwave irradiation.

### 1. Dynamic nuclear polarization mechanisms

To transfer the high polarization of the radicals to the surrounding nuclei, a microwave irradiation is required. This polarization transfer can occur following three mechanisms known as: solid effect, cross effect and thermal mixing. Although they are reported as three distinct mechanisms, it is possible that two of them occurring at the same time.

### a) The solid effect

The solid effect is a mechanism involving an interaction between a single electron spin and a single nuclear spin submitted to a magnetic field. The Electron Spin Resonance (ESR) signal of this radical is presented in Figure 5 with specific off-resonance microwave irradiations at frequency $\upsilon_{\mu w1} = \upsilon_0$ (e) - $\upsilon_0$ (n) and $\upsilon_{\mu w2} = \upsilon_0$ (e) + $\upsilon_0$ (n) (with $\upsilon_0$ (e) and $\upsilon_0$ (n) being the electronic and nuclear Larmor frequency respectively). Both situations lead respectively to a positive nuclear polarization and negative nuclear polarization whereas the on-microwave irradiation causes no polarization.

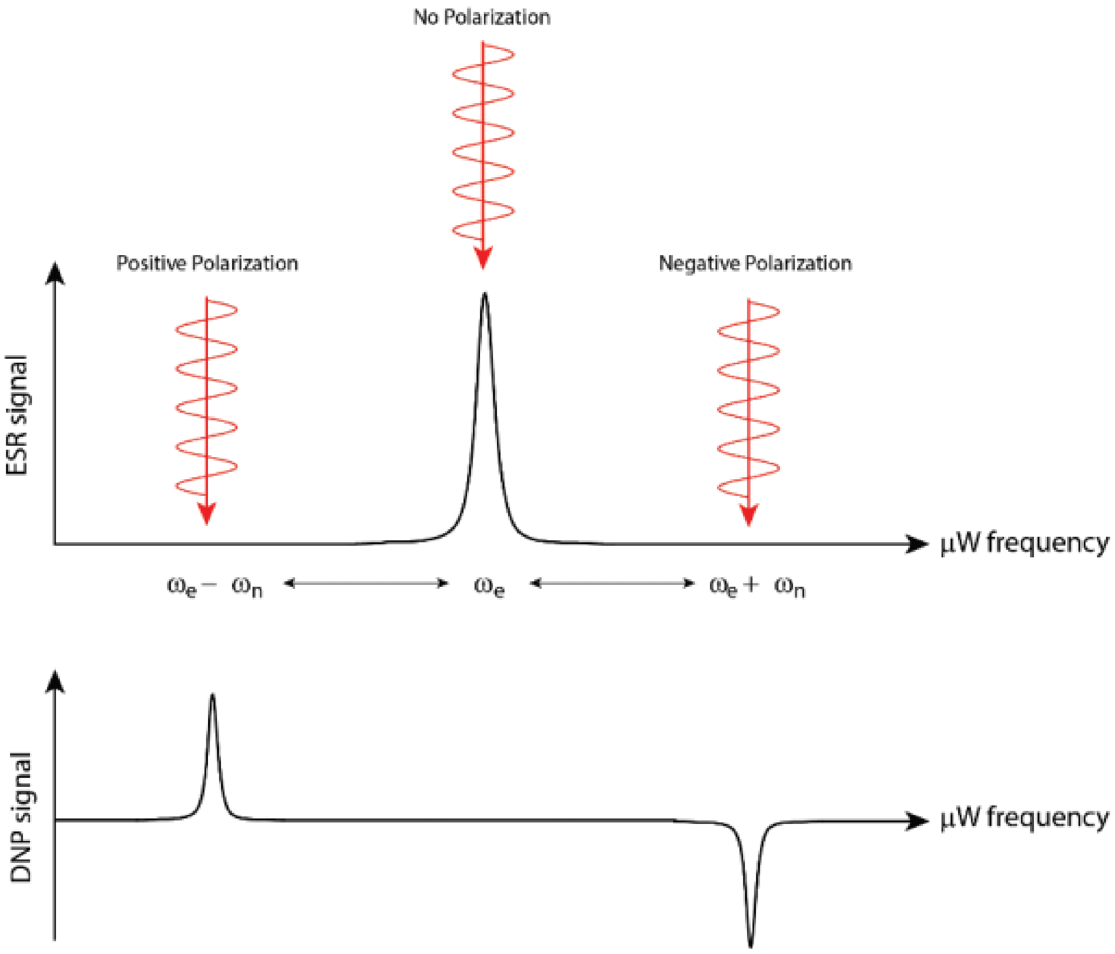

*Figure 5: Electron spin resonance as a function of the microwave irradiation taking values $\upsilon_0$(e) - $\upsilon_0$(n), $\upsilon_0$(e) + $\upsilon_0$(n) or $\upsilon_0$(e) (top) and resulting to a DNP signal showing a positive or negative lobe. Extracted from the thesis of B. Vuichoud.*[3-4]

The solid effect mechanism is explained in detail in Figure 6 with a schematic representation of the three aforementioned situations: positive polarization, negative polarization and no polarization. On the top of this figure, the Boltzmann equilibrium is depicted with a slight population excess in the energy levels: $\beta_e\alpha_n$ and $\beta_e\beta_n$ compared to $\alpha_e\ \alpha_n$ and $\alpha_e\ \beta_n$. On this energy level diagram two forbidden transitions known as zero quantum transition (ZQ) and double quantum transition (DQ) are highlighted.

Positive polarization is achieved by applying a microwave irradiation at a frequency $\upsilon_{\mu w1}$ (DQ). A population excess is thus generated in the energy level $\alpha_e\ \alpha_n$ followed by the allowed electronic relaxation in the energy level $\beta_e\ \alpha_n$ which now displays a population excess. Similarly, negative polarization is achieved by applying a microwave irradiation at a frequency $\upsilon_{\mu w2}$ (ZQ). A population excess is thus generated in the energy level $\alpha_e\ \beta_n$ followed by the allowed electronic relaxation in the energy level $\beta_e\ \beta_n$ which now displays a population excess. The last situation is created by applying a microwave irradiation at a frequency $\upsilon_{\mu w} = \upsilon_0$ (e) which induces the equalization of the spin populations and no polarization enhancement is observed.

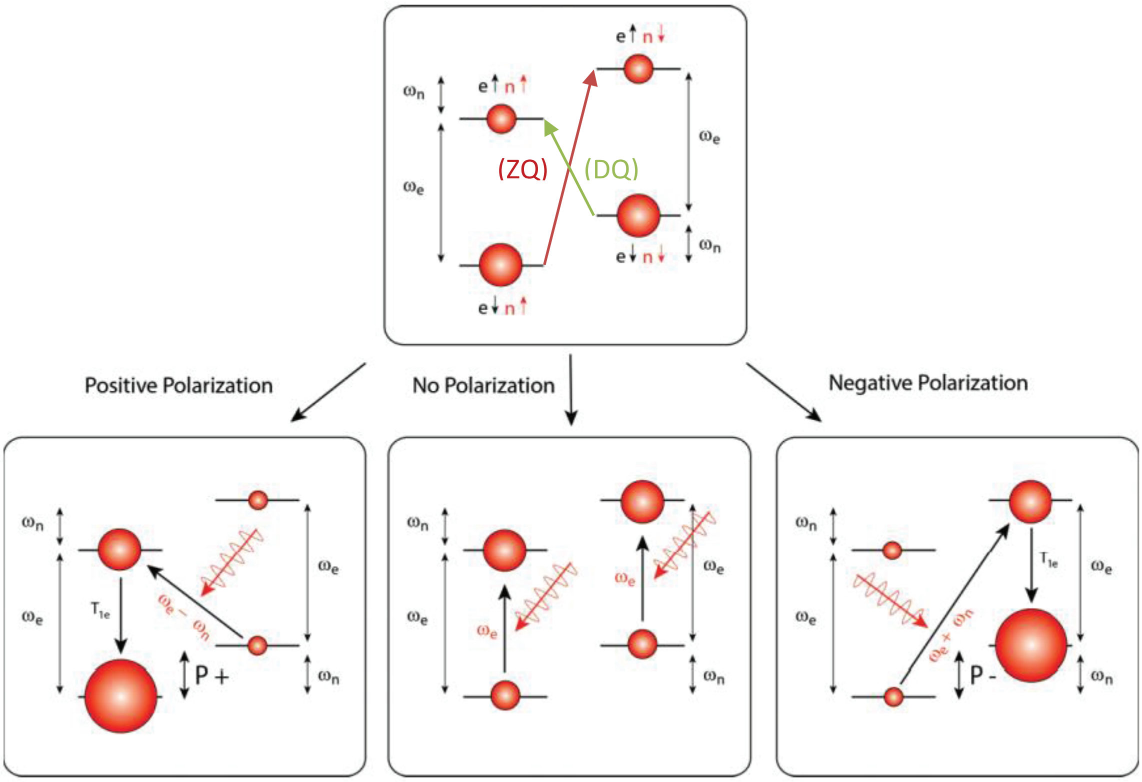

*Figure 6: Representation of the dynamic nuclear polarization phenomenon through a solid effect mechanism involving the interaction between a single electron spin and a single nuclear spin. According to the microwave irradiation, the DNP signal can be positive, negative or absent. Extracted from the thesis of B. Vuichoud*[3-4]

Such a mechanism can occur only when the electron resonance of the radical has a linewidth smaller than the nuclear Larmor frequency. These conditions are fulfilled for example when using trityl radical (OX063) to polarize $^{13}C$ nuclei. In practice, this situation corresponds to a sample with a low electron concentration compare to the nuclei concentration. One can also notice that positive and negative enhancements are separated by twice the Larmor frequency of the nucleus.

### b) The cross-effect

The cross-effect mechanism is a three-spin system involving two electrons ($e_1$ and $e_2$) and one nucleus (n). In this case, the electrons should fulfill two conditions: the electron spins are coupled to each other by dipolar interactions and the difference between their resonance frequencies has to be exactly equal to the nuclear Larmor frequency ($\omega_n = \omega_{e1} - \omega_{e2}$). If both conditions are respected the energy levels $\alpha_{e1}\beta_{e2}\alpha_n$ and $\beta_{e1}\alpha_{e2}\beta_n$ are degenerate. The transition allowing to transfer the polarization from the electron to the nucleus is thus allowed.

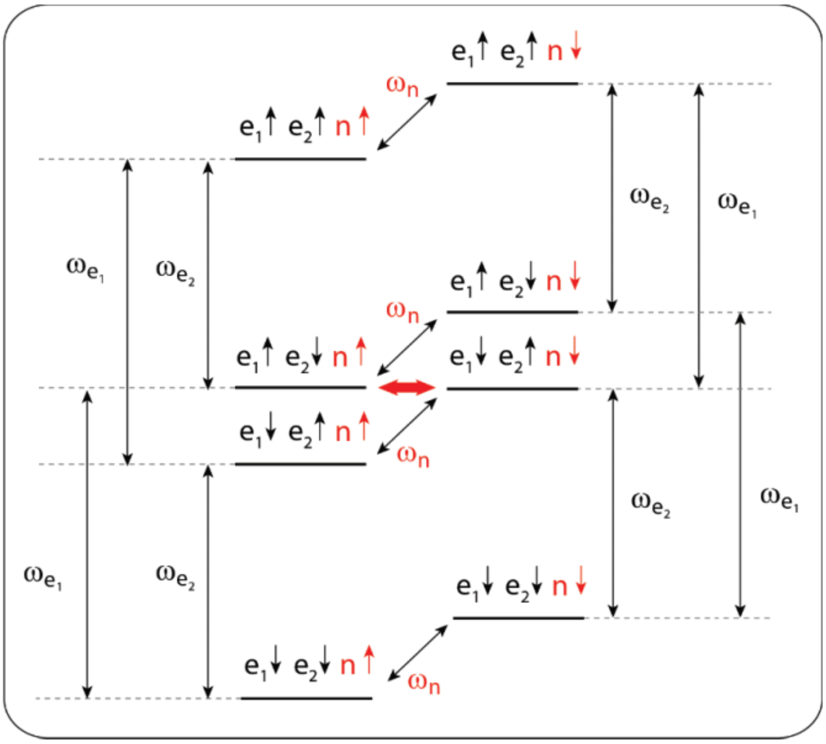

*Figure 7: Representation of the dynamic nuclear polarization phenomenon through a cross-effect mechanism involving a three-spin system composed of two electrons ($e_1$ and $e_2$) and one nucleus (n). Since the energy levels $\alpha_{e1}\beta_{e2}\alpha_n$ and $\beta_{e1}\alpha_{e2}\beta_n$ are degenerated the amount of energy requires is smaller compared to the solid effect. Extracted from the thesis of B. Vuichoud .*[3]

The cross-effect mechanism is thus promoted when the radicals have a broad electron spin resonance compared to the nuclear Larmor frequency. In practice, nitroxide-based radical such as TEMPO radicals are well-suited to hyperpolarize proton nuclei according to a cross-effect mechanism.

### c) The thermal mixing

As suggested by its name, the thermal mixing is described by making an analogy with a thermodynamic system. It is thus defined by a spin temperature denoted $T_S$ and three other concepts known as reservoirs.

- The electron Zeeman reservoir which represents the energy exchange between the electrons.
- The electron dipolar reservoir which represents the dipole-dipole interaction between the electrons.
- The nuclear Zeeman reservoir.

In order to observe a polarization enhancement, the two electronic reservoirs (Zeeman and dipolar) must be in thermal contact. For this purpose, a slight off-resonance microwave irradiation is applied. In addition, the nuclear Larmor frequency should be in the range of the electronic dipolar linewidth so that an energy transfer occurs between both the nuclear reservoir and the electronic reservoir. In this case, the last term: “electronic reservoir” referred to the electron Zeeman and electron dipolar reservoir in thermal contact.

This situation is also depicted in Figure 8 which shows the electron Zeeman system as a function of the electron spin population. Because of a spin $S = ½$, the figure displays two energy levels where the electron spin population is distributed following the Botlzmann’s law. The sub-levels correspond to the dipolar coupling and g-anisotropy known as the electron broadening reservoir. The application of a microwave irradiation (orange arrow) leads to the rearrangement of the electron spin population in the different levels and subsequently polarization.

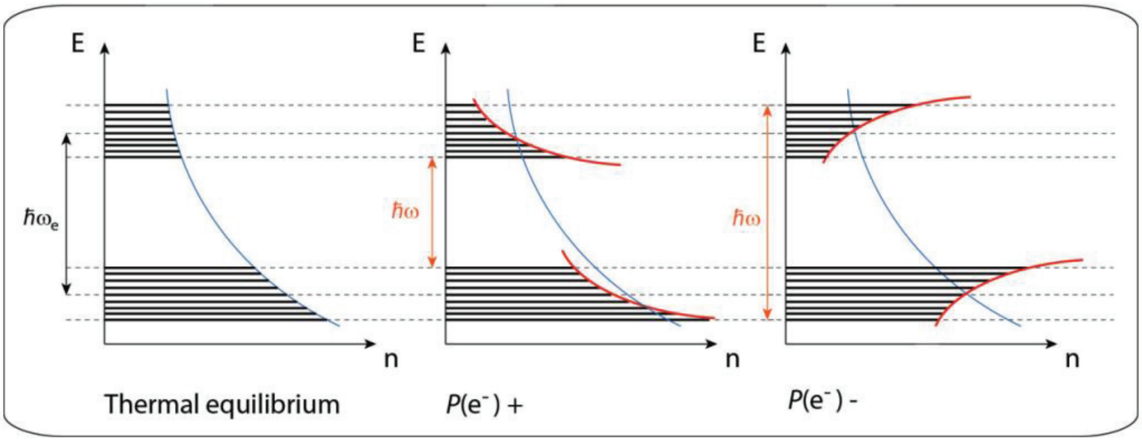

*Figure 8: Electron Zeeman system as a function of the electron spin population. Extracted from the thesis of B. Vuichoud.*[3]

## 2. Proton polarization using TEMPO radicals as polarizing agents

As mentioned before, the hyperpolarization of a molecule through the DNP technique requires the use of paramagnetic species. In the specific case of proton polarization, TEMPO (2,2,6,6-tetramethylpiperidine-1-oxyl) radicals are commonly used. They are highly stable nitroxide-based radicals due to the delocalization of the unpaired electrons over the nitrogen-oxygen bond (Figure 9). The steric hindrance caused by the four methyl groups in α-position of the NO group avoids its recombination with other radicals and the possibility of a H-abstraction leading to nitrone or hydroxylamine (Figure 11).[9-10] The physical properties and the different synthetic routes for its preparation can be found in some recent reviews.[11]

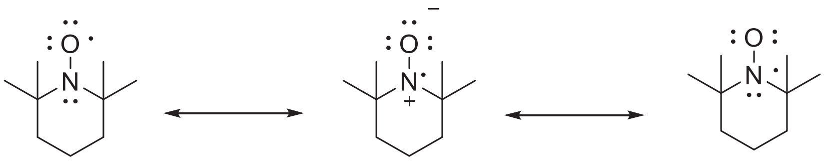

*Figure 9: Resonance structures responsible of the stability of the TEMPO radicals.*

TEMPO radicals are characterized by a specific electron spin resonance which is different for each type of radical. It reflects the frequency at which the electrons absorb the microwave irradiation. The shape of this electrons spin resonance spectrum can be explained by two types of broadening: the homogeneous and inhomogeneous broadening. The homogeneous broadening comes from the dipole-dipole interactions between the radicals. The inhomogeneous broadening is the result of two contributions: the hyperfine coupling and the g-anisotropy. The delocalization of the electrons over the nitrogen oxygen bond causes an interaction between the electrons and the nitrogen (I = 1) which results in a signal with three peaks (the multiplicity is defined as: 2nI+1 = 2x1+ 1 = 3). In addition, the radicals are randomly oriented and distributed which can create a difference in perception of the external magnetic field. This difference is called the g-anisotropy.

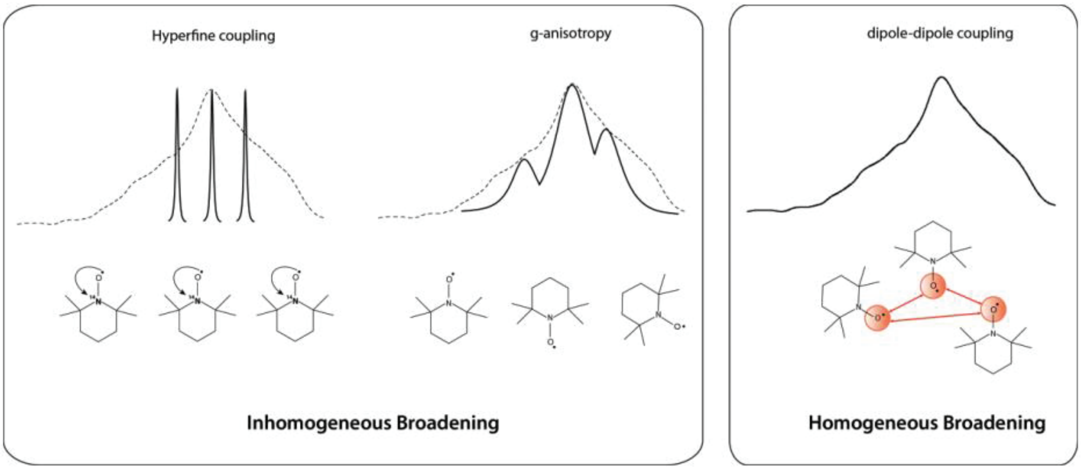

*Figure 10: Electron spin resonance of TEMPO illustrating the hyperfine coupling, g-anisotropy and dipole-dipole coupling. Extracted from the thesis of B. Vuichoud.*[3]

TEMPO and its derivatives (Figure 11) are used in a wide range of research fields such as polymerization initiators,[12] oxidation catalysts,[13-15] antioxidants in biological systems[16] and here in the field of dissolution DNP.

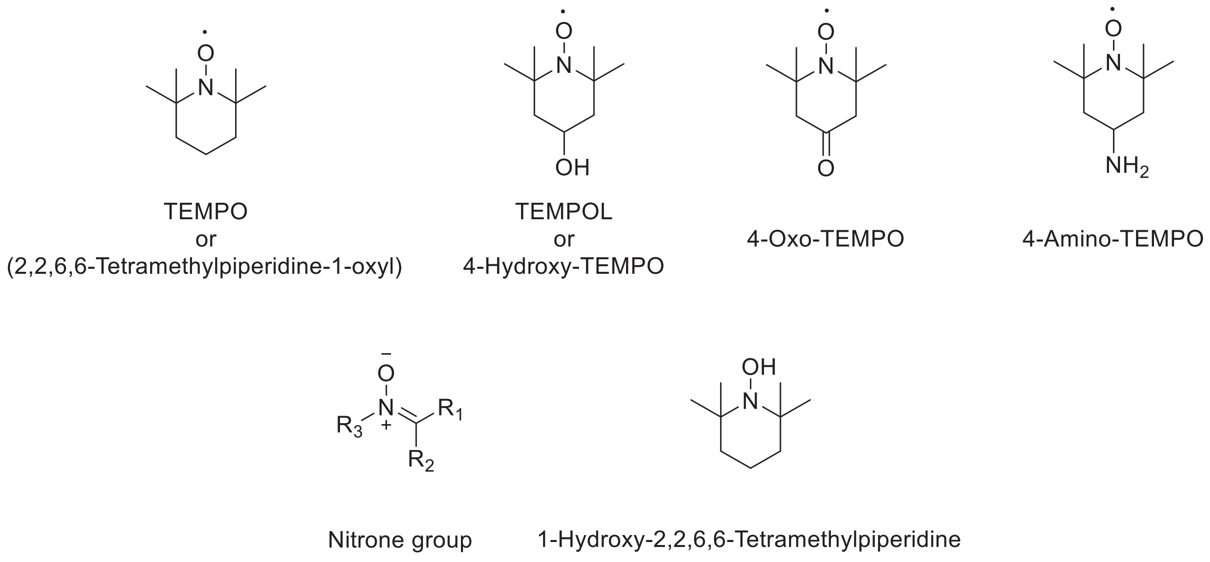

*Figure 11: TEMPO and its derivatives commonly used as well as nitrone groups and hydroxylamine derivative.*

TEMPO radicals are usually mixed with a glass-forming agent such as glycerol or DMSO to avoid aggregation of the radicals on one side and the molecule of interest on other side. In such sample-formulation, the radicals are homogeneously dispersed and different inter-radical distances can be found as the function of the radical concentration. Highly concentrated samples display small inter-radical distances whereas low concentrated samples display large inter-radical distances. We will see later that the radical concentration is an important parameter which must not be neglected.

Although TEMPO radicals are perfectly suitable to polarize protons, they can also be used to polarize carbon nuclei *via* a cross polarization experiment (vide infra).

### 3. Cross polarization experiment as a tool to polarize carbon nuclei from protons

For the same magnetic field, nuclei with a low gyromagnetic ratio such as carbons reach lower polarization values compared to that of nuclei such as protons with a high gyromagnetic ratio. However, polarized carbon nuclei display longer relaxation times than protons at room temperature. The resulting polarization is thus maintained during a longer period of time allowing for example to probe systems with longer response times. The ideal scenario is therefore to reach high polarization values while exhibiting long relaxation times i.e. combining the advantages of both nuclei. This scenario is possible by using a cross-polarization technique which consists in polarizing the proton nuclei with TEMPO radicals and transfer their high polarization to carbon nuclei. The cross-polarization technique is widely used in solid NMR spectroscopy but a suitable design of the coil and new pulse sequences were needed to implement this technique in the specific conditions of the d-DNP. Such improvements have been largely and clearly described in Aurélien Bornet's PhD manuscript.[17]

The evolution of the carbon polarization as a function of time using cross-polarization experiments is shown in Figure 12. Each plateau corresponds to the time required to build the polarization of the protons. The fast increase of carbon polarization corresponds to a polarization transfer from the protons to the carbons. As depicted in this figure, a maximum carbon-polarization is reached using a multiple contact cross-polarization experiment which is responsible of this saw-tooth profile.

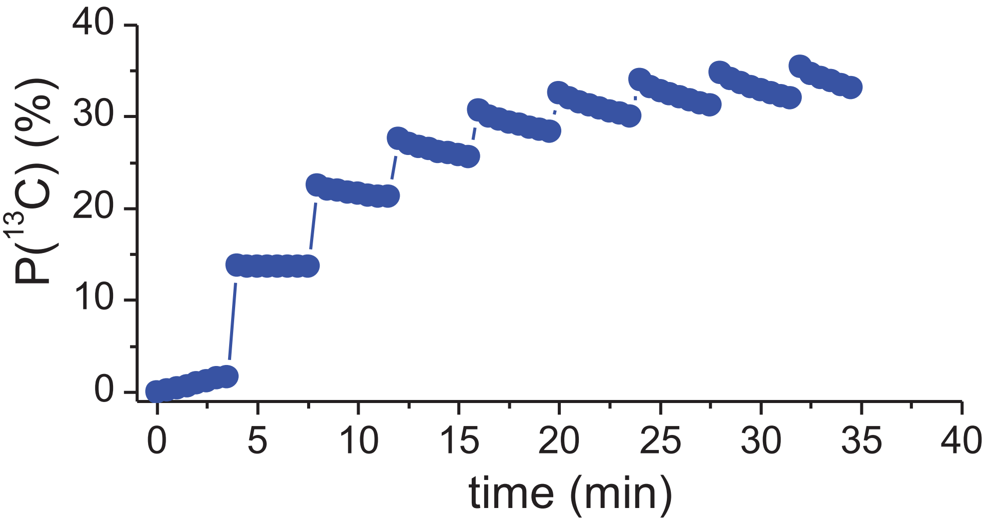

Figure 12: Typical cross-polarization technique used in d-DNP conditions.

In the next section, a full description of the d-DNP device is presented along with a typical d-DNP experiment from the sample preparation to NMR signal acquisition.

## 4. Description of the d-DNP device and typical experiment

The d-DNP device is a complex system composed of a DNP polarizer connected to an NMR spectrometer with a magnetic tunnel[18] (Figure 13). This device is already an advanced version to polarize samples because the tunnel allowing to transfer the hyperpolarized liquid from the DNP polarizer to the NMR spectrometer was developed in 2003 by J. H. Ardenkjaer-Larsen et al..[19] Different d-DNP devices have been developed with some interesting improvements but only the experimental device actually available at the EPFL will be described, since all the samples synthesized in this PhD project were polarized there.

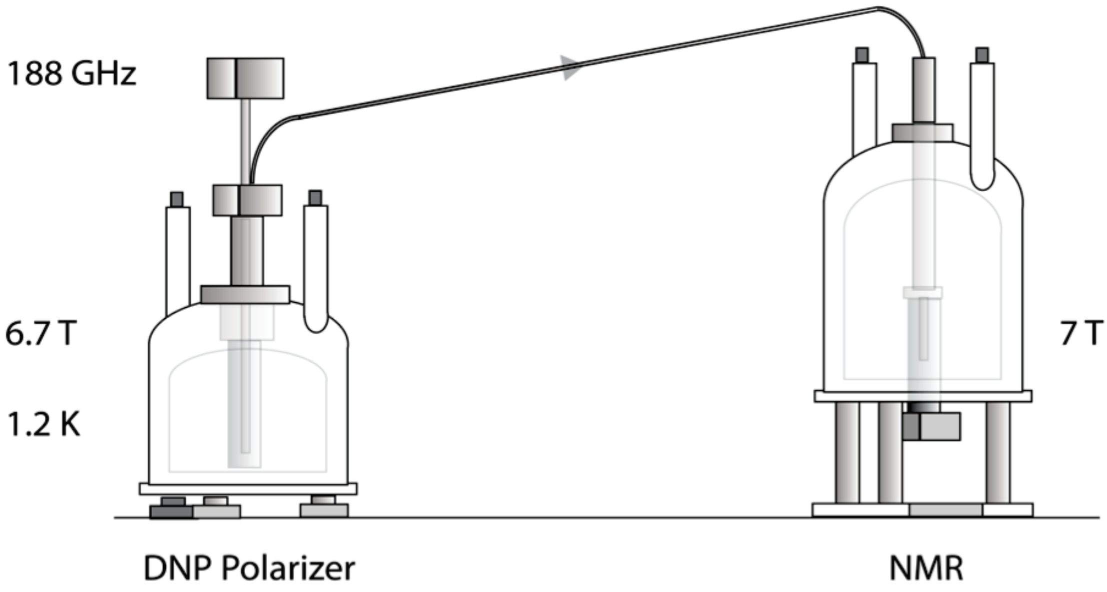

*Figure 13: Schematic representation of the d-DNP device with the DNP polarizer operating at $B_0$ = 6.7 T and T = 1.2 K connected with a magnetic tunnel to a NMR spectrometer.*

The home-built DNP polarizer[20] is composed of a magnet operating at $B_0$= 6.7 T and a cryostat allowing to reach temperatures as low as T = 1.2 K by mean of pumped liquid helium. On the top of the system, a microwave source ($\upsilon_{\mu w}$ = 187.5 – 188.5 GHz and $P_{\mu w}$ = 100 mW) generates the required microwave irradiation to transfer the electron polarization to surrounding nuclei. The microwave is guided *via* a waveguide and focused exactly on the sample through a mirror system.[18]

A typical d-DNP experiment can be divided in four steps which are: sample preparation, polarization, dissolution and NMR acquisition.

The first step of this process, which is of major importance, consists in preparing a mixture commonly called “DNP juice”. The solution is composed of radicals, a glass-forming agent, a solvent and the molecule of interest. Depending on the polarization experiment, nitroxide-based radicals or carbon-centered radicals will be favored. These two examples are the most common radicals used to polarize protons and carbons respectively. However, some research groups have tried to optimize the DNP process by coupling TEMPO radicals with another radical called BDPA for bis(diphenylene)-2-phenyl-allyl *via* an ester group,[21] synthesizing nitroxide-based radicals derivatives[22-23] or they created completely new range of radicals.[24] Nonetheless they are not commercially available and still subjected to additional researches. Through this type of preparation quite high level of proton polarization can be achieved ($P(^1H)$ = 90 % for a typical DNP juice composed of $H_2O$: $D_2O$: glycerol (20:30:50 v:v:v) and 50 mmol of 4-hydroxy-TEMPO), however the subsequent separation of the radicals from the hyperpolarized solution is important to prevent its fast depolarization. For nitroxide-based radicals, sodium ascorbate (vitamin C) can be used. [25] The radicals are reduced in his counterpart containing a hydroxyl group and the scavenger is transformed into a delocalized sodium ascorbyl radical which rapidly disproportionate (Figure 14).[26]

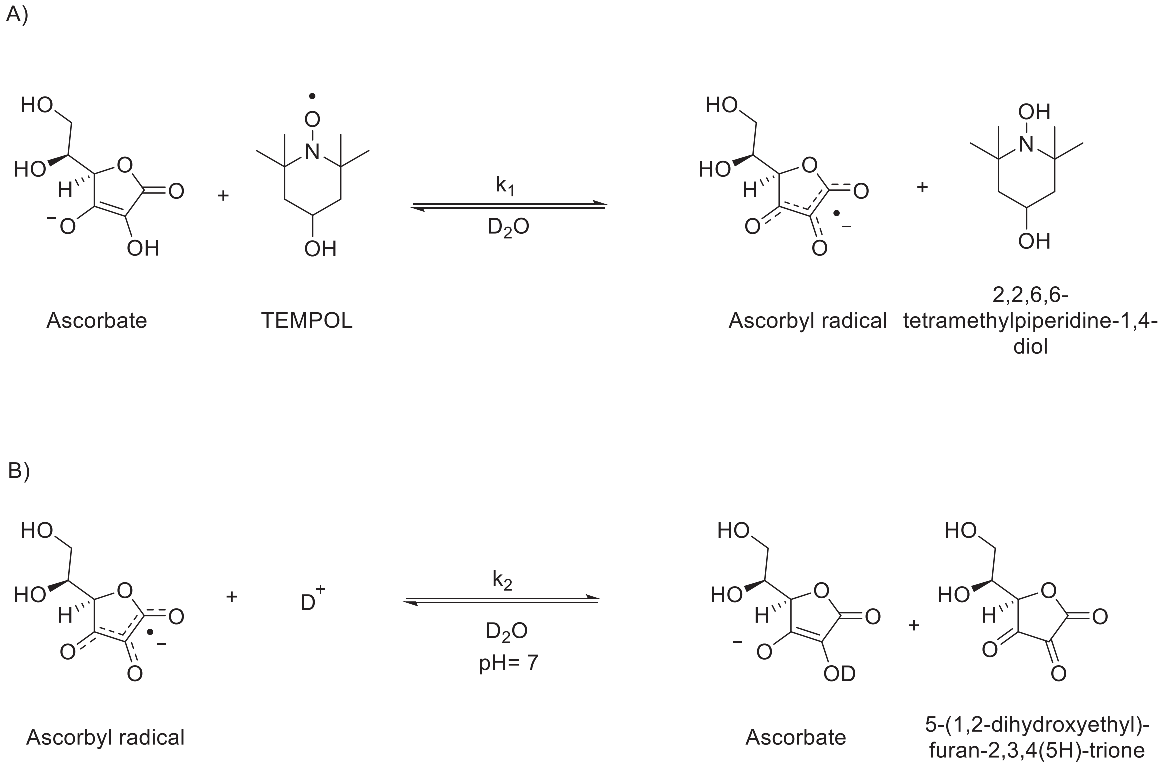

*Figure 14: A) Reduction of TEMPOL by sodium ascorbate leading to the formation of ascorbyl radical and 2,2,6,6-tetramethylpiperidine-1,4-diol B) Disproportionation of the ascorbyl radical into ascorbbate and 5-(1,2-dihydroxyethyl)-furan-2,3,4(5H)-trione.*

Even after disproportionation, some residual products remain in solution and could be undesired depending on the system studied. For carbon-centered radicals, the separation is achieved by solvent extraction[27] or pH modifications of the solution followed by an additional mechanical filtration.[28-29]

The second step is the introduction of the “DNP juice” in the sample holder which is then placed in the DNP polarizer by mean of a long stick. The whole sample is cooled-down to low temperature (1 K– 4 K) and the microwave irradiation is then switched-on to transfer the high polarization of the electrons to the surrounding nuclei. In 2013, it has been shown, at $B_0$ = 3.35 T and temperature ranging from 10 to 50 K, that the frequency-modulation improves the DNP signal.[30] Instead of using a monochromatic microwave irradiation, a frequency-modulated microwave irradiation was used. Based on these results, A. Bornet et al.[31] have investigated similar experiments at lower temperatures (4K – 1K) and higher magnetic field ($B_0$ = 6.7 T) to observe comparable nuclear enhancements. As shown in Figure 15, the frequency is modulated according to a sinusoidal signal (triangular frequency-modulation having similar effect) with a frequency $f_{\mu w}(t) = f_{\mu w} + ½ \Delta f_{\mu w} \sin(2\pi f_{mod} t)$.

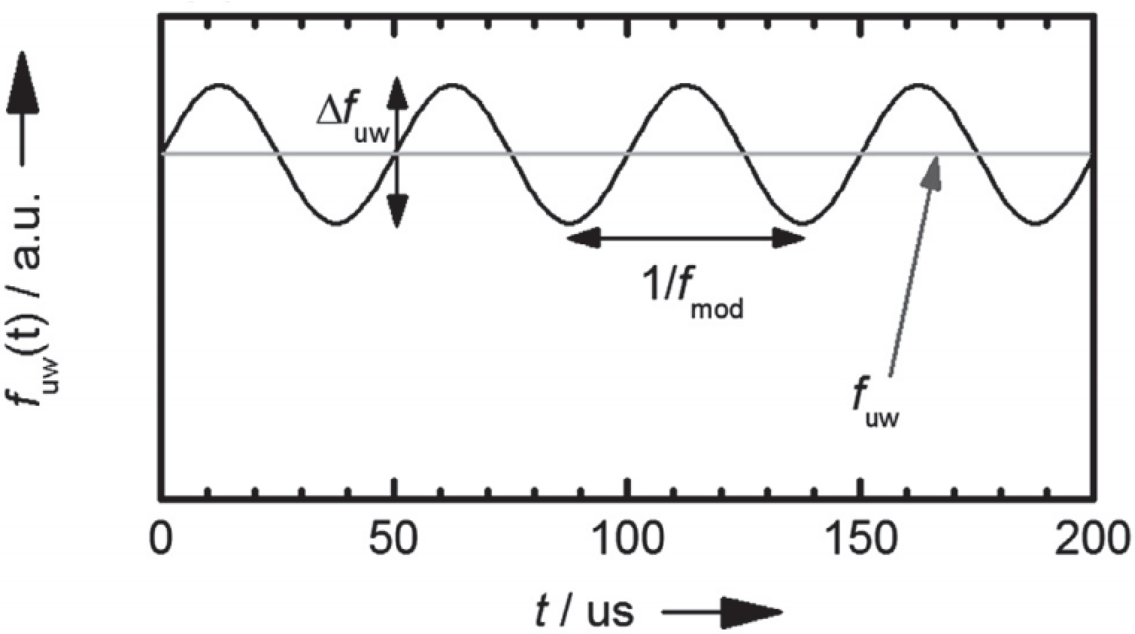

*Figure 15: Sinusoidal modulation of the frequency with $f_{\mu w}(t) = f_{\mu w} + ½ \Delta f_{\mu w} \sin(2\pi f_{mod} t)$ and where $f_{\mu w}$ is the average frequency, $\Delta f_{\mu w}$ is the amplitude of the frequency modulation and $f_{mod}$ the modulation frequency.*

The frequency-modulation was found promising because the amount of paramagnetic species can be reduced up to a factor 2 without hampering the DNP process. For example, a sample containing TEMPOL radicals with a concentration of 25 mM in a 10:40:50 (v:v:v) $H_2O:D_2O$:glycerol-$d_8$ mixture with frequency-modulation provided a proton polarization of ca. $P(^1H) = 60$ % whereas the same mixture with 50 mM of TEMPOL without frequency-modulation provided a proton polarization of ca. $P(^1H) = 40$ %. In addition, using such frequency-modulation allowed to accelerate the DNP build-up times. For the same mixture displaying a radical concentration of 25 mM, the DNP build-up time $\tau_{DNP}$ was equal to 625 s without frequency-modulation and was reduced to 185 s with frequency-modulation. On the EPFL’s system, the operator can choose to modulate or not the irradiation frequency.

Finally, the sample is dissolved and transferred through a magnetic tunnel to an NMR spectrometer or a MRI system. The dissolution process requires the injection of 12 bar pressurized hot water (ca. 10 mL) in the sample holder. This dissolution step must be performed as fast as possible since the depolarization of the sample can occur. It is also important to note that the sample is subjected to a considerable pressure and temperature gradient. This significant variation has to be taking into account for a future sample formulation. The overall dissolution process is schematized in the Figure 16:

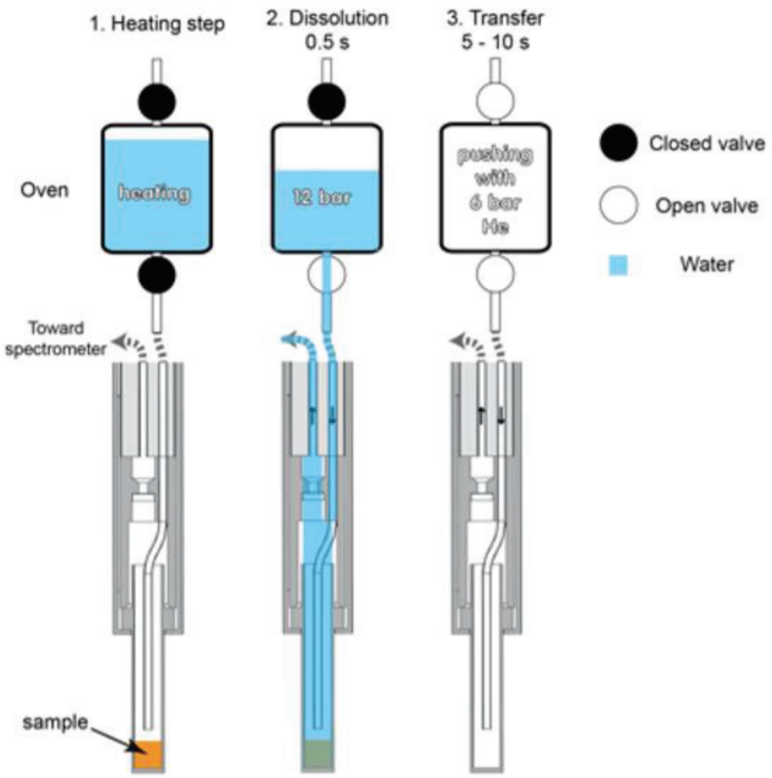

*Figure 16: Dissolution and transfer process using hot and pressurized water.*

## 5. Hyperpolarization of metabolites

The additional dissolution step developed in 2003 by J. H. Ardenkjaer-Larsen[19] allowing to transfer the polarized sample from the DNP polarizer to a NMR or MRI spectrometer has opened an entirely new avenue for *in vivo* and *in vitro* researches. Based on the various metabolisms implied in the Krebs cycle, many groups have used this new technique to assess, control and monitor diseases or healthy tissues. Most of the time, analytes of choice exhibit a labelled $^{13}C$ carboxyl group which is used as a probe because of its long relaxation time T1. Therefore, the polarization of the analyte at room temperature after the d-DNP experiment is maintained during a longer period, allowing to probe different time-dependent systems.  To further increase T1, the deuteration of molecules has been undertaken by several research groups.[32]

However, the use of hyperpolarized molecules for *in-vivo* applications needs specific requirements: the paramagnetic species in the hyperpolarized solution have to be removed and the final pH has to be controlled before injection. For these reasons, buffer such as TRIS (2-amino-2-hydroxymethyl-1,3-propandiol) or HEPES (4-(2-hydroxyethyl)-1-piperazineethanesulfonic acid) are commonly used to adjust the pH in the physiological range of 6.8 to 8.1. Today, [1-$^{13}C$] pyruvate is the reference molecule in Magnetic Resonance Imaging Spectroscopy (MRIS) because of its specific role in oncology. Indeed, the cancer cells disrupt the Krebs cycle by increasing the glycolysis rate therefore increasing the amount of pyruvate. This phenomenon known as Warburg effect is followed, even in presence of dioxygen, by lactic acid fermentation in the cystoplasm which converts pyruvate into lactate in cancer cells instead of oxidizing pyruvate into carbon dioxide and cellular energy in mitochondrias in healthy tissues (Figure 17). One can thus monitor the kinetics of pyruvate conversion into lactate after hyperpolarization to detect a cancer or monitor cancer-evolution.

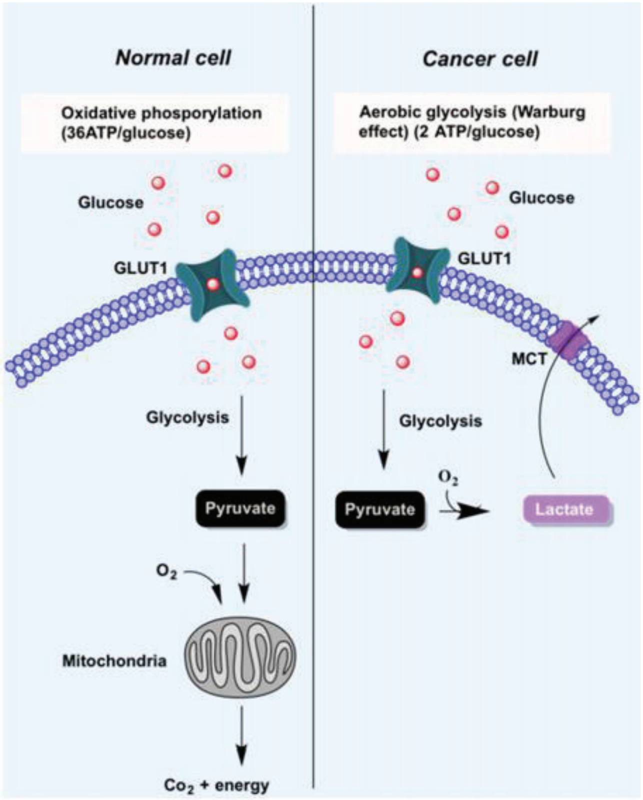

*Figure 17 : Scheme representing the different pathways of the normal cell and the cancer cell. For cancerous cell the transformation of pyruvate into lactate is highlighted in comparison to a normal process.*

Nevertheless, a wide range of molecules were also investigated for *in-vivo* applications covering different types of metabolisms and therefore different diseases or important changes. The table 2 adapted from the article of R. E. Hurd et al.[33] shows a non-exhaustive list of hyperpolarized molecules used in DNP along with their metabolized products.

*Table 2: Hyperpolarized molecules and their corresponding products used in d-DNP.*

| Hyperpolarized molecules | Products | References |
|---|---|---|
| [1-$^{13}$C] pyruvate | [1-$^{13}$C] lactate, [1-$^{13}$C] alanine, [$^{13}$C] bicarbonate, $^{13}CO_2$ | 34 |
| [2-$^{13}$C] pyruvate | [2-$^{13}$C] lactate, [2-$^{13}$C] alanine, [1-$^{13}$C] acetyl-carnitine, [1-$^{13}$C] citrate, [5-$^{13}$C] glutamate | 35-36 |
| [1,2-$^{13}C_2$] pyruvate | [1,2-$^{13}$C] lactate, [1,2-$^{13}$C] alanine, [1-$^{13}$C] acetyl-carnitine, [1-$^{13}$C] citrate, [5-$^{13}$C] glutamate, [$^{13}$C] bicarbonate, $^{13}CO_2$ | 37 |
| [1-$^{13}$C] lactate | [1-$^{13}$C] pyruvate, [1-$^{13}$C] alanine, [$^{13}$C] bicarbonate, $^{13}CO_2$ | 38 |
| [$^{13}$C] bicarbonate | $^{13}CO_2$ | 39 |
| [1,4-$^{13}C_2$] fumarate | [1,4-$^{13}C_2$] malate | 40 |
| [1-$^{13}$C] acetyl methionine | [1-$^{13}$C] methionine | 41 |
| [2-$^{13}$C] fructose | [1-$^{13}$C] fructose-6-phosphate | 42 |
| [5-$^{13}$C] glutamine | [5-$^{13}$C] glutamate | 43 |
| [1-$^{13}$C] ethylpyruvate | [1-$^{13}$C] pyruvate, [1-$^{13}$C] lactate, [1-$^{13}$C] alanine, [$^{13}$C] bicarbonate, $^{13}CO_2$ | 44 |
| [1,1’-$^{13}C_2$] acetic anhydride | Multiple | 45 |
| [1-$^{13}$C] acetate | [1-$^{13}$C] acetyl-carnitine | 46 |
| [$^{13}$C] urea | None | 47 |
| [1-$^{13}$C] dehydro ascorbic acid | [1-$^{13}$C] ascorbic acid | 48-49 |
| [1-$^{13}$C] alanine | [1-$^{13}$C] pyruvate, [1-$^{13}$C] lactate, [$^{13}$C] bicarbonate | 50 |

# III. Improvements of d-DNP formulations

Many efforts have been devoted to the improvement of the d-DNP set-up or the development of NMR sequences however less interest was directed towards the optimization of the sample preparation which remains of major importance for *in-vivo* applications for instance. As shown before, techniques such as precipitation or addition of ascorbic acid have been developed to separate the paramagnetic species from the hyperpolarized liquid but both of them are not suitable for an optimal hyperpolarization process. Immobilization of the radicals into solid supports was also attempted in order to fulfill the aforementioned requirements and some relevant examples, which include the preparation of modified silica gel and agarose supports, polymers and ordered mesoporous silica matrices containing radicals are shown in the following section.

## A. Silica gel and agarose-based supports as potential polarizing matrices

The oldest literature precedents aiming to synthesize polarizing matrices were published in 1981[51] and 1987[52] using flow DNP as hyperpolarization technique. In opposition to static DNP as shown before and denoted only as DNP, flow DNP set-up is composed of two main parts (Figure 18): the first part contains the immobilized spin-label solid retained by a filter in the polarizer and the second consists in a fluid flowing through the polarizing matrix analyzed downstream.

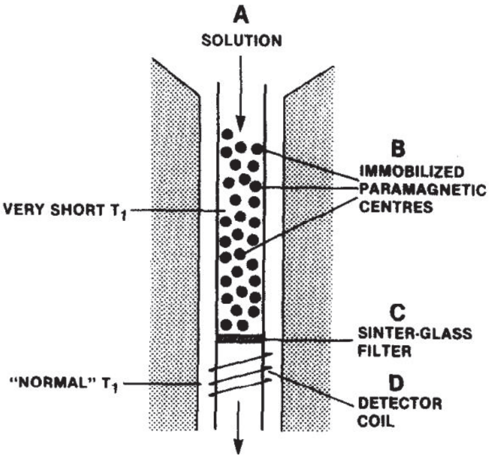

*Figure 18: Schematic representation of the flow DNP set-up where the immobilized paramagnetic species are retained by a sinter-glass filter. The hyperpolarized liquid is detected after a first pass in this system similar to a chromatography column.*

The preparation of a solid phase containing paramagnetic species is essential to use this technique. In these publications, nitroxide radicals were immobilized on glass beads by reaction of a hydroxyl group with dimethyldichlorosilane followed by reaction with TEMPOL radicals in route 1. In route 2, the dimethydichlorosilane was replaced by cyanuric chloride and finally coupled also with TEMPOL radicals (Figure 19).

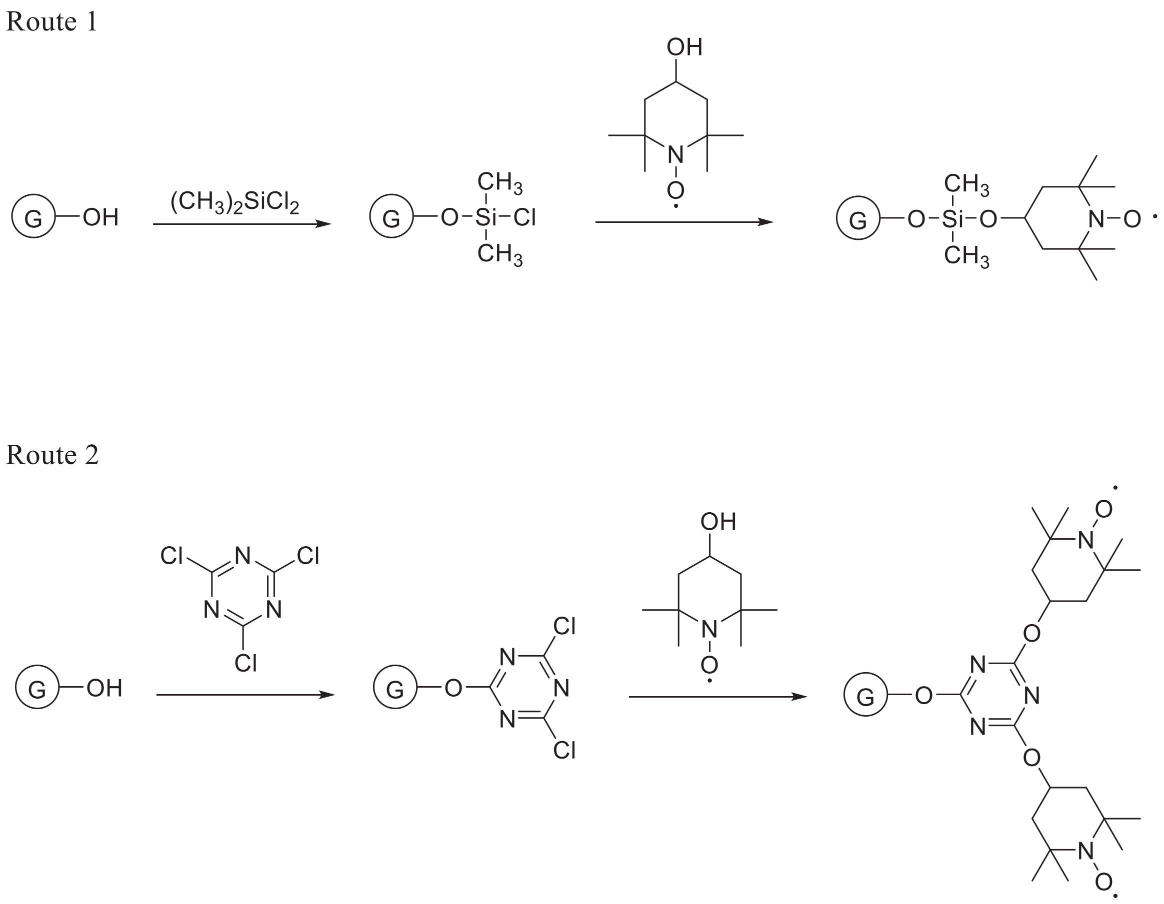

*Figure 19: Preparation of the solid phase containing a TEMPO radical linked via a siloxane bridge in the first reaction and to a triazine cycle in the second reaction.*

Both materials were mixed with different solvent systems and submitted to a pH range of 1 to 11. After one hour of experiment, the glass beads obtained using route 1 were found to be stable independently of the pH whereas some leaching of the radicals was observed with the material synthesized through the second route.

At the same time, they have functionalized polystyrene-divinylbenzene beads through an electrophilic substitution reaction known as Friedel-Craft acylation. The aluminium chloride catalyst reacts with the acetyl chloride to form the $CH_3CO^+$ electrophile which then replaced a proton in the cycle. Finally, the paramagnetic species were coupled via the formation of a C=N bond between the 4-amino-TEMPO and the divinylbenzene derivative.

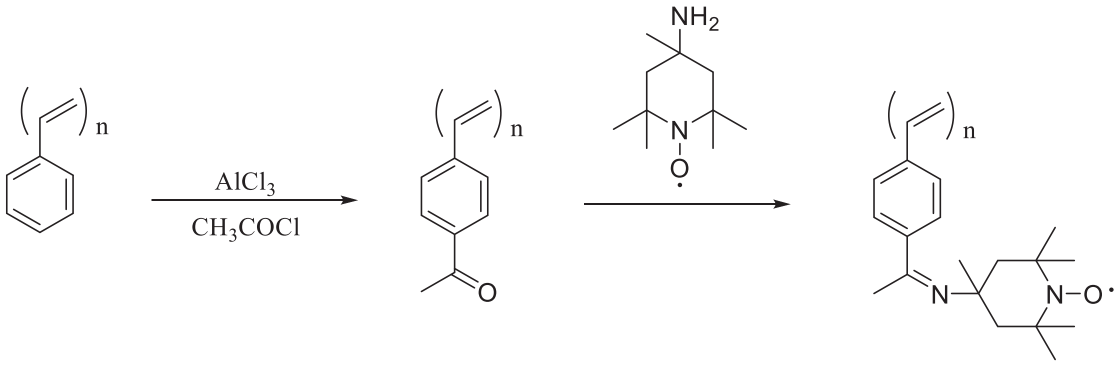

*Figure 20: Schematic representation of the functionalization of polystyrene-divynylbenzene beads.*

The functionalized polystyrene-divinylbenzene beads were found to be stable over the same range of pH however the high degree of cross-linking turned out to be detrimental for the flow. Indeed, a constant and adequate flow was difficult to maintain hampering thus their utilization in flow DNP.

Flow DNP was not investigated in this PhD project but more details about this technique can be found in some recent reviews.[53] Nevertheless, the filtration issues aforementioned can be also encountered in a static d-DNP device especially when dissolving the sample in the polarizer.

In 2008, E. R. McCarney et al.[54] have prepared an agarose-based matrix with different TEMPO radicals (Figure 21) and bought a commercial silica gel containing TEMPO radicals (radical loading of 0.7 mmol/g, mean pore size of 6 nm and grain size ranging from 120-230 mesh) to probe the static and flow DNP performance.

$^{15}$N-perdeutero-4-amino-TEMPO

$^{14}$N-4-amino-TEMPO

*Figure 21: $^{15}$N-perdeutero-4-amino-TEMPO and $^{14}$N-4-amino-TEMPO used to functionalize an agarose-based matrix.*

The agarose-based matrix containing TEMPO derivatives was obtained from commercial agarose containing N-hydroxysuccinimide functional groups able to react with 4-amino-TEMPO according to the following scheme:

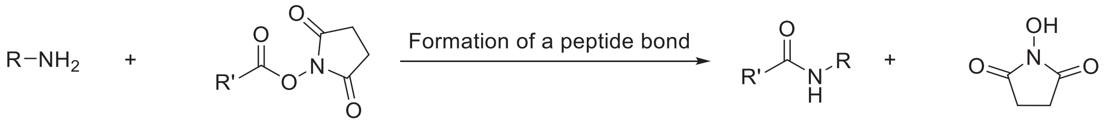

TEMPO derivative

N-hydroxysuccinimide

*Figure 22: Schematic representation of the reaction between amino-TEMPO and N-hydroxysuccinimide leading to the formation of a peptide bond.*

Interestingly, one can observe a linewidth broadening of the TEMPO EPR signals after immobilization on agarose or silica compared to corresponding TEMPO solutions recorded in the same conditions. This observation was attributed to the possibility to reach higher enhancements in the specific experimental conditions employed for this case. Moreover, the authors have claimed higher performances for the agarose matrix in contrast to the commercial silica gel but two distinct radical concentrations were used.

## B. Polymeric materials as potentiel polarizing matrices

Stimuli-responsive polymers[55] are polymer-based materials able to change their chemical and physical properties upon exposure to an external stimulus. This stimulus can be the pH, the electric/magnetic field, the mechanical force or the temperature. Since d-DNP experiments require hyperpolarization at very low temperature and fast dissolution up to room temperature, the use of thermo-responsive polymers[56-57] as polarizing matrices is promising. Above a specific temperature characteristic of each type of thermo-responsive polymer, the structure of the polymer collapses and leads to the expulsion of the liquid previously impregnated into the solid matrix.

This type of polymer was used by B. C. Dollmann et al.[58] to immobilize radicals. They prepared a statistical triblock copolymer by radical terpolymerization between N-ethyl-N-methylacrylamide (EMAAm), methacrylic acid (MMA) and 4-mehtacryloyloxybenzophenone (MABP) initiated by asobisisobutyronitrile (AIBN). The resulting polymer was further cross-linked under UV irradiation and the carboxylic residues were transformed into esters by use of $NEt_3$ and pentafluorophenyltrifluoroacetate (PFTFA) in DCM. Finally, the resulting product was functionalized by 4-amino-TEMPO and led to the expected spin-labeled thermo-responsive polymer.

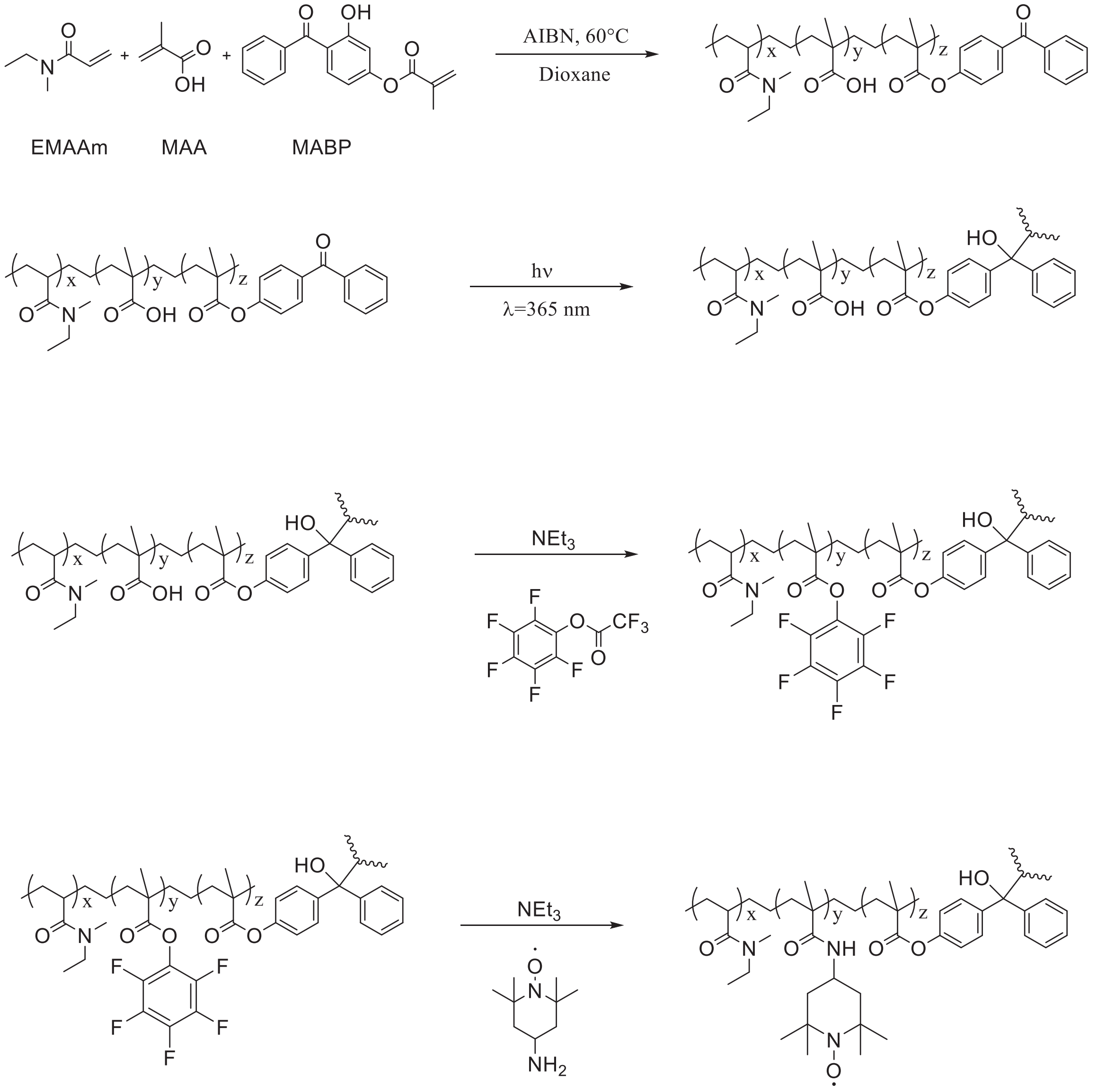

*Figure 23: Radical terpolymerization initiated by AIBN which is subsequently cross-linked by UV irradiation and finally functionalized with 4-amino-TEMPO.*

Figure 24 shows the DNP sample-formulation using such type of spin-labeled thermo-responsive polymers. The preparation consists in impregnating the spin-labeled thermo-responsive polymer with a mixture of water ($H_2O$) and the target-molecule (**Bio**). DNP experiments were further conducted, here represented schematically with the microwave irradiations, and the sample was exposed to a temperature gradient corresponding to the dissolution process using hot water. As a result, the structure of the polymer collapsed, releasing the hyperpolarized mixture of water ($H_2O$*) and target-molecule (**Bio***).

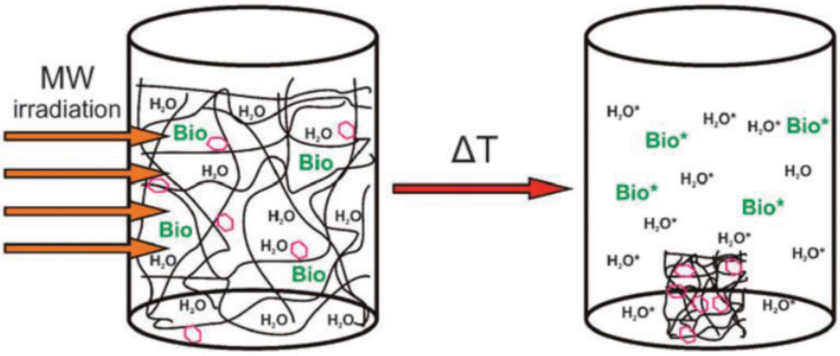

*Figure 246: Schematic representation of a spin-labeled thermoresponsive polymer used in a DNP experiment and subjected to a temperature gradient leading to the collapse of the polymer structure.*

In this publication, two spin-labeled thermo-responsive polymers were prepared with an estimated concentration of 1 mM and 6.8 mM (swollen state). These concentrations correspond respectively to 5 mol% and 15 mol% (molar). In both materials, a temperature above T = 63 °C was necessary to generate a fast (≤ 1 s) collapsing of the structure to liberate the solution. Even at low temperature, it was shown that microwave irradiations (for a microwave power $P_{\mu w}$ above 2 W), led to a local heating, inducing a partial or complete expulsion of the hyperpolarized solution. A part of the impregnated liquid was found out of the polymer and therefore too far from the polarizing agents to be efficiently polarized. A modest enhancement of $\varepsilon = 27$ was observed for water using Overhauser DNP at $B_0 = 0.345$ T.

In 2016, T. Cheng et al.[59] used the same thermo-responsive polymer (SL-hydrogel 15%) to hyperpolarize $d_{10}$-tert-butanol and [1-$^{13}$C]tert-butanol. Unfortunately, low carbon polarizations were recorded after dissolution: P($^{13}$C) = 2 % for $d_{10}$-tert-butanol and P($^{13}$C) = 3 % for [1-$^{13}$C]tert-butanol. These poor carbon polarization values were explained by an insufficient amount of TEMPO radical immobilized on the polymer and the use of an inadequate radical to polarize carbons nuclei. The use of trityl radicals was thus suggested but their accurate immobilization may be difficult as it was already for less bulky TEMPO radicals which exhibited a limited diffusion into the network of the hydrogel.

B. Vuichoud et al.[60] published the preparation of a thermo-responsive polymer which is a poly(N-isopropylacrylamide) decorated with nitroxide radicals dubbed FLAP ("Filterable

Labeled Agents for Polarization"). The synthesis of the FLAP polymer is presented in Figure 25.

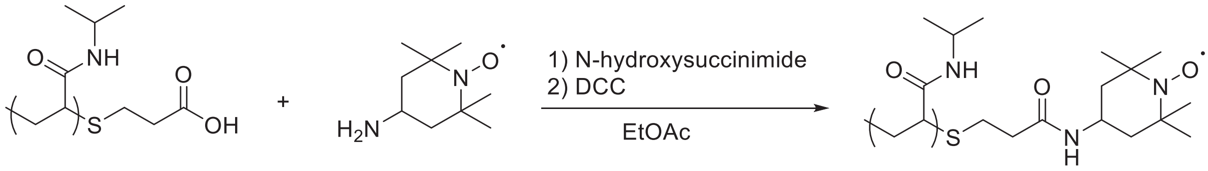

Figure 25: Synthesis of the Filterable Labeled Agents for Polarization (FLAP).

The sample preparation with the FLAP polymer consisted in impregnating 50 mg of a 25 mol% spin-labeled FLAP with 100 µL of a 1 M solution of NaCl in $H_2O$. The wetted powder was subsequently introduced in a polarizer operating at T = 1.2 K and $B_0$ = 6.7 T. Before dissolution, a proton polarization of $P(^1H) = 63{,}3$ % was recorded. Unfortunately, this value decreased as low as $P(^1H) = 6$ % after dissolution. Nonetheless, the FLAP polymer was successfully retained by the filter located in the DNP polarizer and any paramagnetic species were found in the NMR spectrometer as shown by the relaxation time of $T_1\ (^1H) = 36.6$ s. In comparison, the presence of paramagnetic species without the use of the FLAP polymer was conducted and led to a reduced relaxation time $T_1\ (^1H) = 9.8$ s. Moreover, the stability of the FLAP polymer over time was investigated by impregnating the polymer with the same solution and stored two weeks at room temperature. However after this period of time, the performances were found to decrease to *ca.* $P(^1H) = 50$ % at T = 1.2 K and $B_0$ = 6.7 T. This decrease of polarization could be attributed to the adsorption of water into the polymer as suggested by the bi-exponential $^1H$ DNP build-up curves observed after storage.

Additional d-DNP experiments were conducted after impregnation of a mixture of [1-$^{13}$C] sodium pyruvate, [1-$^{13}$C] sodium acetate and [1-$^{13}$C] alanine in the 25 % spin-labeled FLAP. A CP experiment was applied to transfer the proton polarization to the carbon nuclei and, after dissolution, the hyperpolarized liquid was transferred into a NMR tube located in a 500 MHz NMR spectrometer. Carbon polarizations of $P(^{13}C) = 8.3$ % for pyruvate, $P(^{13}C) = 7.6$ % for acetate and $P(^{13}C) = 5.9$ % for alanine were recorded. Although three metabolites were polarized at the same time, low carbon polarizations were obtained.

To summarize, FLAP polymers have provided reasonable proton polarizations at T = 1.2 K. However, the dissolution of the samples led to very low polarizations at room temperature hampering their utilization so far. It is also important to notice that a solution of sodium chloride was impregnated in the FLAP in order to prevent the polymer dissolution below 32 °C. After dissolution, the hyperpolarized liquid was not pure but contains traces of this solution of sodium chloride estimated at a concentration of 20 mM.

In recent years (2015-2017), a new and quite different approach was developed by A. Capozzi et al.[61-62] as inspired by the preliminary studies of T. Eichhorn et al.[63] While in all of the other strategies, the radicals were embedded in a solid matrix, they decided to generate free radicals using UV-irradiations at low temperature (77 K) in neat pyruvic acid or in solution with ethanol or THF. The use of photo-induced radicals is promising as these radicals can spontaneously recombine upon dissolution. However, the radical concentration in the samples was difficult to control by the exposure time to the UV-irradiations and the addition of a solvent led to different radical yields. Nevertheless, this method seems to be promising and open new perspectives for the d-DNP formulation but remained so far limited to the use of pyruvic acid.

In conclusion, through these different examples, one can notice the importance of filtering out the paramagnetic species from the hyperpolarized liquid. It is a persistent issue in all the hyperpolarization techniques: continuous flow DNP and d-DNP. In this context, our research group has developed alternative silica based polarizing matrices, dubbed HYPSO (HYbrid Polarizing SOlids) that will be described in the next section.

## C. Ordered mesoporous silica materials as potential polarizing matrices

The first generation of HYPSO solids were based on the preparation of hybrid mesostructured silicas bearing TEMPO radicals. These silica frameworks were prepared using sol-gel process and their preparation along with their use as polarizing matrices will be depicted hereafter.

Preliminary results were recently published in our group using silica solids as supports to covalently link TEMPO radicals.[64] In this publication and as shown in Figure 26, ordered mesoporous materials were prepared *via* sol-gel process techniques. The addition of a structure-directing agent such as pluronic P123 allowed to prepare a hybrid silica matrix exhibiting a 2D-hexagonal arrangement of its porous network with long parallel pore channels. These silica materials are known as SBA-15 type materials but in this case 3-azidopropylsilane fragments were incorporated in the silica solid with various loadings. In the as-obtained materials, named Mat-Azide, the surface azido groups were further converted in amino groups through a Staudinger reaction and the resulting material was quoted Mat-Amine. This reaction involved the use of a phosphine derivative to generate an iminophosphorane which was further hydrolyzed to yield to the primary amine and the phosphine oxide as by product. Although mild conditions were used, it is usually difficult to remove the phosphine oxide. Finally, the last step of this preparation consisted in a peptide coupling between the surface amino fragments and the organic radical bearing a carboxyl group. With this method, it was thus possible to incorporate nitroxide units starting from the carboxy-TEMPO or carboxy-bTurea compounds. The resulting solid matrices, denoted as Mat-TEMPO and Mat-bTUrea, were thus obtained as depicted in Figure 26.

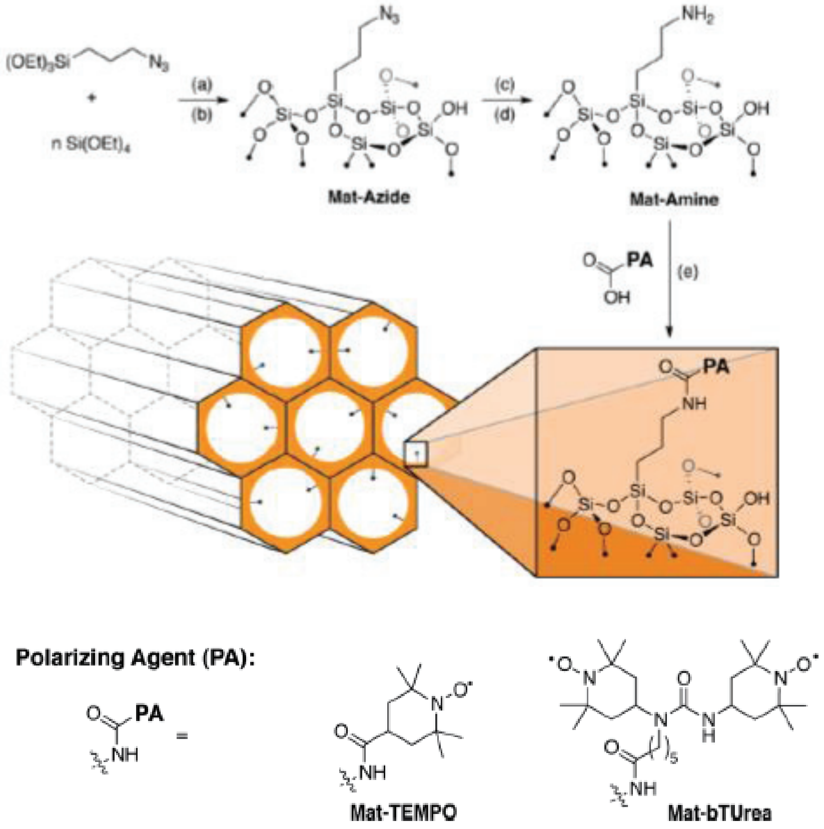

*Figure 26: Preparation of ordered mesoporous silica materials as polarizing matrices (Mat-TEMPO and Mat-bTUrea materials) by incorporation of TEMPO radicals and using sol-gel process.*

Using continuous wave electron paramagnetic resonance spectroscopy, a titration of the TEMPO units was performed and the results showed a quite low incorporation of the radical units into the final materials (from 20 % to 33 % with respect to the parent azido-containing solids).

After extensive characterization of the materials, their performances were evaluated in Magic Angle Spinning DNP (MAS-DNP). Mat-TEMPO matrices were impregnated with 1,1,2,2-Tetrachloroethane or water and the NMR spectra were recorded at 100K with or without microwave irradiation to determine the enhancement factors of $^{1}$H ($\varepsilon_{H}$), $^{13}$C ($\varepsilon_{C\ CP}$) and $^{29}$Si ($\varepsilon_{Si\ CP}$). The carbon or silicon enhancements were not obtained by direct polarization but by cross-polarization from the protons of the impregnated liquid. Results are plotted in the two graphs of the Figure 27.

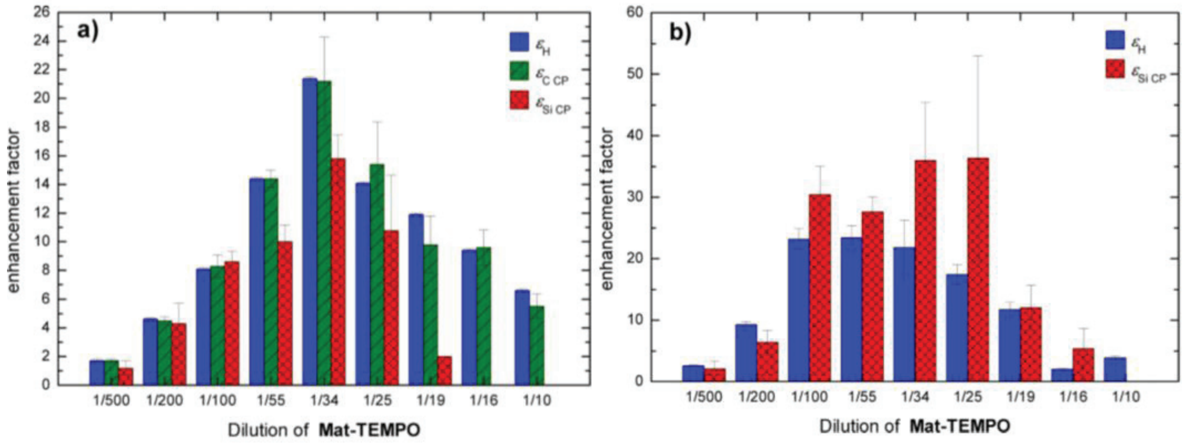

*Figure 27: a) Enhancement factors of the $^{1}$H, $^{13}$C and $^{29}$Si as a function of the radical concentration for the Mat-TEMPO impregnated with 1,1,2,2-Tetrachloroethane b) Enhancement factors of the $^{1}$H, $^{13}$C and $^{29}$Si as a function of the radical concentration for the Mat-TEMPO impregnated with water.*

First of all, as shown in Figure 27.a), one can notice the existence of an optimal radical concentration for a starting dilution of 1/34 in azido groups giving thus the maximal enhancements of [$\varepsilon_{H}$, $\varepsilon_{C\ CP}$, $\varepsilon_{Si\ CP}$] = [21, 21, 16]. In figure 10.b), the Mat-TEMPO materials impregnated with water gave similar results with optimum results for 1/34 and 1/25 diluted materials. The enhancement factors were [$\varepsilon_{H}$, $\varepsilon_{Si\ CP}$] = [22, 36] and [$\varepsilon_{H}$, $\varepsilon_{Si\ CP}$] = [17, 36] respectively. These experiments highlight the possibility to polarize liquid without using glass-forming agent. The good polarization values for MAS DNP can be explained by a regular distribution of the radicals within the pores of the polarizing matrices as well as the control over the inter-radical distances.

Because of the potential of these polarizing matrices for DNP applications and more specifically *in-vivo* applications, labeled metabolic tracers were impregnated. An aqueous solution of [2,3-$^{13}$C]-L-alanine and [1-$^{13}$C] pyruvic acid dissolved in water were impregnated into 1/34-Mat-TEMPO and $^{13}$C CP MAS NMR spectra with or without microwave irradiations were recorded. First results revealed an enhancement factor $\varepsilon_{C\ CP}$ = 39 for labeled alanine and $\varepsilon_{C\ CP}$ = 36 for pyruvic acid.

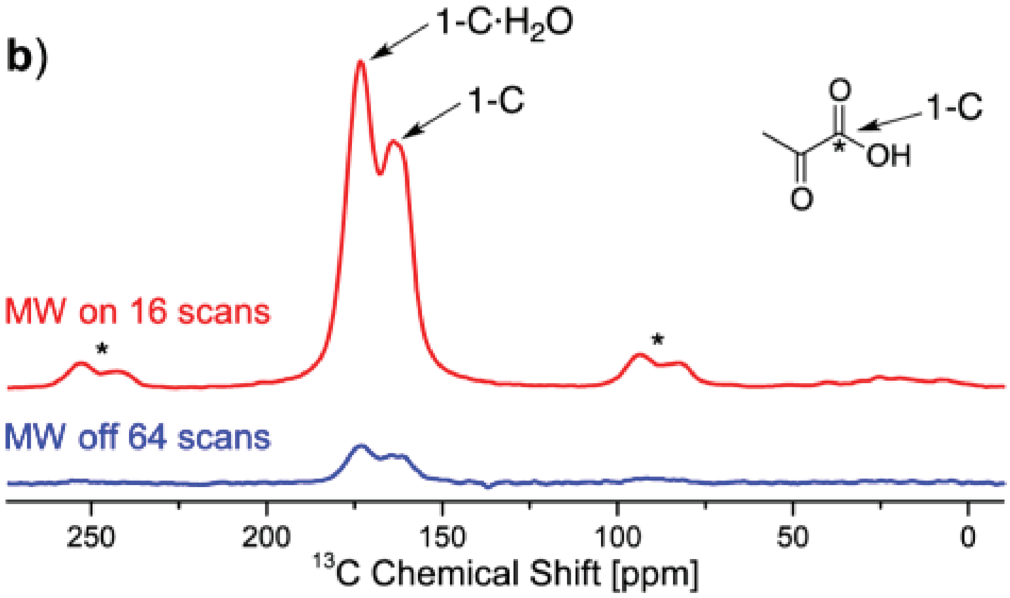

*Figure 28: Carbon enhancement of the [1-$^{13}$C] pyruvic acid after CP MAS and using 1/34 Mat-TEMPO. From the left to the right, the stars correspond to the keto and the 2-hydrated pyruvic acid.*[1-2]

Again, promising results were found here and led to further developments of such solids for d-DNP applications (vide infra).

The aforementioned ordered mesoporous SBA-15 type materials, dubbed HYPSO 1, were first used in d-DNP and published in a “Proceedings of National Academy of Sciences of the United states of America” article.[65] Here, the d-DNP experiments were performed with a magnetic field $B_0$ = 6.7 T and temperature T = 1.2 K (the home-built d-DNP polarizer is presented in this chapter part. I-E). Optimal HYPSO 1 with a concentration of 88 µmol of radical per gram was divided into three portions of 20 mg and impregnated with the following solutions: A) 3M solution of sodium [1-$^{13}$C] pyruvate in $D_2O/H_2O$ (9/1) B) 3 M solution of sodium [1-$^{13}$C] acetate in $D_2O/H_2O$ (9/1) and C) a mixture of sodium fumarate ($CH_3CH(NH_2)^{13}CONHCH_2{}^{13}COOH$) and alanine-glycine in $D_2O/H_2O$ (9/1). After insertion of the polarizing matrix in the d-DNP polarizer, CP experiments were used to transfer the high electron polarization to the protons and finally the carbons of the impregnated liquid. Finally, each sample was dissolved by means of hot pressurized water and HYPSO 1 was filtered through a simple cellulose fiber filter settled in the d-DNP polarizer. The hyperpolarized solutions were then analyzed by $^{13}$C liquid state NMR with a spectrometer (300 MHz) and compared to their thermal equilibrium (Fig. 29).

After dissolution and comparison with their thermal equilibrium, P($^{13}$C) = 16,5 % and P($^{13}$C) = 25,3 % were respectively recorded for the hyperpolarized solution of sodium [1-$^{13}$C] acetate and the hyperpolarized solution of sodium [1-$^{13}$C] pyruvate (Fig. 29 A. and

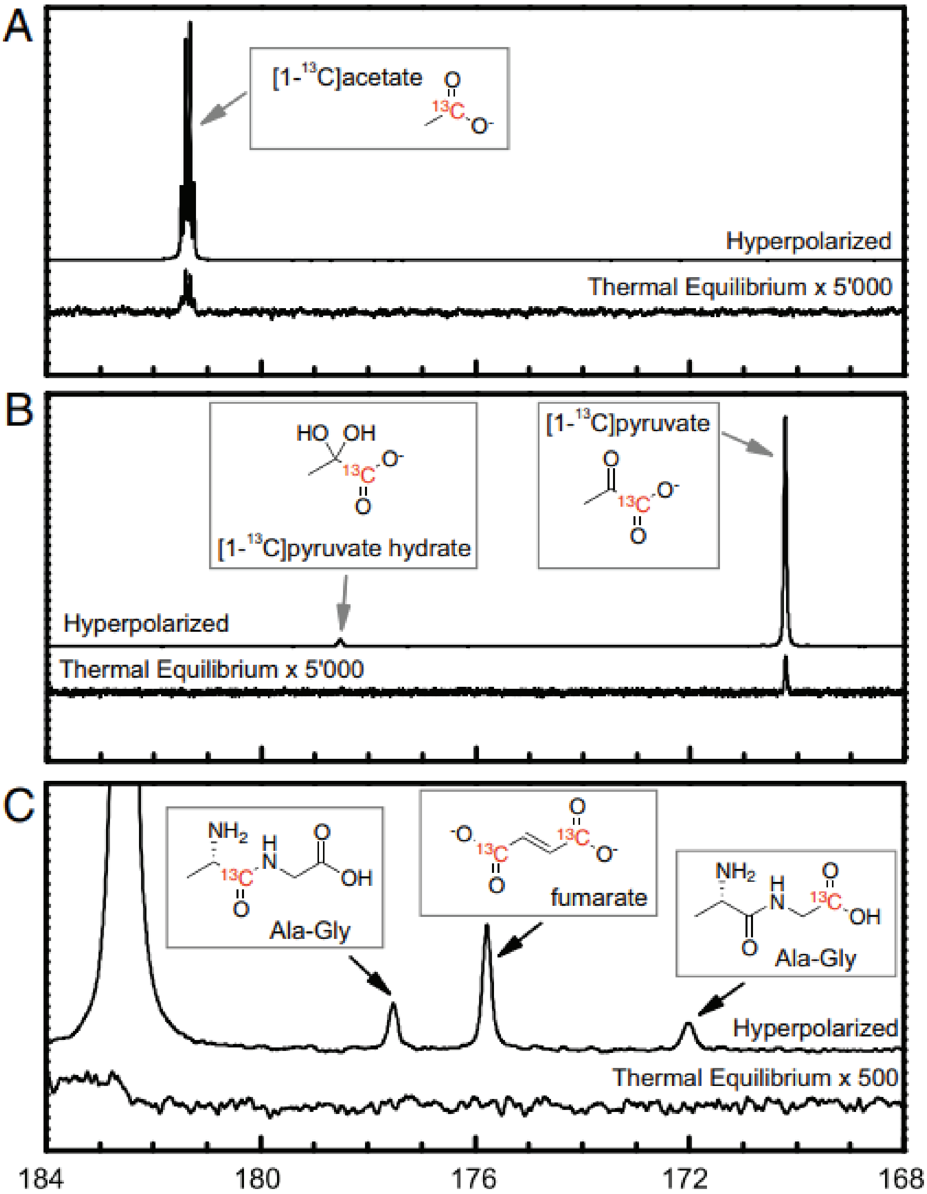

*Figure 29: $^{13}$C NMR spectrum after hyperpolarization of [1-$^{13}$C] acetate (A), [1-$^{13}$C] pyruvate (B), L-alanine-glycine and fumarate (C) using HYPSO 1. In each example, the hyperpolarized signal is compared to its thermal equilibrium.*

B.). In order to show the diversity of solutions which can be hyperpolarized, the polarization of a mixture of fumarate and alanine-glycine was also recorded. The two carbonyl carbons of fumarate gave $P(^{13}C) = 19{,}9\ \%$ and the alanine-glycine $P(^{13}C) = 15\ \%$ & $P(^{13}C) = 13{,}6\ \%$.These first results are promising and highlights the potential of HYPSO materials in d-DNP. The strong immobilization of the TEMPO radicals (no leaching of the radicals) onto the polarizing matrices was also assessed after dissolution by measuring the $^{13}C$ T1 which was *ca.*50 s.

One of the main advantages of these polarizing matrices, beside the absence of radicals in the hyperpolarized solutions, could be the possibility to polarize samples without using a glass-forming agent as far as no agglomeration of radical can occur due to their homogeneous distribution along the silica pore channels. It was proven without any doubt by comparison of the DNP performances of a typical DNP juice containing glass-forming agents and HYPSO materials without glass-forming agents. For this purpose, the HYPSO 1 material was impregnated with a mixture of $H_2O:D_2O$ (1:9) and a typical DNP juice composed of $H_2O:D_2O$:glycerol-$d_8$ ([10:40:50 (vol:vol:vol)]) was prepared. Both samples were polarized and the $^1H$ DNP build-up curves exhibited a quite comparable feature at T = 4.2 K (see Figure 30).

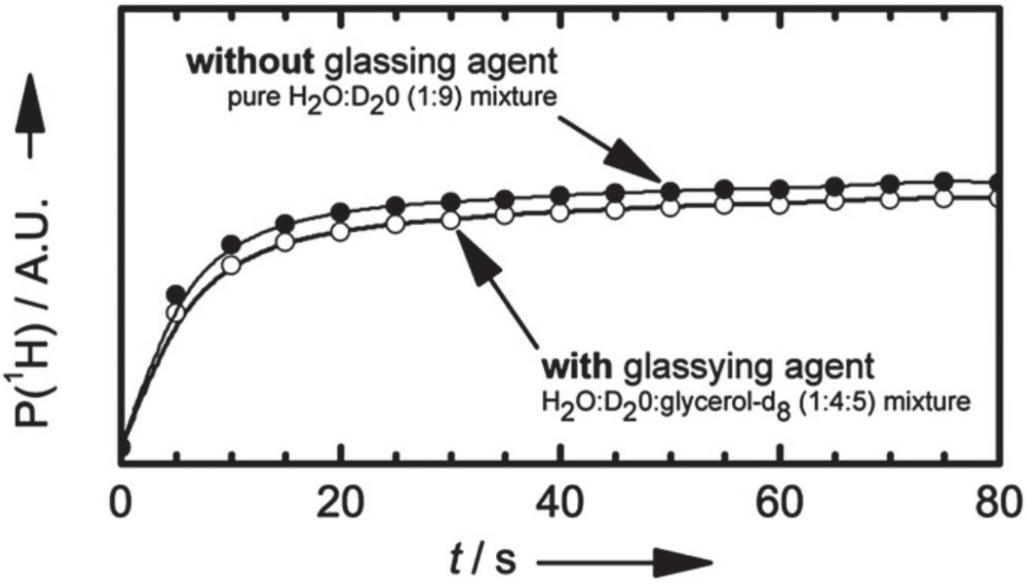

*Figure 30: $^1H$ DNP build-up curves as a function of the time for HYPSO 1 impregnated with or without a glass-forming agent at T= 4.2 K.*

In this publication, indirect cross-polarization $^1H \rightarrow {}^{13}C$ using TEMPO radicals was favored rather than direct polarization with trityl radicals because the polarization transfer was faster. For instance, a carbon polarization $P(^{13}C) = 40\ \%$ was reached in 20 minutes and measured after dissolution. Nevertheless, since cross-polarization is not commercially available, one would prefer direct $^{13}C$ polarization with trityl radicals which are the more suitable radicals in this case. Hence, using the same synthesis, TEMPO radicals were replaced by trityl radicals and the obtained materials were called HYPSO 1.2. Only one material with a radical concentration of 16 µmol/g was impregnated with a 3M solution of [1-$^{13}$C] pyruvate in $D_2O$. As shown in Figure 31, the direct polarization of $P(^{13}C) = 15\ \%$ was reached within 2 hours. The DNP build-up time was fitted with a mono-exponential function displaying a $\tau_{DNP}\ (^{13}C) = 104.6$ min and giving a carbon polarization of $P(^{13}C) = 22.9\ \%$ at saturation.

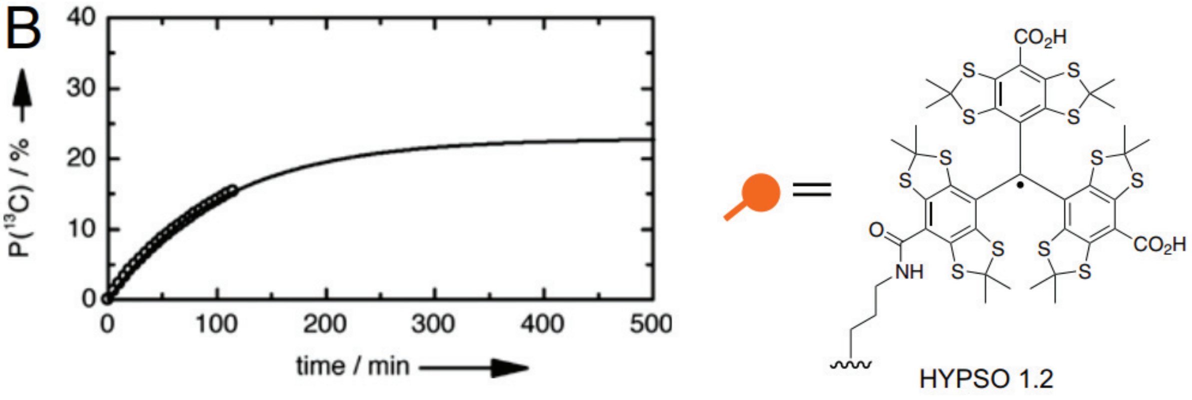

*Figure 31: Direct $^{13}C$ polarization of a 3 M solution of [1-$^{13}$C] pyruvate previously impregnated into HYPSO 1.2.*

Based on these results, a new strategy to synthesize HYPSOs was investigated in order to increase the radical incorporation yield. The radical incorporation was performed by a click reaction (copper catalyzed cycloaddition, CuAAC) between the surface azido fragments and the TEMPO radical bearing alkynyl group. The newly synthesized solids (HYPSO 2) allowed to reach $P(^{13}C) > 30\ \%$ in the polarizer after impregnation of a 3M solution of sodium [1-$^{13}$C] pyruvate. As these results are part of this PhD, they will be presented in chapter 2.

In conclusion, ordered mesoporous materials containing TEMPO radicals were synthesized using a multi-step synthesis. However, EPR experiments showed a quite low conversion of the azido surface fragments into the corresponding polarizing agents when using a peptide coupling. For the first time, Mat-TEMPO (HYPSO 1) matrices were used as polarizing supports in MAS-DNP. The enhancement factors of $[\varepsilon_{H}, \varepsilon_{C\ CP}, \varepsilon_{Si\ CP}] = [21, 21, 16]$ were measured for the optimal 1/34 Mat-TEMPO material impregnated with 1,1,2,2-Tetrachloroethane. Additional experiments consisting in impregnating water in the Mat-TEMPO (HYPSO 1) matrices gave maximum enhancement factors of $[\varepsilon_{H,}\ \varepsilon_{Si\ CP}] = [22, 36]$ and $[\varepsilon_{H,}\ \varepsilon_{Si\ CP}] = [17, 36]$ for the dilutions 1/34 and 1/25 respectively. As *in-vivo* applications could be one of the major utilization of these polarizing matrices, preliminary results were obtained for the polarization of [2,3-$^{13}$C]-L-alanine and [1-$^{13}$C] pyruvic acid in MAS DNP. Enhancement factors of $\varepsilon_{C\ CP} = 39$ and $\varepsilon_{C\ CP} = 36$ respectively were measured using 1/34 Mat-TEMPO material.

Using a d-DNP set-up, the impregnation of HYPSO 1 ([R] = 88 µmol/g) with a solution of sodium [1-$^{13}$C] acetate, sodium [1-$^{13}$C] pyruvate and a mixture of fumarate/alanine-glycine led to P($^{13}$C) = 16.5 %, P($^{13}$C) = 25.3 %, P($^{13}$C) = 19.9 %, P($^{13}$C) = 15 % / P($^{13}$C) = 13.6 % respectively, after dissolution. Even after the dissolution process, the radicals remained strongly attached onto the silica supports (as shown by the important $^{13}$C T1 *ca.* 50 s) and the advantage of using these matrices without any glass-forming agents was also demonstrated. Although the previous results were measured using indirect cross-polarization $^{1}$H -> $^{13}$C, direct $^{13}$C polarization was inspected with HYPSO 1.2 materials containing trityl radicals as polarizing agents. As expected, a long build-up time was measured with a potential maximum polarization of P($^{13}$C) = 22.9 %.

These results are encouraging and prompted us to develop other polarization matrices to reach higher polarization values, which is the goal of this PhD project.

# IV. References

1. Hellstrom, N.; Almqvist, S.-O., Hydration and dehydration of pyruvic acid. *Journal of the Chemical Society B: Physical Organic* **1970,** (0), 1396-1400.
2. Margolis, S. A.; Coxon, B., Identification and quantitation of the impurities in sodium pyruvate. *Analytical Chemistry* **1986,** *58* (12), 2504-2510.
3. Basile, V., Novel sample formulations for pure and persistent hyperpolarized solutions via dissolution dynamic nuclear polarization **2017**.
4. Maroń, M. K.; Takahashi, K.; Shoemaker, R. K.; Vaida, V., Hydration of pyruvic acid to its geminal-diol, 2,2-dihydroxypropanoic acid, in a water-restricted environment. *Chemical Physics Letters* **2011,** *513* (4), 184-190.
5. Hirsch, M. L.; Kalechofsky, N.; Belzer, A.; Rosay, M.; Kempf, J. G., Brute-Force Hyperpolarization for NMR and MRI. *Journal of the American Chemical Society 137* (26), 8428-8434.
6. Krjukov, E. V.; O'Neill, J. D.; Owers-Bradley, J. R., Brute Force Polarization of 129Xe. *Journal of Low Temperature Physics* **2005,** *140* (5), 397-408.
7. Hirsch, M. L.; Smith, B. A.; Mattingly, M.; Goloshevsky, A. G.; Rosay, M.; Kempf, J. G., Transport and imaging of brute-force 13C hyperpolarization. *Journal of Magnetic Resonance* **2015,** *261*, 87-94.
8. Carver, T. R.; Slichter, C. P., Polarization of Nuclear Spins in Metals. *Physical Review* **1953,** *92* (1), 212-213.
9. Megiel, E., Surface modification using TEMPO and its derivatives. *Advances in Colloid and Interface Science* **2017,** *250*, 158-184.
10. Gertz I. Likhtenshtein, J. Y., Shin'ichi Nakatsuji, Alex I. Smirnov, Rui Tamura, Nitroxides: applications in chemistry, biomedicine and materials science. **2008**.
11. Tebben, L.; Studer, A., Nitroxides: Applications in Synthesis and in Polymer Chemistry. *Angewandte Chemie International Edition* **2011,** *50* (22), 5034-5068.
12. Nicolas, J.; Guillaneuf, Y.; Lefay, C.; Bertin, D.; Gigmes, D.; Charleux, B., Nitroxide-mediated polymerization. *Progress in Polymer Science* **2013,** *38* (1), 63-235.
13. Vogler, T.; Studer, A., Applications of TEMPO in Synthesis. *Synthesis* **2008,** *2008* (13), 1979-1993.
14. Zhonggao Zhou and Liangxian, L., TEMPO and its Derivatives: Synthesis and Applications. *Current Organic Chemistry* **2014,** *18* (4), 459-474.
15. Nesterova, O. V.; Nesterov, D. S.; Krogul-Sobczak, A.; Guedes da Silva, M. F. C.; Pombeiro, A. J. L., Synthesis, crystal structures and catalytic activity of Cu(II) and Mn(III) Schiff base complexes: Influence of additives on the oxidation catalysis of cyclohexane and 1-phenylehanol. *Journal of Molecular Catalysis A: Chemical* **2017,** *426*, 506-515.
16. Soule, B. P.; Hyodo, F.; Matsumoto, K.-i.; Simone, N. L.; Cook, J. A.; Krishna, M. C.; Mitchell, J. B., The chemistry and biology of nitroxide compounds. *Free Radical Biology and Medicine* **2007,** *42* (11), 1632-1650.
17. Aurélien, B., De l'usage des protons, hyperpolarisés pour augmenter la sensibilité de la RMN. **2015**.
18. Milani, J.; Vuichoud, B.; Bornet, A.; Miéville, P.; Mottier, R.; Jannin, S.; Bodenhausen, G., A magnetic tunnel to shelter hyperpolarized fluids. *Review of Scientific Instruments* **2015,** *86* (2), 024101.

19. Ardenkjaer-Larsen, J. H.; Fridlund, B. r.; Gram, A.; Hansson, G.; Hansson, L.; Lerche, M. H.; Servin, R.; Thaning, M.; Golman, K., Increase in signal-to-noise ratio of > 10,000 times in liquid-state NMR. *Proceedings of the National Academy of Sciences* **2003,** *100* (18), 10158-10163.

20. Comment, A.; Van den Brandt, V.; Uffmann, K.; Kurdzesau, F.; Jannin, S.; Konter, J.A.; Hautle, P.; Wenckebach, W.Th.; Gruetter, R.; Van der Klink, J.J., Design and performance of a DNP prepolarizer coupled to a rodent MRI scanner. *Concepts in Magnetic Resonance Part B: Magnetic Resonance Engineering* **2007,** *31B* (4), 255-269.

21. Pinto, L. F.; Marin-Montesinos, I.; Lloveras, V.; Munoz-Gomez, J. L.; Pons, M.; Veciana, J.; Vidal-Gancedo, J., NMR signal enhancement of >50 000 times in fast dissolution dynamic nuclear polarization. *Chemical Communications* **2017,** *53* (26), 3757-3760.

22. Nitroxide Radicals: Properties, Synthesis and Applications. In *Stable Radicals*.

23. Kubicki, D. J.; Casano, G.; Schwarzwalder, M.; Abel, S.; Sauvee, C.; Ganesan, K.; Yulikov, M.; Rossini, A. J.; Jeschke, G.; Coperet, C.; Lesage, A.; Tordo, P.; Ouari, O.; Emsley, L., Rational design of dinitroxide biradicals for efficient cross-effect dynamic nuclear polarization. *Chemical Science* **2016,** *7* (1), 550-558.

24. Muñoz-Gómez, J.-L.; Marín-Montesinos, I.; Lloveras, V.; Pons, M.; Vidal-Gancedo, J.; Veciana, J., Novel PTM–TEMPO Biradical for Fast Dissolution Dynamic Nuclear Polarization. *Organic Letters* **2014,** *16* (20), 5402-5405.

25. Miéville, P.; Ahuja, P.; Sarkar, R.; Jannin, S.; Vasos, P. R.; Gerber-Lemaire, S.; Mishkovsky, M.; Comment, A.; Gruetter, R.; Ouari, O.; Tordo, P.; Bodenhausen, G., Scavenging Free Radicals To Preserve Enhancement and Extend Relaxation Times in NMR using Dynamic Nuclear Polarization. *Angewandte Chemie International Edition* **2010,** *49* (35), 6182-6185.

26. Bielski, B. H. J.; Allen, A. O.; Schwarz, H. A., Mechanism of the disproportionation of ascorbate radicals. *Journal of the American Chemical Society* **1981,** *103* (12), 3516-3518.

27. Harris, T.; Bretschneider, C.; Frydman, L., Dissolution DNP NMR with solvent mixtures: Substrate concentration and radical extraction. *Journal of Magnetic Resonance* **2011,** *211* (1), 96-100.

28. Ardenkjaer-Larsen, J. H.; Leach, A. M.; Clarke, N.; Urbahn, J.; Anderson, D.; Skloss., T. W., Dynamic nuclear polarization polarizer for sterile use intent. *NMR in Biomedicine* **2011,** *24* (8), 927-932.

29. Leach AM, M. P., Telfeyan E, Whitt DB, General Electric Co. (2009) Method and apparatus for the dissolution and filtration of a hyperpolarized agent with a neutral dissolution media. US Patent US2009263325-A1.

30. Hovav, Y.; Feintuch, A.; Vega, S.; Goldfarb, D., Dynamic nuclear polarization using frequency modulation at 3.34T. *Journal of Magnetic Resonance* **2014,** *238*, 94-105.

31. Bornet, A.; Milani, J.; Vuichoud, B.; Perez Linde, A. J.; Bodenhausen, G.; Jannin, S., Microwave frequency modulation to enhance Dissolution Dynamic Nuclear Polarization. *Chemical Physics Letters* **2014,** *602*, 63-67.

32. Niedbalski, P.; Parish, C.; Kiswandhi, A.; Kovacs, Z.; Lumata, L., Influence of $^{13}$C Isotopic Labeling Location on Dynamic Nuclear Polarization of Acetate. *The Journal of Physical Chemistry A* **2017,** *121* (17), 3227-3233.

33. Hurd, R. E.; Yen, Y.-F.; Chen, A.; Ardenkjaer-Larsen, J. H., Hyperpolarized $^{13}$C metabolic imaging using dissolution dynamic nuclear polarization. *Journal of Magnetic Resonance Imaging* **2012,** *36* (6), 1314-1328.

34. Barb, A. W.; Hekmatyar, S. K.; Glushka, J. N.; Prestegard, J. H., Exchange facilitated indirect detection of hyperpolarized $^{15}ND_2$-amido-glutamine. *Journal of Magnetic Resonance* **2011,** *212* (2), 304-310.

35. Schroeder, M. A.; Atherton, H. J.; Ball, D. R.; Cole, M. A.; Heather, L. C.; Griffin, J. L.; Clarke, K.; Radda, G. K.; Tyler, D. J., Real-time assessment of Krebs cycle metabolism using hyperpolarized 13C magnetic resonance spectroscopy. *The FASEB Journal* **2009,** *23* (8), 2529-2538.

36. Marjańska, M.; Iltis, I.; Shestov, A. A.; Deelchand, D. K.; Nelson, C.; Uğurbil, K.; Henry, P.-G., In vivo 13C spectroscopy in the rat brain using hyperpolarized [1-$^{13}$C]pyruvate and [2-$^{13}$C]pyruvate. *Journal of Magnetic Resonance* **2010,** *206* (2), 210-218.

37. Chen, A. P.; Hurd, R. E.; Schroeder, M. A.; Lau, A. Z.; Gu, Y.-P.; Lam, W. W.; Barry, J.; Tropp, J.; Cunningham, C. H., Simultaneous investigation of cardiac pyruvate dehydrogenase flux, Krebs cycle metabolism and pH, using hyperpolarized [1,2-$^{13}C_2$]pyruvate in vivo. *NMR in Biomedicine* **2012,** *25* (2), 305-311.

38. Chen, A. P.; Kurhanewicz, J.; Bok, R.; Xu, D.; Joun, D.; Zhang, V.; Nelson, S. J.; Hurd, R. E.; Vigneron, D. B., Feasibility of using hyperpolarized [1-$^{13}$C]Lactate as a substrate for in vivo metabolic $^{13}$C MRSI studies. *Magnetic Resonance Imaging* **2008,** *26* (6), 721-726.

39. Gallagher, F. A.; Kettunen, M. I.; Day, S. E.; Hu, D.-E.; Ardenkjær-Larsen, J. H.; Zandt, R. i. t.; Jensen, P. R.; Karlsson, M.; Golman, K.; Lerche, M. H.; Brindle, K. M., Magnetic resonance imaging of pH in vivo using hyperpolarized 13C-labelled bicarbonate. *Nature* **2008,** *453*, 940.

40. Gallagher, F. A.; Kettunen, M. I.; Hu, D.-E.; Jensen, P. R.; Zandt, R. i. t.; Karlsson, M.; Gisselsson, A.; Nelson, S. K.; Witney, T. H.; Bohndiek, S. E.; Hansson, G.; Peitersen, T.; Lerche, M. H.; Brindle, K. M., Production of hyperpolarized [1,4-$^{13}C_2$]malate from [1,4-$^{13}C_2$]fumarate is a marker of cell necrosis and treatment response in tumors. *Proceedings of the National Academy of Sciences* **2009,** *106* (47), 19801-19806.

41. Chen, A. P.; Hurd, R. E.; Gu, Y.-P.; Wilson, D. M.; Cunningham, C. H., $^{13}$C MR reporter probe system using dynamic nuclear polarization. *NMR in Biomedicine* **2011,** *24* (5), 514-520.

42. Keshari, K. R.; Wilson, D. M.; Chen, A. P.; Bok, R.; Larson, P. E. Z.; Hu, S.; Criekinge, M. V.; Macdonald, J. M.; Vigneron, D. B.; Kurhanewicz, J., Hyperpolarized [2-$^{13}$C]-Fructose: A Hemiketal DNP Substrate for In Vivo Metabolic Imaging. *Journal of the American Chemical Society* **2009,** *131* (48), 17591-17596.

43. Gallagher, F. A.; Kettunen, M. I.; E., Day, S. E.; Hu, D. E.; Karlsson, M.; Gisselsson, A.; Lerche, M. H.; Brindle, K. M., Detection of tumor glutamate metabolism in vivo using 13C magnetic resonance spectroscopy and hyperpolarized [1-$^{13}$C]glutamate. *Magnetic Resonance in Medicine* **2011,** *66* (1), 18-23.

44. Hurd, R. E.; Yen, Y. F.; Mayer, D.; Chen, A.; Wilson, D.; Kohler, S.; Bok, R.; Vigneron, D.; Kurhanewicz, J.; Tropp, J.; Spielman, D.; Pfefferbaum, A., Metabolic imaging in the anesthetized rat brain using hyperpolarized [1-13C] pyruvate and [1-$^{13}$C] ethyl pyruvate. *Magnetic Resonance in Medicine* **2010,** *63* (5), 1137-1143.

45. Wilson, D. M.; Hurd, R. E.; Keshari, K.; Van Criekinge, M.; Chen, A. P.; Nelson, S. J.; Vigneron, D. B.; Kurhanewicz, J., Generation of hyperpolarized substrates by secondary labeling with [1,1-$^{13}$C] acetic anhydride. *Proceedings of the National Academy of Sciences* **2009,** *106* (14), 5503-5507.

46. Mikkelsen, E. F. R.; Mariager, C. Ø.; Nørlinger, T.; Qi, H.; Schulte, R. F.; Jakobsen, S.; Frøkiær, J.; Pedersen, M.; Stødkilde-Jørgensen, H.; Laustsen, C., Hyperpolarized [1-13C]-acetate Renal Metabolic Clearance Rate Mapping. *Scientific Reports* **2017,** *7* (1), 16002.

47. Golman, K.; Ardenkjær-Larsen, J. H.; Petersson, J. S.; Månsson, S.; Leunbach, I., Molecular imaging with endogenous substances. *Proceedings of the National Academy of Sciences* **2003,** *100* (18), 10435-10439.

48. Bohndiek, S. E.; Kettunen, M. I.; Hu, D.-e.; Kennedy, B. W. C.; Boren, J.; Gallagher, F. A.; Brindle, K. M., Hyperpolarized [1-$^{13}$C]-Ascorbic and Dehydroascorbic Acid: Vitamin C as a Probe for Imaging Redox Status in Vivo. *Journal of the American Chemical Society* **2011,** *133* (30), 11795-11801.

49. Keshari, K. R.; Kurhanewicz, J.; Bok, R.; Larson, P. E. Z.; Vigneron, D. B.; Wilson, D. M., Hyperpolarized $^{13}$C dehydroascorbate as an endogenous redox sensor for in vivo metabolic imaging. *Proceedings of the National Academy of Sciences* **2011,** *108* (46), 18606-18611.

50. Jensen, P. R.; Karlsson, M.; Meier, S.; Duus, J. O.; Lerche, M. H., Hyperpolarized Amino Acids for In Vivo Assays of Transaminase Activity. *Chemistry – A European Journal* **2009,** *15* (39), 10010-10012.

51. Bruck, D.; Dudley, R.; Fyfe, C. A.; Van Delden, J., Sample magnetization using immobilized free radicals for use in flow NMR systems. *Journal of Magnetic Resonance (1969)* **1981,** *42* (1), 51-59.

52. Gitti, R.; Wild, C.; Tsiao, C.; Zimmer, K.; Glass, T. E.; Dorn, H. C., Solid/liquid intermolecular transfer of dynamic nuclear polarization. Enhanced flowing fluid proton NMR signals via immobilized spin labels. *Journal of the American Chemical Society* **1988,** *110* (7), 2294-2296.

53. Flow NMR. In *eMagRes*.

54. McCarney, E. R.; Han, S., Spin-labeled gel for the production of radical-free dynamic nuclear polarization enhanced molecules for NMR spectroscopy and imaging. *Journal of Magnetic Resonance* **2008,** *190* (2), 307-315.

55. Wei, M.; Gao, Y.; Li, X.; Serpe, M. J., Stimuli-responsive polymers and their applications. *Polymer Chemistry* **2017,** *8* (1), 127-143.

56. Bioseparation Using Thermoresponsive Polymers. In *Encyclopedia of Biocolloid and Biointerface Science 2V Set*.

57. Mohammed, M. N.; Yusoh, K. B.; Shariffuddin, J. H. B. H., Poly(N-vinyl caprolactam) thermoresponsive polymer in novel drug delivery systems: A review. *Materials Express* **2018,** *8* (1), 21-34.

58. Dollmann, B. C.; Junk, M. J. N.; Drechsler, M.; Spiess, H. W.; Hinderberger, D.; Munnemann, K., Thermoresponsive, spin-labeled hydrogels as separable DNP polarizing agents. *Physical Chemistry Chemical Physics* **2010,** *12* (22), 5879-5882.

59. Cheng, T.; Mishkovsky, M.; Junk, M. J.; Münnemann, K.; Comment, A., Producing Radical-Free Hyperpolarized Perfusion Agents for In Vivo Magnetic Resonance Using Spin-Labeled Thermoresponsive Hydrogel. *Macromolecular Rapid Communications* **2016,** *37* (13), 1074-1078.

60. Vuichoud, B.; Bornet, A.; De Nanteuil, F.; Milani, J.; Canet, E.; Ji, X.; Miéville, P.; Weber, E.; Kurzbach, D.; Flamm, A.; Konrat, R.; Gossert, A. D.; Jannin, S.; Bodenhausen, G., Filterable Agents for Hyperpolarization of Water, Metabolites, and Proteins. *Chemistry – A European Journal* **2016,** *22* (41), 14696-14700.

61. Capozzi, A.; Hyacinthe, J.-N.; Cheng, T.; Eichhorn, T. R.; Boero, G.; Roussel, C.; van der Klink, J. J.; Comment, A., Photoinduced Nonpersistent Radicals as Polarizing Agents for X-Nuclei Dissolution Dynamic Nuclear Polarization. *The Journal of Physical Chemistry C* **2015,** *119* (39), 22632-22639.

62. Capozzi, A.; Cheng, T.; Boero, G.; Roussel, C.; Comment, A., Thermal annihilation of photo-induced radicals following dynamic nuclear polarization to produce transportable frozen hyperpolarized 13C-substrates. *Nature Communications* **2017,** *8*, 15757.

63. Eichhorn, T. R.; Takado, Y.; Salameh, N.; Capozzi, A.; Cheng, T.; Hyacinthe, J.-N.; Mishkovsky, M.; Roussel, C.; Comment, A., Hyperpolarization without persistent radicals for in vivo real-time metabolic imaging. *Proceedings of the National Academy of Sciences* **2013,** *110* (45), 18064-18069.

64. Gajan, D.; Schwarzwälder, M.; Conley, M. P.; Grüning, W. R.; Rossini, A. J.; Zagdoun, A.; Lelli, M.; Yulikov, M.; Jeschke, G.; Sauvée, C.; Ouari, O.; Tordo, P.; Veyre, L.; Lesage, A.; Thieuleux, C.; Emsley, L.; Copéret, C., Solid-Phase Polarization Matrixes for Dynamic Nuclear Polarization from Homogeneously Distributed Radicals in Mesostructured Hybrid Silica Materials. *Journal of the American Chemical Society* **2013,** *135* (41), 15459-15466.

65. Gajan, D.; Bornet, A.; Vuichoud, B.; Milani, J.; Melzi, R.; van Kalkeren, H. A.; Veyre, L.; Thieuleux, C.; Conley, M. P.; Grüning, W. R.; Schwarzwälder, M.; Lesage, A.; Copéret, C.; Bodenhausen, G.; Emsley, L.; Jannin, S., Hybrid polarizing solids for pure hyperpolarized liquids through dissolution dynamic nuclear polarization. *Proceedings of the National Academy of Sciences* **2014,** *111* (41), 14693-14697.

# Chapter 2: Hybrid Polarizing Solids based on ordered mesoporous silica

# Table of contents

# I. Introduction

Porous solids are classified according to the International Union of Pure and Applied Chemistry (IUPAC) in three categories:[1]

- Microporous solids with a pore diameter below 2 nm
- Mesoporous solids including all the porous solids with a pore diameter ranging from 2 nm to 50 nm
- Macroporous solids with large pores exceeding 50 nm

Made of a crystalline aluminosilicate network, zeolites belong to the microporous solids family. The framework of these porous solids is composed of a tetrahedral arrangement of inorganic units where the central cations are surrounded by four oxygen atoms occupying each apex ($[SiO_4]^{4-}$ or $[AlO_4]^{5-}$). Their physical and chemical properties made them good candidates for purification of water,[2] catalysis (ZSM5, USY zeolites),[3-4] energy storage[5] and ion exchange.[6] Other types of materials such as Metal-Organic Frameworks (MOFs) have also a microporous structure. This specific structure is composed of single metallic ions or clusters of metallic ions linked by organic molecules. The choice of the units, metals and organic linkers, is important since the properties of the as-obtained materials will depend on it. Applications using MOFs ranging from catalysis,[7] separation to sensors[8] can be found in the literature. However, the small pores size becomes a limitation if the size of the substrates to be studied exceeds the pore dimension.

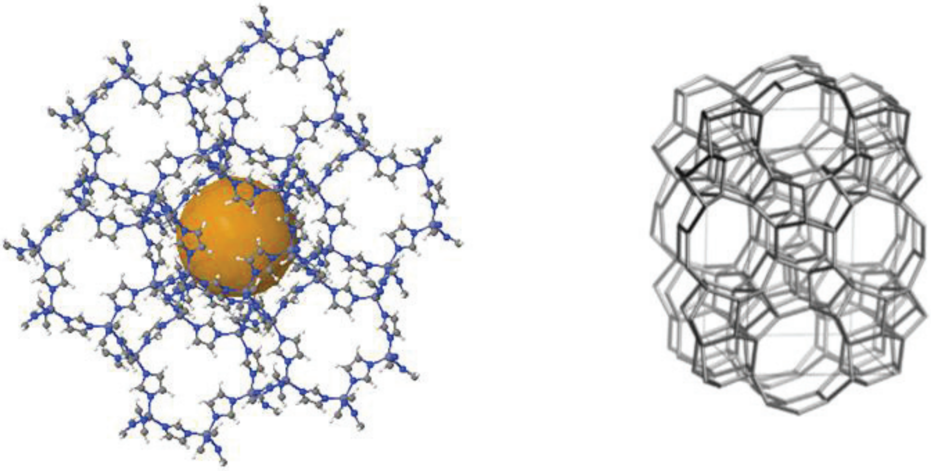

*Figure 1: Example of zeolite: ZSM-5 and MOF with an MFI type structure.*

In this context, porous solids with larger pores were developed and studied. As an example, ordered mesoporous materials were synthesized. Indeed, they have a well-defined pore arrangement, high surface area, high pore volume and the pore size can be easily modulated. They are composed of an amorphous silica framework displaying siloxane bridges Si-O-Si with residual silanol groups Si-OH on their surface. These latter are hydrophilic whereas the siloxane bridges are hydrophobic. The silanol groups are of great interest since they can be used to modify the surface by the grafting of organometallic precursors. In most of the cases, ordered mesoporous solids are prepared through a Cooperative Templating Mechanism (CTM). This preparation route is based on a self-assembly of surfactant micelles in interaction with the silicon precursor leading to a long-range order organization of the porous network. Different type of solids can be prepared depending on the nature of the surfactant (ionic or non-ionic), the temperature, the surfactant:silicon ratio, the nature of the co-solvents and the nature of the catalyst (acid, basic, nucleophilic). The first ordered mesoporous materials denoted FSM[9] for Folded Sheets Mesoporous were obtained using quaternary ammonium surfactant. Then, scientists from Mobil have prepared new types of materials belonging to the M41S family[10-12] with various porous network arrangements: cubic (MCM-48),[13-14] lamellar (MCM-50)[15] and hexagonal (MCM-41).[14]

Later, SBA-type materials standing for Santa Barbara Amorphous materials were also prepared using block copolymers[16-17] such as SBA-15 and SBA-16. These materials display larger pores (SBA-15: mean pore diameter of 10 nm) and thicker walls (SBA-15: from 2 to 6 nm) compared to M41S which give them a higher hydrothermic stability.

In order to compare the matrix effect on the polarization performances, our research focuses here on the preparation of TEMPO containing solids with SBA-15 and SBA-16 architectures. The synthesis as well as some physical features of such materials are presented in the following paragraphs.

# II. Ordered mesoporous silica: SBA-15 and SBA-16 type materials

The preparation of ordered mesoporous silica materials requires a thorough knowledge of the sol-gel chemistry. This process involves a succession of reactions which have to be precisely controlled to have access of a wide range of materials and even hybrid materials. The important points of this technique are described in the following section along with the parameters influencing each steps.

## A. Sol gel process

Today known as sol-gel process coming from the contraction of “solution-gelification”, this process allows to produce solid samples by mean of a precursor which undergoes upstream hydrolysis and condensation reactions. In the typical case of silicon alkoxides with a general formula $Si(OR)_4$ such as tetraethylorthosilicate (TEOS) and tetramethylorthosilicate (TMOS) for the most common, the hydrolysis and condensation reactions are slow. They are therefore catalyzed by acids, bases or nucleophiles species or even coordination complexes such as rhodium complexes.

The sol-gel process is thus characterized by the following reactions: i) Formation of the sol, ii) Formation of the gel, iii) Aging and iv) Drying.

### 1. Formation of the sol

The sol is a colloidal solution with particle sizes ranging from 1 nm to 100 nm obtained after hydrolysis and partial condensation. As shown in Figure 2, the hydrolysis reaction involves the interaction between a silicon precursor and water to form silanol groups. These freshly synthesized silanols groups have the possibility to condensate with other silicon precursors Si-OR (alcoxolation) or other silanol species Si-OH (oxolation). In both cases, the formation of siloxane bridges is observed.

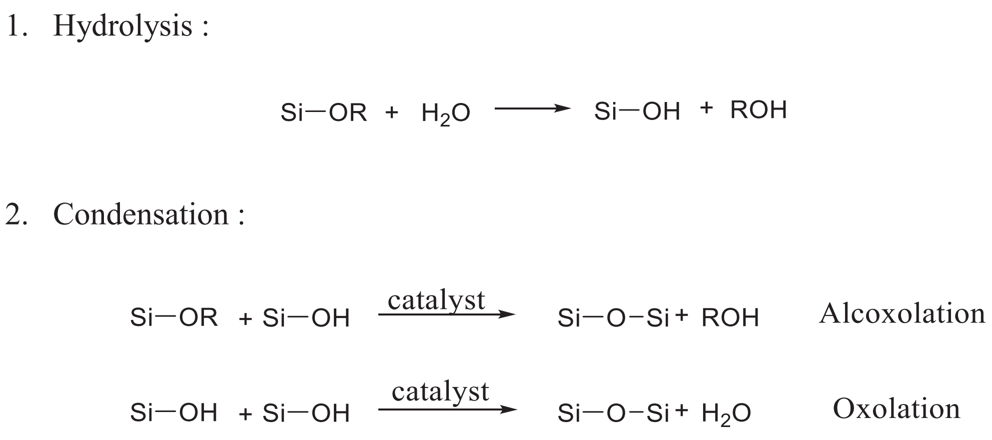

*Figure 2: Hydrolysis and condensation reactions occurring during the sol-gel process.*

### 2. Formation of the gel

After many condensation reactions, the liquid sample becomes more and more viscous until reaching the "gelation time". At this point, a tri-dimensional network called gel is formed which the structure is highly dependent on the rate of the hydrolysis and condensation. The resulting gel appears as an elastic and wetted sample with the remaining liquid trapped in the cavities formed by the network.

### 3. Aging

The aging of the gel corresponds to the prolongation of the condensation reactions which reinforced the tri-dimensional network. These reactions increase the cross-linking of the network and a phenomenon of syneresis is observed. The gel network shrinks spontaneously and the liquid trapped into the pores is released.

### 4. Drying

Drying a wet gel is a sensitive process because of the capillary forces resulting of the evaporation of the liquid out of the pore network. A slow drying helps to the conservation of the pore network whereas a fast drying can cause some cracks into the structure or even sometimes the collapse of the structure.

A wet gel can be dried by an increase of the temperature which causes the shrinkage of the gel which allows surface silanol groups to get spatially closer. The surface silanols can react with each other to form siloxane bridges which further consolidate the structure. In addition, the pore size becomes smaller and the surface tension of the liquid larger. When the gel is no longer deformable, *ca.* with a high surface tension and close to the cracking, the liquid is evaporated from the gel and only a thin film of liquid remained on the pore walls. Finally, the thin film of remaining liquid is removed *via* diffusion in the gas phase.

Another drying process is also used: the supercritical drying in which temperature and pressure are chosen to insure the transformation of the liquid into a supercritical fluid. This process allows to prevent the cracking of the gel and the collapse of the porous network because the capillary forces are no more in action. However, the use of such method leads to materials with different porous features (with respect to what is obtained under classical drying conditions) and this point will be addressed with much more details in Chapter 4.

Based on this sol-gel process, ordered mesoporous silica materials were developed. Typical examples are SBA-15 and SBA-16. The main features of these silica-based materials as well as their synthesis are described hereafter.

## B. Preparation of SBA-15 type materials

SBA-15 type materials were first developed by D. Zhao et al. in 1998.[16] The authors used a non-ionic triblock copolymer, namely pluronic P123, composed of a hydrophobic central block of poly(propylene oxide) (PO) surrounded by two hydrophilic external blocks of poly(ethylene oxide) (EO) frequently denoted as $(EO)_X(PO)_y(EO)_Z$. As shown in Figure 3, the silica materials were obtained through a cooperative templating mechanism (CTM). The increase in concentration up to the critical micellar concentration allows to form spherical micelles which further self-organize into rod-like micelles. Over time, a hexagonal mesophase composed of these rod-shaped micelles is created while, tetraorthosilicate (TEOS), used as the silicon source got hydrolyzed and polycondensated under acidic conditions. The last step of this process consisted in removing the structure directing agent (P123) to liberate the porosity. This removal must be handled carefully since it could affect the structure itself, resulting in lower surface areas, lower pores volume or complete collapse of the structure. A wide range of techniques to remove the structure-directing agent can be found in the literature such as water/pyridine extraction,[18] soxhlet extraction,[19] calcination,[20] supercritical fluid extraction,[21] microwave digestion[22-23] or photocalcination.[24]

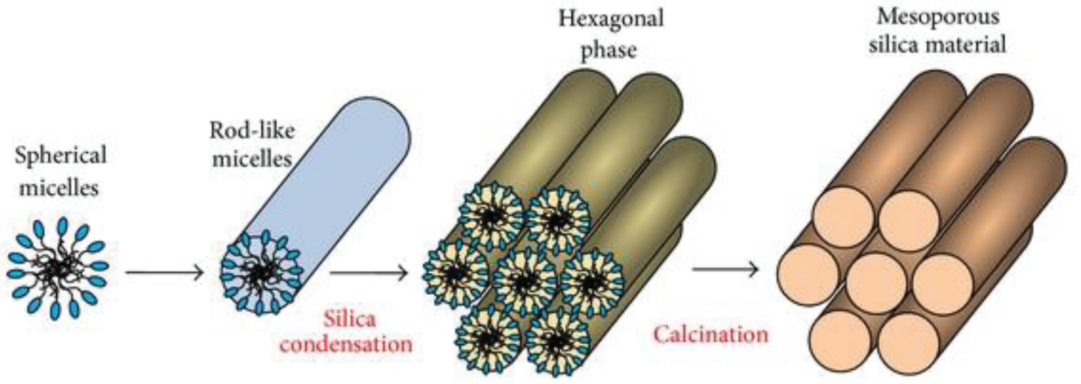

*Figure 3: Schematic representation of the SBA-15 formation. Extracted from: Lombardo, D; Kiselev, M. A.; Magazù, S.; Calandra, P., amphiphiles self assembly : basic concepts and future perspectives of supramolecular approaches. Advances in condensed matter physics* ***2015****, 22.*

SBA-15 type ordered mesoporous silica materials displays a 2D hexagonal arrangement of mesopores (*p6mm*) with a mean pore diameter around 10 nm and a wall thickness of c.a 2-6 nm. They exhibit a high surface area (600-1000 $m^2/g$) and large pore volume (0.8-1 $cm^3/g$). These types of solids were used in a wide range of applications such as drug delivery,[25] solar cells,[26] batteries,[27] catalysis[28] and separation.[29-31]

## C. Preparation of SBA-16 type materials

Similarly to SBA-15, SBA-16 mesoporous silica materials were prepared through the same mechanism (CTM). Instead of Pluronic P123, Pluronic F127 was used with TEOS as the silicon source. Various conditions can be found in the literature to create such types of solids as for example the use of a mixture of pluronic P123 and pluronic F127 or a ternary water/butanol/Pluronic F127 system.[32] This type of synthesis leads to a 3D cubic organization of the porous network as shown by TEM micrograph (Fig. 4). SBA-16-type materials have large mesopores (5-15 nm) interconnected by micropores (1-2 nm). They exhibit high surface area (500 to 900 $m^2/g$) and pore volumes ranging from 0.6 to 0.8 $cm^3/g$. This network arrangement belongs to *Im3m* space group where each mesoporous cavity is connected to eight other cavities.

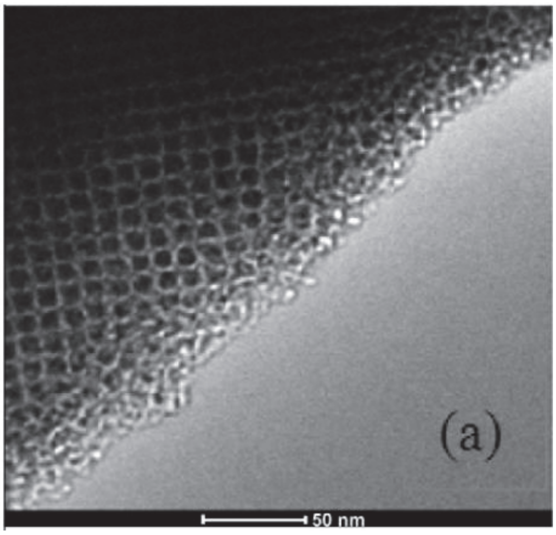

*Figure 4: Transmission electron microscopy picture of SBA-16 type material.*[33]

SBA-16 mesoporous silica materials were used as catalysts,[34] for metal incorporation,[34] for further functionalization, as templates and in electronic.[32]

SBA-15 and SBA-16 could be good candidates as supports to covalently linked TEMPO radicals for d-DNP applications. The mesoporous silicas are of interest because they could be easily filtered and will not interfere with microwave irradiations. Moreover, their synthesis is versatile and allows to incorporate various organic precursors during their preparation. Here, a mono-silylated azido precursor was directly incorporated during the preparation of SBA-15 and SBA-16 mesoporous silica materials. These azido-units were further coupled with TEMPO radicals by click-chemistry and the resulting solids were used to polarize liquids. In the next section, an overview of the different techniques used in the literature to functionalize silica supports with TEMPO radicals are described. The advantages and drawbacks of each method are presented and discussed.

# III. Functionalization of amorphous and ordered mesoporous silica with TEMPO moieties

Several approaches can be conducted to covalently link a molecule of interest onto a silica surface. Due to the numerous applications of functionalized silica and hence the diversity of grafted moieties, this study will be limited to the incorporation of TEMPO radicals onto silica surfaces.

Three different methodologies can be adopted to covalently link TEMPO radicals onto silica materials:

i) Direct incorporation of the functional groups during the preparation of the mesoporous silica materials. This method is commonly denoted as direct synthesis or co-condensation approach and has the advantage to yield hybrid materials in one step. However, some of the freshly inserted functionalities may not be accessible for further reactions since they are embedded in the silica framework. Moreover, this insertion can affect the organization of the mesoporous silica material itself and resulting in some changes of the physical features.[35]

ii) Post-functionalization of existing silica materials. In this case, silanol groups which are located onto the surface of the materials are used as reactive sites to anchor the molecule of interest. The advantage of this approach lies in the modification of the surface after the formation of the mesoporous materials. Hence, the organization of the mesoporous materials stays unchanged and not disturbed.[36] However, the grafting rate is limited by the density of silanol groups on the surface.[37-38] In addition, the preferential grafting of the organic moieties occurs near to the entries of the mesopores which leads to an uneven covering of the solids with organic groups. In some cases, this can totally obstruct the pore-entrance preventing the access to the inner porosity.[39]

iii) Entrapment of the TEMPO radicals into the silica matrix. Here, the radicals are not covalently linked onto the silica-surface but physically entrapped in the silica framework. Although this strategy seems to be the easiest and fastest way to incorporate organic fragments, some of these functionalities can be released from the silica matrix.

Many studies in this field have been performed for catalytic applications and the silica-supported TEMPO catalysts were used for example to selectively oxidize alcohols into aldehydes.[40] The different strategies to introduce the TEMPO units are presented and discussed hereafter.

The first example, described by N. Tsubokawa et al. in 1995,[41] aimed to immobilize TEMPO moieties on commercial amorphous silicas to oxidize alcohols. Ultrafine silica powders containing surface silanol groups were first treated with 4-trimethoxysilyl-1,2,5,6-tetrahydrophtalic anhydride acid (TPSA) in toluene. This lead to the convalent bonding of the targeted silyl-1,2,5,6-tetrahydrophtalic anhydride acid fragments. These groups were further transformed into TEMPO radicals by contacting a TEMPOL compound with N,N'-Dicyclohexylcarbodiimide (DCCI) as catalyst. One of the advantage of this method lies in the possibility to anchor an expensive reagent on a support for further recovery and reuse. Moreover, this heterogeneous system allows a better separation of the product from the catalyst at the end of the catalytic process. However, it was found that the yield of the final step (reaction between TEMPOL radicals and the surface anhydride acid moieties) was quite low: 20-30 %. Only 0,2 mmol/g of TEMPO groups were grafted on the silica support. This result arises directly from the grafting technique itself which implies a preferential functionalization at the entries of the pores. The accessibility to the inner silanol groups is thus impossible due to the steric hindrance of the grafted functionalities.

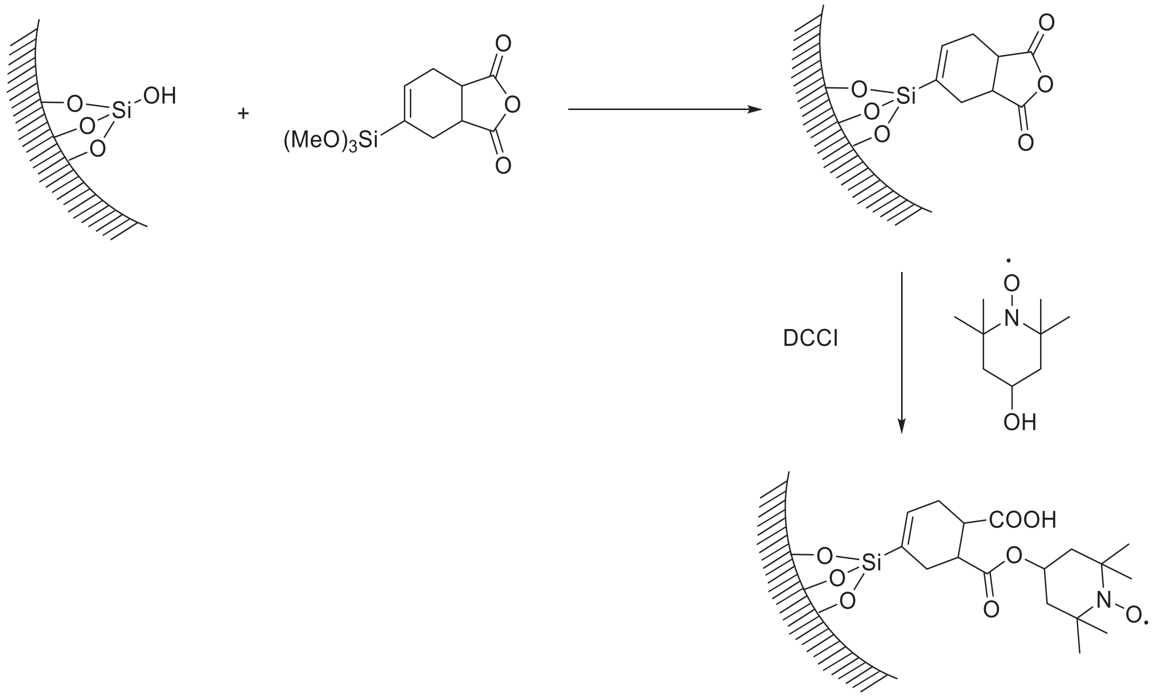

*Figure 5: Immobilization of TEMPO radicals through a multi-step synthesis using acid anhydride groups.*

With the same vein, C. Bolm and T. Fey et al[42-43] prepared a silica-supported TEMPO catalyst with two distinct TEMPO derivatives. A commercially available aminopropyl-functionalized silica obtained from the grafting of 3-aminopropyltriethoxysilane (APTES) on silica supports was further employed in a one-step reductive amination. In this reaction, the amino-groups react first with the carbonyl groups to form imines which are subsequently reduced by sodium cyanoborohydride. The conversion rate was improved and a value as high as 54% was reached.

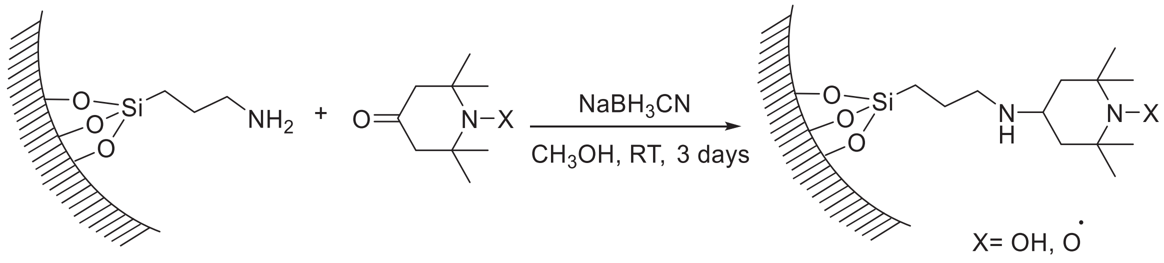

*Figure 6: One-step reductive amination from a commercial aminopropyl-functionalized silica.*

Then, the possibility to graft TEMPO radicals onto ordered mesoporous silica materials was investigated. First of all, three routes were developed to anchor TEMPO groups on MCM-41(Mobil Composition of Matter n°41) materials (see Figure 7). These materials have a pore network similar to that of SBA-15 solids albeit with smaller pores ranging from 1.5 to 10 nm.

The route 1 is a multistep synthesis starting with a typical Williamson ether preparation. In presence of sodium hydride, the TEMPOL precursors are deprotonated to form alkoxides and gaseous dihydrogen. The alkoxides then react with allyl bromide giving rise to 4-allyloxy-TEMPO. The resulting silylated TEMPO precursors are further obtained by hydrosilylation using hydrogenotrimethoxysilane and chloroplatinic acid as catalyst. The grafting reaction is then performed in dry toluene under reflux.

The second route consists in preparing first the MCM-41 support and then use the silanol groups to graft 3-aminopropylsilyl groups. The supported amino groups were further treated with 4-carboxy-TEMPO in presence of N,N'-dicyclohexyldicarbodiimide (DCCI) to yield to the TEMPO-amido-supported groups.

The last route relies on the coupling of $NH_2$-grafted solids with the N-hydroxysuccinimide ester of 4-carboxy-TEMPO to get the TEMPO-amide supported groups.

Here, the formation of urea as by-product (route 2) is avoided.

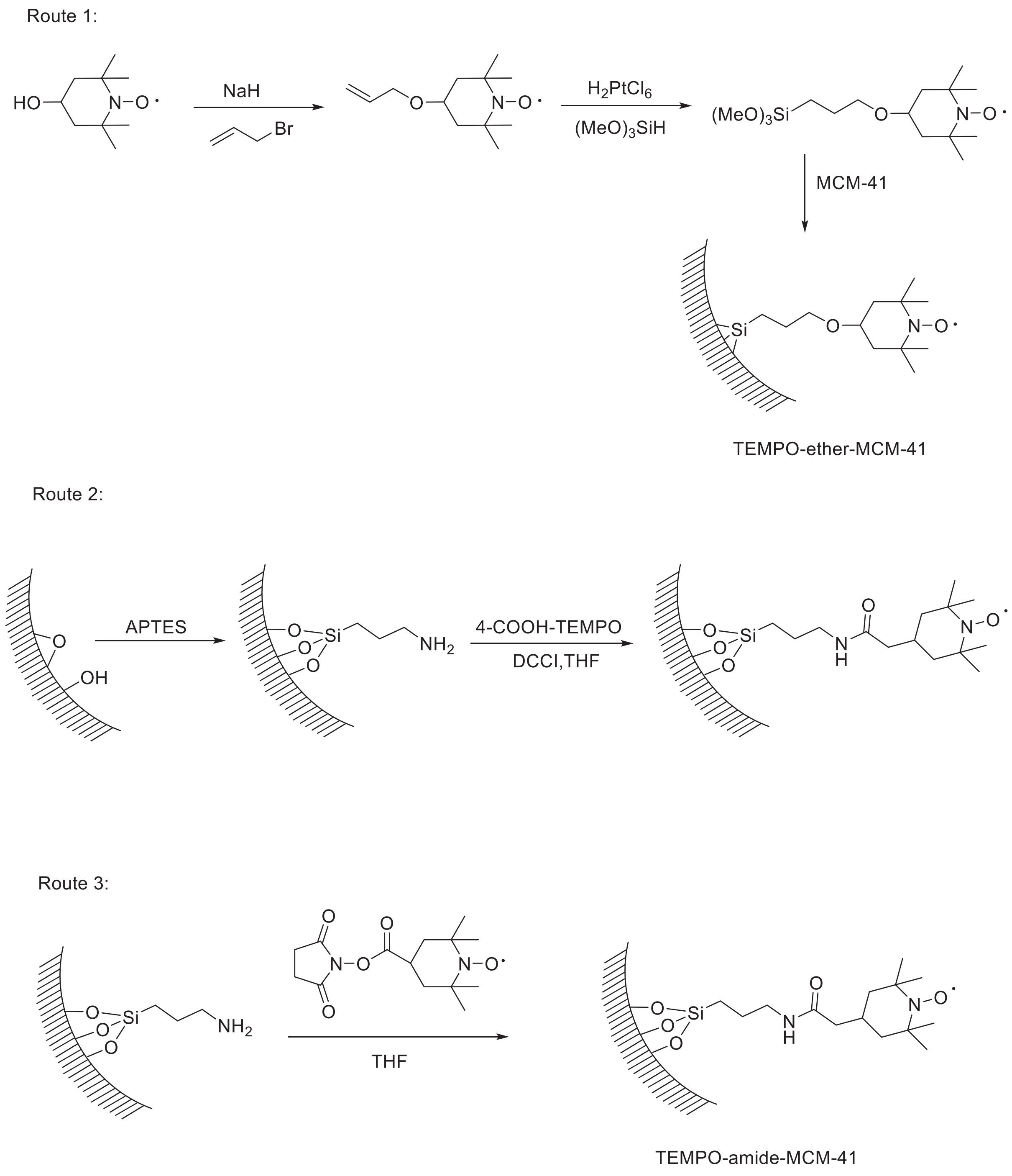

*Figure 7: Different routes allowing to link TEMPO radicals onto ordered mesoporous silica materials.*

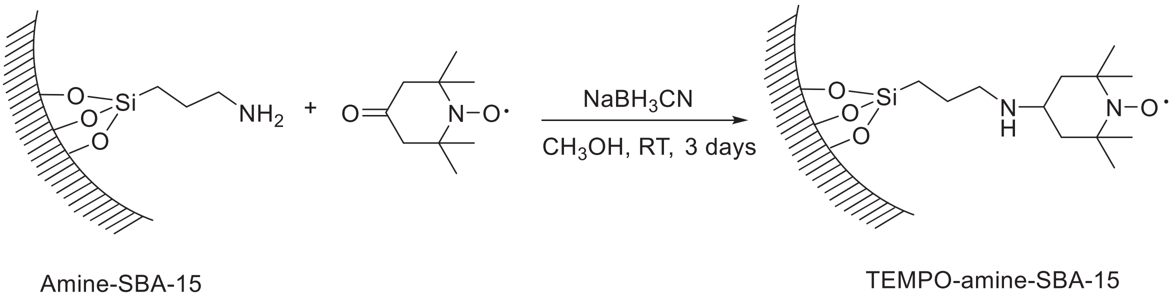

*Figure 8: Preparation of SBA-15 mesoporous materials containing TEMPO radicals.*

Inspired by the previously described synthesis developped by C. Bolm and T. Fey, SBA-15 mesoporous materials coated with aminopropyl fragments were converted into the corresponding TEMPO-amino-SBA-15 solids. In this example, the same type of reaction involving the formation of an imine which is subsequently reduced by $NaBH_3CN$ is performed. SBA-15 mesoporous materials were used instead of amorphous commercial aminopropyl-functionalized silicas.

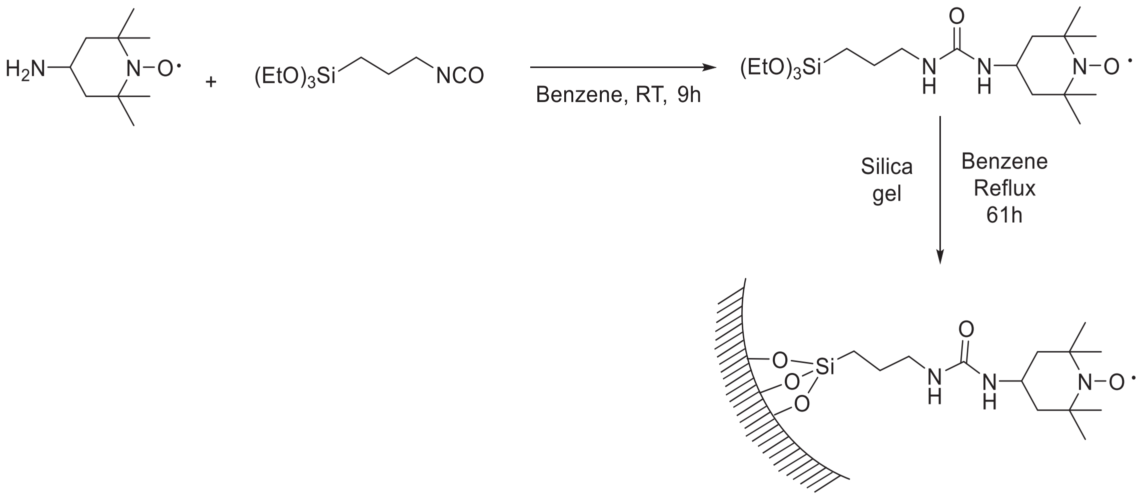

*Figure 9: Preparation of silica gel coating with TEMPO radicals through the method of Tanaka et al.*

Another strategy developed by H. Tanaka et al. consisted first in the preparation of a urea-TEMPO silylated precursor by reaction between TEMPO radical containing an amino group in position 4 and the 3-(triethoxysilyl)propyl isocyanate in Benzene. The silylated product was then refluxed in benzene for 61 h with the silica gel leading to covalent grafting of the TEMPO fragments on the silica surface.

Although the choice of the strategy to incorporate reactive organic species onto the surface of silica is essential, the nature of the functionality selected is also fundamental. It has been proven that it is not obvious to control the regular distribution of the functional groups into the pore channels. The precursor has to be sufficiently hydrophobic to enter the core of the micelle and not too bulky to avoid the perturbation of the system. [44-49]

In conclusion, a wide range of reactions using several TEMPO derivatives was developed. As shown in this section, the post-functionalization of commercial aminopropyl-functionalized silica supports or homemade silica supports is widely developed. All of them successfully led to the immobilization of TEMPO units silica surfaces albeit with different loadings. However, none of these methods have been selected because of the click chemistry potential which could provide higher conversion rates to transform the precursors into TEMPO radicals. Moreover, the direct synthesis should be more appropriate to homogeneously disperse the TEMPO radicals in a silica matrix.

The next part of this chapter will be devoted to the direct synthesis of hybrid silica matrices containing TEMPO units by sol-gel using a templating route as a way to secure the regular dispersion of the TEMPO fragments in the whole silica sample.

## IV. Hybrid ordered mesoporous silica containing TEMPO radicals

We have decided to develop hybrid ordered mesoporous silica materials with two different pore network architectures: SBA-15 and SBA-16. Noteworthy, SBA-15 and SBA-16 type materials were preferred here because of their interesting physical features: their high porous volume offer the possibility to impregnate a high quantity of liquid to be further polarized. Moreover, their thick silica walls could be an asset to tolerate the harsh conditions of the DNP experiments (T= 1.2 K).

The hybrid SBA-15 and SBA-16 materials were prepared by co-hydrolysis and co-condensation of a 3-azidopropyltriethoxysilane precursor with TEOS in acidic conditions using tri-block copolymers as structure directing agents. Different molar ratios of 3-azidopropyltriethoxysilane and TEOS were used: 1/34, 1/60, 1/100, 1/140 and 1/320.

A schematic representation of the multi-step synthesis for both materials is depicted in Figure 10.

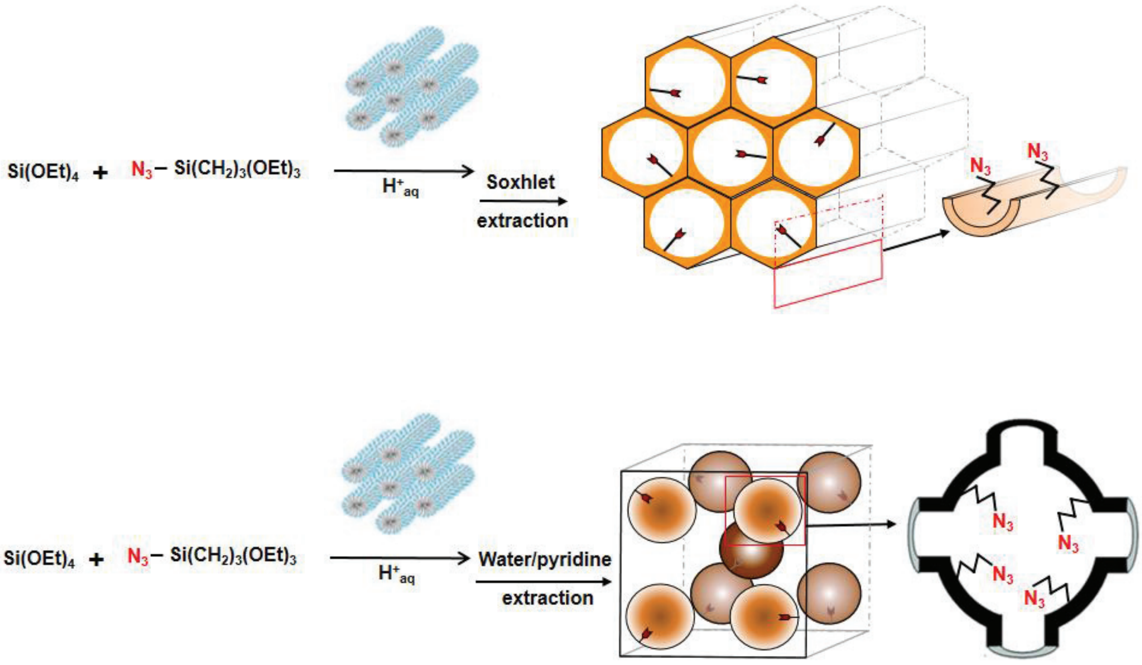

*Figure 10: Schematic representation of the multi-step synthesis leading to azido-functionalized SBA-15 and SBA-16. The different structures are the result of different tri-block copolymers used in specific conditions.*

The hybrid SBA-15 and SBA-16 solids were prepared using a classical procedure and more details concerning the experimental protocols are provided in the supporting information at the end of this chapter.

The second step of the materials' synthesis consisted in a Copper-catalyzed Alkyne-Azide Cycloaddition (CuAAC) reaction between the surface azido moieties and the TEMPO radical bearing an alkynyl group. The experimental conditions of this synthesis are briefly depicted in Figure 11.

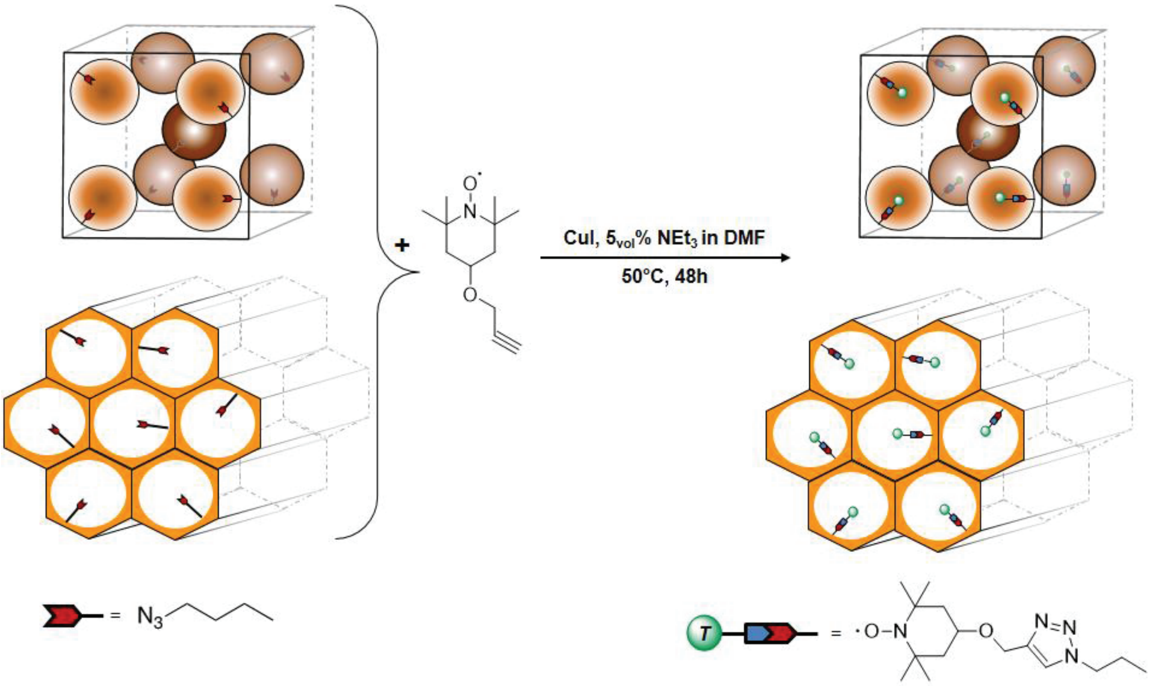

*Figure 11: Copper(I)-catalyzed Alkyne-Azide cycloaddition performed on azido-functionalized SBA-16 and SBA-15 materials.*

To carry out these reactions, some organic intermediates such as the 3-azidopropyltriethoxysilane and the o-propargyl were synthesized. Their preparations are described in the following paragraphs along with the click chemistry reaction.

## A. Preparation of precursors and multi-step synthesis leading to ordered mesoporous silica coated with TEMPO moieties

Two precursors: the silylated azido-derivative and the TEMPO radical bearing an alkynyl group, are compulsory to yield to the TEMPO containing solids. These two precursors were thus prepared separately:

i) The nucleophilic substitution of 3-chloropropyltriethoxysilane with sodium azide in presence of Tetra-n-Butylammonium Bromide (TBAB) has led to the formation of 3-azidopropyltriethoxysilane (see SI at the end of the chapter for detailed description of the synthetic protocol).[50]

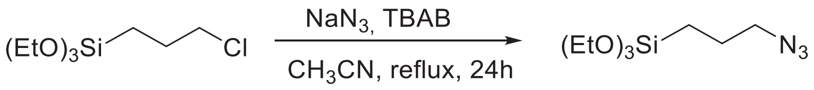

The final product was characterized by $^1$H NMR ($CD_2Cl_2$,300 MHz): δ 0.62-0.65 (m, 2H), 1.2 (t, J = 6.6 Hz, 9H), 1.67 (m, 2H), 3.26 (t, J = 7 Hz, 2H), 3.79 (q, 6H).

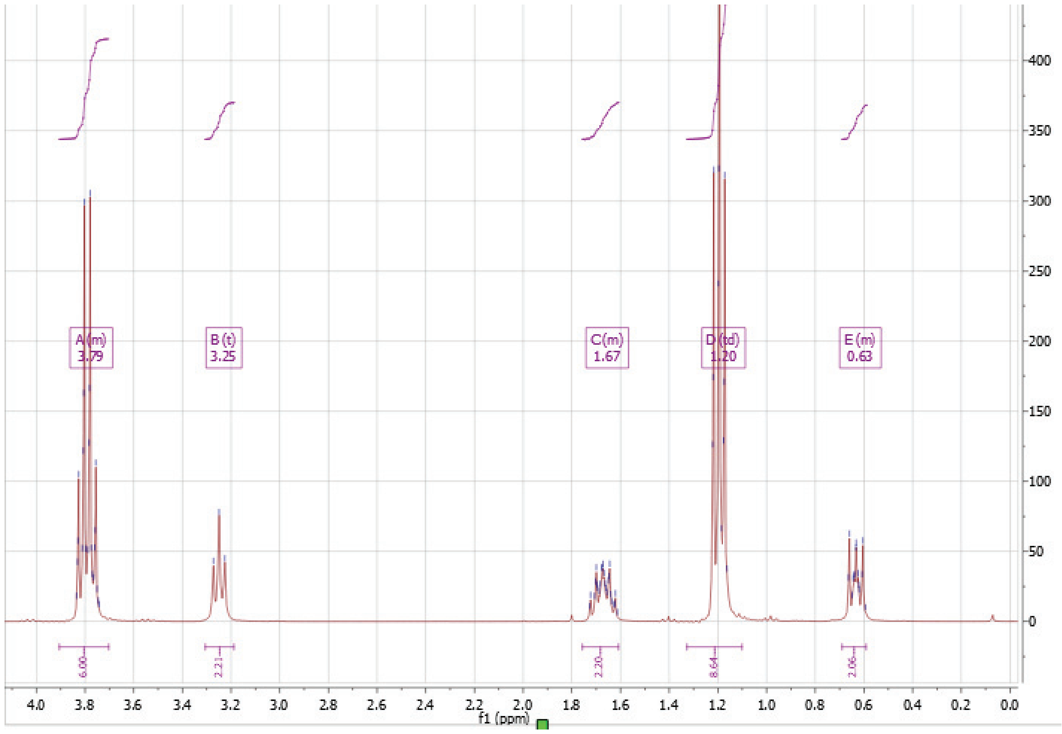

*Figure 12: $^1$H NMR spectra of the 3-azidopropyltriethoxysilane at 300 MHz.*

ii) The Williamson ether synthesis allows to couple the TEMPOL fragments with an allyl bromide to form the desired alkyne derivative bearing the TEMPO unit (see SI at the end of the chapter for detailed description of the synthetic protocol):

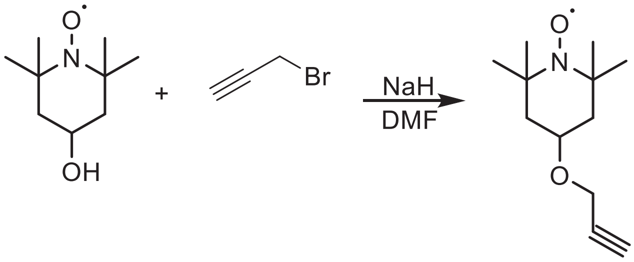

After preparation and characterization of the two precursors, hybrid SBA-15 and SBA-16 containing propyl azido fragments were prepared *via* a direct synthesis.[18] This one-pot synthesis method consisted in the co-hydrolysis and co-condensation of tetraethyl orthosilicate and (3-azidopropyl)triethoxylsilane in the presence of structure-directing agent such as pluronic P123 and pluronic F127 triblock copolymer to obtain the targeted SBA-15 and SBA-16 type solids respectively (Fig. 10). Finally, the two ordered mesoporous silica materials were clicked with TEMPO radicals through a CuAAC (Fig. 11).

In order to obtain the first silica materials dubbed HYPSO 2, pluronic P123 in aqueous HCl (pH= 1.5) was mixed with (3-azidopropyl)triethoxylsilane and TEOS (amounts adjusted depending on the desired dilution). Then, the whole mixture was homogenized at room temperature by stirring 3h and was placed in a pre-heated oil bath (T= 45 °C). The temperature was monitored inside the round bottom flask to introduce precisely the NaF when the solution reached 40 °C. Then, the reaction mixture was maintained at 45 °C under stirring for the next 72h. The resulting material was filtered and washed with $H_2O$, EtOH and $Et_2O$. At this stage, the porous network is filled by the surfactant which was removed by soxhlet extraction. The resulting white solid was filtered, washed with $Et_2O$ and dried under high vacuum ($10^{-5}$ mbar) at 135°C for 15h. Then, the azido-units were coupled under argon with o-propargyl TEMPO and a solution of CuI in DMF and $NEt_3$ for 48h at 50 °C. The resulting material was filtered, washed and dried under high vacuum ($10^{-5}$ mbar) at 50°C for 15h.

Similarly, HYPSO 3 silica materials were prepared by mixing at room temperature, the pluronic F127, NaCl in aqueous HCl and water in a Teflon bottle for 1h30. Then, the reaction mixture was heated up to 40 °C for 1h and TEOS and 3-azidopropyltriehtoxysilane were added. The Teflon bottle was closed again and vigourously stirred at 40 °C for 20h prior to be introduced in a pre-heated oven settled at 100 °C for 2h without agitation. The resulting white solid was filtered and washed with EtOH and acetone. After having crushed the solid in a mortar, it was dried at 100 °C under high vacuum ($10^{-5}$ mbar) for 5h. The pluronic F127 was removed by water/pyridine treatment prior to be washed, dried at 100 °C under high vacuum ($10^{-5}$ mbar) for 15h and stored in a glovebox.

Finally, the azido units were coupled with o-propargyl TEMPO under argon using the same protocol than HYPSO 2 materials.

The azido-functionalized SBA-15 and SBA-16 intermediates denoted as $N_3$_SBA-15 and $N_3$_SBA-16 respectively were characterized by several techniques as well as the corresponding materials after the CuAAC reaction (vide infra). These materials are entitled HYPSO 2 and HYPSO 3 respectively.

## B. Characterization of the hybrid ordered silica materials

The physical and chemical features of the mesoporous silica solids were carefully analyzed by $N_2$ adsorption/desorption, EPR, DRIFT, SAXS and TEM. These data are essentials for the description of the hybrid materials and to study the influence of the materials features on the polarization properties.

### 1. $N_2$ adsorption/desorption experiments and TEM micrographs

#### a) $N_2$ adsorption/desorption experiments

As shown in Table 1, HYPSO 2 samples display high surface areas ranging from 767 to 866 $m^2.g^{-1}$ and porous volumes from 1.07 to 1.19 $cm^3.g^{-1}$. Then, the long pore channels of the SBA-15, on which are based the HYPSO 2, are characterized by a pore diameter of 8-9 nm. As an example, the adsorption/desorption isotherm and Barrett-Joyner-Halenda (BJH) plot are presented in Figure 13 and 14 for 1/34_HYPSO-2.

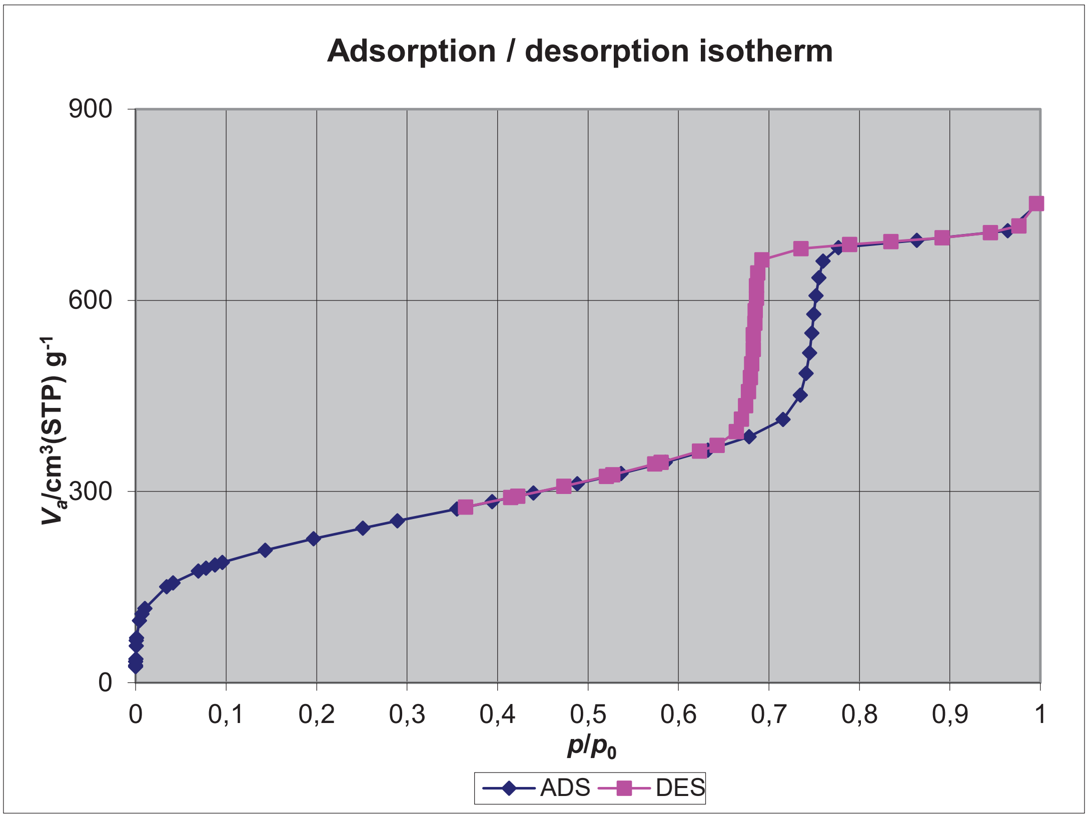

*Figure 13: Adsorption/desorption isotherm for 1/34_HYPSO-2.*

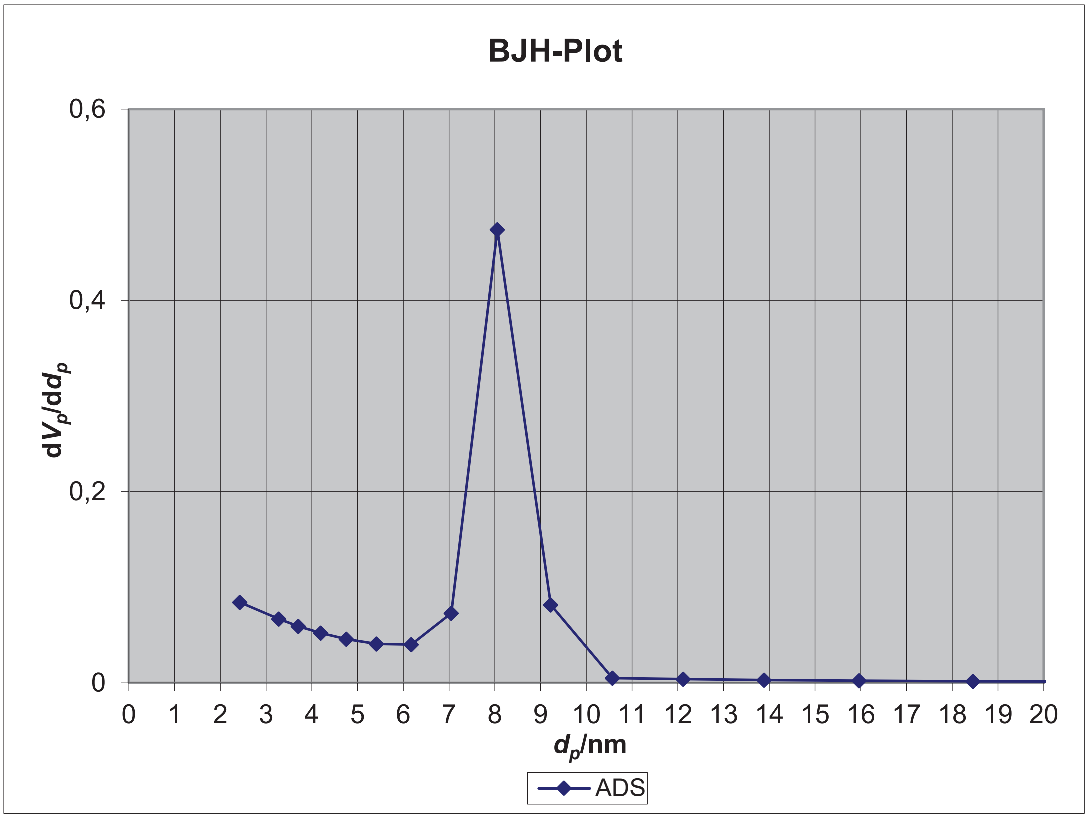

*Figure 14: Mesopore mean diameter for 1/34_HYPSO-2.*

All the data recorded are summarized in the table below:

*Table 1: Surface area, porous volume and pore diameter for HYPSO 2.*

| Materials | [≡SiR] $\mu mol_{\equiv SiR}\,.g^{-1}$ | $S_{BET}$ $m^2.g^{-1}$ | $V_p$(tot.)$^a$ $cm^3.g^{-1}$ | $D_p{}^b$ nm |
|---|---|---|---|---|
| 1/34_HYPSO-2 | 472 | 832 | 1.15 | 8 |
| 1/60_HYPSO-2 | 272 | 767 | 1.07 | 8 |
| 1/100_HYPSO-2 | 164 | 866 | 1.19 | 9 |
| 1/140_HYPSO-2 | 118 | 849 | 1.15 | 8 |

a: total pore volume corresponding to the quantity of $N_2$ adsorbed at $P/P_0 = 0.99$, b: Mesopore mean diameter calculated using the BJH model (adsorption branch).

As expected for the synthesis of mesoporous SBA-16 type solids, all the samples display type IV isotherms. Surface areas ranging from 714 to 983 $m^2.g^{-1}$ and from 913 to 1184 $m^2.g^{-1}$ were obtained for HYPSO 3 and $N_3$_SBA-16 materials respectively. A bimodal distribution was highlighted using the BJH model for the cavities of the SBA-16 and the MP model for the windows inter-connecting these cavities. Narrow pore sizes of 6-7 nm for cavities and 1-2 nm for the windows were obtained. Moreover, an abrupt desorption at $P/P_0 = 0.45$ was found and attributed to a “ink bottle” effect as expected for this type of architecture. Indeed, the desorption occurred *via* smaller pores which are in this case the windows between the cavities. According to the α-plot model, 37-46 % of the total pore volume of 0,62-0,82 $cm^3.g^{-1}$ are micropores. As an example, the adsorption/desorption isotherm, BJH plot and MP-plot are presented in Figures 15 and 16 for 1/34_HYPSO-3.

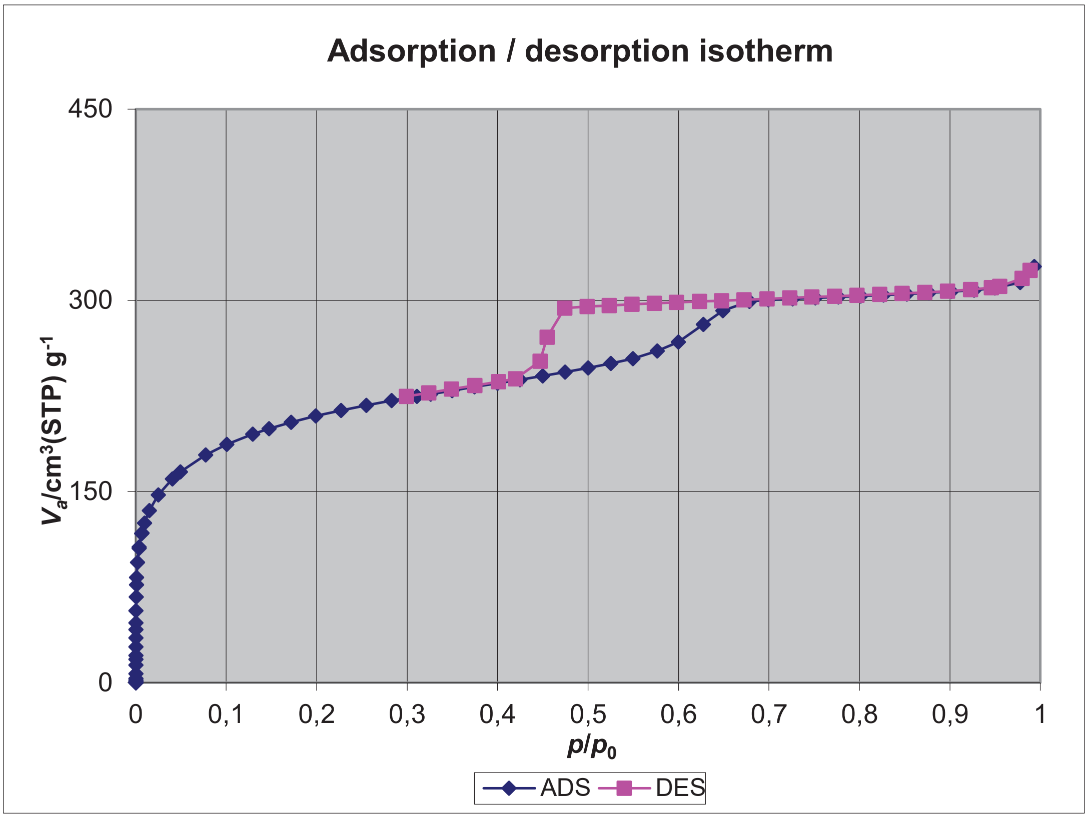

*Figure 15: Adsorption/desorption isotherm for 1/34_HYPSO-3.*

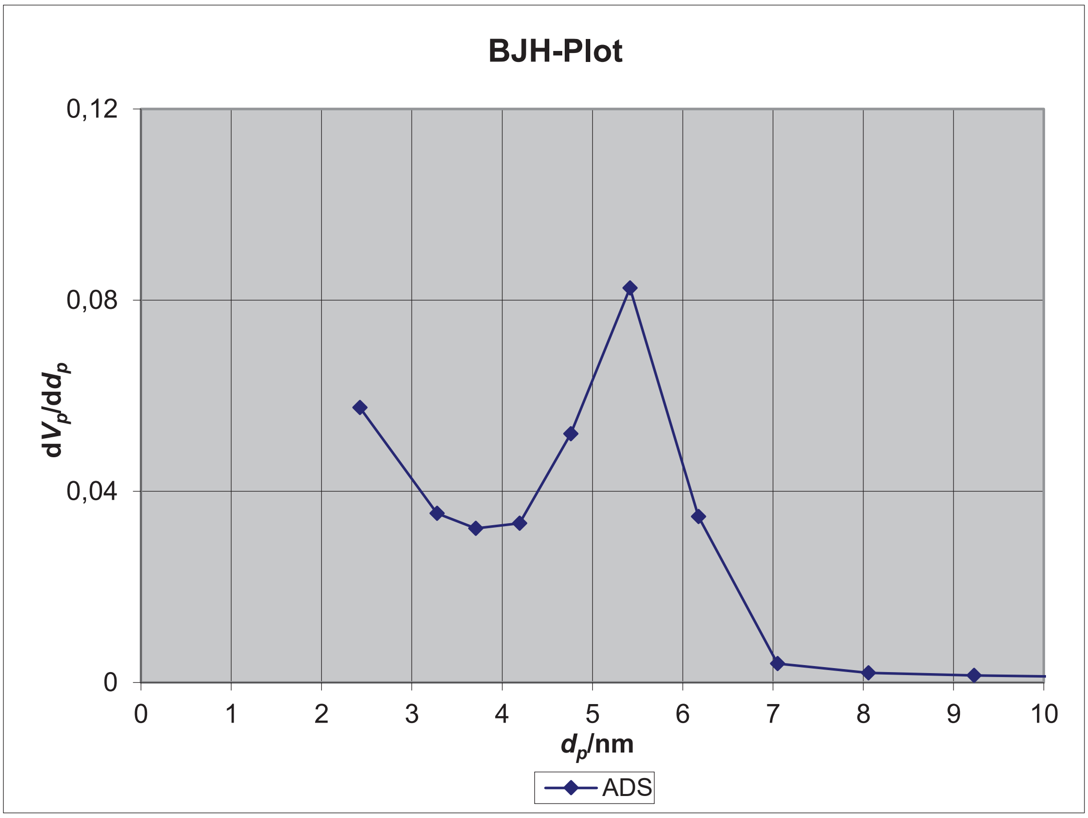

*Figure 16: Mesopore mean diameter for 1/34_HYPSO-3.*

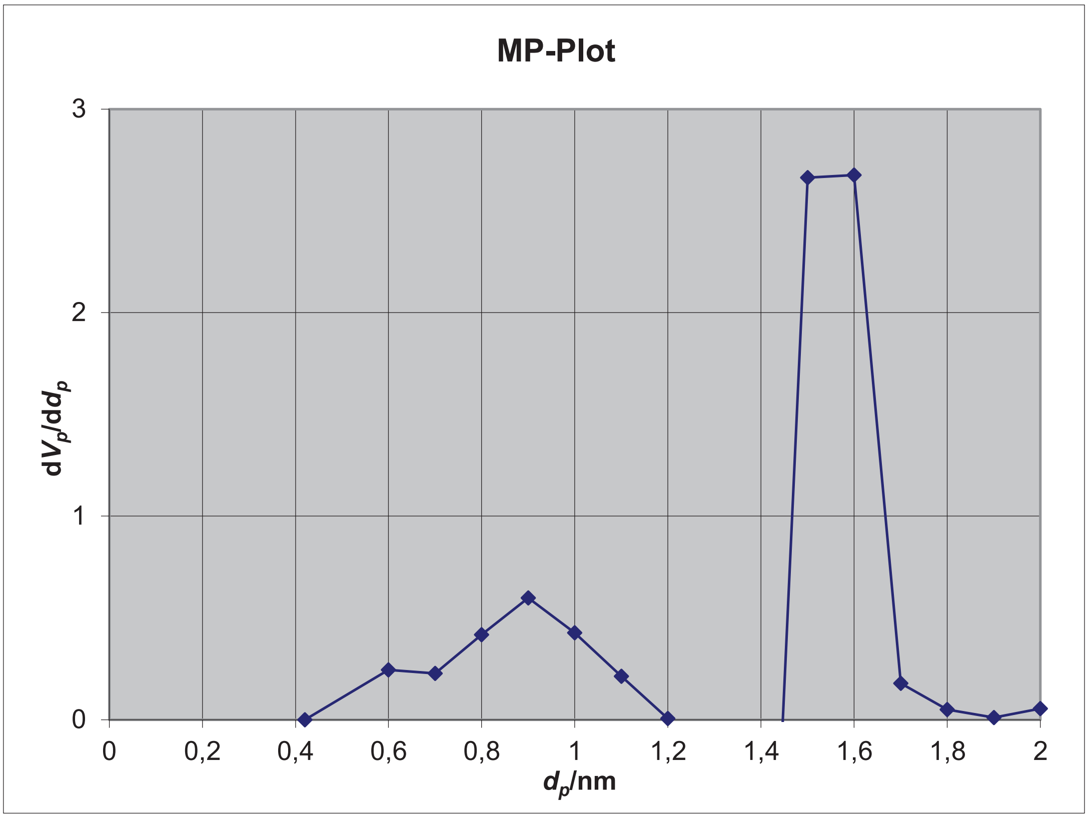

*Figure 17: MP-plot for 1/34_HYPSO-3.*

All the data recorded were summarized in the table below:

*Tableau 2 : Surface area, porous volume and pore diameter for $N_3$_SBA-16 and HYPSO 3.*

| Materials | [≡SiR] μmol$_{\equiv SiR}$ .g$^{-1}$ | S$_{BET}$ m$^2$.g$^{-1}$ | V$_p$(tot.)$^a$ cm$^3$.g$^{-1}$ | V$_p$(μ.)$^b$ cm$^3$.g$^{-1}$ | D$_p$$^c$ nm |
|---|---|---|---|---|---|
| 1/34_$N_3$_SBA-16 | 472 | 1012 | 0,68 | 0,31 | 2/ 6 |
| 1/34_HYPSO-3 | 472 | 729 | 0,50 | 0,19 | 2/ 5 |
| 1/60_ $N_3$_SBA-16 | 272 | 1010 | 0,66 | 0,29 | 2/ 6 |
| 1/60_HYPSO-3 | 272 | 752 | 0,52 | 0,22 | 2/ 5 |
| 1/100_ $N_3$_SBA-16 | 164 | 913 | 0,62 | 0,11 | 2/ 6 |
| 1/100_HYPSO-3 | 164 | 893 | 0,63 | 0,26 | 1/ 6 |
| 1/140_ $N_3$_SBA-16 | 118 | 1184 | 0,82 | 0,33 | 1/ 7 |
| 1/140_HYPSO-3 | 118 | 983 | 0,69 | 0,26 | 2/ 7 |
| 1/320_ $N_3$_SBA-16 | 52 | 1068 | 0,75 | 0,48 | 2/ 7 |
| 1/320_HYPSO-3 | 52 | 714 | 0,48 | 0,27 | 2/ 5 |

a: total pore volume corresponding to the quantity of $N_2$ adsorbed at $P/P_0 = 0.99$, b: Micropore volume calculated from the $\alpha_s$ plot model, c: Micropore mean diameter calculated using MP model/mesopore mean diameter calculated using the BJH model (adsorption branch).

### b) Transmission Electron Microscopy pictures

TEM micrographs were recorded for $N_3$_SBA-15 and $N_3$_SBA-16 materials by depositing a droplet of ethanol containing the powdered solid on a Cu grid covered by a carbon film and further evaporation of the solvent. In Figure 18, two pictures, which are illustrative of all the $N_3$_SBA-15 and $N_3$ SBA-16 materials, are presented with a magnification of 20 nm. These pictures highlight the high degree of porous structuration of the SBA-16 type and SBA-15 materials which are highly ordered.

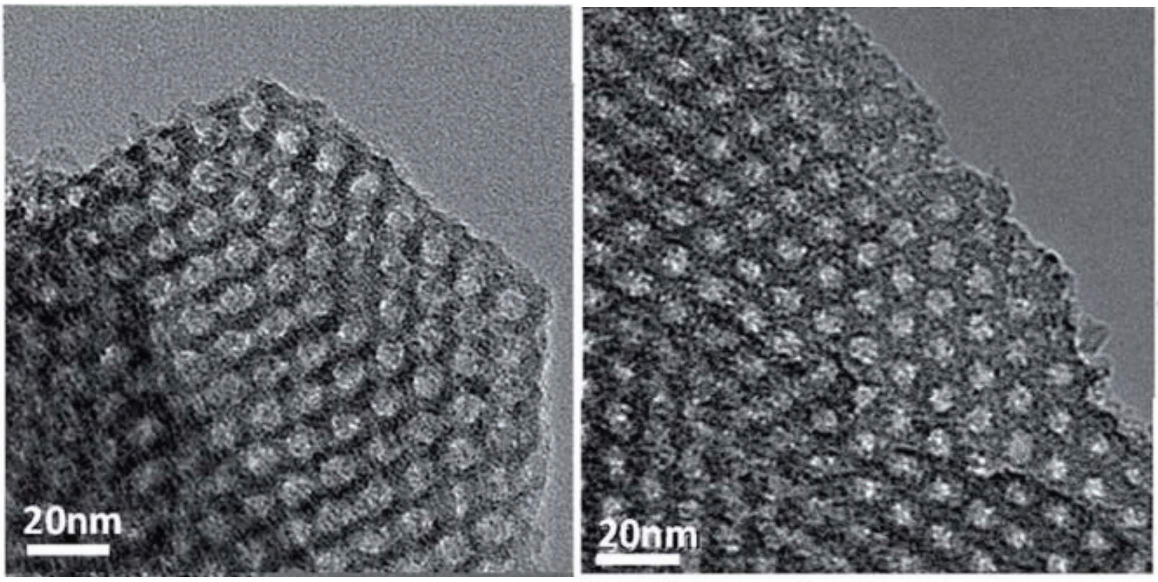

*Figure 18: TEM pictures of hexagonal 1/100 $N_3$_SBA-15 in the [001] axis and of cubic 1/140 $N_3$_SBA-16 in the [111] axis.*

## 2. Small angle X-ray scattering (SAXS)

All the samples were analyzed by small angle X-ray diffraction to determine the interplane spacings and the lattice parameter. The micropore mean length ($L_{\mu pore}$) was also calculated for each sample. The results are summarized in Table 3 and Figure 19 shows an example for HYPSO 2 and HYPSO 3 materials. As an example, 1/100_HYPSO 3 material exhibited an intense peak at *ca* $2\theta= 0.75$ characteristic of the (110) plane and thus suggesting the presence of a cubic-centered body lattice. 1/100-HYPSO 2 material was also characterized by a strong peak on its diffractogram (Figure 19) and two additional peaks which can be indexed on a hexagonal lattice as (200) and (110) reflections.

The results highlight thus a retention of the cubic and hexagonal structure even after immobilization of the TEMPO radicals onto the silica matrices.

*Table 3: Small angle X-ray scattering for $N_3$_SBA-16, HYPSO 2 and HYPSO 3 materials.*

| Materials | Structure | d(110)$^a$ nm | $a_0$$^b$ (nm) | $L_{\mu pore}$$^c$ (nm) |
|---|---|---|---|---|
| 1/34_$N_3$_SBA-16 | Cubic | 11.2 | 15.8 | 9.6 |
| 1/34_HYPSO-3 | Cubic | 11.2 | 15.8 | 10.4 |
| 1/60_ $N_3$_SBA-16 | n.d | n.d | n.d | n.d |
| 1/60_HYPSO-3 | Cubic | 11.0 | 15.6 | 10.2 |
| 1/100_ $N_3$_SBA-16 | n.d | n.d | n.d | n.d |
| 1/100_HYPSO-3 | Cubic | 10.5 | 14.9 | 8.6 |
| 1/140_ $N_3$_SBA-16 | n.d | n.d | n.d | n.d |
| 1/140_HYPSO-3 | Cubic | 11.6 | 16.4 | 9.3 |
| 1/320_ $N_3$_SBA-16 | n.d | n.d | n.d | n.d |
| 1/320_HYPSO-3 | Cubic | 12.5 | 17.7 | 12.3 |
| 1/34_HYPSO-2 | Hexagonal | 11 | 12.7 | 4.6 |
| 1/60_HYPSO-2 | Hexagonal | 10.8 | 12.4 | 4.4 |
| 1/100_HYPSO-2 | Hexagonal | 10.8 | 12.4 | 3.2 |
| 1/140_HYPSO-2 | Hexagonal | 10.5 | 12.1 | 4.1 |

a: The interplane spacings of SBA-15 and SBA-16 are d(100) and d(110) respectively, b: The lattice parameter is given by $a = d(110) x\sqrt{2}$, c: Micropore mean length, calculated as: $L_{\mu pore} = (d(110) * 2/(\cos(\pi/4) - 2 * Dmeso)/2$.

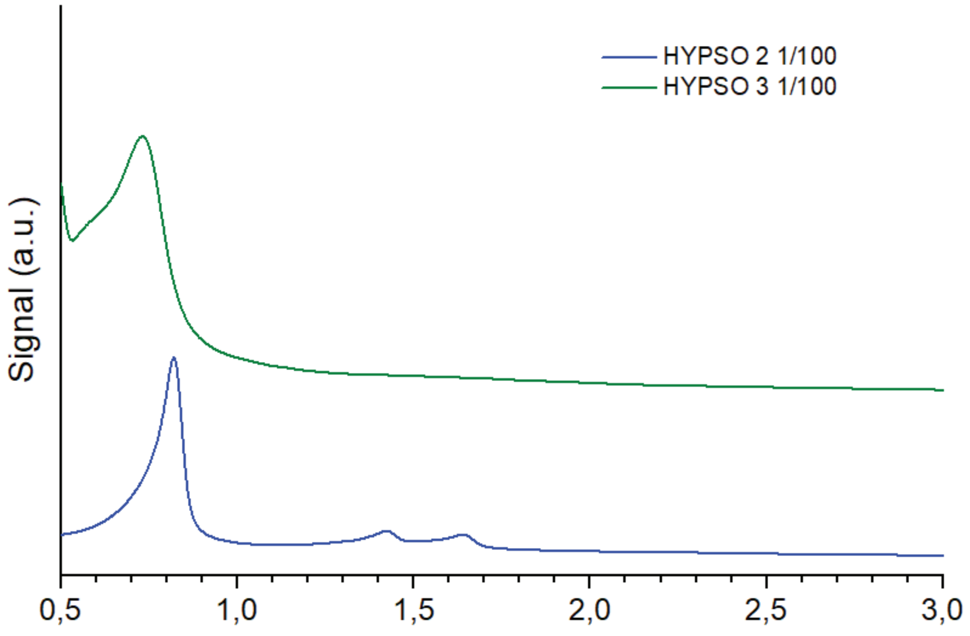

*Figure 19: Diffractograms for 1/100_HYPSO-2 and 1/100_HYPSO-3 samples.*

## 3. Evaluation and quantification of the species on the surface: EPR analysis and DRIFT spectroscopy

DRIFT spectroscopy was used to probe the surface of the different grafted and un-grafted samples. Two types of samples were thus analyzed: i) SBA-16 solids containing the azidopropyl fragment and ii) materials containing the TEMPO units after the CuAAC reaction. As an example, the DRIFT spectra of 1/60_$N_3$_SBA-16 and 1/60_HYPSO 3 materials are presented in Figure 20.

First of all, the 1/60_$N_3$_SBA-16 spectrum presents a strong and sharp absorption peak located at 3700 $cm^{-1}$ for the isolated -OH groups (stretching band ν(O-H)). Slightly shifted toward lower frequencies, at 3400 $cm^{-1}$, a strong and broad absorption peak stands for the stretching -OH groups bonded to each other through weak H bonds. The 3 bands located around 2900 $cm^{-1}$ are typical peaks for ν(C-H) of alkane groups corresponding to the triazole, the propyl linker and the aliphatic groups of TEMPO. As expected, the azido peak ν(N=N) can be identified at 2210 $cm^{-1}$.

Similar signals can be found for the 1/60_HYPSO 3 material with slight differences. Two peaks located at 3400 $cm^{-1}$ and 1620 $cm^{-1}$ are shifted toward lower frequencies but this perturbation was not considered since it is too weak to be significative. However, the difference in intensity for the peak attributed to the -$N_3$ groups was taking into account to quantity the efficiency of the cycloaddition ($Cu_{AAC}$ yield). This peak was integrated for the two samples and those of the unclicked materials set to 100 %. The same peak was integrated for the clicked sample and a yield corresponding to the ratio of $N_3$ converted into 1,2,3-triazole cycle was deducted. This study was systematically performed and the corresponding data are summarized in Table 4.

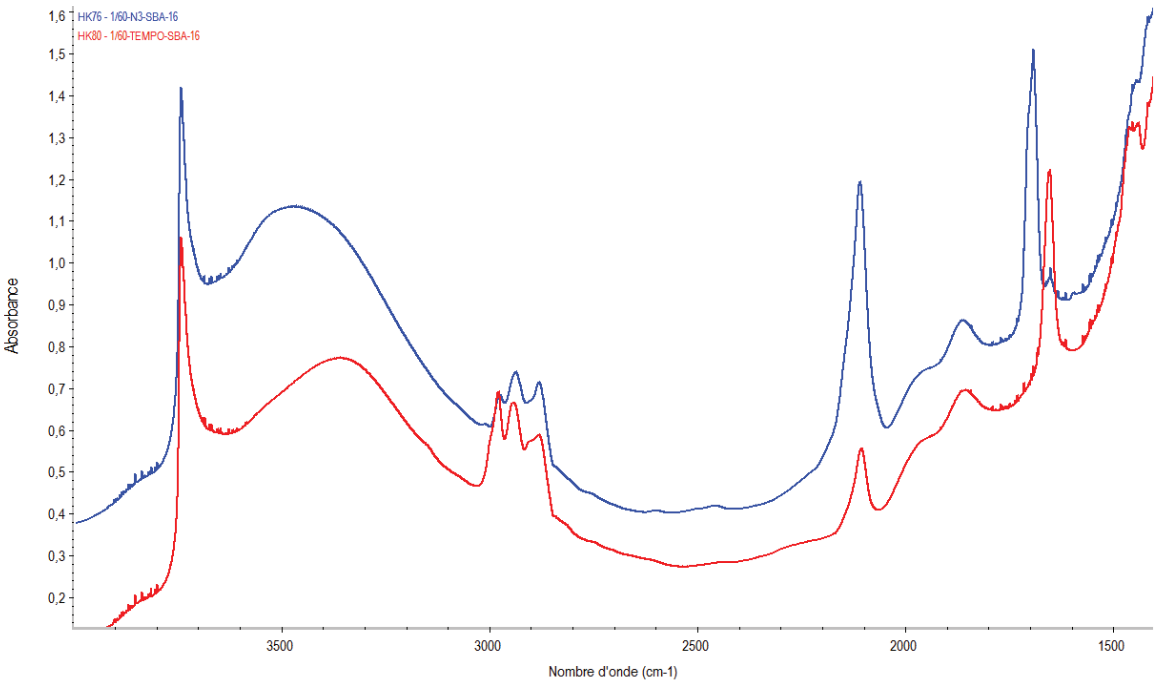

*Figure 20 : Comparison between DRIFT spectra of 1/60_$N_3$_SBA-16 (blue) and 1/60_HYPSO 3 materials (red)*

As shown in table 4, yields ranging from 64 % to 88 % for the more efficient cycloaddition was found. The yield decreases when the quantity of starting azido species decreases. This trend could be explained by a lack of accessibility of the azido groups that may be embedded in the silica walls or located into very small pores.

*Table 4: Radical concentrations determined by EPR spectroscopy and DRIFT analysis allowing to probe the surface.*

| Dilutions | [$N_3$] (µmol.g$^{-1}$) | [R] (µmol.g$^{-1}$) | [R] (µmol.cm$^{-3}$) | EPR yield (%) | Cu$_{AAC}$ yield (%) |
|---|---|---|---|---|---|
| 1/34 | 472 | 246 | 491 | 52 | 88 |
| 1/60 | 272 | 135 | 260 | 50 | 81 |
| 1/100 | 164 | 79 | 125 | 48 | 77 |
| 1/140 | 118 | 50 | 72 | 41 | 74 |
| 1/320 | 52 | 33 | 67 | 63 | 64 |

In addition to DRIFT analysis, Continuous Wave Electron Paramagnetic Resonance (CW-EPR) was performed on samples displaying supported TEMPO radicals. Analysis at room temperature allowed to precisely determine the radical concentrations whereas inter-radical distances were evaluated at 110 K (more details can be found in the supporting information).

To quantify the radical concentration in the solids, solutions of TEMPO in toluene with different radical concentrations were prepared as standards for calibration purposes. The corresponding EPR spectra were recorded and the peaks integrated to plot the calibration curve. Samples freshly synthesized were simply placed in EPR tubes and transferred in the EPR spectrometer. The quantity of radical [R] (µmol.cm$^{-3}$) was determined taking into account the total pore volume of the materials. As can be seen in table 4, percentages ranging (EPR yield) from 41 % to 63 % were calculated. The discrepancy between the results obtained by EPR and DRIFT may be attributed to the decomposition of some TEMPO radicals during the CuAAC reaction along with mathematical errors due to the fact that the concentration of radical is reported with respect of the porous volumes. Overall, we can conclude here that the incorporation of TEMPO, albeit not quantitative is higher than that obtained using other reported coupling reactions such as peptide coupling.

The inter-radical distances of the HYPSO solids were also evaluated by measuring the linewidths of the EPR signals since the aggregation of the radicals can lead to fast depolarization or very low polarization. Distances above 2 nm can be determined since the EPR signal is broadened by electron-electron dipolar couplings and spin exchange.[51] For larger distances, the dipolar linewidth is masked by inhomogeneous broadening (*ca.* 12 G). In this study, the central line of the EPR signal was used because it is less broadened by the g-tensor and hyperfine anisotropies and is therefore the most sensitive to the dipolar broadening.

For this purpose, samples were impregnated with 1,1,2,2-Tetrachloroethane and linewidths of EPR spectra were measured with an EPR spectrometer maintained to 110 K using a nitrogen flow. Data obtained for HYPSO 2 and HYPSO 3 were plotted in Figure 21 with an estimated error of 5%.

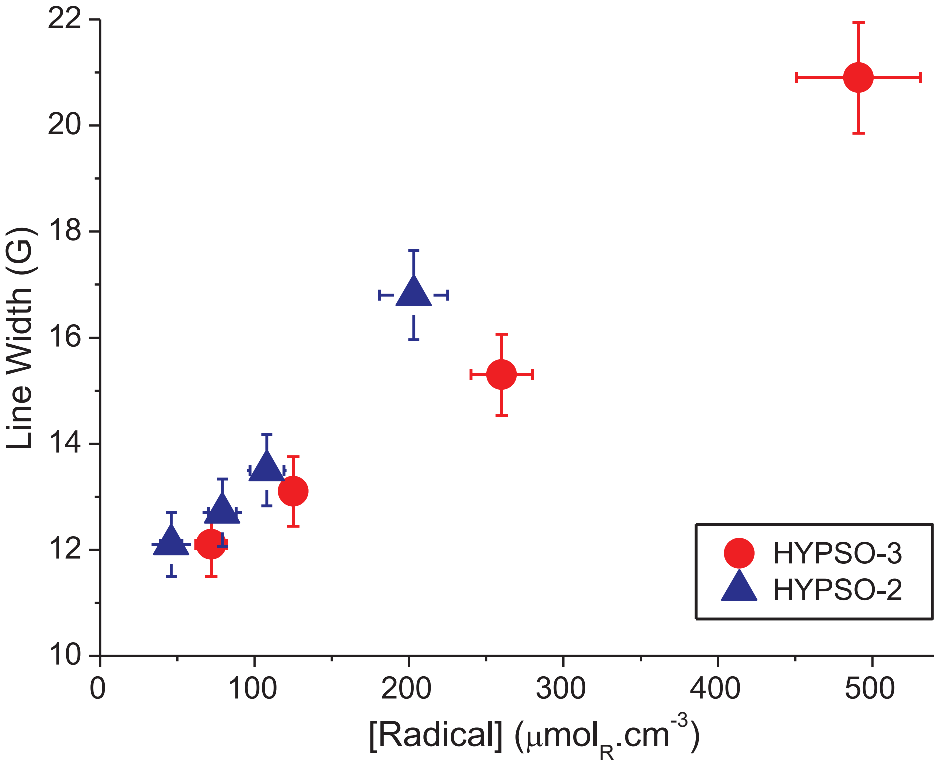

*Figure 21: EPR linewidths measured at 110 K as a function of the radical concentration for HYPSO 2 and HYPSO 3.*

EPR linewidths of 12.1; 13.1; 15.3 and 20.9 G were determined for HYPSO 3 with a dilution factor of 1/140, 1/100, 1/60 and 1/34 respectively. One can notice an increase of the linewidths with increase in the radical concentration. The values observed are almost proportional to the radical concentration. In comparison, the linewidths for HYPSO 2 are narrower which can be attributed to a more uniform 3D distribution of the radicals.

In conclusion, DRIFT spectroscopy has highlighted the presence of $N_3$ moieties onto the surface of the mesoporous silica materials. The conversion of these fragments into TEMPO radicals was also evaluated and compared to the radical concentration measured by EPR. Using EPR linewidths, we were also able to show the absence of radical aggregation and the random distribution of the species onto the surface of the materials.

## C. Polarization of ordered mesoporous silica HYPSO 2 and HYPSO 3

HYPSO 2 and HYPSO 3 materials were further tested as polarizing matrices after impregnation of a $H_2O$:$D_2O$ mixture. DNP experiments were performed at two distinct temperatures (4.2 K and 1.2 K) and the measured polarization values were compared to the radical concentration for each porous network (HYPSO 2 or HYPSO 3). In addition, HYPSO 3 was also impregnated with a 3M solution of sodium [1-$^{13}$C]-acetate which was further polarized by cross-polarization. The results are presented and discussed below with a complete description of the polarization process starting from the sample preparation to the data processing allowing to deduce the polarization values and the build-up times.

### 1. Preparation of ordered mesoporous silica for d-DNP experiments

The standard procedure consisted in filling 90 to 100 % of the pore volume of the mesoporous samples by incipient wetness impregnation. This method commonly used for the synthesis of heterogeneous catalysts consists in impregnating into a solid the molecule of interest previously dissolved in an aqueous medium. The capillary action pulls the solution into the pores which stays blocked inside of the porous network. Impregnated materials were then loaded in a holder and introduced in the polarizer.

### 2. Data processing

The DNP build-up curves were fitted with the following equation:

$$y(t) = P_{\max}[\,1 - \exp(-\frac{t}{\tau_{DNP}})\,]$$

The parameters of this equation are defined such follows:

$P_{\max}$ represents the maximum polarization reached for the considered sample

$\tau_{DNP}$ corresponds to the time required to reach 63 % of polarization for the considered sample. Five times $\tau_{DNP}$ correspond to 99 % of $P_{\max}$ for the considered sample.

### 3. Hyperpolarization of HYPSO matrices

HYPSO 2 and HYPSO 3 bearing TEMPO radicals with concentrations ranging from 67 to 263 µmol.cm$^{-3}$ were impregnated with a benchmark solution of $H_2O$ : $D_2O$ (2 : 8). In addition, SBA-15 and SBA-16 type solids containing only azido propyl groups onto their surface were impregnated with a solution of 40 mM TEMPOL in $H_2O$ : $D_2O$ : glycerol-d$_8$ (10 : 40 : 50) and used as standards. A classical DNP juice composed of $H_2O$:$D_2O$:glycerol-d$_8$ (10:40:50) doped with 40 mM TEMPOL was also used to compare the polarization values at the purely liquid state-of-the art polarization value. All the samples were proton polarized and the experiments were proceeded at 4.2 and 1.2 K using microwave frequency modulation.

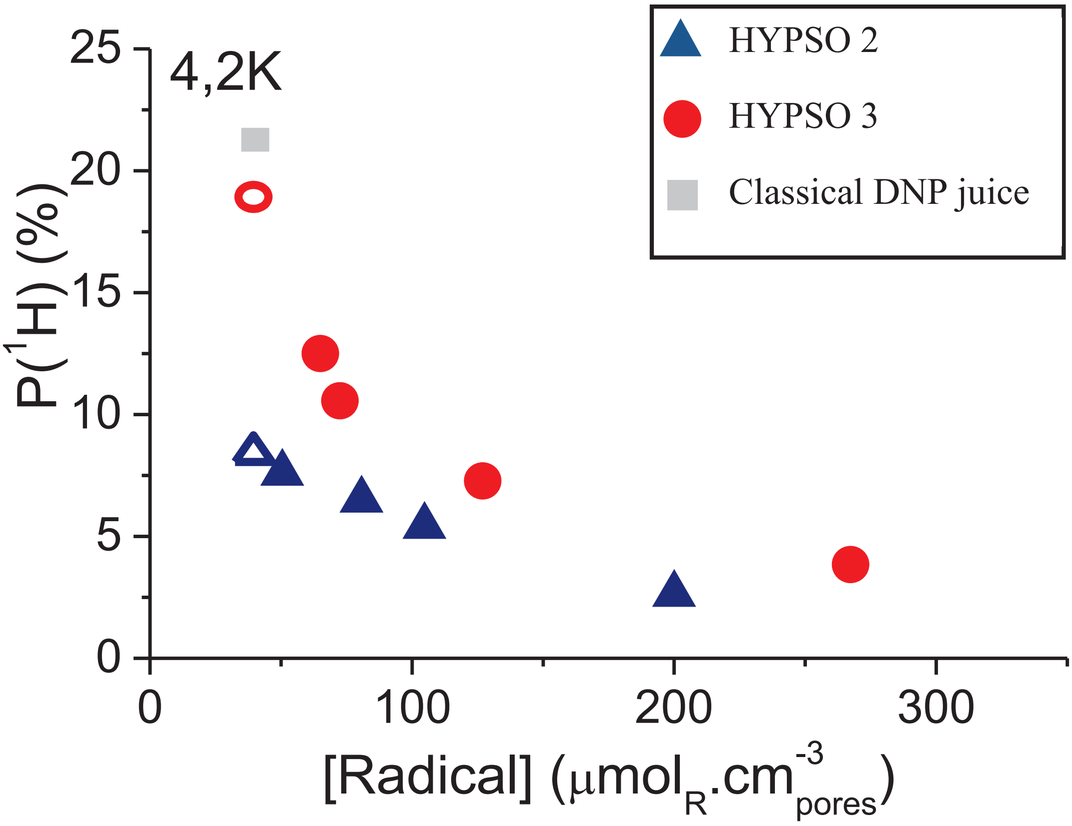

*Figure 22: HYPSO 2 and HYPSO 3 with different radical concentration impregnated with a mixture of $H_2O$:$D_2O$ and polarized at 4.2 K.*

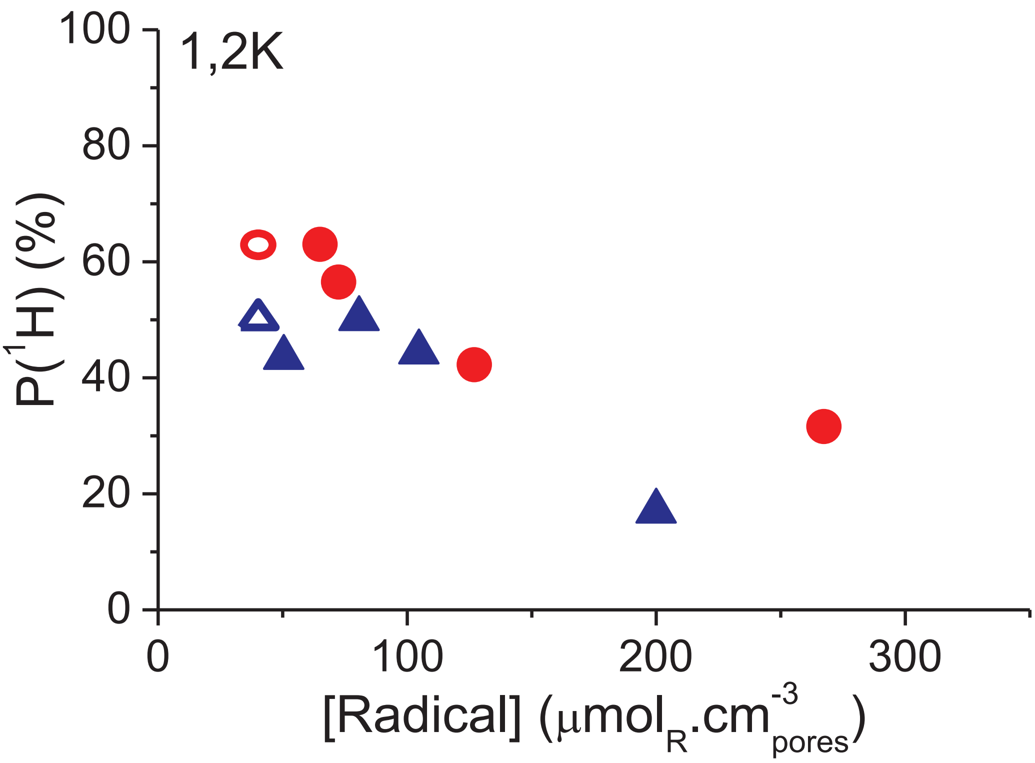

*Figure 23: HYPSO 2 and HYPSO 3 with different radical concentration impregnated with a mixture of $H_2O$:$D_20$ and polarized at 1.2 K.*

First of all, it is important to notice that four types of samples were polarized with the following characteristics:

- HYPSO 2 which are ordered mesoporous silica solids displaying long pore channels with a diameter of 8-10 nm stacked in a 2D-hexagonal arrangement. These samples were obtained using the Pluronic P123 instead of the Pluronic F127 (HYPSO 3) to get this specific arrangement. These samples are loaded with different concentrations of the same TEMPO radical.

- HYPSO 3 which are ordered mesoporous silica solids displaying a 3D structure where the pores are interconnected. These samples are also loaded with different concentrations of the same TEMPO radical.

- SBA-15 or SBA-16 type solids containing azido propyl linkers onto their surfaces loaded with a solution of TEMPOL. Here, two solids were analyzed 1/140_$N_3$_SBA-15 and 1/140_$N_3$_SBA-16.

- Classical DNP juice: Liquid sample (no silica matrix) composed of $H_2O$:$D_2O$:glycerol-$d_8$ (10:40:50) doped with 40 mM TEMPOL.

At 4.2 K, the samples exhibited lower polarization values as expected because the polarization process is highly dependent on the temperature. Indeed, when increasing the temperature, the electrons are less polarized which means they will transfer a significantly lower amount of their polarization. In this specific case, a maximum proton polarization of $P(^1H)$ = 21.5 % was observed for the TEMPOL DNP reference. This can be directly compared with the two following solids: 1/140_$N_3$_SBA-15 and 1/140_$N_3$_SBA-16 which gave a $P(^1H)$ = 9 % and $P(^1H)$ = 19 % respectively. Whereas, SBA-16 type materials could achieve a proton polarization close to the DNP isotropic mixture, SBA-15 type materials exhibited a low proton polarization value. This observation thus has a direct link with the silica framework which is the only difference between the materials. The measurements suggest that it is easier to transfer the polarization from the electrons to the surrounding nuclei when using HYPSO 3 type sample. The small windows allowing to interconnect the pores of HYPSO 3 could be responsible for a better polarization transfer in the 3 dimensions of the matrix.

At the same temperature, the HYPSOs previously impregnated with the benchmark solution of $H_2O$:$D_2O$ provided proton polarization values even more pronounced at low radical concentrations. Indeed, a maximum proton polarization of $P(^1H)$ = 13 % for HYPSO 3 and $P(^1H)$ = 8 % for HYPSO 2 were obtained for the lower concentrations. A similar behavior was observed for HYPSOs materials, SBA-16 type materials like HYPSO 3 displayed again higher polarization values than SBA-15 type materials like HYPSO 2. The hypothesis of a matrix effect is confirmed independently of the immobilization of the TEMPO radicals.

At 1.2 K, 1/140_$N_3$_SBA-15 and 1/140_$N_3$_SBA-16 were able to reach $P(^1H)$ = 50 % and $P(^1H)$ = 63 % respectively. These polarization values are also the maximum measured for HYPSO 2 and HYPSO 3 at this same temperature. Since the temperature is a non-negligible parameter for the DNP process, it is not surprising to get higher polarization in this case compared to the previous experiments performed at 4.2 K. We can also notice that HYPSO 3 need a lower radical concentration to reach higher polarization compared to HYPSO 2 thus confirming a better polarization transfer. The polarization differences already observed at 4.2 K for the azido-materials only impregnated with TEMPO radicals are also observed on HYPSOs at this temperature.

In conclusion, higher proton polarization values were observed at low temperature as expected. The presence of silica was found inert with respect to the polarization experiments as similar polarization values were recorded at 4.2 K and 1.2 K with or without silica matrix. SBA-16 type architecture allowed to reach higher polarization values than those obtained for SBA-15 solids. This result suggests that the organization of the porous network has an impact on the polarization performances: HYPSO 3 which displays a 3D pore network arrangement is much more efficient than HYPSO 2 which is composed of a 2D hexagonal arrangement of long pore channels. This 3D architecture may ease the spin diffusion with respect to the 2D architecture. In the latter architecture the polarization propagation only proceeds toward a unique direction which is the one of the pore channels.

### 4. $^1$H polarization transfer to carbon nuclei using cross-polarization in HYPSO 3 as polarizing matrix:

$^{13}$C polarization experiments can be operated either by direct polarization of the carbon nuclei or by cross-polarization from proton to carbon. The first approach is usually performed with carbon-centered radicals such as 1,3-bisdiphenylene-2-phenylallyl (BDPA) or trityl radicals (Figure 24) in conventional glassy DNP formulations.

The BDPA radical also known as the Koeslch’s radical was first synthesized in 1957. [52] The delocalization of the radical onto the two fluorene groups make it a persistent free radical. Through a solid effect mechanism, BDPA was used in a polystyrene matrix[53-57], coupled to TEMPO moieties[58] or even more recently used in sulfolane[59] for the first time in dissolution-DNP. However, BDPA radicals have a major drawback which is their low solubility in water[59], thus hampering the dissolution step.

Trityl radicals were first synthesized by M. Gomberg[60] in 1900 with the triphenylmethyl radical. They were rapidly modified to increase their solubility by adding different functional groups. In Figure 24, two radicals known as CT03 and OX063 are presented. They are respectively decorated with $CH_3$ and $CH_2$-$CH_2$-OH chains which give them a complete different solubility. They were developed by Nycommed Innovations (GE Healthcare) and used in d-DNP.

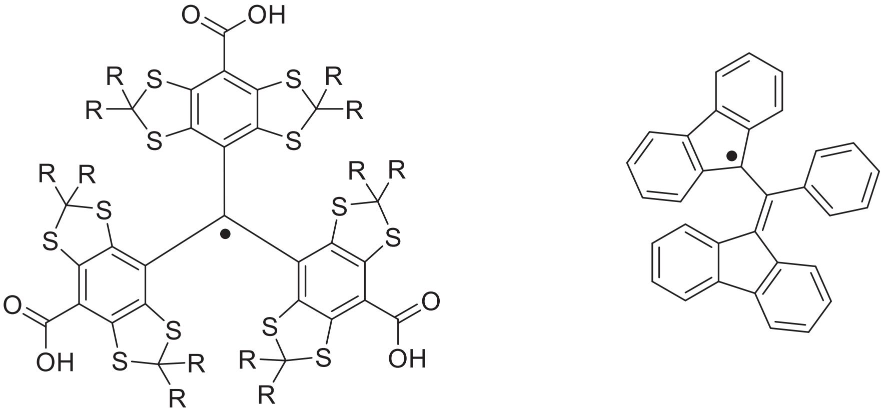

R = $CH_2CH_2OH$ (OX063)
R = $CH_3$ (Finland or CT03)

BDPA

*Figure 24: Representation of the trityl and BDPA radicals used to polarize carbons.*

The second approach largely employed in solid NMR was further developed in DNP. This technique consists in transferring the magnetization of high gamma nuclear spins ($^{1}H$) to low gamma nuclear spins ($^{13}C$, $^{15}N$, $^{129}Xe$ …) in order to improve the polarization of a targeted compound. The idea of this technique is to combine the advantages of high and low gamma nuclei which means important polarization rates and long life-times.

BDPA and trityl radicals have narrow EPR lines but remain expensive compared to TEMPO radicals (OX063 being the most expensive). Moreover, higher polarization rates can be expected for protons than carbons because of their physical characteristics ($\gamma^{1}{}_{H} > \gamma^{13}{}_{C}$). For these reasons, TEMPO species were used to polarize protons and the polarization was transferred to molecules bearing carbons by cross polarization. With a spin equal to 0, $^{12}C$ is impossible to detect by NMR or MRI and its low natural abundance in $^{13}C$ is close to 1%. Labelled compounds were thus employed and in particular sodium [1-$^{13}C$]-acetate was investigated to probe different metabolic pathway[61-66].

### a) Experimental section

Optimal HYPSO 3 with a radical concentration of [R]= 67 umol.cm$^{-3}$ was first impregnated with a 3M solution of sodium [1-$^{13}$C]-acetate in $H_2O$:$D_2O$ (1:9). The solid was then introduced in a home-built d-DNP polarizer[63] with a magnetic field of $B_0$ = 6.7 T at 1.2 K. The polarizer, equipped with a probe optimized for CP[67] experiment, allowed to transfer the proton polarization to carbon. Details concerning the pulse sequence can be find in the following articles.[68-71]

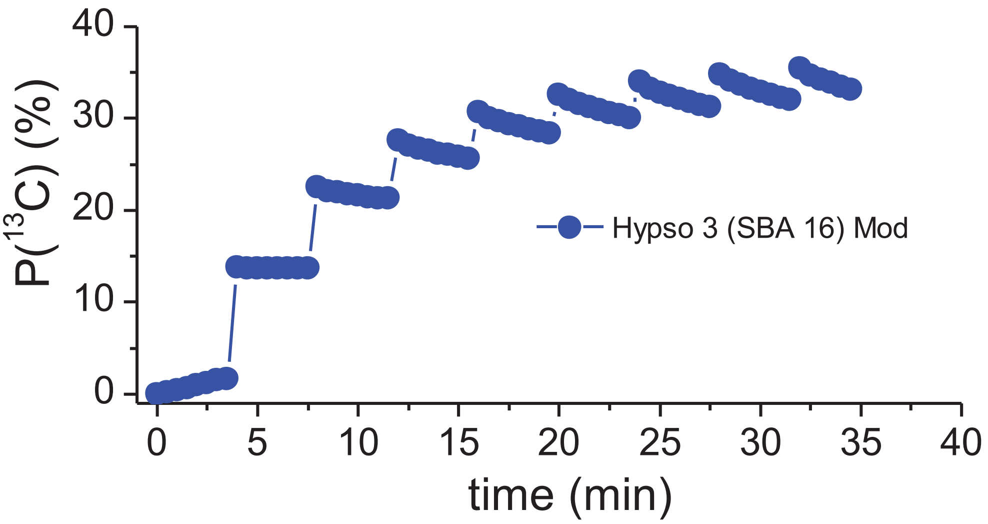

*Figure 25: Cross-polarization experiment on HYPSO 3 impregnated with a mixture of 3M solution of sodium [1-$^{13}$C]-acetate in $H_2O$:$D_2O$*

As shown in Figure 25, the proton polarization was transferred by cross-polarization using 8 contacts each 4 minutes to reach a $P(^{13}C)$ of 36 % after *ca.* 30 minutes. The difference of the polarization $P(^1H)$ = 63 % and $P(^{13}C)$ = 36 % obtained in this case could be explained by first the chemical difference between the analytes and second by a polarization loss during the transfer from proton to carbon P($^1$H -> $^{13}$C). As performed in conventional dissolution-DNP experiment, hot pressurized water was used to expel the solution of sodium [1-$^{13}$C]-acetate from the solid and this solution was further transferred to the NMR spectrometer through a magnetic tunnel. After NMR acquisition, the liquid was filtrated, centrifugated and analyzed by EPR. Unfortunately, EPR signal coming from TEMPO radicals were found in the aliquot but in very low concentration close to 1 µmol.L$^{-1}$. This may arise from the presence of some silica grains which were not accurately filtered off.

## 5. Investigation of the build-up times of HYPSO materials

As defined above, the build-up time $\tau_{DNP}$ corresponds to the time required to reach 63 % of the maximal polarization for a considered sample. It allows thus to evaluate the polarization time which should be in the optimal case as fast as possible. The build-up times of HYPSO 2 and HYPSO 3 were recorded at two temperatures: 4.2 K and 1.2 K and compared to the $N_3$ materials and the classical DNP juice.

### a) Measurement of the build-up times at 4.2 K

The same DNP polarizer operating at $B_0$ = 6.7 T was used to measure the build-up times on several samples. The obtained values were fitted using a monoexponential curve which does not take into account polarization by spin diffusion. As a reference, a classical DNP solution containing TEMPOL radicals in a $H_2O$:$D_2O$:Glycerol-$d_8$ mixture was prepared. As shown in Figure 26, the glassy mixture displays a build-up time of *ca* 75 s which is comparable to that obtained with the $N_3$_SBA-15 sample impregnated with the same solution. The polarization times are therefore not affected by the presence of SBA-15 type silica matrices. However, the impregnation of TEMPOL radicals in $N_3$_SBA-16 materials gave a longer build-up time of 145 s.

HYPSO 2 solids containing TEMPO radicals with a concentration ranging from 50 µmol.cm$^{-3}$ to 200 µmol.cm$^{-3}$ were also impregnated with a mixture of $H_2O$:$D_2O$ (2:8). The open triangles correspond to sample analyzed without frequency-modulation and the full triangles with frequency-modulation. Four values are plotted on the Figure 26 where 3 full triangles are behind 3 open triangles. The build-up times were found to increase when the radical concentration decreases. As a reminder, at this temperature the maximum proton polarization was obtained for the sample containing 50 µmol.cm$^{-3}$ of radical. A small difference can be noticed at this concentration with or without frequency-modulation but this gap is not significant.

Recorded build-up times using HYPSO 3 materials were also studied with or without switching on the frequency-modulation. Data are plotted in Figure 26 using the same symbols code: the open circles correspond to build-up times without frequency-modulation and the full circles to build-up times with frequency-modulation. Even in this case, the frequency modulation did not allow to get higher polarization values. However, one can notice fast build-up times for samples displaying concentrations of 127 and 267 µmol.cm$^{-3}$. Although these values are very interesting, the reached polarization levels are quite low. Therefore, samples with lower radical concentrations were preferred as they provide a good compromise between relatively high proton polarizations and not too long build-up times.

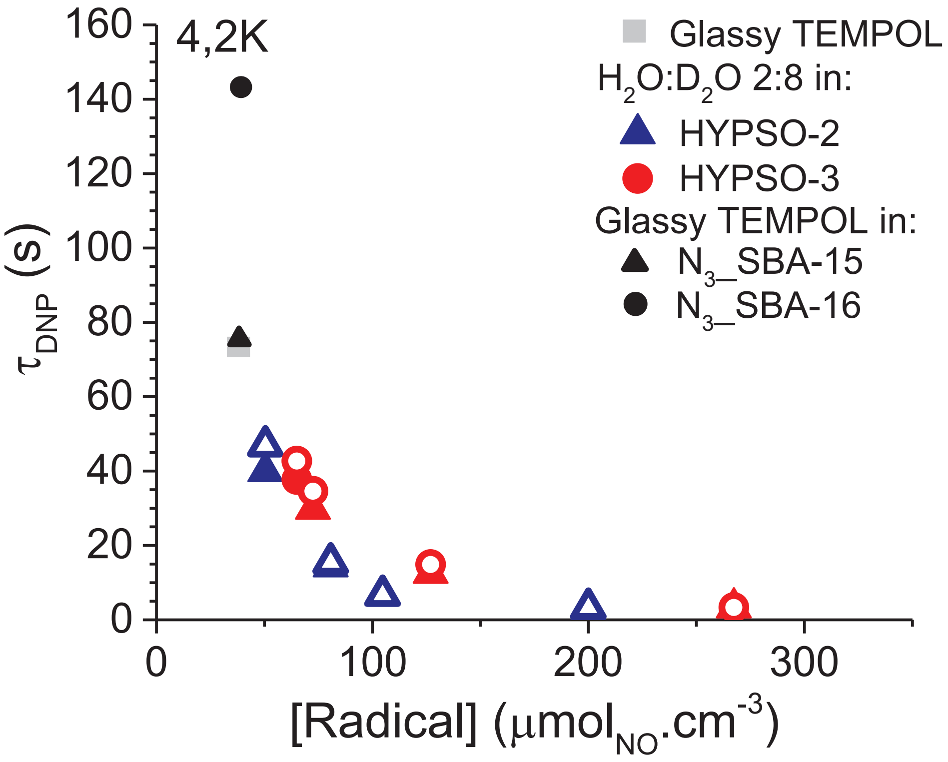

*Figure 26: Build-up times as a function of the radical concentration for samples analyzed at 4.2 K.*

In conclusion, it is clear that the frequency-modulation has no impact on the build-up times at this temperature. Moreover, HYPSO 3 materials display shorter build-up times than HYPSO 2 solids arising from their specific 3D architecture.

### b) *Measurement of the build-up times at 1.2 K*

At 1.2 K, the build-up times are longer and exceed largely the maximum of 150 s recorded at 4.2 K. $N_3$_SBA-15 and $N_3$_SBA-16 materials were again impregnated with a glassy mixture constituted of TEMPOL as polarizing agents. Build-up times around 325 s and 500 s were recorded for $N_3$_SBA-15 and $N_3$_SBA-16 materials respectively. This bigger difference at this temperature emphasizes a build-up time longer for SBA-16 type materials.

HYPSO materials were also analyzed by impregnation of a mixture of $H_2O$:$D_2O$. At this temperature, a general trend consisting in reducing the build-up times by applying frequency-modulation is observed for samples with a concentration below 72 µmol.cm$^{-3}$. Higher radical concentrations display analogous results with or without frequency-modulation. Then, optimal HYPSO 2 ([R]= 50 µmol.cm$^{-3}$ ) reveals a lower build-up time when frequency-modulation is applied ( $T_{DNP}$ = 150 s ).

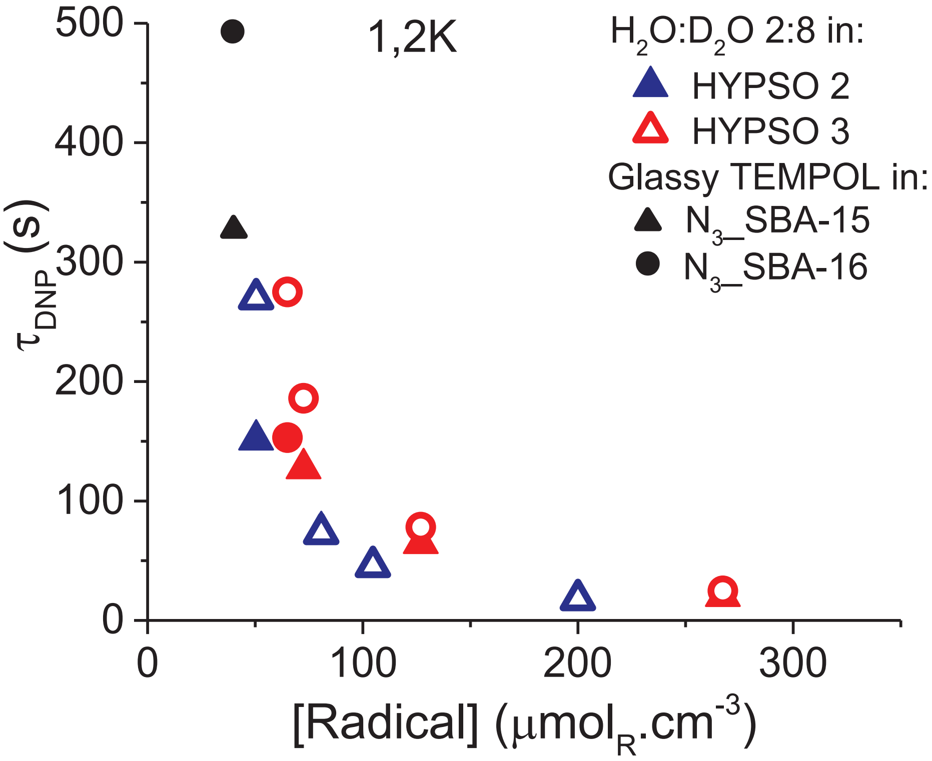

*Figure 27: Build-up times as a function of radical for temperature T= 1.2 K.*

In conclusion, similar results were observed at 4.2 K for $N_3$_SBA-15 materials and the state-of-the art DNP juice. At the same temperature, $N_3$_SBA-16 materials displayed a significant difference with a build-up time almost doubled. However, this long build-up time corresponds to an increase of the proton polarization value. At 1.2 K, the frequency-modulation turned out to be significant for radical concentrations below 72 μmol.cm$^{-3}$. Regarding HYPSO materials, SBA-16 type materials showed better performances for a concentration of 72 μmol.cm$^{-3}$ with frequency-modulation.

## V. Conclusions

The methodology (direct synthesis using a templating route) used to synthesize HYPSO materials has successfully led to silica materials containing TEMPO radicals covalently linked onto their silica surface. For this purpose, two main precursors, the 3-azidopropyltriethoxysilane and the alkyne derivative bearing TEMPO units were first prepared and fully characterized. Through a copper(I)-catalyzed alkyne-azide cycloaddition, the incorporation of TEMPO radicals on silica materials were successfully achieved with various loadings and a yield of ca. 50% (according to EPR). HYPSO 2 and HYPSO 3 display two different architectures (2D hexagonal vs 3D cubic for HYPSO 2 and HYPSO 3 respectively). These solids were used as polarizing matrices and the polarization levels as well as the build-up times were measured. In general, samples coated with a high radical concentration allow to reach short build-up times but also low proton polarizations. A compromise between high polarization values and short build-up times must be done. The optimal HYPSO 3 containing 72 μmol.cm$^{-3}$ of radicals displays a shorter build-up time as compared to the HYPSO 2 solid with 50 μmol.cm$^{-3}$ of radicals with higher performances in polarization, $P(^1H) = 63$ % and $P(^1H) = 50$ % respectively. This difference was attributed to a more homogeneous 3D distribution of radicals in HYPSO 3 and an interconnection of the pores which allows a better nuclear spin diffusion in the solid.

# SUPPORTING INFORMATION

## VI. Precursor synthesis

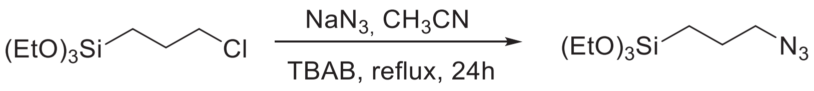

In a 500 mL Schlenk, sodium azide (4,08 g; 1,5 equiv. 62,8 mmol) and tetrabutylammonium bromide (TBAB; 2,66 g; 0,2 equiv. 8,3 mmol) were dried overnight under vacuum at 130°C. Dry acetonitrile (120 mL) and 3-chloropropyltriethoxysilane (9,8 mL; 40,70 mmol) were added and reflux under argon overnight. After the reaction, the solvent was removed under reduced pressure. The crude mixture was then diluted in pentane and the suspension was filtered under argon to yield to a colorless liquid.

$^1$H NMR ($CD_2Cl_2$,300 MHz): δ 0,62-0,65 (m, 2H), 1,2 (t, J = 6,6 Hz, 9H), 1,67 (m, 2H), 3,26 (t, J = 7 Hz, 2H), 3,79 (q, 6H).

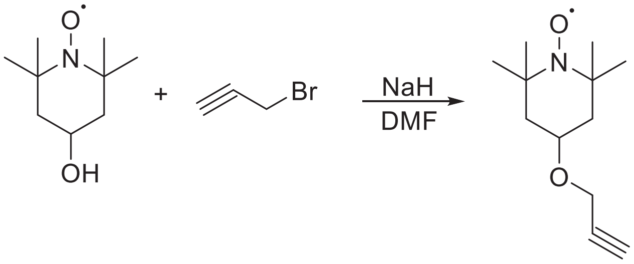

In a 500 mL three-neck round bottom flask and under argon, NaH (60% in mineral oil; 1,3 equiv. 2,71 g; 67,93 mmol) and dry DMF (DMF was refluxed, distilled on $CaH_2$ and stored for 24h on 3 Å molecular sieve; 300 mL) were mixed. Once, the reaction mixture was cooled down to 0 °C, 4-hydroxy-TEMPO (9 g; 52,25 mmol) was added portionwise and stirred at room temperature for 30 minutes. Then, propargyl bromide (7,85 mL; 52,25 mmol) was added dropwise at 0°C. The solution changes rapidly from orange to black color and before adding water (250 mL), the resulting mixture is stirred for 3h at room temperature. The solution is extracted with EtOAc (5 x 80 mL) and the combined organic phases were washed with water (5 x 80 mL) and dried over $MgSO_4$, filtered, evaporated under reduced pressure and purified by column chromatography (silica gel, 10% EtOAc in hexane) giving rise to the desired product as an orange solid.

# VII. Materials synthesis

## A. SBA-15 type solids

### 1. Insertion of azido moieties

Typical procedure is given for 1/34_N3_SBA-15 material: In a round bottom flask containing the (3-azidopropyl)triethoxysilane (341 mg, 1 equiv) and TEOS (9. 75 g, 34 equiv) a solution of pluronic P123 (1.5mol% with respect to siloxy-precursors) in aqueous HCl (pH= 1.5) was added. Then, the mixture was stirred for 3h at room temperature and placed in a pre-heated oil bath settled to T= 45 °C. The temperature of the solution was carefully monitored and NaF (1.5mol% with respect to siloxy-precursors) was added when the reaction mixture reached T= 40 °C. Finally, the reaction mixture was stirred at 45 °C for 72h. The resulting material was filtered and washed with $H_2O$ (3 x 3 times the gel volume), EtOH (3 x 3 times the gel volume) and $Et_2O$ (3 x 3 times the gel volume). In order to remove the surfactant (P123), the resulting material was placed into a soxhlet cartridge and extracted with EtOH for 48h. The material was filtered and washed with $Et_2O$ and dried under high vacuum ($10^{-5}$ mbar) at 135 °C for 15h.

### 2. Insertion of TEMPO radicals through CuAAC

Copper-catalyzed alkyne-azide cycloaddition (CuAAC) was used to couple the azido fragments with TEMPO radicals. Typical click-chemistry is presented for the 1/34_$N_3$_SBA-15 material previously described.

Under argon atmosphere, o-propargyl TEMPO (965 mg, 5 equiv) was added to a suspension of $N_3$_SBA-15 materials (2 g) in DMF (20 mL) and $NEt_3$ (1 mL) and CuI (5.1 mg, 5mol%). The mixture was stirred for 72h at 50 °C and then filtrated and washed with DMF (2 x 20 mL), EtOH (3 x 20 mL), $Et_2O$ (3 x 20 mL). Finally, the product obtained was dried under high vacuum ($10^{-5}$ mbar) at 50 °C for 15h.

## B. SBA-16 type solids

The following procedure is inspired from A. Boullanger, New J. Chem. 2010, 34, 738-743.

### 1. Insertion of azido moieties

The typical procedure for 1/100_N3_SBA-16 material is: Pluronic F127 (2g), NaCl (7.19, ratio F127 to Si-based reactant: 35 equiv) in aqueous 2 M HCl (20mL, 0.5 mL/mmol siloxy-precursors) and water (60mL, 1.5 mL/mmol siloxy-precursors) were dissolved in a closed 250 mL teflon bottle at room temperature for 1h30 and then for 1 h at 40 °C. Then, TEOS (8.31 g, 100 equiv) and (3-azidopropyl)triethoxylsilane (99mg, 1 equiv) were simultaneously added. The bottle was closed again and vigorously stirred at 40 °C for 20 h before it was placed in a pre-heated oven at 100 °C for 2 h without agitation. The white precipitate was filtered and washed with EtOH (3 × 1/3 of initial reaction volume) and acetone (3 × 1/3 of initial reaction volume). The resulted solid was then crushed in a mortar and dried at 100 °C under vacuum ($10^{-5}$ mbar) for 5 h. Then the material is stirred in water/pyridine solution (1:1, 1.5 mL/mmol siloxy-precursors) adjusted to pH 6.5 by aqueous HCl (2 M) at 70 °C for 16 h. Next, the material is filtered and washed with EtOH (3 × 1/3 of reaction volume) and acetone (3 × 1/3 of reaction volume) and dried at 100 °C under vacuum ($10^{-5}$ mbar) for 15 h.

### 2. Insertion of TEMPO radicals through CuAAC

Copper-catalyzed alkyne-azide cycloaddition (CuAAC) was used to couple the azido fragments with TEMPO radicals. Typical click-chemistry is presented for the 1/100_$N_3$_SBA-16 materials previously described.

Under an argon atmosphere, O-propargyl TEMPO (342 mg, 2.67 mmol) was added to a suspension of 1/100_$N_3$_SBA-16 (2 g, 0.535 mmol azide) in DMF (20 mL) and $Et_3N$ (880 µL). Then a solution of CuI (3.1 mg, 16 µmol) in DMF/$Et_3N$ (1:1, 240 µL) was added. The mixture was stirred for 72 h at 50 °C and then filtrated and washed with DMF (2 × 20 mL), EtOH (3 × 20 mL), $Et_2O$ (2 × 20 mL). The product was then dried under vacuum ($10^{-5}$ mbar) at 50 °C for 15 h.

# VIII. Characterization

## A. $N_2$ adsorption/desorption

Experiments were performed at 77 K using a BELSORB-Max from BEL-JAPAN. Before $N_2$ adsorption, the samples were outgassed at $10^{-5}$ mbar and T= 408 K for 12 h. The pore diameter distribution and the mean pore diameter ($d_p$) were calculated using Barrett–Joyner–Halenda (BJH) method. The specific surface area ($S_{BET}$) was calculated using the Brunauer–Emmett–Teller (BET) equation.

## B. Diffuse Reflectance Infrared Fourrier Transform Spectroscopy (DRIFTS)

Diffuse Reflectance Infrared Fourrier Transform spectroscopy is an analytical technique where an infrared beam interacts with the particles and is reflected off the surface depending on the properties of the powder. Preparation of the sample is really simple and consists only in introducing the powder in the cell. DRIFT spectra were recorded on a Nicolet 6700-FT spectrometer using a cell equipped with $CaF_2$ windows. Typically, 64 scans were accumulated for each spectrum (resolution 4 $cm^{-1}$).

## C. Continuous Wave Electron Paramagnetic Resonance (CW EPR) parameters and sample preparation

CW EPR spectra were recorded on a Bruker EMX X Band spectrometer (9.5 GHz microwave frequency). Conversion time was set to 40.96 ms, time constant to 5.12 ms and 1024 data points were recorded. The modulation frequency was 100 kHz and the modulation amplitude 1 Gauss. In all measurements, attenuation was varied such that no saturation was observed.

### 1. Determination of the radical concentration

The samples were filled in a 3.0 mm quartz tube with a maximum sample height of 3 mm. The sample position in the cavity was carefully optimized. The spectra were recorded at room temperature and with a sweep width of 600 Gauss and attenuation between 26 and 14 dB. The amount of radical was determined by double integration of the CW spectra and referencing to calibration curve of TEMPO in toluene solutions measured for the concentration range between 0.4 and 80 mM. An additional correction for the difference in the incident microwave power has been taken into account. Data was processed with OriginLab.

### 2. Peak linewidth procedure and measurement

Each sample was impregnated with 1,1,2,2-Tetrachloroethane and filled in a 3.0 mm quartz tube. All spectra were recorded at 110K using a nitrogen flow cryostat. Attenuation was varied from 32 to 23 dB. The EPR spectrum of a nitroxide radical consists of three lines due to strong hyperfine interaction with the $^{14}$N nucleus. For the line-width measurements we have used the central line, which is less broadened by the g-tensor and hyperfine anisotropies and which therefore is the most sensitive to the dipolar broadening. For the obtained signal to noise levels, the estimated linewidth error bars were around 5 %.

## D. Transmission Electron Microscopy (TEM)

Conventional TEM micrographs were performed at the “Centre Technologique des Microstructures”, UCBL, Villeurbanne, France, using a JEOL 2100F electron microscope. The acceleration voltage was 200 kV. The samples were prepared by dispersing a drop of the ethanol suspension of a ground sample on a Cu grid covered by a carbon film.

## E. Nuclear Magnetic Resonance (NMR)

Liquid NMR spectra were recorded on BRUKER AVANCE 300 spectrometer (300 MHz).

## F. Small Angle X-Ray Diffraction (SA-XRD)

Small-Angle X-ray scattering (SAXS) on powder was carried out with a Bruker D8 Avance diffractometer (33 kV & 45 mA) with CuKα radiation ($\lambda = 0.154$ nm) in the Service Diffraction RX, IRCE Lyon, France. The diffraction patterns were collected in the 2θ angle range [0.45°-7.0°] at a scanning rate of 0.1°/min. The interplane spacings, d(hkl) for different Miller indices (hkl) were calculated using the Bragg's law ($nk = 2d\sin\theta$). The lattice parameter (a0) for the hexagonal structured mesoporous material is given by $a0 = 2d(100)/\sqrt{3}$.

# IX. References

1. J. Rouquerol, D. A., C. W. Fairbridge, D. H. Everett, J. M. Haynes, N. Pernicone, J. D. F. Ramsay, K. S. W. Sing and K. K. Unger, Recommendations for the characterization of porous solids (Technical Report). *Pure Appl. Chem.* **1994,** *66* (8), 1739-1758.
2. Roque-Malherbe, R., Complementary approach to the volume filling theory of adsorption in zeolites. *Microporous and Mesoporous Materials* **2000,** *41* (1), 227-240.
3. Valtchev, V.; Mintova, S., Hierarchical zeolites. *MRS Bulletin* **2016,** *41* (9), 689-693.
4. Davis, M. E., New vistas in zeolite and molecular sieve catalysis. *Accounts of Chemical Research* **1993,** *26* (3), 111-115.
5. Weitkamp, J.; Fritz, M.; Ernst, S., Zeolites as media for hydrogen storage. *International Journal of Hydrogen Energy* **1995,** *20* (12), 967-970.
6. Schmidt, W., Application of Microporous Materials as Ion-Exchangers. In *Handbook of Porous Solids*, Wiley-VCH Verlag GmbH: 2008; pp 1058-1097.
7. Liao, P.-Q.; Shen, J.-Q.; Zhang, J.-P., Metal–organic frameworks for electrocatalysis. *Coordination Chemistry Reviews* **2017**.
8. Heinke, L.; Tu, M.; Wannapaiboon, S.; Fischer, R. A.; Wöll, C., Surface-mounted metal-organic frameworks for applications in sensing and separation. *Microporous and Mesoporous Materials* **2015,** *216*, 200-215.
9. Tsuneo, Y.; Toshio, S.; Kazuyuki, K.; Chuzo, K., The Preparation of Alkyltriinethylaininonium–Kaneinite Complexes and Their Conversion to Microporous Materials. *Bulletin of the Chemical Society of Japan* **1990,** *63* (4), 988-992.
10. Beck, J. S.; Vartuli, J. C.; Roth, W. J.; Leonowicz, M. E.; Kresge, C. T.; Schmitt, K. D.; Chu, C. T. W.; Olson, D. H.; Sheppard, E. W.; McCullen, S. B.; Higgins, J. B.; Schlenker, J. L., A new family of mesoporous molecular sieves prepared with liquid crystal templates. *Journal of the American Chemical Society* **1992,** *114* (27), 10834-10843.
11. Kresge, C. T.; Leonowicz, M. E.; Roth, W. J.; Vartuli, J. C.; Beck, J. S., Ordered mesoporous molecular sieves synthesized by a liquid-crystal template mechanism. *Nature* **1992,** *359*, 710.
12. Kresges, C. T.; Leonowicz, M. E.; Roth, W. J.; Vartuli, J. C., Composition of synthetic porous crystalline material, its synthesis. **1990**.
13. Anderson, M. W., Simplified description of MCM-48. *Zeolites* **1997,** *19* (4), 220-227.
14. Kresge, C. T.; Vartuli, J. C.; Roth, W. J.; Leonowicz, M. E., The discovery of ExxonMobil's M41S family of mesoporous molecular sieves. In *Studies in Surface Science and Catalysis*, Terasaki, O., Ed. Elsevier: 2004; Vol. 148, pp 53-72.
15. Kolb, H. C.; Sharpless, K. B., The growing impact of click chemistry on drug discovery. *Drug Discovery Today* **2003,** *8* (24), 1128-1137.
16. Zhao, D.; Feng, J.; Huo, Q.; Melosh, N.; Fredrickson, G. H.; Chmelka, B. F.; Stucky, G. D., Triblock Copolymer Syntheses of Mesoporous Silica with Periodic 50 to 300 Angstrom Pores. *Science* **1998,** *279* (5350), 548-552.
17. Zhao, D.; Huo, Q.; Feng, J.; Chmelka, B. F.; Stucky, G. D., Nonionic Triblock and Star Diblock Copolymer and Oligomeric Surfactant Syntheses of Highly Ordered, Hydrothermally Stable, Mesoporous Silica Structures. *Journal of the American Chemical Society* **1998,** *120* (24), 6024-6036.
18. Boullanger, A.; Alauzun, J.; Mehdi, A.; Reye, C.; Corriu, R. J. P., Generic way for functionalised well-ordered cubic mesoporous silica via direct synthesis approach. *New Journal of Chemistry* **2010,** *34* (4), 738-743.
19. de Ávila, S. G.; Silva, L. C. C.; Matos, J. R., Optimisation of SBA-15 properties using Soxhlet solvent extraction for template removal. *Microporous and Mesoporous Materials* **2016,** *234*, 277-286.

20. Hsu, Y.-C.; Hsu, Y.-T.; Hsu, H.-Y.; Yang, C.-M., Facile Synthesis of Mesoporous Silica SBA-15 with Additional Intra-Particle Porosities. *Chemistry of Materials* **2007,** *19* (5), 1120-1126.
21. Huang, L.; Poh, C.; Ng, S. C.; Hidajat, K.; Kawi, S., Preparation of Supported Mesoporous Thin Films Concerning Template Removal by Supercritical Fluid Extraction. *Langmuir* **2005,** *21* (4), 1171-1174.
22. Tian, B.; Liu, X.; Yu, C.; Gao, F.; Luo, Q.; Xie, S.; Tu, B.; Zhao, D., Microwave assisted template removal of siliceous porous materials. *Chemical Communications* **2002,** (11), 1186-1187.
23. W. Gallis, C. C. L., Rapid Calcination of Nanostructured Silicate Composites by Microwave Irradiation. **2001,** *13* (1), 23-26.
24. Hozumi, Y. Y., T. Kameyama, K. Hiraku, H. Sugimura, O. Takai, M. Okido, Photocalcination of Mesoporous Silica Films Using Vacuum Ultraviolet Light. **2000,** *12* (13), 985-987.
25. Mamaeva, V.; Sahlgren, C.; Lindén, M., Mesoporous silica nanoparticles in medicine—Recent advances. *Advanced Drug Delivery Reviews* **2013,** *65* (5), 689-702.
26. Bagheri, S.; Mohd Hir, Z. A.; Yousefi, A. T.; Abdul Hamid, S. B., Progress on mesoporous titanium dioxide: Synthesis, modification and applications. *Microporous and Mesoporous Materials* **2015,** *218*, 206-222.
27. Sun, J.; Sun, Y.; Gai, L.; Jiang, H.; Tian, Y., Carbon-coated mesoporous LiTi2(PO4)3 nanocrystals with superior performance for lithium-ion batteries. *Electrochimica Acta* **2016,** *200*, 66-74.
28. Wang, X.; Lin, K. S. K.; Chan, J. C. C.; Cheng, S., Direct Synthesis and Catalytic Applications of Ordered Large Pore Aminopropyl-Functionalized SBA-15 Mesoporous Materials. *The Journal of Physical Chemistry B* **2005,** *109* (5), 1763-1769.
29. Zhao, J.; Gao, F.; Fu, Y.; Jin, W.; Yang, P.; Zhao, D., Biomolecule separation using large pore mesoporous SBA-15 as a substrate in high performance liquid chromatography. *Chemical Communications* **2002,** (7), 752-753.
30. Yasmin, T.; Müller, K., Synthesis and characterization of surface modified SBA-15 silica materials and their application in chromatography. *Journal of Chromatography A* **2011,** *1218* (37), 6464-6475.
31. Liu, X.; Li, L.; Du, Y.; Guo, Z.; Ong, T. T.; Chen, Y.; Ng, S. C.; Yang, Y., Synthesis of large pore-diameter SBA-15 mesostructured spherical silica and its application in ultra-high-performance liquid chromatography. *J Chromatogr A* **2009,** *1216* (45), 7767-7773.
32. Rivera-Muñoz, E. M.; Huirache-Acuña, R., Sol Gel-Derived SBA-16 Mesoporous Material. *International Journal of Molecular Sciences* **2010,** *11* (9), 3069.
33. Andrade, G. F.; Soares, D. C. F.; dos Santos, R. G.; Sousa, E. M. B., Mesoporous silica SBA-16 nanoparticles: Synthesis, physicochemical characterization, release profile, and in vitro cytocompatibility studies. *Microporous and Mesoporous Materials* **2013,** *168*, 102-110.
34. Sadjadi, S.; Heravi, M. M., Current advances in the utility of functionalized SBA mesoporous silica for developing encapsulated nanocatalysts: state of the art. *RSC Advances* **2017,** *7* (49), 30815-30838.
35. Maria Chong, A. S.; Zhao, X. S.; Kustedjo, A. T.; Qiao, S. Z., Functionalization of large-pore mesoporous silicas with organosilanes by direct synthesis. *Microporous and Mesoporous Materials* **2004,** *72* (1), 33-42.
36. Lim, M. H.; Stein, A., Comparative Studies of Grafting and Direct Syntheses of Inorganic−Organic Hybrid Mesoporous Materials. *Chemistry of Materials* **1999,** *11* (11), 3285-3295.
37. García, N.; Benito, E.; Guzmán, J.; Tiemblo, P.; Morales, V.; García, R. A., Functionalization of SBA-15 by an acid-catalyzed approach: A surface characterization study. *Microporous and Mesoporous Materials* **2007,** *106* (1), 129-139.
38. Zhuravlev, L. T., The surface chemistry of amorphous silica. Zhuravlev model. *Colloids and Surfaces A: Physicochemical and Engineering Aspects* **2000,** *173* (1), 1-38.

39. Lesaint, C.; Lebeau, B.; Marichal, C.; Patarin, J., Synthesis of mesoporous silica materials functionalized with n-propyl groups. *Microporous and Mesoporous Materials* **2005,** *83* (1), 76-84.
40. Megiel, E., Surface modification using TEMPO and its derivatives. *Advances in Colloid and Interface Science* **2017,** *250*, 158-184.
41. Tsubokawa, N.; Kimoto, T.; Endo, T., Oxidation of alcohols with copper(II) salts mediated by nitroxyl radicals immobilized on ultrafine silica and ferrite surface. *Journal of Molecular Catalysis A: Chemical* **1995,** *101* (1), 45-50.
42. Bolm, C.; Fey, T., TEMPO oxidations with a silica-supported catalyst. *Chemical Communications* **1999,** (18), 1795-1796.
43. Fey, T.; Fischer, H.; Bachmann, S.; Albert, K.; Bolm, C., Silica-Supported TEMPO Catalysts: Synthesis and Application in the Anelli Oxidation of Alcohols. *The Journal of Organic Chemistry* **2001,** *66* (24), 8154-8159.
44. Corriu, R. J. P.; Hoarau, C.; Mehdi, A.; Reye, C., Study of the accessibility of phosphorus centres incorporated within ordered mesoporous organic-inorganic hybrid materials. *Chemical Communications* **2000,** (1), 71-72.
45. Corriu, R. J. P.; Embert, F.; Guari, Y.; Mehdi, A.; Reye, C., A simple route to organic-inorganic hybrid materials containing Eu complexes. *Chemical Communications* **2001,** (12), 1116-1117.
46. Mouawia, R.; Mehdi, A.; Reye, C.; Corriu, R., Synthesis of bifunctionalized-pore mesoporous organosilica. Study of the accessibility and the distribution of functions in the pore channels. *New Journal of Chemistry* **2006,** *30* (7), 1077-1082.
47. Mouawia, R.; Mehdi, A.; Reye, C.; Corriu, R. J. P., Bifunctional ordered mesoporous materials: direct synthesis and study of the distribution of two distinct functional groups in the pore channels. *Journal of Materials Chemistry* **2008,** *18* (35), 4193-4203.
48. Yang, Q.; Liu, J.; Yang, J.; Kapoor, M. P.; Inagaki, S.; Li, C., Synthesis, characterization, and catalytic activity of sulfonic acid-functionalized periodic mesoporous organosilicas. *Journal of Catalysis* **2004,** *228* (2), 265-272.
49. Rosenholm, J. M.; Lindén, M., Wet-Chemical Analysis of Surface Concentration of Accessible Groups on Different Amino-Functionalized Mesoporous SBA-15 Silicas. *Chemistry of Materials* **2007,** *19* (20), 5023-5034.
50. Zhang, G.; Wang, Y.; Wen, X.; Ding, C.; Li, Y., Dual-functional click-triazole: a metal chelator and immobilization linker for the construction of a heterogeneous palladium catalyst and its application for the aerobic oxidation of alcohols. *Chemical Communications* **2012,** *48* (24), 2979-2981.
51. Jeschke, G.; Koch, A.; Jonas, U.; Godt, A., Direct Conversion of EPR Dipolar Time Evolution Data to Distance Distributions. *Journal of Magnetic Resonance* **2002,** *155* (1), 72-82.
52. Koelsch, C. F., Syntheses with Triarylvinylmagnesium Bromides. α,γ-Bisdiphenylene-β-phenylallyl, a Stable Free Radical. *Journal of the American Chemical Society* **1957,** *79* (16), 4439-4441.
53. Can, T. V.; Caporini, M. A.; Mentink-Vigier, F.; Corzilius, B.; Walish, J. J.; Rosay, M.; Maas, W. E.; Baldus, M.; Vega, S.; Swager, T. M.; Griffin, R. G., Overhauser effects in insulating solids. *The Journal of Chemical Physics* **2014,** *141* (6), 064202.
54. Afeworki, M.; McKay, R. A.; Schaefer, J., Selective observation of the interface of heterogeneous polycarbonate/polystyrene blends by dynamic nuclear polarization carbon-13 NMR spectroscopy. *Macromolecules* **1992,** *25* (16), 4084-4091.
55. Afeworki, M.; Schaefer, J., Mechanism of DNP-enhanced polarization transfer across the interface of polycarbonate/polystyrene heterogeneous blends. *Macromolecules* **1992,** *25* (16), 4092-4096.

56. Afeworki, M.; Schaefer, J., Molecular dynamics of polycarbonate chains at the interface of polycarbonate/polystyrene heterogeneous blends. *Macromolecules* **1992,** *25* (16), 4097-4099.

57. Afeworki, M.; Vega, S.; Schaefer, J., Direct electron-to-carbon polarization transfer in homogeneously doped polycarbonates. *Macromolecules* **1992,** *25* (16), 4100-4105.

58. Dane, E. L.; Maly, T.; Debelouchina, G. T.; Griffin, R. G.; Swager, T. M., Synthesis of a BDPA-TEMPO Biradical. *Organic Letters* **2009,** *11* (9), 1871-1874.

59. Lumata, L.; Ratnakar, S. J.; Jindal, A.; Merritt, M.; Comment, A.; Malloy, C.; Sherry, A. D.; Kovacs, Z., BDPA: An Efficient Polarizing Agent for Fast Dissolution Dynamic Nuclear Polarization NMR Spectroscopy. *Chemistry – A European Journal* **2011,** *17* (39), 10825-10827.

60. Gomberg, M., on the preparation of triphenylchlormethane. *Journal of the American Chemical Society* **1900,** *22* (11), 752-757.

61. Jensen, P. R.; Meier, S.; Ardenkjaer-Larsen, J. H.; Duus, J. O.; Karlsson, M.; Lerche, M. H., Detection of low-populated reaction intermediates with hyperpolarized NMR. *Chemical Communications* **2009,** (34), 5168-5170.

62. Jensen, P. R.; Peitersen, T.; Karlsson, M.; in 't Zandt, R.; Gisselsson, A.; Hansson, G.; Meier, S.; Lerche, M. H., Tissue-specific Short Chain Fatty Acid Metabolism and Slow Metabolic Recovery after Ischemia from Hyperpolarized NMR in Vivo. *The Journal of Biological Chemistry* **2009,** *284* (52), 36077-36082.

63. Comment, A.; van den Brandt, B.; Uffmann, K.; Kurdzesau, F.; Jannin, S.; Konter, J. A.; Hautle, P.; Wenckebach, W. T.; Gruetter, R.; van der Klink, J. J., Design and performance of a DNP prepolarizer coupled to a rodent MRI scanner. *Concepts in Magnetic Resonance Part B: Magnetic Resonance Engineering* **2007,** *31B* (4), 255-269.

64. Mishkovsky, M.; Comment, A.; Gruetter, R., In vivo detection of brain Krebs cycle intermediate by hyperpolarized magnetic resonance. *Journal of Cerebral Blood Flow & Metabolism* **2012,** *32* (12), 2108-2113.

65. Kurdzesau, F.; Brandt, B. v. d.; Comment, A.; Hautle, P.; Jannin, S.; Klink, J. J. v. d.; Konter, J. A., Dynamic nuclear polarization of small labelled molecules in frozen water–alcohol solutions. *Journal of Physics D: Applied Physics* **2008,** *41* (15), 155506.

66. Golman, K.; Petersson, J. S., Metabolic Imaging and Other Applications of Hyperpolarized $^{13}$C. *Academic Radiology 13* (8), 932-942.

67. Bornet, A.; Jannin, S., Optimizing dissolution dynamic nuclear polarization. *Journal of Magnetic Resonance* **2016,** *264*, 13-21.

68. Pines, A.; Gibby, M. G.; Waugh, J. S., Proton-enhanced NMR of dilute spins in solids. *The Journal of Chemical Physics* **1973,** *59* (2), 569-590.

69. Pines, A.; Gibby, M. G.; Waugh, J. S., Proton-Enhanced Nuclear Induction Spectroscopy. A Method for High Resolution NMR of Dilute Spins in Solids. *The Journal of Chemical Physics* **1972,** *56* (4), 1776-1777.

70. Hartmann, S. R.; Hahn, E. L., Nuclear Double Resonance in the Rotating Frame. *Physical Review* **1962,** *128* (5), 2042-2053.

71. Bornet, A. De l'usage des protons hyperpolarisés pour augmenter la sensibilité de la RMN. EPFL.

# Chapter 3: Hybrid Polarizing solids based on porous silica spheres

# Table of contents

# I. Introduction

The matrix effect observed between HYPSO 2 and HYPSO 3 due to the difference of the architecture of the porous network has highlighted the importance of the physical features of the polarizing matrices. In ordered mesoporous silica materials, higher polarization values were measured when increasing the pore interconnectivity. Hence, non-structured silica materials with higher interconnectivity may provide even higher polarization performances. For this reason, we have decided to post-functionalize commercially available porous silica spheres commonly used in High Performance Liquid Chromatography (HPLC) or Supercritical Fluid Chromatography (SFC) with TEMPO radicals. On the one hand, these silica spheres could resist to the dissolution step which is performed by flushing the frozen sample (1-4 K) with hot pressurized water and on the other hand, their porosity would provide the possibility to impregnate important quantities of liquids to be polarized. These silica spheres have silanol groups onto their surface that will be used to create a silica layer containing azido units to be further coupled with TEMPO radicals. At the same time, we have decided to study the influence of the pore size and the particle size on the polarization values. Silica spheres with pore diameters ranging from 6 nm to 28 nm with a constant particle size of 15 µm were first post-functionalized with TEMPO radicals. Subsequently, silica spheres with a similar pore size of 6 nm and particle sizes ranging from 20 µm to 500 µm were also coated with silica layer containing TEMPO radicals.

Using these commercially available porous silica spheres and this post-functionalization strategy, the preparation of the polarizing matrices was more straightforward and the entire process could be more easily scalable. The preparation of these new polarizing matrices with a non-structured silica pore network could also ease the expulsion of the hyperpolarized liquid during the dissolution process and the increase of the particle size could facilitate the filtration and the recovery of the polarizing matrices.

In this chapter, a first part is dedicated to the process to obtain well-controlled silica spheres. Then, the new methodology to post-functionalize the porous silica spheres is presented with the polarization performances as a function of the pore size or the particle size. Finally, the carbon polarization after dissolution is presented as well as the first MRI pictures showing the possibility to use this type of porous matrices to acquire images using a single NMR scan thus opening perspectives for MRI *in-vivo* applications.

## II. Preparation of well-controlled spherical silica particles

The production of suspensions containing monodispersed silica spheres can be precisely controlled by using the so-called Stöber process. This process allows to have a control over the size of the as-obtained spherical silica particles. Many research groups have worked on this process and have provided different models aiming to explain their mechanism of formation. In this section, we will focus on the description of the Stöber process along with the presentation of the different mechanistic models.

### A. Control over the silica particles size by mean of Stöber process

Investigated first by G. Kolbe in 1956[3] and further developed by W. Stöber and A. Fink in 1968,[2] the synthetic process nowadays known as Stöber process have emerged. Initially, the idea was to produce a colloidal system containing silica particles of uniform size and shape. As shown in Figure 1, this process is a two-step process involving hydrolysis and polycondensation reactions in alcoholic medium using a basic catalyst. The first reaction takes place by mixing a tetraalkoxysilane precursor in a water/alcohol solution and ammonia as catalyst. The alcoxy-groups of the silane precursor are thus transformed into silanol groups with release of alcohol and the latter are rapidly and concomitantly condensed into siloxane bridges.

Hydrolysis and polycondensation:

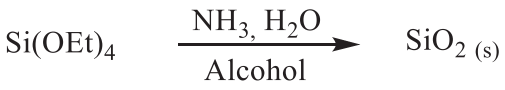

$$Si(OEt)_4 \xrightarrow[\text{Alcohol}]{NH_3,\ H_2O} SiO_{2\ (s)}$$

*Figure 1: Synthesis of silica spheres using the so-called Stöber process.*

Various systems can thus be obtained by changing the composition of the alcoholic medium and the length of the alkyl chain of the alcoxysilane precursor. Reported results showed that the use of methanol provided smaller particles than those yielded using *n*-butanol as solvent. However, the size distribution was broader when using *n*-butanol and a mixture of methanol:butanol (1:1) was thus used to reach more uniform big particles. These observations were accompanied by faster reaction rates along with small particles when shortening the alkyl chain of the tetraalcoxysilane precursor (i.e. tetramethyl orthosilicate).

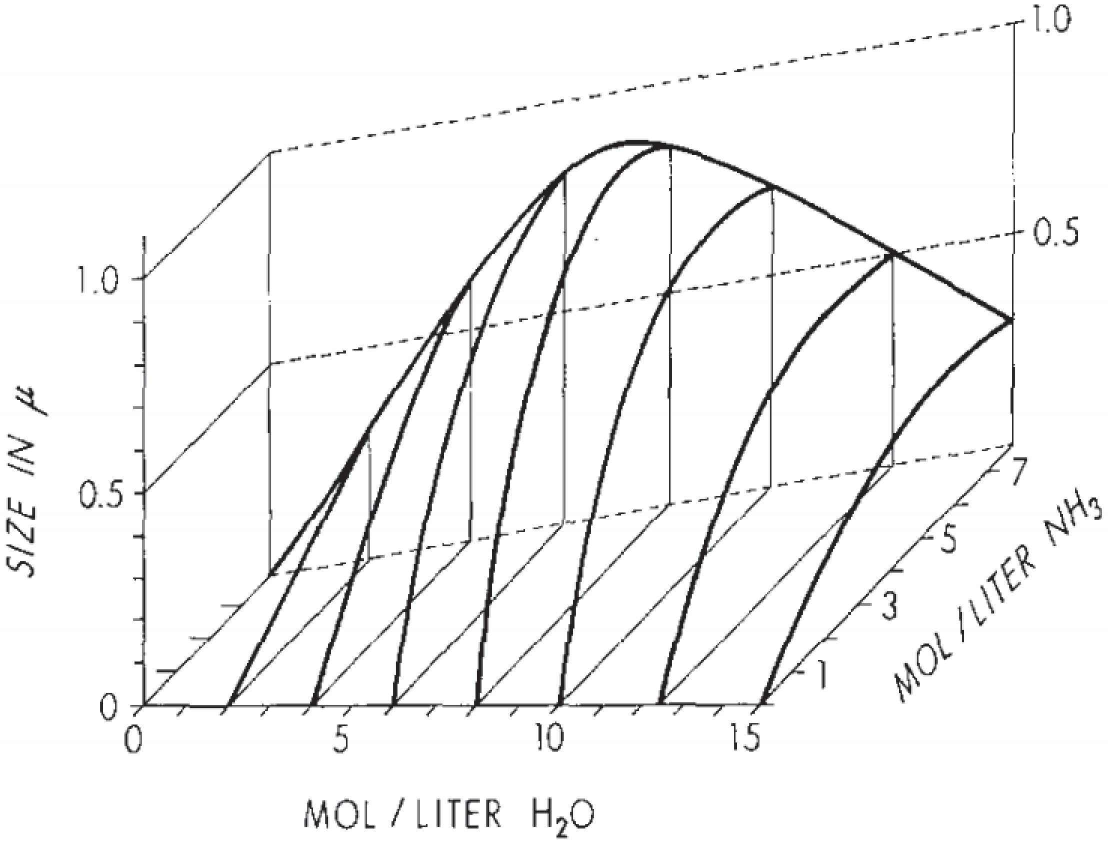

*Figure 2: Diagram showing the dependence of the silica spheres as a function of the composition of the water : ammonia mixture using a constant concentration of tetraethyl orthosilicate (0.28 mol/L) in ethanol extracted from the publication of W. Stöber.*[2]

At the reverse, slower reaction rates and bigger particles were yielded when using tetrapentyl orthosilicate in *n*-propanol and *n*-butanol. Moreover, the absence of ammonia led to the flocculation of the system with particles displaying irregular shapes. The ammonia is thus responsible of the spherical shape of these particles, but not only, because high concentration of ammonia led to spherical particles with larger sizes. To summarize, Figure 2 shows the dependence of the silica spheres as a function of the composition of the water:ammonia mixture using a constant concentration of alkoxysilane (0.28 mol/L) in ethanol.

On Figure 3 (left), a TEM micrograph displays the spherical silica spheres obtained by using $Si(OEt)_4$ and ethanol as solvent. However, the preparation of silica spheres exceeding a size of 1 µm was impossible using this system. Therefore, alkoxysilane precursors with longer alkyl chains were used but led to silica particles with a broader size distribution and sometimes to samples with particles displaying two different sizes. For this reason, a new composition containing 0.2 mol/L of the tetrapentyl-orthosilicate, 5 mol/L of water and a saturated ammonia solution in ethanol was used. Figure 3 (right) shows the resulting silica spheres with a particle size of ca. 1 µm (median particle size of 1.38 µm).

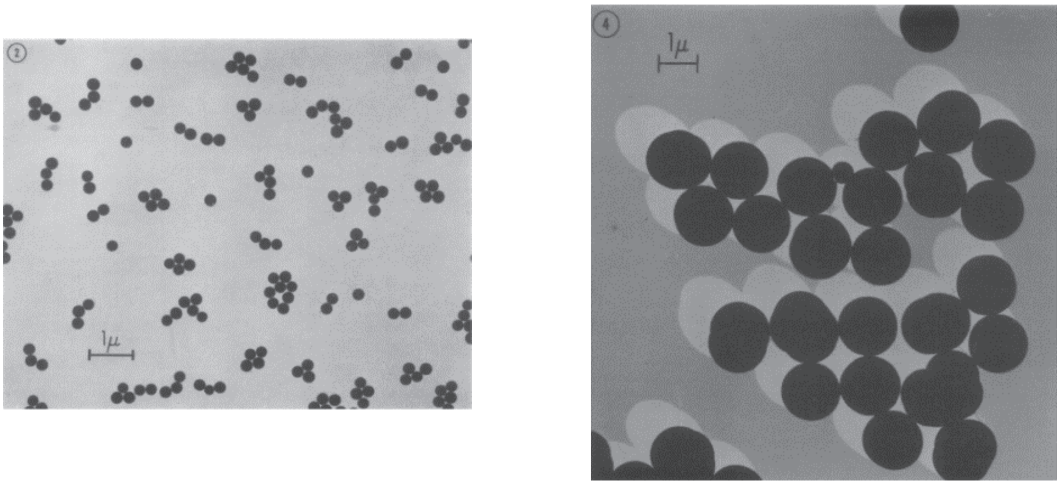

*Figure 3: Electron micrographs of the silica spheres obtained in ethanol with a tetraethyl orthosilicate as silica source (left) and tetrapentyl orthosilicate (right) extracted from the publication of W. Stöber et al.*[2]

To conclude, spherical silica particles of different sizes can be successfully produced using the Stöber process. As shown before, the concentration of the silane precursor, ammonia or the nature of the solvent have a noticeable impact on the size, shape and dispersion of the resulting silica particles. This process is easy to perform and additional purification techniques are not necessary. However, these experiments were reproduced on different days by using different reagents but the results were not precisely reproducible. Since the publication of this report, better control over the particle size or narrower size distribution were achieved by adjusting for example the nature of the solvent, the temperature or the concentration.[4-6] G. Bogush et al.[4] developed for example silica particles with a narrow pore size distribution using a mixture containing 0.2M of TEOS, 1M of ammonia and 2M of $H_2O$ in ethanol at T= 25 °C. Nevertheless, 36 years after, A. Van Blaaderen concluded that *"A general agreement on the processes responsible for the particle formation and growth, final monodispersity, particle size, and shape has not yet emerged "*.[7] The following models based on kinetic considerations[8-10] or by a controlled aggregation mechanism of particles[11-13] are described hereafter.

## B. Stöber process mechanisms: Nucleation and growth

Nucleation and growth are the two main steps for the synthesis process of particles. The nucleation corresponds to the formation of the first particles which grow differently according to the complexity of the system. This nucleation phenomenon is commonly divided into homogeneous and heterogeneous nucleation. Whereas the first term describes a spontaneous and random nucleation, the second term refers to the nucleation which occurs at the nucleation sites on solid surfaces due to the presence of impurities for example. In both cases, they highlight the transition between a homogeneous solution and a mixture containing particles. Based on these two characteristic steps, three models have emerged to describe the formation of these particles and are known as:

- **I.** LaMer and Dinegar model[14]
- **II.** Ocaña model[15]
- **III.** Sugimoto model

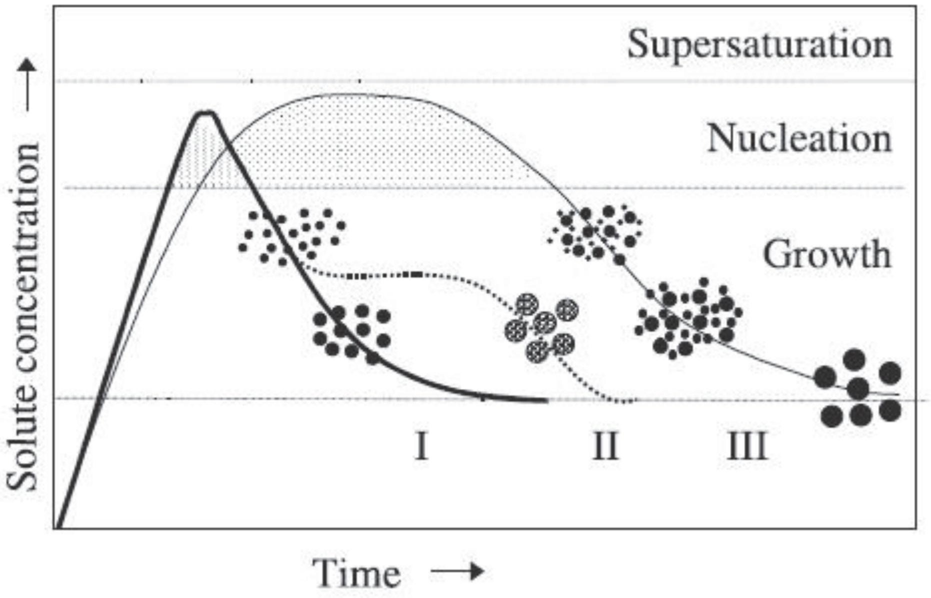

*Figure 4 : Formation processes leading to uniform particle sizes:* ***I.*** *LaMer and Dinegar model* ***II.*** *Ocaña model* ***III.*** *Sugimoto model. Extracted from the publication of P. Tartaj et al.*[1]

V. K. Lamer and R. H. Dinegar describe a model where the nuclei are formed at the same time through a homogeneous nucleation and then grow. In this situation, the nucleation and growth are considered are two distinct steps which occur one after the other. The possibility to generate new nuclei during the growth is not considered and therefore the possibility to get particles with different sizes is thus not possible. In Figure 4, the bold line **I** represents this model in three phases: pre-nucleation, nucleation and growth. During the first phase, the solute concentration increases until its solubility limit (critical concentration of sursaturation). Subsequently, the nucleation starts spontaneously and the solute concentration decreases leading to the ending of the nucleation. Finally, the freshly synthesized nuclei start to grow to generate particles with an uniform size.

Although the LaMer and Dinegar model mentions a short and fast nucleation, it has been proven that is not always the case specifically when complex systems are used. The Sugimoto model (solid line **III**) explains thus the particles growth by a coalescence phenomenon known as the Ostwald ripening and the Ocaña model (dash line **II**) describes the generation of particles with an uniform size by aggregation of small particles.

Whatever the mechanism involved, the Stöber process allows to produce size- and shape-controlled particles by adjusting the experimental parameters. However, these silica spheres are not porous.

## III. Preparation of porous silica spheres

From the pioneer results of W. Stöber et al., the synthetic routes were further optimized to yield porous silica spheres. The formation of porous silica spheres can be obtained through different experimental procedures which have a direct impact on the final features of the silica nanoparticles such as for example the pore size, the pore distribution, the particle size or the structuration of the porous network.

In 1997, M. Grün et al.[16] reported the preparation of M41S-type mesoporous silica spheres through the modification of the Stöber process. This process is based on the use of tetraalcoxysilane combined with ammonia in alcoholic medium (Stöber process) and the addition of a cationic surfactant. In these preliminary results, the reaction mixture was composed of tetraethoxysilane as the silica source, *n*-hexadecyltrimethylammonium bromide or *n*-hexadecylpyridinium chloride as cationic surfactants, aqueous ammonia as the catalyst and ethanol as the alcoholic solvent. Mesoporous silica spheres with a mean pore size of 3 nm were obtained with *n*-hexadecyltrimethylammonium bromide or *n*-hexadecylpyridinium chloride. Both samples displayed surface area ranging from 1050 to 1200 $m^2/g$ and a pore volume from 0.8 to 0.9 $cm^3/g$. However, the granulometry was not fully controlled: most of the particles were spherical but some aggregates were also present. Since the publication of this first report, many research groups have synthesized porous silica spheres through different methods using for instance emulsion-based chemistry. [17-24]

This method lies on the preparation of emulsions which consist in mixing two non-miscible liquids through the addition of an emulsifier to stabilize the whole mixture. Systems consisting in droplets of water dispersed in oil (W/O) or droplets of oil dispersed in water (O/W) are thus generated. The droplets are what we usually called the “discontinuous phase” whereas the other is defined as the “continuous phase”. More complex systems can also be created by emulsifying a W/O emulsion in aqueous phase to yield to a double emulsion W/O/W (or O/W/O for the O/W emulsion). Porous silica nanoparticles are thus obtained by polymerization of the continuous phase of the emulsion.[24] The pore size is controlled by the size of the droplets and the pore interconnection by the ratio of the dispersed phase. A high ratio of the dispersed phase compared to the continuous phase give rise to a highly interconnected porosity.

For example, A. Imhof et al.[25] prepared porous silica spheres by using a first oil-in-formamide emulsion which was further fractionated to obtain the desired degree of size uniformity. The sodium dodecyl sulfate was used as emulsifier to stabilize the emulsion. Then, a solution containing an alkoxysilane precursor, such as TMOS or TEOS, was mixed with formamide and water (silane/water with a ratio in the range of 3-10). The silane precursor was then partially hydrolyzed leading to its partial solubility in formamide. Finally, the resulting sol was dispersed in the first emulsion and the size of the droplet was adjusted by centrifugation. A small amount of ammonia was added to induce gelation (several hours) of the system by increasing the pH. The resulting gel was washed in alcohol, dried and calcined to remove the organic parts. As a result, silica materials were obtained with uniform spherical pore size ranging from 50 nm to 10 µm. Other systems were described using titania and zirconia but they will not be investigated in this chapter.[25-26]

However, emulsions require to use an emulsifier such as surfactant which can be replaced by solid particles to create the so-called Pickering emulsions.[27-28]

More interestingly, porous silica spheres known as Kromasil are available with different pore size ranging from 6 nm to 100 nm. They are produced on a large scale and commonly used for high performance liquid chromatography. Their synthesis is based on the preparation of a sol emulsified in a polar organic solvent. After gelation upon heating, porous silica spheres are then generated by evaporation under reduced pressure. The pore-size being governed by the choice of the starting silane precursor.

In the following part of the chapter, we will focus on the use of non-hierarchically ordered mesoporous silica spheres similar to Kromasil ones which display a high pore-interconnectivity.

# IV. Surface modification of non-hierarchically porous silica spheres

The introduction of organics into silica solids can be performed using different methods as presented in chapter 2: the direct synthesis or the post-functionalization. Since we have decided to use commercial non-hierarchically ordered mesoporous silica spheres, the post-functionalization is the method of choice to introduce surface TEMPO groups. In the next section, the characteristics of the commercial non-hierarchically mesoporous silica spheres are presented. Different pore size and particle size were selected for post-functionalization with TEMPO radicals. This strategy to modify the surface of the silica spheres is also presented hereafter.

# V. Preparation of hybrid polarizing solids based on silica spheres

## A. Description of the starting silica materials

The starting silica materials are non-hierarchically ordered mesoporous silica spheres with different pore sizes and particles sizes. Two types of porous silica spheres were selected: i) Porous silica spheres with a constant particle size around 15 µm and pore size ranging from ca. 5-6 nm to 28 nm and ii) Porous silica spheres with a constant pore size of ca. 4-6 nm and particle size ranging from 20 µm to 500 µm. According to the supplier (SiliCycle), the pore diameter, average particle size, specific surface area and pore volume are presented for both series in the following tables.

*Table 1: Non-hierarchically ordered mesoporous silica spheres with a constant particle size of ca. 15 µm and pore size ranging from 6 nm to 28 nm (data provided by the supplier).*

| **Name of the silica sample** | **SiliaSphere spherical silica gel (S10008B)** | **SiliaSphere spherical silica gel (S10008F-A)** | **SiliaSphere spherical silica gel (S10008G-A)** | **SiliaSphere spherical silica gel (S10008M)** |
|---|---|---|---|---|
| **Pore diameter (nm)** | 6 | 7.3 | 12.4 | 28.8 |
| **Particle size average D50 (µm)** | 14 | 14.5 | 14.5 | 15.7 |
| **Specific surface area ($m^2/g$)** | 452 | 528 | 320 | 108 |
| **Pore volume ($cm^3/g$)** | 0.68 | 0.97 | 0.99 | 0.83 |

*Table 2: Non-hierarchically ordered mesoporous silica spheres with a constant pore size of 6 nm and particle size ranging from 20 µm to 500 µm (data provided by the supplier).*

| **Name of the silica sample** | **SiliaFlash irregular silica gel (R10023B)** | **SiliaFlash irregular silica gel (R10050B)** | **SiliaFlash irregular silica gel (R10060B)** | **SiliaFlash irregular silica gel (R10070B)** |
|---|---|---|---|---|
| **Pore diameter (nm)** | 6 | 6 | 6 | 6 |
| **Particle sizes (µm)** | 20 - 45 | 60 - 120 | 120 - 200 | 200 - 500 |
| **Specific surface area ($m^2/g$)** | 546 | 526 | 455 | 512 |
| **Pore volume ($cm^3/g$)** | 0,72 | 0,72 | 0,66 | 0,80 |

According to the supplier, these non-hierarchically ordered porous silica have a spherical shape without cracks and a narrow particle size distribution. They are mainly used for purification and high pressure chromatography (High Performance Liquid Chromatography and Supercritical Fluid Chromatography) which is an asset for our study. Indeed, this shows that they are well-suited to tolerate harsh conditions such as high pressure which is used during the dissolution process. This characteristic suggests also that no fine particles are produced in these conditions.

After washing with DCM and an EDTA solution to remove eventual traces of metallic impurities which could decrease the polarization values, the porous silica spheres were dried under high vacuum ($10^{-5}$ mbar) at 135 °C and stored in the glovebox. The porous silica spheres were again analyzed by $N_2$ adsorption/desorption to probe any changes (Tables 3 and 4). As expected, similar pore diameter, surface area and pore volume were found for all the samples after these washings.

*Table 3: Non-hierarchically ordered porous silica spheres with a constant particle size of ca. 15 um and pore size ranging from 6 nm to 28 nm after washing with DCM and an EDTA solution.*

| **Name of the silica sample** | **SiliaSphere spherical silica gel (S10008B)** | **SiliaSphere spherical silica gel (S10008F-A)** | **SiliaSphere spherical silica gel (S10008G-A)** | **SiliaSphere spherical silica gel (S10008M)** |
|---|---|---|---|---|
| **Pore diameter (nm)**[a] | 5.4 | 8.1 | 12.1 | 28.3 |
| **Specific surface area ($m^2/g$)**[b] | 446 | 478 | 330 | 100 |
| **Pore volume ($cm^3/g$)**[c] | 0.65 | 0.92 | 0.96 | 0.78 |

a: Pore diameter calculated using the BJH model (desorption branch), b: Specific surface area calculated using the BET model, c: Total pore volume corresponding to the quantity of $N_2$ adsorbed at $P/P_0 = 0.99$.

*Table 4: Non-hierarchically ordered porous silica spheres with a constant pore size of 6 nm and particle size ranging from 20 µm to 500 µm after washing with DCM and an EDTA solution.*

| **Name of the silica sample** | **SiliaFlash irregular silica gel (R10023B)** | **SiliaFlash irregular silica gel (R10050B)** | **SiliaFlash irregular silica gel (R10060B)** | **SiliaFlash irregular silica gel (R10070B)** |
|---|---|---|---|---|
| **Pore diameter (nm)[a]** | 4.8 | 4.8 | 4.8 | 5.4 |
| **Specific surface area ($m^2/g$)[b]** | 538 | 477 | 457 | 470 |
| **Pore volume ($cm^3/g$)[c]** | 0.73 | 0.67 | 0.69 | 0.72 |

a: Pore diameter calculated using the BJH model (desorption branch), b: Specific surface area calculated using the BET model, c: Total pore volume corresponding to the quantity of $N_2$ adsorbed at $P/P_0 = 0.99$.

## B. Surface modification of the porous silica spheres with TEMPO radicals

The surface modification was inspired from the publication of C.-H. Chu et al.[29] aiming to prepare a silica support containing Si-H surface groups by the coating of a polyhydrogenosiloxane layer on the surface of silica supports. The gel was prepared by hydrolysis of the silane precursor and its further condensation onto the silica support as follows:

Hydrolysis:

$$HSiX_3 \quad + \quad 3H_2O \quad \longrightarrow \quad HSi(OH)_3 \quad + \quad 3HX$$

Polycondensation:

$$nHSi(OH)_3 \quad \longrightarrow \quad (HSiO_{3/2})_n \quad + \quad 3/2\ nH_2O$$

X is a hydrolytically labile group such as halide or alcoxy.

The silane was thus covalently linked to the silica support by formation of new siloxane bridges from the surface silanol-groups of the starting silica support. As a result, a silica layer containing the hydrogenosilane groups was yielded onto the surface of the support.

Since paramagnetic species are needed for DNP, the hydrogenotrialkoxysilane precursor was replaced by the 3-azidopropyltriethoxysilane to generate the functional silica layer. Similarly to previous experiments, the azido moieties were then coupled with TEMPO radicals through a copper catalyzed alkyne-azide cycloaddition reaction (Fig. 5). Depending on the concentration of azido-groups to be introduced, a THF solution containing different molar ratios of tetraethoxysilane and 3-azidopropyltriethoxysilane was added to a $HCl_{aq}$ : THF suspension of porous silica spheres before heating at 70 °C for 1h. The solid was further recovered by filtration, washed three times with a water:THF (20:80) mixture, ethanol and diethyl ether and dried under high vacuum ($10^{-5}$ mbar) at 135 °C overnight (see the experimental section for detailed procedures). Note that the concentrations of the two silane precursors were carefully controlled in order to be sufficiently high to create a strong cross-linking between the silica layer and the support while avoiding the clogging of the support's porosity. The surface azido groups were further coupled with the TEMPO radicals according to the previously described procedure (see experimental section). The final materials were washed with an EDTA solution, ethanol and diethyl ether prior to be dried under high vacuum ($10^{-5}$ mbar) overnight at 50 °C and stored in a glovebox. As usually, these final materials were stored in the glovebox.

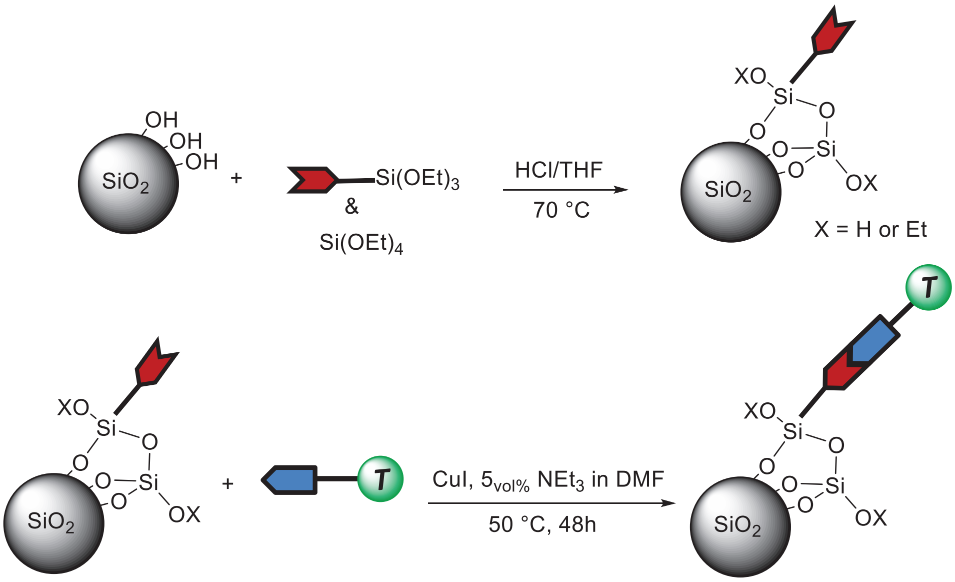

*Figure 5: Formation of the silica layer containing the azido groups which are then coupled with TEMPO radicals through a copper-catalyzed alkyne-azide cycloaddition.*

Subsequently, the materials were characterized and polarized to probe the influence of the pore size and particle size. In addition, external paramagnetic species such as the dioxygen of the atmosphere was removed in one of the formulation to quantify its impact on the polarization values. Finally, and for the first time MRI pictures were obtained with HYPSO 5 impregnated with a 3 M solution of sodium [1-$^{13}$C] acetate.

# VI. Characterization of the silica spheres coated with TEMPO radicals

## A. $N_2$ adsorption/desorption experiments and EPR

$N_2$ adsorption/desorption experiments were performed on all samples. The specific surface area, pore volume and pore size were deduced from this analysis and the radical concentrations were also calculated from EPR.

### 1. Porous silica spheres with different particle size

In Table 5, porous silica spheres with a pore size of 6 nm (according to the supplier but in fact 4-6 nm) and particle size ranging from 20 µm to 500 µm were analyzed after introduction of the TEMPO radicals. Specific surface ranging from 258 $m^2.g^{-1}$ to 447 $m^2.g^{-1}$ along with a pore volume ranging from ca. 0.4 to 0.6 $cm^3.g^{-1}$ were measured. EPR analysis showed radical concentrations from ca. 15 to 30 $\mu mol.cm^{-3}$ for these same samples.

*Table 5: Porous silica spheres with a constant pore size and particle size ranging from 20 µm to 500 µm for a radical concentration from 10 to 30 µmol.cm$^{-3}$.*

| Entry | $S_{BET}$ $^{a}$ m$^2$.g$^{-1}$ | Vp(tot.)$^{b}$ cm$^3$.g$^{-1}$ | Dp$^{c}$ nm | [R] µmol.cm$^{-3}$ | Particle size µm |
|---|---|---|---|---|---|
| **1** | 414 | 0.52 | 4.2 | 25 | 20 - 45 |
| **2** | 260 | 0.34 | 4.2 | 26 | 20 - 45 |
| **3** | 447 | 0.57 | 4.2 | 28 | 20 - 45 |
| **4** | 442 | 0.57 | 3.7 | 23 | 60 - 120 |
| **5** | 258 | 0.35 | 3.7 | 26 | 60 - 120 |
| **6** | 346 | 0.48 | 3.7 | 31 | 60 - 120 |
| **7** | 429 | 0.63 | 3.7 | 17 | 120 - 200 |
| **8** | 393 | 0.61 | 3.7 | 20 | 120 - 200 |
| **9** | 374 | 0.57 | 3.7 | 23 | 120 - 200 |
| **10** | 442 | 0.65 | 5.4 | 14 | 200 - 500 |
| **11** | 407 | 0.65 | 5.4 | 20 | 200 - 500 |
| **12** | 407 | 0.47 | 3.7 | 23 | 200 - 500 |
| **13** | 422 | 0.69 | 5.4 | 25 | 200 - 500 |

a: Specific surface area calculated using the BET model, b: Total pore volume corresponding to the quantity of $N_2$ adsorbed at $P/P_0$ = 0.99, c: Pore diameter calculated using the BJH model (desorption branch).

Table 6 displays the same type of results but for samples with a constant pore size of 6 nm (according to the supplier but in fact 4-6 nm) and particle size ranging from 200 to 500 µm. With this type of polarizing matrices specific surface area ranging from 258 m$^2$.g$^{-1}$ to 447 m$^2$.g$^{-1}$ and pore volume of ca. 0.5-0.7 cm$^3$.g$^{-1}$ were measured.

*Table 6: Porous silica spheres with a constant pore size and particle size ranging from 200 to 500 µm.*

| Entry | $S_{BET}$$^{a}$ m$^2$.g$^{-1}$ | Vp(tot.)$^{b}$ cm$^3$.g$^{-1}$ | Dp$^{c}$ nm | [R] µmol.cm$^{-3}$ |
|---|---|---|---|---|
| **10** | 442 | 0.65 | 5.4 | 14 |
| **11** | 407 | 0.65 | 5.4 | 20 |
| **12** | 307 | 0.47 | 3.7 | 23 |
| **13** | 422 | 0.69 | 5.4 | 25 |
| **14** | 447 | 0.64 | 3.7 | 34 |
| **15** | 416 | 0.62 | 3.7 | 38 |
| **16** | 436 | 0.61 | 3.7 | 41 |
| **17** | 440 | 0.63 | 3.7 | 43 |
| **18** | 432 | 0.60 | 3.7 | 72 |

a: Specific surface area calculated using the BET model, b: Total pore volume corresponding to the quantity of $N_2$ adsorbed at $P/P_0$ = 0.99, c: Pore diameter calculated using the BJH model (desorption branch).

In summary and independently of the particle size, high surface areas and high pore volumes were measured. Moreover, using this method, we were able to prepare materials exhibiting similar textures and different radical concentration.

## 2. Porous silica spheres with different pore size

$N_2$ adsorption/desorption and EPR analysis were also performed on polarizing matrices with a constant particle size of ca. 15 µm and pore size ranging from 6 nm to 28 nm. As shown in Table 7 to Table 10, the specific surface areas measured are lower when increasing the pore size. For example, surface areas from 194 $m^2.g^{-1}$ to 386 $m^2.g^{-1}$ for samples with a pore size of 6 nm (according to the supplier but in fact 4-5 nm) and from 90 $m^2.g^{-1}$ to 126 $m^2.g^{-1}$ for samples with a pore size of 28 nm (according to the supplier but in fact 28-31 nm) were obtained.

*Table 7: Porous silica spheres with a pore size Dp of ca. 4-5 nm and a constant particle size of ca. 15 µm.*

| Entry | $S_{BET}$ [a] $m^2.g^{-1}$ | Vp(tot.)[b] $cm^3.g^{-1}$ | Dp[c] nm | [R] $\mu mol.cm^{-3}$ |
|---|---|---|---|---|
| **19** | 221 | 0.31 | 4.8 | 22.3 |
| **20** | 194 | 0.29 | 3.7 | 27 |
| **21** | 378 | 0.51 | 4.8 | 46.1 |
| **22** | 386 | 0.53 | 4.8 | 75.3 |
| **23** | 380 | 0.50 | 4.8 | 78.8 |
| **24** | 276 | 0.37 | 4.8 | 103.5 |

a: Specific surface area calculated using the BET model, b: Total pore volume corresponding to the quantity of $N_2$ adsorbed at $P/P_0 = 0.99$, c: Pore diameter calculated using the BJH model (desorption branch).

*Table 8: Porous silica spheres with a pore size of Dp= 8 nm and a constant particle size of ca. 15 µm.*

| Entry | $S_{BET}$ [a] $m^2.g^{-1}$ | Vp(tot.)[b] $cm^3.g^{-1}$ | Dp[c] nm | [R] $\mu mol.cm^{-3}$ |
|---|---|---|---|---|
| **25** | 342 | 0.75 | 8.1 | 12 |
| **26** | 320 | 0.70 | 8.1 | 17 |
| **27** | 335 | 0.71 | 7.1 | 21 |
| **28** | 340 | 0.72 | 8.1 | 24 |

*Table 9: Porous silica spheres with a pore size of Dp= 12 nm and a constant particle size of ca. 15 µm.*

| Entry | $S_{BET}$ [a] $m^2.g^{-1}$ | Vp(tot.)[b] $cm^3.g^{-1}$ | Dp[c] nm | [R] $\mu mol.cm^{-3}$ |
|---|---|---|---|---|
| **29** | 283 | 0.9 | 12.1 | 11 |
| **30** | 250 | 0.8 | 12.1 | 22 |
| **31** | 222 | 0.62 | 10.6 | 42 |
| **32** | 103 | 0.30 | 10.6 | 43 |
| **33** | 311 | 0.88 | 10.6 | 51 |

a: Specific surface area calculated using the BET model, b: Total pore volume corresponding to the quantity of $N_2$ adsorbed at $P/P_0 = 0.99$, c: Pore diameter calculated using the BJH model (desorption branch).

*Table 10: Porous silica spheres with a pore size of Dp= 28 nm and a constant particle size of ca. 15 µm.*

| **Entry** | **$S_{BET}$ [a]**<br>**$m^2.g^{-1}$** | **Vp(tot.) [b]**<br>**$cm^3.g^{-1}$** | **Dp [c]**<br>**nm** | **[R]**<br>**$\mu mol.cm^{-3}$** |
|---|---|---|---|---|
| **34** | 114 | 0.84 | 30.8 | 1 |
| **35** | 98 | 0.79 | 28.3 | 4 |
| **36** | 119 | 0.90 | 21.6 | 7 |
| **37** | 93 | 0.65 | 28.3 | 11 |
| **38** | 126 | 0.74 | 24.5 | 12 |
| **39** | 117 | 0.76 | 28.3 | 13 |
| **40** | 109 | 0.68 | 28.3 | 13 |
| **41** | 110 | 0.71 | 28.3 | 17 |
| **42** | 116 | 0.78 | 28.3 | 21 |
| **43** | 90 | 0.70 | 28.3 | 26 |

a: Specific surface area calculated using the BET model, b: Total pore volume corresponding to the quantity of $N_2$ adsorbed at $P/P_0 = 0.99$, c: Pore diameter calculated using the BJH model (desorption branch).

## B. Transmission electron microscopy and electron tomography pictures

In order to get insight into the pore structuration and interconnectivity of the samples, Transmission Electron Microscopy (TEM) and Electron Tomography (ET) pictures were recorded for three types of solids: HYPSO 2, HYPSO 3 and these new solids dubbed here HYPSO 5. While TEM micrographs give a glimpse of the difference between the samples, ET pictures provide a clear idea of the pore structuration and interconnectivity. HYPSO 2 solids display distinctively a 2D hexagonal arrangement of long parallel pore-channels as expected for SBA-15 type solids. HYPSO 3 solids show a 3D cubic arrangement of interconnected cage like pores which were found to improve the polarization performances. Finally, HYPSO 5 display a non-structured framework with a highly interconnected pore-network. The polarization results are presented in the next section for these new porous silica materials.

HYPSO 2

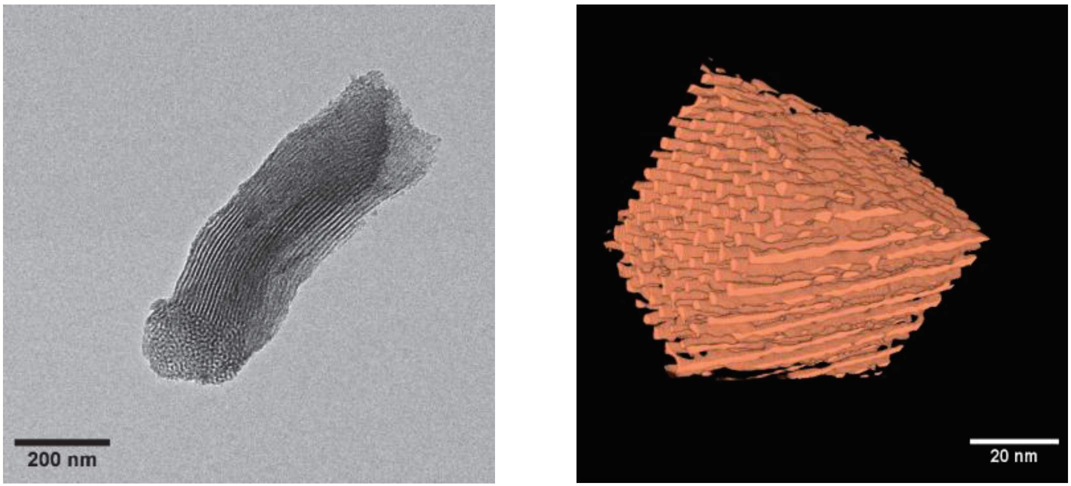

HYPSO 3

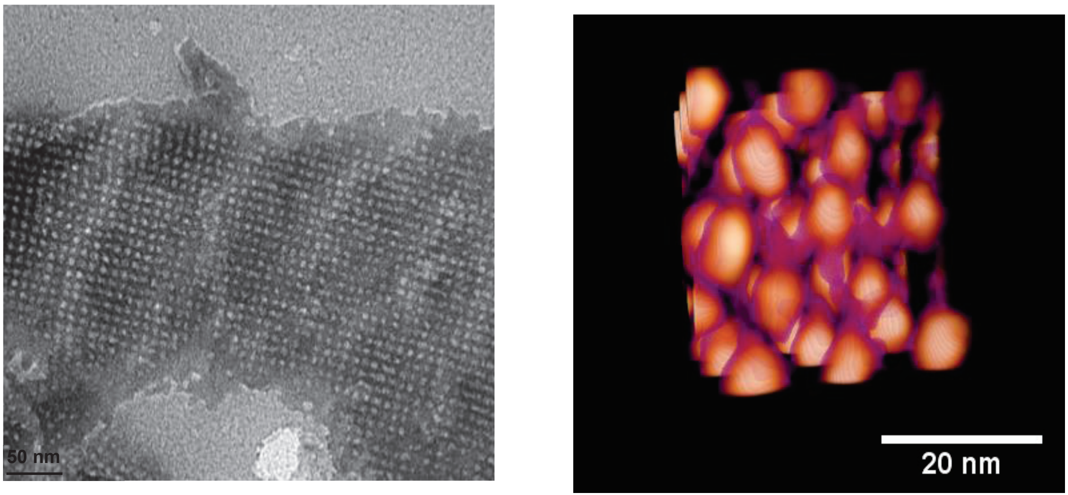

HYPSO 5

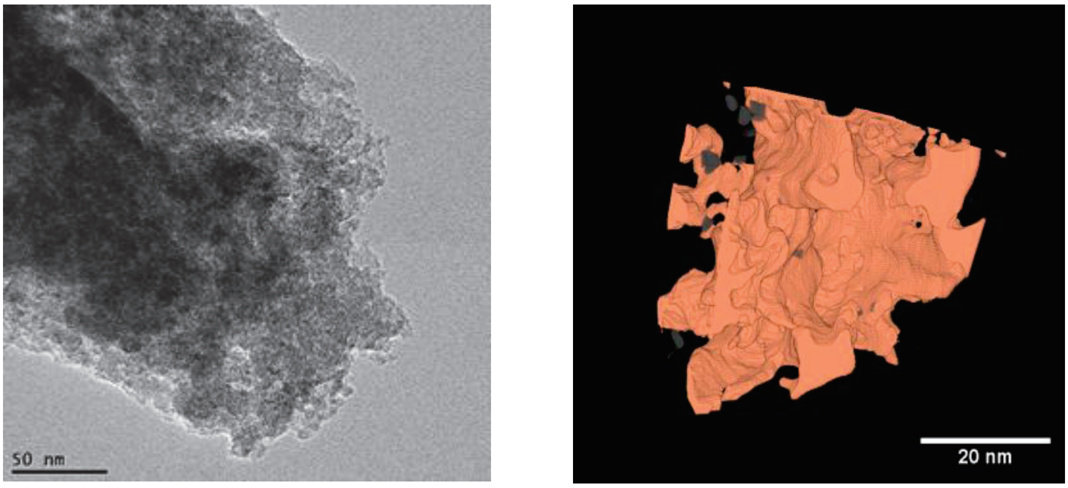

*Figure 6: Transmission Electron Microscopy (TEM) and Electron Tomography (ET) pictures of HYPSO 2 (Top), HYPSO 3 (Middle) and HYPSO 5 (Bottom).*

# VII. Polarization of HYPSO 5 silica spheres

## A. Experimental conditions

HYPSO 5 silica spheres displaying a constant pore size of ca. 6 nm and particle size ranging from 20 µm to 500 µm as well as HYPSO 5 silica spheres with a constant particle size of ca. 15 µm and pore size ranging from 6 nm to 28 nm were analyzed by DNP using frequency-modulation. Prior to be polarized, a benchmark solution of $H_2O$:$D_2O$ (8:2) was impregnated by IWI in the polarizing matrices. Then, the samples were loaded in the holder which was directly inserted in the polarizer settled at 1.2 K.

## B. Particle-size influence of HYPSO 5

The use of large porous silica particles could improve the dissolution step by avoiding the presence of fine silica particles in the NMR spectrometer. For this reason, particles exhibiting pore diameter of 6 nm and the biggest particle sizes (200 to 500 µm) were first studied. In Figure 7, the proton polarization values recorded at T= 1.2 K were plotted as a function of the radical concentration. In comparison to previous data obtained for HYPSO 2 and HYPSO 3, similar trend ("volcano" curve) could be observed. The more diluted and the more concentrated samples displayed the lowest polarization values with a $P(^1H)$ = 54 % for a radical concentration of 20 µmol.cm$^{-3}$ and $P(^1H)$ = 65 % for a radical concentration of 72 µmol.cm$^{-3}$. It is not worth nothing that these low polarization values were comparable or higher to the maximum polarization recorded for HYPSO 2 ($P(^1H)$ = 50 % with an optimal radical concentration of 79 µmol.cm$^{-3}$) and HYPSO 3 ($P(^1H)$ = 63 % with an optimal radical concentration of 67 µmol.cm$^{-3}$). Overall, the most important result is the remarkable proton polarization of $P(^1H)$ = 99 % obtained for a radical concentration of only 34 µmol.cm$^{-3}$. This result strongly suggests the beneficial impact of the pore-connectivity on the polarization performances.

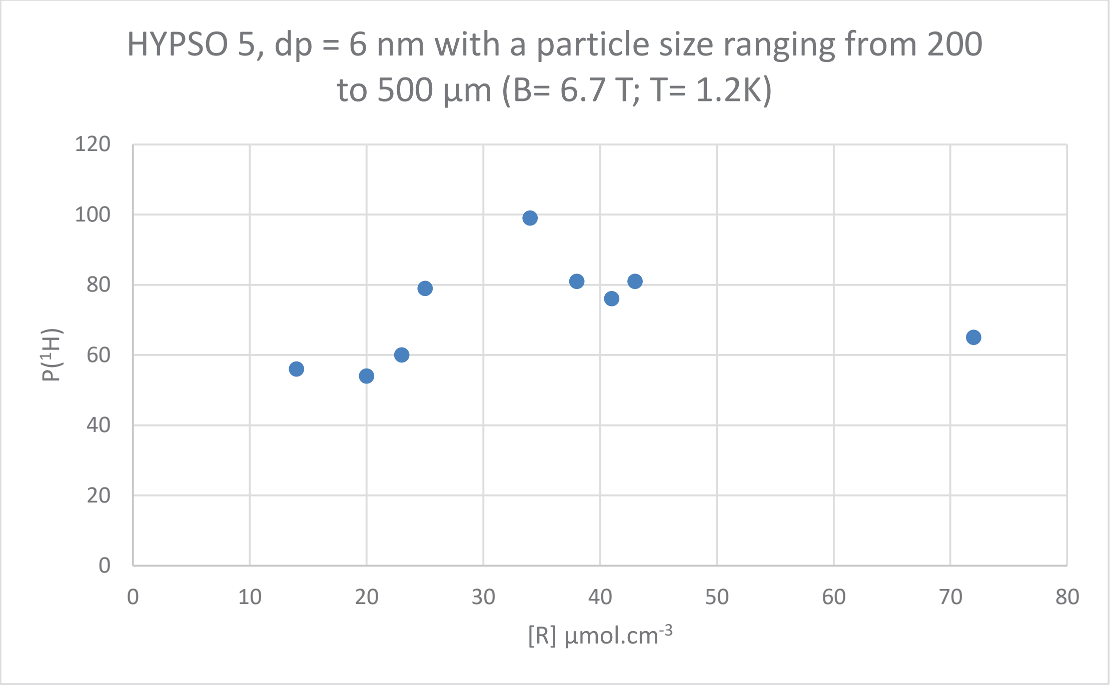

*Figure 7: Proton polarization values as a function of the radical concentration for HYPSO 5 displaying a pore diameter of 6 nm and particle size ranging from 200 to 500 um.*

In order to compare the DNP performances between the conventional homogeneous DNP juice and the solid matrices, the $^1$H DNP build-up curves of all the samples were recorded at T= 1.2 K. A conventional homogeneous DNP "juice" was prepared by mixing 50 mmol of 4-hydroxy-TEMPO in a $H_2O$: $D_2O$: glycerol (20:30:50 v:v:v) solution and the selected polarizing solids were: i) HYPSO 5 with pore size of 6 nm and particle size ranging from 200 to 500 µm, optimal, ii) the optimal HYPSO 2 ([R]= 79 µmol.cm$^{-3}$) and iii) the optimal HYPSO 3 ([R]= 67 µmol.cm$^{-3}$). For sake of comparison with the DNP "juice", the three matrices were impregnated with a benchmark solution composed of $H_2O$:$D_2O$ (2:8) without the use of glycerol as glassy agent (found useless with the solid matrices).

As shown in Figure 8, the samples displayed four different $^1$H DNP profiles. From these curves, two information could be extracted: the maximum proton polarization value and the rapidity to reach this maximum. HYPSO 2 and HYPSO 3 exhibited a similar behavior in the first minutes (almost up to 5 minutes) and reached, as expected, the lowest maximum polarization values. For HYPSO 5, the build-up time was higher and the plateau was barely reached after 20 minutes if compared to HYPSO 2, HYPSO 3 and the DNP "juice". However, HYPSO 5 reached a polarization value as high as P($^1$H)= 99 % (± 5%) after 20 minutes that exceeded those of all the other samples and particularly that of the DNP "juice" ( $P(^1H)$= 90 % ).

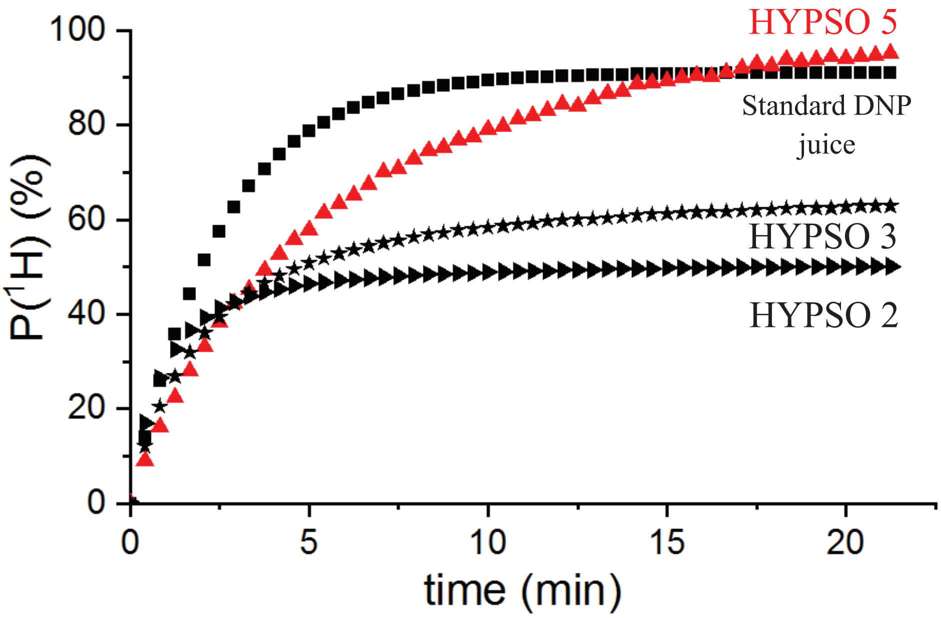

*Figure 8: $^1H$ DNP build-up curves for three samples displaying different pore network: HYPSO 2 with a radical concentration of 79 µmol.cm$^{-3}$ (black triangles), HYPSO 3 with a radical concentration of 67 µmol.cm$^{-3}$ (black stars), HYPSO 5 with a radical concentration of 34 µmol.cm$^{-3}$ (red triangles) and a standard DNP juice (black squares).*

Additional experiments were conducted with TEMPO containing silica spheres of various particle size: 20-45 µm, 60-120 µm, 120-200 µm and 200-500 µm and a radical concentration between 10 µmol.cm$^{-3}$ to ca. 30 µmol.cm$^{-3}$. The samples with different radical concentrations were loaded with the benchmark solution of $H_2O$:$D_2O$ (2:8). During these experiments, frequency-modulation was used and the samples were polarized at T= 1.2 K and $B_0$= 6.7 T.

Figure 9 shows the proton polarization values as a function of the radical concentration for these samples. In this specific case, two types of error should be considered. One related to the quantification of the radical concentration and the other related to the measurement of the polarization values. Despite these uncertainties, the proton polarization values recorded were different and were apparently a little dependent on the particle size. For instance, at [R] = 23 µmol.cm$^{-3}$ the proton polarization for the samples with a particle size of: 60 – 120 µm, 120 – 200 µm and 200 – 500 µm were respectively $P(^1H)$= 67 %, $P(^1H)$= 52 % and $P(^1H)$= 60 %. A difference of $P(^1H)$= 15% was observed between samples with a particle size of 60-120 µm and samples with a particle size of 120-200 µm. Moreover, as the physical features of the starting silica spheres are not all exactly the same (pore volume between 0.66 and 0.8 $cm^3.g^{-1}$ and specific surface area ranging from 455 to 546 $m^2.g^{-1}$) the description of the radical in $\mu mol.cm^{-3}$ was not fully consistent, albeit it was found the most appropriate.

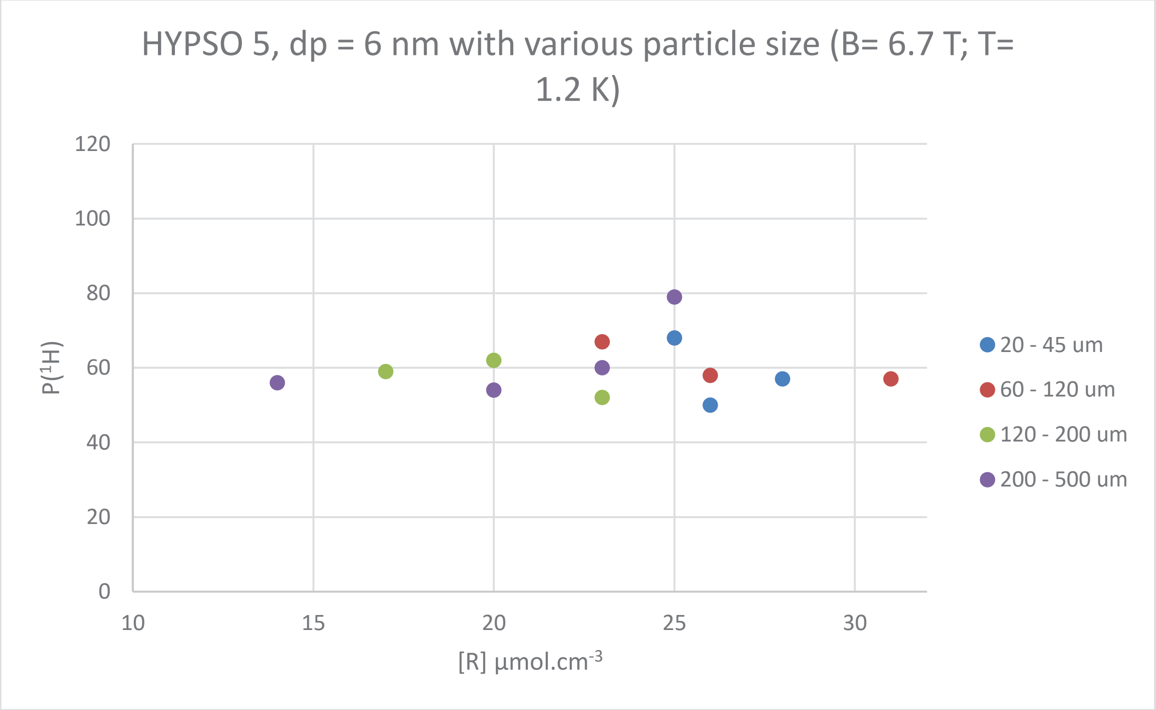

*Figure 9: Proton polarization values as a function of the radical concentration for HYPSO 5 displaying a pore diameter of 6 nm and particle size ranging from 20 um to 500 um.*

In a nutshell, the proton polarization values were found slightly different (50-70%) for these polarizing matrices depending on the particle size and the radical concentration; one exception being the silica spheres with particle size ranging from 200 µm to 500 µm which showed a proton polarization of 80 % for a radical concentration of 25 $\mu mol.cm^{-3}$.

## C. Pore-size influence of HYPSO 5

The influence of the pore size was also investigated on this new type of samples. As before, all the samples were impregnated with the benchmark mixture of $H_2O$:$D_2O$ (2:8) and polarized at T= 1.2 K using frequency-modulation. Diameters ranging from 6 nm to 28 nm were selected to probe any polarization changes from small to large pores.

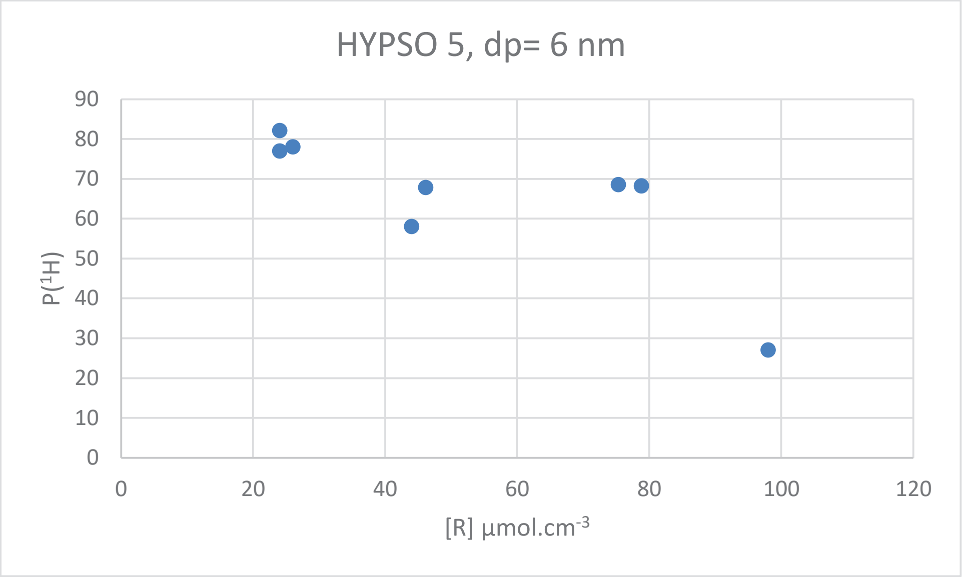

*Figure 10: Proton polarization values as a function of the radical concentration for HYPSO 5 with a pore size of 6 nm.*

As shown in Figure 10, proton polarization values ranging from 82 % to 27 % were recorded for HYPSO 5 with a pore diameter of 6 nm, depending on the radical concentration. The maximum was found for a radical concentration of [R]= 24 µmol.cm$^{-3}$ and the minimum for [R]= 98 µmol.cm$^{-3}$. More importantly, low radical concentrations were found suitable to polarize efficiently. These polarizing matrices could be compared with those displaying a pore size of 6 nm and particle size of 200-500 µm (section VI. B. Fig. 7). On these previous polarizing matrices, a maximum proton polarization of P($^1$H)= 99% was recorded for a radical concentration of [R]= 34 µmol.cm$^{-3}$. Here, the maximum proton polarization value (82 %) was found at [R]= 24 µmol.cm$^{-3}$. This difference (17 %) could be explained by a difference in particle size of ca. 15 µm.

In Figure 11, the proton polarization values as a function of the radical concentration are presented for samples with a pore diameter of 8 nm. For this pore size, a maximum proton polarization of P($^1$H) = 80 % was recorded at [R] = 21 µmol.cm$^{-3}$.

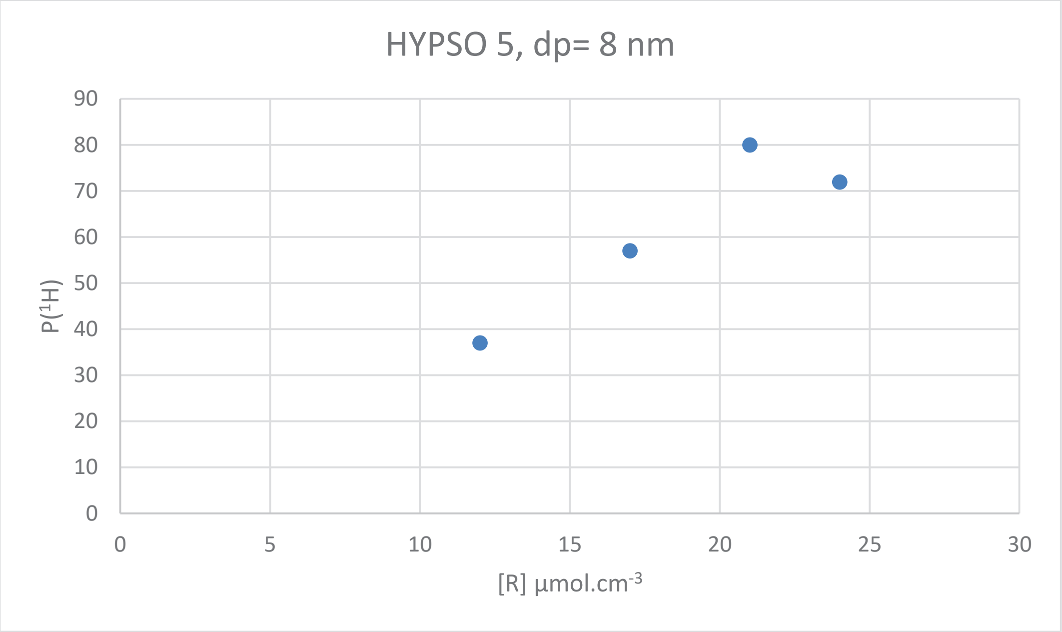

*Figure 11: Proton polarization values as a function of the radical concentration for HYPSO 5 with a pore diameter of 8 nm.*

Similarly, samples with a pore size of 12 nm were impregnated and polarized at T= 1.2 K. A maximum proton polarization of P($^1$H) = 60 % was found at higher concentration of [R]= 43 µmol.cm$^{-3}$. (Fig. 12)

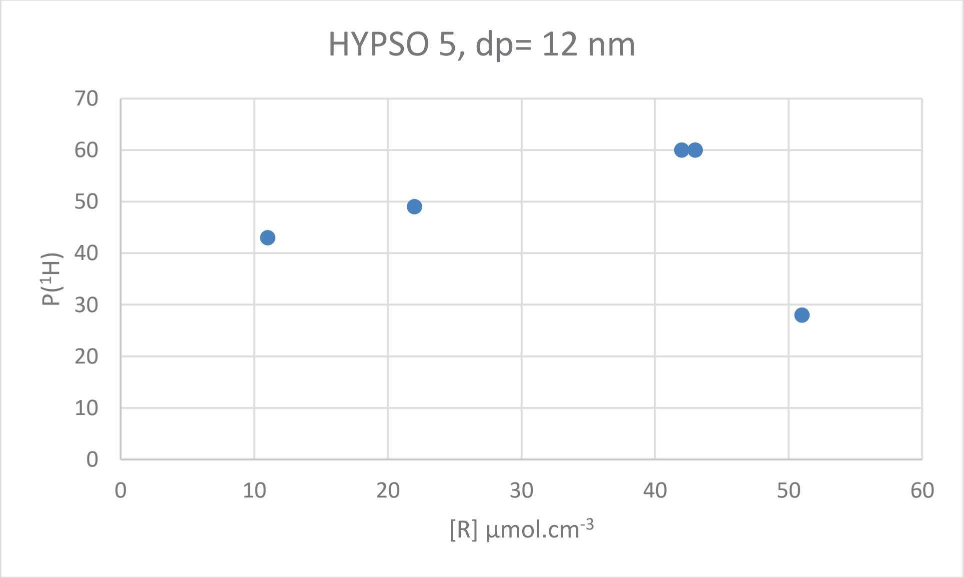

*Figure 12: Proton polarization values as a function of the radical concentration for HYPSO 5 with a pore size of 12 nm.*

From these three series, it seems that high polarization can be reached whatever the pore-size and that difference in pore diameter between 6 and 8 nm is not enough to observe any polarization difference. However, when doubling the pore size from 6 to 12 nm, it seems that slightly lower polarization values are obtained and that the bigger the pores, the higher is the radical concentration is needed to reach high polarization values.

| Dp (nm) | Maximum P($^1$H) (%) | [R] (µmol.cm$^{-3}$) |
|---|---|---|
| **6** | 82 | 24 |
| **8** | 80 | 21 |
| **12** | 60 | 43 |

We therefore expected to reach lower polarization values at higher radical concentration when using silica spheres with even bigger pores (i.e. 28 nm).

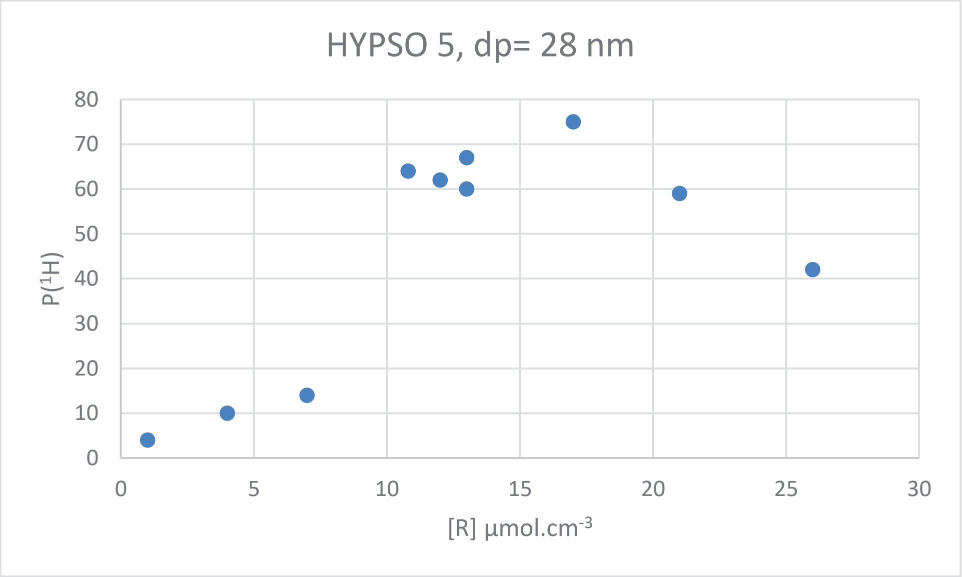

*Figure 13: Proton polarization values as a function of the radical concentration for HYPSO 5 with a pore size of 28 nm.*

Counter-intuitively, a radical concentration of 17 µmol.cm$^{-3}$ was found optimal to reach the maximum proton polarization of P($^1$H) = 75 % (see figure 13) and this result is quite similar to those obtained with the silica spheres of small pore diameters (6 and 8 nm). It is therefore difficult to draw a trend to explain the influence of the pore diameters on the polarization performances.

Overall, one can notice that high polarization values can be reached whatever the pore size and the granulometry of the silica spheres if appropriate radical concentrations are chosen and that the pore-interconnectivity is the key parameter for reaching remarkable polarization values. These results also suggest that the polarization of complex molecules could be effective using polarizing matrices with big pores.

## D. Proton polarization transfer to carbon by cross-polarization experiment using HYPSO 5 as polarizing matrix

Since remarkable proton polarization values were recorded for a benchmark solution of $H_2O$:$D_2O$ (2:8) in HYPSO 5, we have decided to investigate the $^{13}C$ polarization. On this experiment, HYPSO 5 with a radical concentration of 24 µmol.cm$^{-3}$, a pore diameter of 6 nm and particle size of 14 µm was selected. The sample was impregnated with a 3M solution of sodium [1-$^{13}C$] acetate in $H_2O$:$D_2O$ (2:8). After introduction of the wetted polarizing matrix in the DNP polarizer settled at T= 1.2 K, a first proton polarization of P($^1H$) = 70 % was recorded. Subsequently, this high proton polarization value was transferred to the surrounding carbon nuclei by applying a cross-polarization experiment every 6 minutes. As a result, a high carbon polarization value of P($^{13}C$) = 51 % was reached (Figure 14). In comparison to the previous experiment where a maximum of P($^1H$) = 99 % was recorded, the reached lower polarization value is related to the use of a completely different analyte. Nevertheless, the reached proton and carbon polarization values were found high.

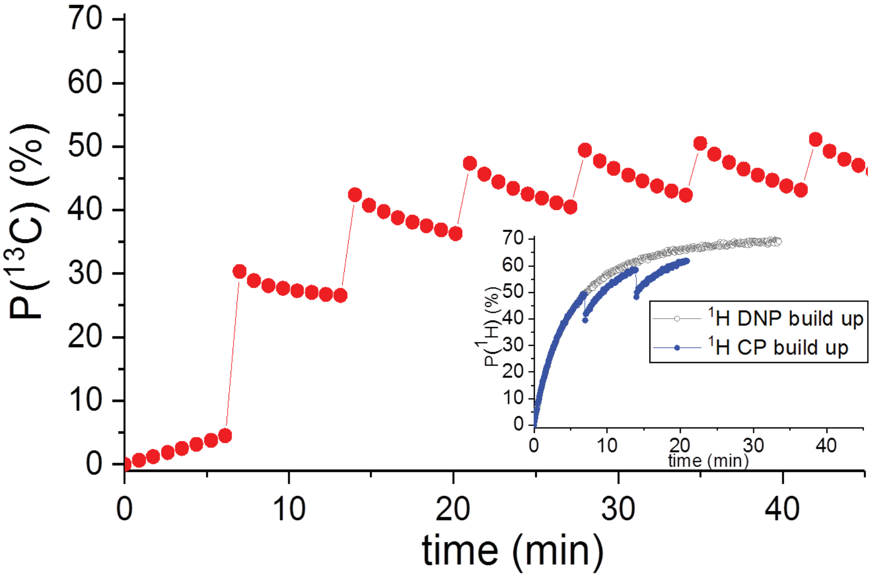

*Figure 14: $^{13}$C Build-up curve with CP for HYPSO 5 impregnated with a 3M solution of [1-$^{13}$C] sodium acetate in $H_2O$:$D_2O$ (2:8). Inset: curves for $^{1}$H DNP build-up without cross-polarization (gray) and $^{1}$H DNP build-up with cross-polarization (blue) for HYPSO 5 loaded with a 3M solution of [1-$^{13}$C] sodium acetate in $H_2O$:$D_2O$ (2:8).*

## E. Filtration outside the DNP polarizer

In a typical dissolution-DNP experiment, the hyperpolarized liquid is filtered from the polarizing matrix in the DNP polarizer under magnetic field. As explained in chapter 1, a dissolution stick equipped with a small oven heating and pressurizing the water is manually coupled with the holder previously placed in the DNP polarizer settled at low temperature. The dissolution sequence is then triggered by pushing a button on the dissolution stick which is maintained in the DNP polarizer by the operator while the pressurized hot water is injected to dissolve the hyperpolarized liquid. Because of the pressure, it exists some risks that the hot water leach into the DNP polarizer full of helium if the dissolution stick is not properly coupled to the sample holder. For this reason, preliminary tests of filtration were performed out of the polarizer and out of the magnetic field by introducing an on-line PTFE syringe filter (pore size of 0.45 µm) just before the magnetic tunnel and directly outgoing from the DNP polarizer. The figure 15 shows the actual device where the magnets are disposed in a frame obtained by 3D printing few centimeters from the top of DNP polarizer. The PTFE filter can be installed on-line between the magnets and the top of the DNP polarizer.

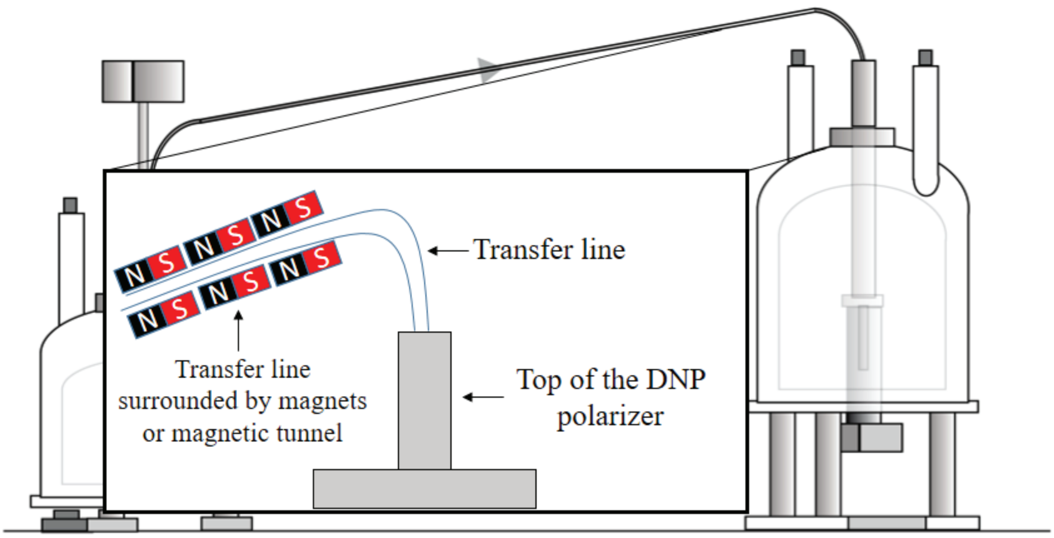

*Figure 15: Schematic representation of the DNP polarizer connected to the transfer line equipped few centimeters after the top of the DNP polarizer with the magnets (magnetic tunnel).*

Unfortunately, all of these filtration trials performed with previous polarizing matrices such as HYPSO 2 led to a complete loss of the polarization when performing the filtration outside of the magnetic field. This fast depolarization outside of the magnetic field could be explained by a prolonged contact between the hyperpolarized liquid and the paramagnetic species on the surface of the polarizing matrix which are known to relax rapidly the nuclei at room temperature.

However, and mainly because the architecture of the HYPSO 5 could ease the release of the hyperpolarized liquid from the polarizing matrix as compared to HYPSO 2, we have decided to re-novel the experiment with HYPSO 5. The typical 3M solution of sodium [1-$^{13}$C] acetate in $H_2O$:$D_2O$ (2:8) was impregnated in HYPSO 5 ([R] = 26 µmol.cm$^{-3}$) with a mean pore diameter of 6 nm and a particle size of 14 µm. The wetted solid matrix was introduced in the DNP polarizer and the polarization transferred from the protons to the carbons by cross-polarization experiments. After dissolution, a polarization of P($^{13}$C) = 19 % was recorded and the $T_1$ of HDO in solution was measured and gave $T_1$(HDO) = 30 s showing that no radical was found after the PTFE filter. This reasonable carbon polarization was reached because the highly interconnected structure of the HYPSO 5 allowed to accelerate the release of the hyperpolarized liquid from the polarizing matrix and thus to use a filter outside of the magnetic field.

# VIII. Magnetic resonance imaging

## A. Non-invasive molecular probes used in $^{13}$C-MRI DNP

As shown in chapter 1, a wide range of molecular probes are available to monitor *in-vivo* and *in-vitro* metabolisms. $^{13}$C-MRI coupled to DNP could be a method of choice for example if compared to Positron-Emission Tomography (PET) which is commonly employed to probe metabolic processes in neurology, cardiology or oncology using an analog of glucose: $^{18}$F-fluorodeoxyglucose ($^{18}$F-FDG). This latter contains a radioisotope of fluorine which is produced prior to the detection by a medical cyclotron (Figure 16).

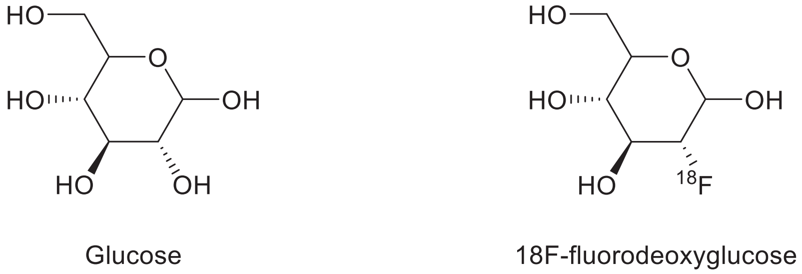

*Figure 16: Molecular structure of glucose and $^{18}$F-fluorodeoxyglucose.*

In a typical analysis, the radiopharmaceutical tracer is injected intravenously into the patient. Similarly to glucose, the $^{18}$F-FDG is transported into the cells and is phosphorylated to $^{18}$F-FDG-6-phosphate through the hexokinase (or glucokinase). After this transformation, the metabolism of the $^{18}$F-FDG-6-phosphate is blocked. The hydroxyl group which was replaced by a fluorine nucleus at the C-2 position of the ring (Figure 16) is essential to follow the Krebs cycle. Hence, the $^{18}$F-FDG is trapped and emit positron (half-life of 110 minutes) which interact with electrons to give two photons moving in the opposite direction and finally detect by a γ-camera to give a picture.

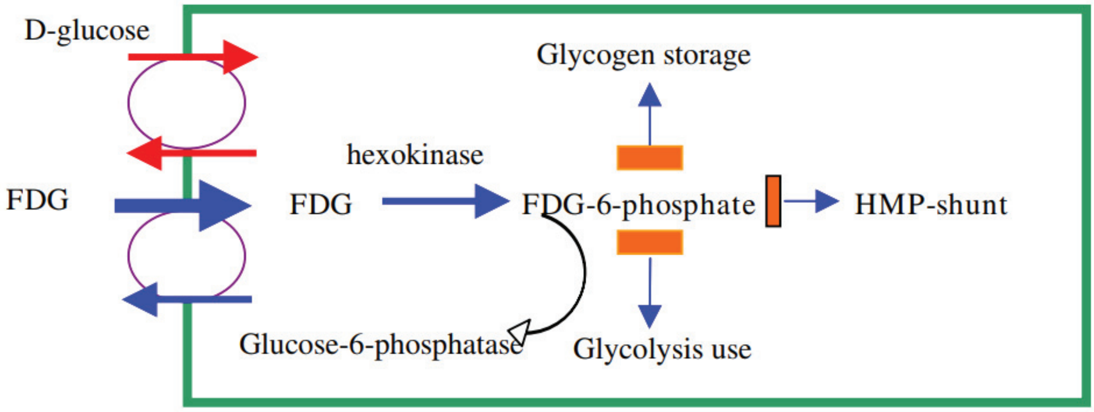

*Figure 17: Entrapment mechanism of $^{18}$F-FDG glucose*

As a result, $^{18}$F-FDG PET analysis allows to distinguish areas which consume a large quantity of glucose and therefore can detect cancer (Warburg effect chapter 1). However, in a recent paper of H. Gutte et al.,[30] the difficulty to discriminate a muscle from a tumor on the right front leg of a canine cancer patient was pointed out. As shown in Figure 18 (B), the tumor and the muscle appear in yellow indicating a high glucose uptake and accumulation. In addition, one can notice the low quality of the picture obtained with FDG-PET compared to that obtained by $^{1}$H-MRI.

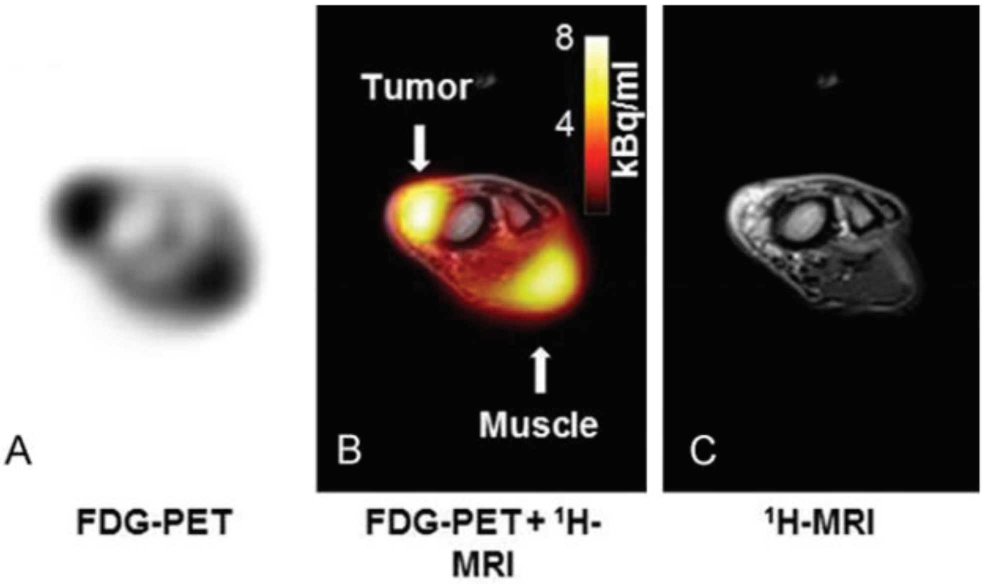

*Figure 18: Pictures of a right front leg of a canine cancer patient acquired by: (A) FDG-PET, (B) FDG-PET + $^{1}$H-MRI and (C) $^{1}$H-MRI*

Despite these observations, the two medical imaging techniques must not be opposed but should be considered as complementary based on the expected responses.[31-32] $^{1}$H-MRI provides a better visualization of the anatomical details whereas FDG-PET allows the metabolic assessment of the tissues.

In 2015, A. Flori et al.[33] have hyperpolarized a sodium [1-$^{13}$C]acetate solution to assess the real-time cardiac metabolism of pigs. This metabolic probe was selected because it is the most abundant extra- and intra-cellular short-chain fatty acid. Acetate is physiologically present in human blood with a concentration around 0,05-0,2 mM.[34-35] Moreover, the inadequate glassy property of this molecule in DNP remains a challenge to tackle.

For this reason, we have also decided to hyperpolarize a solution of sodium acetate because the HYPSO matrices could be of interest to increase the signal to noise ratio of this molecular probe. The impregnation of the HYPSO material with the solution of sodium acetate and the operating conditions are described in the following paragraph. The first $^{13}$C MRI pictures on a phantom were also recorded and presented hereafter.

## B. Hyperpolarization of sodium [1-$^{13}$C] acetate and MRI pictures

HYPSO 5 was loaded with a sodium [1-$^{13}$C]acetate solution and polarized at 1,2 K. The hyperpolarized liquid was then expelled from the polarizing matrix by means of small amount of superheated $D_2O$ (10 bar, 450 K). In order to be able to filter the silica spheres, a cellulose filter was installed output the dissolution stick itself settled in the polarizer. It has to be noticed that in general when the filter was placed outside of the polarizer, just before the magnetic tunnel, the freshly generated polarization decreases rapidly to its equilibrium value losing thus the possibility to increase signals. The hyperpolarized solution recovered free of any glass-forming or radicals was subsequently injected in a 5 mm NMR tube containing a slightly off-centered 2 mm capillary filled with $D_2O$ and used as phantom. In the field of medical imaging, a phantom is a designed object as model to evaluate the performance of imaging devices. It is more readily available and avoid to expose a living subject to possible risks. In this experiment, the phantom was installed in a 500 MHz NMR spectrometer equipped with a triple gradient probe and images of a thin slice were acquired using a FLASH sequence.[36] The images obtained after hyperpolarization of the sodium [1-$^{13}$C]acetate solution are presented in the figure 19.

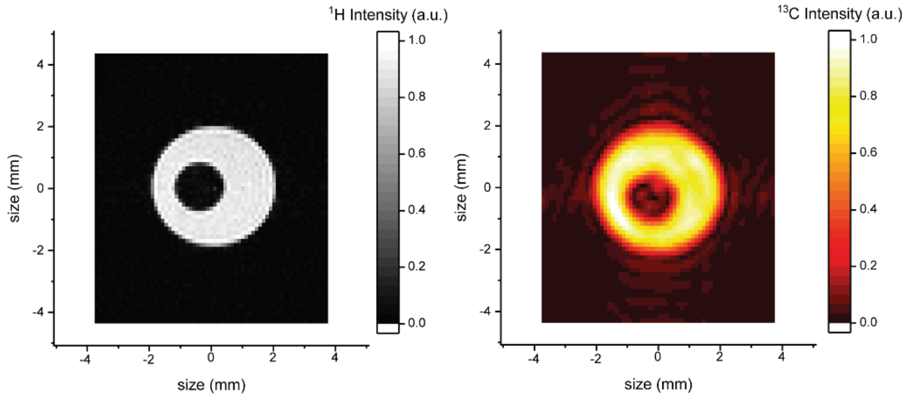

*Figure 19: $^1$H (left) and $^{13}$C pictures (right) acquired after hyperpolarization and dissolution of a solution of 3M sodium [1-$^{13}$C]acetate in $H_2O$:$D_2O$ (2:8) impregnated into HYPSO 5.*

In both images, a black circle located in the center appears which correspond to the capillary filled with $D_2O$. $^{13}$C image highlights for the first time the possibility to use HYPSO 5 as polarizing matrix to efficiently hyperpolarize and record MRI pictures after dissolution of sodium [1-$^{13}$C]acetate.

## IX. Conclusion

In conclusion, the new methodology to post-functionalize commercial mesoporous silica spheres has allowed to prepare polarizing matrices with different pore size and particle size. The TEMPO radicals were introduced on the silica spheres in a two-step process: i) coating of the silica sphere with a silica layer containing azido groups and ii) introduction of the TEMPO units *via* a click reaction with the surface azido groups. The post-functionalization of porous silica spheres with different particle size suggests that this parameter has an influence on the proton polarization values. However, an optimum with a particle size of 200-500 µm was found to reach remarkable polarization performances and to ease the filtration during the dissolution process. However, changing the pore size of the porous silica spheres from 6 nm to 28 nm has highlighted that high polarization values (60 – 80 %) can always be reached with radical concentration ranging from 20 to 40 µmol.cm$^{-3}$. In addition, polarizing matrices with larger pore size provide the possibility to hyperpolarize larger molecules/systems with decent polarization values.

Of the different materials developed, the non-structured silica spheres exhibiting a high pore-interconnectivity gave higher performances P($^1$H)= 99 % (± 5 %) which even exceeded those of the state-of-the-art DNP “juice”. In comparison to previous systems, the time to prepare the polarizing matrices were reduced and the entire process could potentially be easily scalable. Concerning these specific silica materials, the impregnated liquid was better released from these systems than from previous systems. It was thus possible for the first time to install a syringe filter between the magnetic tunnel and the top of the DNP polarizer to secure and ease the dissolution process.

Finally, a high carbon polarization value of $P(^{13}C)= 51\ \%$ for a solution of sodium acetate was recorded after dissolution using these silica spheres (HYPSO 5 of dp = 6 nm). Moreover, a first MRI picture using solid as polarizing matrix was recorded on a phantom constituted of a NMR tube containing a capillary tube filled with $D_2O$.

# SUPPORTING INFORMATION

# X. Preparation of the silica spheres

For the precursor's synthesis, the procedures are described in the supporting information of the chapter 2.

Before post-functionalization, the starting porous silica spheres were washed with DCM (3x50 mL) and an EDTA solution (3x50 mL) to eventually remove the paramagnetic species. The resulting porous silica spheres were then dried under high vacuum ($10^{-5}$ mbar) at 135°C for 12h.

## A. Insertion of azido moieties

The procedure to insert the azido moieties is described hereafter but the quantity inserted for each HYPSO is summarized in the following tables.

Prior to be heat up at 70 °C, porous silica spheres (1000 mg) were mixed with THF (20 mL) and an aqueous solution of HCl ([C]= 2.3 M, 1.4 mL). Then, a solution containing tetraethylorthosilicate (Tables 9-14), 3-azidopropyltriethoxysilane (Tables 9-14) and THF (Tables 9-14) was prepared. A small aliquot (9 mL) of this solution was added dropwise over a period of 15-20 minutes. Finally, the reaction mixture is stirred under reflux for 1h. The solid was further recovered by filtration, washed three times with 50 mL of a mixture of water/THF (20:80), ethanol (3x50 mL) and diethyl ether (3x50 mL) and dried under high vacuum ($10^{-5}$ mbar) at 135°C overnight.

*Table 11: Proportion for porous silica spheres with a pore size of 6 nm and particle size ranging from 200 to 500 µm.*

| Entry | Tetraethylorthosilicate (mg) | 3-azidopropyltriethoxysilane (mg) | THF (mL) |
|---|---|---|---|
| **10** | 2589.4 | 84.6 | 87 |
| **11** | 2598.3 | 70.0 | 87 |
| **12** | 2581.2 | 89.8 | 87 |
| **13** | 2573.0 | 100.8 | 87 |
| **14** | 2523.3 | 162.5 | 87 |
| **15** | 2538.9 | 141.0 | 87 |
| **16** | 2554.0 | 117.2 | 87 |
| **17** | 2524.0 | 157.1 | 87 |
| **18** | 2438.5 | 258.1 | 87 |

*Table 12: Porous silica spheres with a constant pore size of 6 nm a particle size ranging from 20 to 500 µm.*

| Entry | Tetraethylorthosilicate (mg) | 3-azidopropyltriethoxysilane (mg) | THF (mL) | Particle size (µm) |
|---|---|---|---|---|
| **1** | 2760.5 | 90.7 | 87 | 20 - 45 |
| **2** | 2756.0 | 97.5 | 87 | 20 - 45 |
| **3** | 2772.9 | 74.0 | 87 | 20 - 45 |
| **4** | 2661.6 | 82.9 | 87 | 60 - 120 |
| **5** | 2670.3 | 72.0 | 87 | 60 - 120 |
| **6** | 2653.5 | 89.4 | 87 | 60 - 120 |
| **7** | 2302.0 | 73.0 | 87 | 120 -200 |
| **8** | 2309.0 | 63.7 | 87 | 120 -200 |
| **9** | 2294.6 | 81.6 | 87 | 120 -200 |
| **10** | 2589.4 | 84.6 | 87 | 200 -500 |
| **11** | 2598.3 | 72.3 | 87 | 200 -500 |
| **12** | 2581.2 | 89.8 | 87 | 200 -500 |
| **13** | 2573.0 | 100.8 | 87 | 200 -500 |

*Table 13: Porous silica spheres with a pore size of Dp= 6 nm and particle size of ca. 15 µm.*

| Entry | Tetraethylorthosilicate (mg) | 3-azidopropyltriethoxysilane (mg) | THF (mL) | Particle size (µm) |
|---|---|---|---|---|
| **19** | 2325.0 | 25.0 | 87 | 15 |
| **20** | 2304.0 | 49.0 | 87 | 15 |
| **21** | 2283.0 | 74.0 | 87 | 15 |
| **22** | 2262.0 | 99.0 | 87 | 15 |
| **23** | 2241.9 | 124.6 | 87 | 15 |
| **24** | 2222.0 | 146.9 | 87 | 15 |

*Table 14: Porous silica spheres with a pore size of Dp= 8 nm and particle size of ca. 15 µm.*

| Entry | Tetraethylorthosilicate (mg) | 3-azidopropyltriethoxysilane (mg) | THF (mL) | Particle size (µm) |
|---|---|---|---|---|
| **25** | 1960.0 | 91.3 | 87 | 15 |
| **26** | 1966.6 | 81.8 | 87 | 15 |
| **27** | 1976.3 | 77.1 | 87 | 15 |
| **28** | 1948.0 | 103.8 | 87 | 15 |

*Table 15: Porous silica spheres with a pore size of Dp= 12 nm and particle size of ca. 15 µm.*

| Entry | Tetraethylorthosilicate (mg) | 3-azidopropyltriethoxysilane (mg) | THF (mL) | Particle size (µm) |
|---|---|---|---|---|
| **29** | 1599.3 | 74.2 | 87 | 15 |
| **30** | 1564.1 | 118.5 | 87 | 15 |
| **31** | 1536.6 | 147.8 | 87 | 15 |
| **32** | 1514.8 | 173.1 | 87 | 15 |
| **33** | 1460.8 | 239.2 | 87 | 15 |

*Table 16: Porous silica spheres with a pore size of Dp= 28 nm and particle size of ca. 15 µm.*

| Entry | Tetraethylorthosilicate (mg) | 3-azidopropyltriethoxysilane (mg) | THF (mL) | Particle size (µm) |
|---|---|---|---|---|
| **34** | 481.6 | 97.7 | 89 | 15 |
| **35** | 483.4 | 99.6 | 89 | 15 |
| **36** | 473.7 | 108.5 | 89 | 15 |
| **37** | 493.0 | 80.0 | 89 | 15 |
| **38** | 508.5 | 67.8 | 89 | 15 |
| **39** | 471.5 | 108.5 | 89 | 15 |
| **40** | 497.0 | 76.0 | 89 | 15 |
| **41** | 484.0 | 91.0 | 89 | 15 |
| **42** | 459.8 | 120.1 | 89 | 15 |
| **43** | 492.0 | 81.5 | 90 | 15 |

### B. Insertion of TEMPO radicals through CuAAC

Copper-catalyzed alkyne-azide cycloaddition (CuAAC) was used to couple azido fragments with TEMPO radicals. Typical click-chemistry is presented for the silica spheres containing azido fragments previously described.

Under argon atmosphere, o-propargyl TEMPO (Tables) was added to a suspension of $N_3$-silica spheres (1g) in DMF (5 mL). Then, a fresh stock solution of CuI (15 mg, 78.76 µmol) was prepared in DMF/$NEt_3$ (5 mL/ 2 mL) and an aliquot (Tables) was added to the latter solution. The mixture is stirred for 72h at 50 °C and then filtrated and washed with a EDTA solution (2 x 20 mL), DMF (2 x 20 mL), EtOH (3 x 20 mL), $Et_2O$ (3 x 20 mL). Finally, the product obtained is dried under high vacuum ($10^{-5}$ mbar) at 50 °C for 15h.

*Table 17: Proportion for porous silica spheres with a pore size of 6 nm and particle size ranging from 200 to 500 µm.*

| Entry | O-propargyl TEMPO (mg) | Solution of CuI (mL) |
|---|---|---|
| **10** | 22.2 | 0.6 |
| **11** | 17.8 | 0.5 |
| **12** | 23.7 | 0.7 |
| **13** | 25.2 | 0.7 |
| **14** | 41.0 | 1.2 |
| **15** | 35.3 | 1.0 |
| **16** | 30.3 | 0.8 |
| **17** | 40.4 | 1.2 |
| **18** | 65.6 | 1.9 |

Table 18: Porous silica spheres with a constant pore size of 6 nm a particle size ranging from 20 to 500 µm.

| Entry | O-propargyl TEMPO (mg) | Solution of CuI (mL) |
|---|---|---|
| **1** | 26.7 | 0.6 |
| **2** | 24.1 | 0.7 |
| **3** | 19.5 | 0.5 |
| **4** | 23.9 | 0.6 |
| **5** | 22.2 | 0.5 |
| **6** | 24.2 | 0.7 |
| **7** | 18.8 | 0.5 |
| **8** | 17.1 | 0.5 |
| **9** | 20.1 | 0.6 |
| **10** | 22.2 | 0.6 |
| **11** | 17.8 | 0.5 |
| **12** | 23.7 | 0.7 |
| **13** | 25.2 | 0.7 |

Table 19: Porous silica spheres with a pore size of Dp= 6 nm and particle size of ca. 15 µm.

| Entry | O-propargyl TEMPO (mg) | Solution of CuI (mL) |
|---|---|---|
| **19** | 6.3 | 0.2 |
| **20** | 12.6 | 0.4 |
| **21** | 18.9 | 0.5 |
| **22** | 25.2 | 0.7 |
| **23** | 31.5 | 0.9 |
| **24** | 37.9 | 1.1 |

*Table 20: Porous silica spheres with a pore size of Dp= 8 nm and particle size of ca. 15 µm.*

| Entry | O-propargyl TEMPO (mg) | Solution of CuI (mL) |
|---|---|---|
| **25** | 23.9 | 0.7 |
| **26** | 23.2 | 0.6 |
| **27** | 20.8 | 0.5 |
| **28** | 27.9 | 0.7 |

*Table 21: Porous silica spheres with a pore size of Dp= 12 nm and particle size of ca. 15 µm.*

| Entry | O-propargyl TEMPO (mg) | Solution of CuI (mL) |
|---|---|---|
| **29** | 12.2 | 0.3 |
| **30** | 17.3 | 0.4 |
| **31** | 37.9 | 1.1 |
| **32** | 44.2 | 1.3 |
| **33** | 36.1 | 0.9 |

*Table 22: Porous silica spheres with a pore size of Dp= 28 nm and particle size of ca. 15 µm.*

| Entry | O-propargyl TEMPO (mg) | Solution of CuI (mL) |
|---|---|---|
| **34** | 24.0 | 0.7 |
| **35** | 25.2 | 0.7 |
| **36** | 26.5 | 0.8 |
| **37** | 20.8 | 0.6 |
| **38** | 17.8 | 0.5 |
| **39** | 28.3 | 0.8 |
| **40** | 19.5 | 0.6 |
| **41** | 23.3 | 0.7 |
| **42** | 30.7 | 0.9 |
| **43** | 19.2 | 0.3 |

# XI. Characterization

## A. $N_2$ adsorption/desorption experiments

Experiments were performed at 77 K using a BELSORB-Max from BEL-JAPAN. Before $N_2$ adsorption, the samples were outgassed at $10^{-5}$ mbar at 408 K for 12 h. The pore diameter distribution and the mean pore diameter ($d_p$) were calculated using Barrett–Joyner–Halenda (BJH) method. The specific surface area ($S_{BET}$) was calculated using the Brunauer–Emmett–Teller (BET) equation.

## B. Diffuse Reflectance Infrared Fourrier Transform Spectroscopy (DRIFTS)

Preparation of the sample consist in filling a cell equipped with $CaF_2$ windows with the powder. DRIFT spectra were recorded on a Nicolet 6700-FT spectrometer and 64 scans were accumulated for each spectrum (resolution 4 $cm^{-1}$).

## C. Transmission Electron Microscopy (TEM)

Conventional TEM micrographs were performed at the "Centre Technologique des Microstructures", UCBL, Villeurbanne, France, using a JEOL 2100F electron microscope. The acceleration voltage was 200 kV. The samples were prepared by dispersing a drop of the ethanol suspension of a ground sample on a Cu grid covered by a carbon film.

## D. Electron Tomography (ET)

Electron tomography (ET) pictures were recorded on a TEM JEOL JEM-2100F equipped with a GATAN Ultrascan 1000 CDD camera. The JEOL TEMography software package was used for the automated acquisitions and 3D reconstructions. Moreover, 3D views of the reconstructed structures were obtained with ImageJ software. For each sample, a series of tilted images was collected from -70° to 70°, with the Saxton scheme (variable angular step improving the 3D reconstruction with a reduced number of images to preserve the beam sensitive structure of the samples). The samples HYPSO 2 and HYPSO 5 were recorded without any specific preparation. However, HYPSO 3 was impregnated under vacuum with an epoxy resin to completely fulfil the pores and thin sections of 50 nm obtained by ultramicrotomy were observed.

## E. Dynamic Nuclear Polarization

Typically, HYPSO materials were analyzed through the d-DNP system represented in Figure 20. After impregnation with the adequate analyte, the polarizing matrix was introduced in the polarizer with a magnetic field of $B_0 = 6.7$ T and a temperature of 4.2 K or 1.2 K. A microwave source of 94 GHz was used to transfer the polarization from the electrons to the molecule of interest. Frequency can be modulated with an amplitude of $\Delta v_{\mu w} = 100$ MHz and $f_{mod} = 10$ kHz or not modulated. The DNP build-up of $^{1}$H spins is measured with 1° nutation angle pulses followed by an acquisition period of 1ms. The resulting free induction decay is Fourier transformed, phased and integrated to obtain a value of $^{1}$H spin for the corresponding acquisition period. This sequence is applied every 5 seconds during at least 250 seconds (up to 1500 seconds for long build up time), thus, obtaining at least 50 values of $^{1}$H spin.

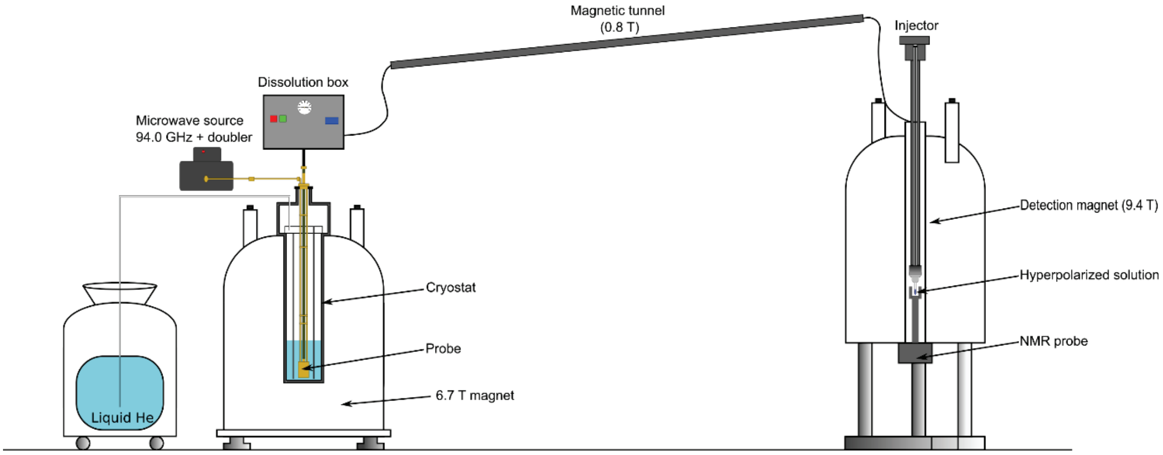

*Figure 20: Representation of the polarizer coupled to a NMR spectrometer via a magnetic tunnel. (private communication of Mathieu Baudin)*

# XII. References

1. Pedro, T.; María del Puerto, M.; Sabino, V.-V.; Teresita, G.-C.; Carlos, J. S., The preparation of magnetic nanoparticles for applications in biomedicine. *Journal of Physics D: Applied Physics* **2003,** *36* (13), R182.
2. Stöber, W.; Fink, A.; Bohn, E., Controlled growth of monodisperse silica spheres in the micron size range. *Journal of Colloid and Interface Science* **1968,** *26* (1), 62-69.
3. Kolbe, G., Dissertation, Jena, . **1956**.
4. Bogush, G. H.; Tracy, M. A.; Zukoski, C. F., Preparation of monodisperse silica particles: Control of size and mass fraction. *Journal of Non-Crystalline Solids* **1988,** *104* (1), 95-106.
5. Giesche, H., Synthesis of monodispersed silica powders I. Particle properties and reaction kinetics. *Journal of the European Ceramic Society* **1994,** *14* (3), 189-204.
6. Wang, H.-C.; Wu, C.-Y.; Chung, C.-C.; Lai, M.-H.; Chung, T.-W., Analysis of Parameters and Interaction between Parameters in Preparation of Uniform Silicon Dioxide Nanoparticles Using Response Surface Methodology. *Industrial & Engineering Chemistry Research* **2006,** *45* (24), 8043-8048.
7. Van Blaaderen, A.; Van Geest, J.; Vrij, A., Monodisperse colloidal silica spheres from tetraalkoxysilanes: Particle formation and growth mechanism. *Journal of Colloid and Interface Science* **1992,** *154* (2), 481-501.
8. Matsoukas, T.; Gulari, E., Dynamics of growth of silica particles from ammonia-catalyzed hydrolysis of tetra-ethyl-orthosilicate. *Journal of Colloid and Interface Science* **1988,** *124* (1), 252-261.
9. Matsoukas, T.; Gulari, E., Monomer-addition growth with a slow initiation step: A growth model for silica particles from alkoxides. *Journal of Colloid and Interface Science* **1989,** *132* (1), 13-21.
10. Matsoukas, T.; Gulari, E., Self-sharpening distributions revisited—polydispersity in growth by monomer addition. *Journal of Colloid and Interface Science* **1991,** *145* (2), 557-562.
11. Kim, S.; Zukoski, C. F., A model of growth by hetero-coagulation in seeded colloidal dispersions. *Journal of Colloid and Interface Science* **1990,** *139* (1), 198-212.
12. Bogush, G. H.; Zukoski, C. F., Studies of the kinetics of the precipitation of uniform silica particles through the hydrolysis and condensation of silicon alkoxides. *Journal of Colloid and Interface Science* **1991,** *142* (1), 1-18.
13. Bogush, G. H.; Zukoski, C. F., Uniform silica particle precipitation: An aggregative growth model. *Journal of Colloid and Interface Science* **1991,** *142* (1), 19-34.
14. LaMer, V. K.; Dinegar, R. H., Theory, Production and Mechanism of Formation of Monodispersed Hydrosols. *Journal of the American Chemical Society* **1950,** *72* (11), 4847-4854.
15. Ocaña, M.; Rodriguez-Clemente, R.; Serna, C. J., Uniform colloidal particles in solution: Formation mechanisms. *Advanced Materials* **1995,** *7* (2), 212-216.
16. Michael, G.; Iris, L.; K., U. K., The synthesis of micrometer- and submicrometer-size spheres of ordered mesoporous oxide MCM-41. *Advanced Materials* **1997,** *9* (3), 254-257.
17. Huo, Q.; Feng, J.; Schüth, F.; Stucky, G. D., Preparation of Hard Mesoporous Silica Spheres. *Chemistry of Materials* **1997,** *9* (1), 14-17.
18. Yang, H.; Vovk, G.; Coombs, N.; Sokolov, I.; A. Ozin, G., Synthesis of mesoporous silica spheres under quiescent aqueous acidic conditions. *Journal of Materials Chemistry* **1998,** *8* (3), 743-750.
19. Gallis, K. W.; Eklund, A. G.; Jull, S. T.; Araujo, J. T.; Moore, J. G.; Landry, C. C., The Use of Mesoporous Silica in Liquid Chromatography. *Advanced Materials* **1999,** *11* (17), 1452-1455.

20. Unger, K. K.; Kumar, D.; Grün, M.; Büchel, G.; Lüdtke, S.; Adam, T.; Schumacher, K.; Renker, S., Synthesis of spherical porous silicas in the micron and submicron size range: challenges and opportunities for miniaturized high-resolution chromatographic and electrokinetic separations. *Journal of Chromatography A* **2000,** *892* (1), 47-55.
21. Nooney, R. I.; Thirunavukkarasu, D.; Chen, Y.; Josephs, R.; Ostafin, A. E., Synthesis of Nanoscale Mesoporous Silica Spheres with Controlled Particle Size. *Chemistry of Materials* **2002,** *14* (11), 4721-4728.
22. Yano, K.; Fukushima, Y., Particle size control of mono-dispersed super-microporous silica spheres. *Journal of Materials Chemistry* **2003,** *13* (10), 2577-2581.
23. Ma, Y.; Qi, L.; Ma, J.; Wu, Y.; Liu, O.; Cheng, H., Large-pore mesoporous silica spheres: synthesis and application in HPLC. *Colloids and Surfaces A: Physicochemical and Engineering Aspects* **2003,** *229* (1), 1-8.
24. Gustafsson, H.; Holmberg, K., Emulsion-based synthesis of porous silica. *Advances in Colloid and Interface Science* **2017,** *247*, 426-434.
25. Imhof, A.; Pine, D. J., Ordered macroporous materials by emulsion templating. *Nature* **1997,** *389*, 948.
26. Arnout, I.; J., P. D., Uniform Macroporous Ceramics and Plastics by Emulsion Templating. *Advanced Materials* **1998,** *10* (9), 697-700.
27. Chevalier, Y.; Bolzinger, M.-A., Emulsions stabilized with solid nanoparticles: Pickering emulsions. *Colloids and Surfaces A: Physicochemical and Engineering Aspects* **2013,** *439*, 23-34.
28. B.P., B., Macroporous Silica From Solid-Stabilized Emulsion Templates. *Advanced Materials* **2002,** *14* (24), 1824-1827.
29. Chu, C. H.; Jonsson, E.; Auvinen, M.; Pesek, J. J.; Sandoval, J. E., A new approach for the preparation of a hydride-modified substrate used as an intermediate in the synthesis of surface-bonded materials. *Analytical Chemistry* **1993,** *65* (6), 808-816.
30. Gutte, H.; Hansen, A. E.; Henriksen, S. T.; Johannesen, H. H.; Ardenkjaer-Larsen, J.; Vignaud, A.; Hansen, A. E.; Børresen, B.; Klausen, T. L.; Wittekind, A.-M. N.; Gillings, N.; Kristensen, A. T.; Clemmensen, A.; Højgaard, L.; Kjær, A., Simultaneous hyperpolarized (13)C-pyruvate MRI and (18)F-FDG-PET in cancer (hyperPET): feasibility of a new imaging concept using a clinical PET/MRI scanner. *American Journal of Nuclear Medicine and Molecular Imaging* **2015,** *5* (1), 38-45.
31. Nakamoto, R.; Nakamoto, Y.; Ishimori, T.; Fushimi, Y.; Kido, A.; Togashi, K., Comparison of PET/CT with sequential PET/MRI using an MR-compatible mobile PET system. *Journal of Nuclear Medicine* **2017**.
32. Bailey, D. L.; Pichler, B. J.; Gückel, B.; Barthel, H.; Beer, A. J.; Botnar, R.; Gillies, R.; Goh, V.; Gotthardt, M.; Hicks, R. J.; Lanzenberger, R.; la Fougere, C.; Lentschig, M.; Nekolla, S. G.; Niederdraenk, T.; Nikolaou, K.; Nuyts, J.; Olego, D.; Riklund, K. Å.; Signore, A.; Schäfers, M.; Sossi, V.; Suminski, M.; Veit-Haibach, P.; Umutlu, L.; Wissmeyer, M.; Beyer, T., Combined PET/MRI: from Status Quo to Status Go. Summary Report of the Fifth International Workshop on PET/MR Imaging; February 15–19, 2016; Tübingen, Germany. *Molecular Imaging and Biology* **2016,** *18* (5), 637-650.
33. Menichetti, L.; Frijia, F.; Flori, A.; Wiesinger, F.; Lionetti, V.; Giovannetti, G.; Aquaro, G. D.; Recchia, F. A.; Ardenkjaer-Larsen, J. H.; Santarelli, M. F.; Lombardi, M., Assessment of real-time myocardial uptake and enzymatic conversion of hyperpolarized [1-13C]pyruvate in pigs using slice selective magnetic resonance spectroscopy. *Contrast Media & Molecular Imaging* **2012,** *7* (1), 85-94.
34. Skutches, C. L.; Holroyde, C. P.; Myers, R. N.; Paul, P.; Reichard, G. A., Plasma acetate turnover and oxidation. *The Journal of Clinical Investigation* **1979,** *64* (3), 708-713.
35. Eichhorn, T. R.; Takado, Y.; Salameh, N.; Capozzi, A.; Cheng, T.; Hyacinthe, J.-N.; Mishkovsky, M.; Roussel, C.; Comment, A., Hyperpolarization without persistent radicals

for in vivo real-time metabolic imaging. *Proceedings of the National Academy of Sciences of the United States of America* **2013,** *110* (45), 18064-18069.

36. Haase, A.; Frahm, J.; Matthaei, D.; Hänicke, W.; Merboldt, K. D., FLASH imaging: Rapid NMR imaging using low flip-angle pulses. *Journal of Magnetic Resonance* **2011,** *213* (2), 533-541.

# Chapter 4: Hybrid polarizing solids based on silica xerogels

# Table of contents

# I. Introduction

In the previous chapters, polarizing matrices were obtained either by the preparation of ordered mesoporous materials or by post-functionalization of silica spheres of various sizes. Depending on the system and mostly for samples with fine silica particles, the dissolution step could be hampered by filtration issues. These problems are related to the use of hot pressured water to recover the solution containing the hyperpolarized sample that may carry some fine silica particles outside the polarizer or may lead to filter-blocking. If the silica grains containing TEMPO radicals are found in the hyperpolarized solution, the measured polarization can be suboptimal or can completely disappear. Hence, we have developed alternative polarizing matrices functionalized by TEMPO radicals of controlled granulometry to fix this problem. Beside silica spheres, we thus will focus here on the preparation of monolithic samples while maintaining a large pore interconnectivity. Samples were prepared using sol-gel process *via* two different synthetic routes. In the first route, the TEMPO radicals are directly introduced at the beginning of the sol-gel process. The second route consists in preparing functional silica-materials containing azido groups which are further transformed into TEMPO fragments. The direct incorporation of the TEMPO groups lead to samples with a monolithic shape (rigid cylinders) and an orange color. In the second case, relative large silica beads are produced due to the cracking of the monoliths during the TEMPO introduction.

This chapter therefore describes the preparation of the aerogels and xerogels. The two different synthetic processes to produce xerogel cylinders or beads are detailed here along with the complete characterization of the resulting solids. Different parameters such as the build-up times, relaxation times and the polarization values were measured to probe the behavior of these new polarizing matrices. In addition, the quantity expelled from the solids was evaluated by $^1$H NMR after dissolution of the samples. Since the different formulations allowed to perform an easy and fast filtration, the silica matrices were recovered and re-used to polarize a sample in a second polarization-dissolution cycle.

# II. From silica powders to monolithic materials

Sol-gel process or derivative methods were used in this PhD project to develop new hybrid ordered mesoporous materials or functionalized silica spheres with TEMPO groups. It is now obvious that this technique is a versatile way to produce any kind of supports decorated with organic groups of interest. Moreover, we have proved that it is perfectly suitable for d-DNP analysis and MRI applications. In order to optimize the entire DNP process, we first focused on the possibility to improve the filtration by changing the granulometry of the polarizing matrices. One of the possible solutions was to prepare aerogel or xerogel silica-based materials which displayed similar textures and chemical compositions. Indeed, their high porosity could host the TEMPO radicals and the solution to be polarized and their monolithic shape could improve the filtration step. The silica networks were tailored to mimic those of HYPSO 5 solids.

As depicted in Figure 1, the only difference between the two materials preparation relies on the drying step. Whereas the solvent is removed under supercritical $CO_2$ drying for the aerogels, the xerogels are dried under ambient pressure. Their synthesis involve the use of alkoxysilanes which react under specific conditions to create a viscous solution known as the "sol". After a certain period of time (the gelation time), the sol polymerized to give a gel swollen by the solvent. A network was thus created and its mechanical strength could be reinforced by adjusting the aging time. The difference in the drying step as presented above can generate significant changes on the structure and properties of the materials.

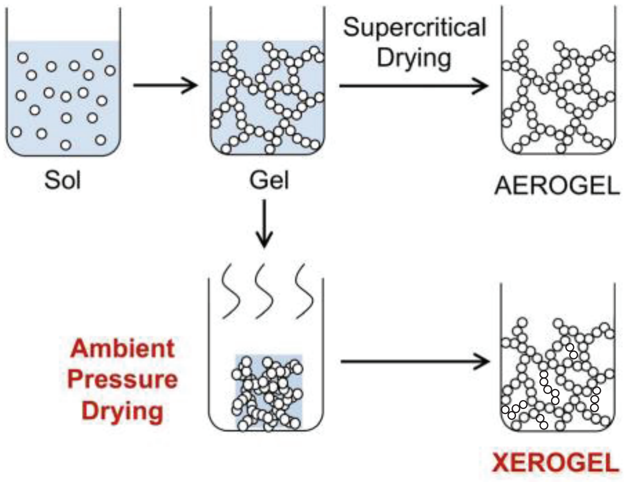

*Figure 1: Schematic representation of the synthesis process leading to aerogel or xerogel materials.*[1]

The next section will be divided in three parts: the first and the second section will describe the main characteristics of the aerogels and xerogels as well as the salient points of their synthesis. Then, the polarization values and build-up times will be presented and discussed in regard of the d-DNP process constraints.

# III. Aerogel

## A. Introduction

First reported in 1931 by S. S. Kistler[2], the aerogels display : a low density (30 – 50 kg.m$^{-3}$), a high porosity (85 – 99%) and a high specific surface area (500 – 1300 m$^2$.g$^{-1}$). They are mainly used for their thermal insulator property but their applications are relatively wide from aerospace[3] to biomedical applications.[4]

The drying process used to prepare the xerogels is important for determining their textural properties. Arising from some perturbations when expelling the solvent from the pore network of the materials, the drying step can induce cracking or collapse of the materials' porosity. These perturbations are capillary constraints as defined by the Laplace-Young equation:

$$\boxed{P = \frac{-2\gamma}{R}\cos\theta}$$

- P: capillary pressure (N.m$^{-2}$)
- R: meniscus radius (m)
- $\gamma$: surface tension of the liquid (mN.m$^{-1}$)
- $\theta$: wetting angle

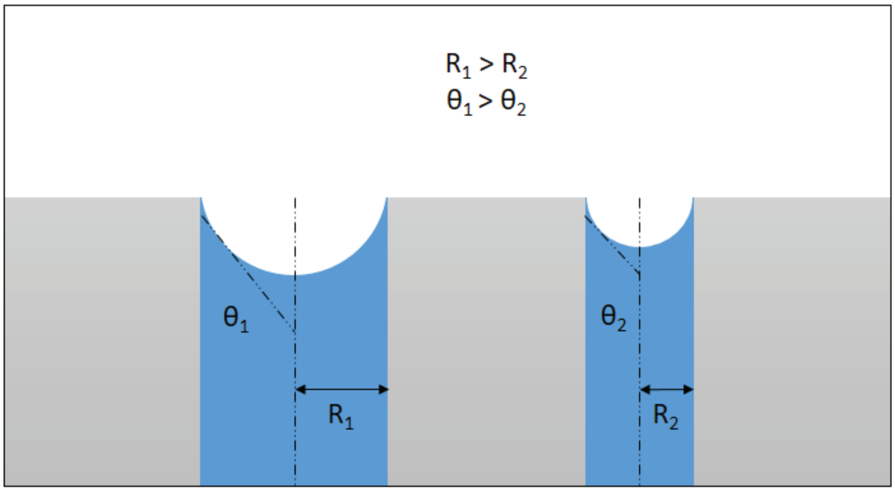

*Figure 2: Schematic representation of pores with a radius $R_1$ or $R_2$ on which different capillary forces are applied.*

A schematic representation of the pores with different sizes is shown in Figure 2. The indices 1 and 2 refer respectively to a large pore with a radius $R_1$ and a small pore with a radius $R_2$. The pressure exerted into these pores are denoted $P_1$ and $P_2$ and the wetting angles $\theta_1$ and $\theta_2$. The situation as presented here is an ideal case because in reality the pores are not perfectly cylindrical and can display some asperities. The Laplace-Young equation shows that decreasing of the pore size (R) results in increasing capillary forces and cracking can thus preferentially occur on the smaller pores of the final material. To avoid such cracking, for a given material where it is not possible to increase or calibrate the pore size, one can act on the surface tension between the interfaces by changing the solvent or by introducing additives. Solvent extraction can also be performed with supercritical $CO_2$. The method consists in substituting the liquid used during the synthesis to a fluid which has a surface tension equal to zero. The capillary stress thus disappears, giving rise to materials with a monolithic shape without cracks.

In Figure 3, a carbon dioxide phase diagram is plotted and allows to localize the critical point above which supercritical drying can be performed. In the specific case of carbon dioxide, the critical pressure and temperature are respectively: $P_c = 73.8$ bar and $T_c = 31.1$ °C. In these specific conditions the substance is a supercritical fluid which has a peculiar behavior at the boundary between a liquid and a gas.

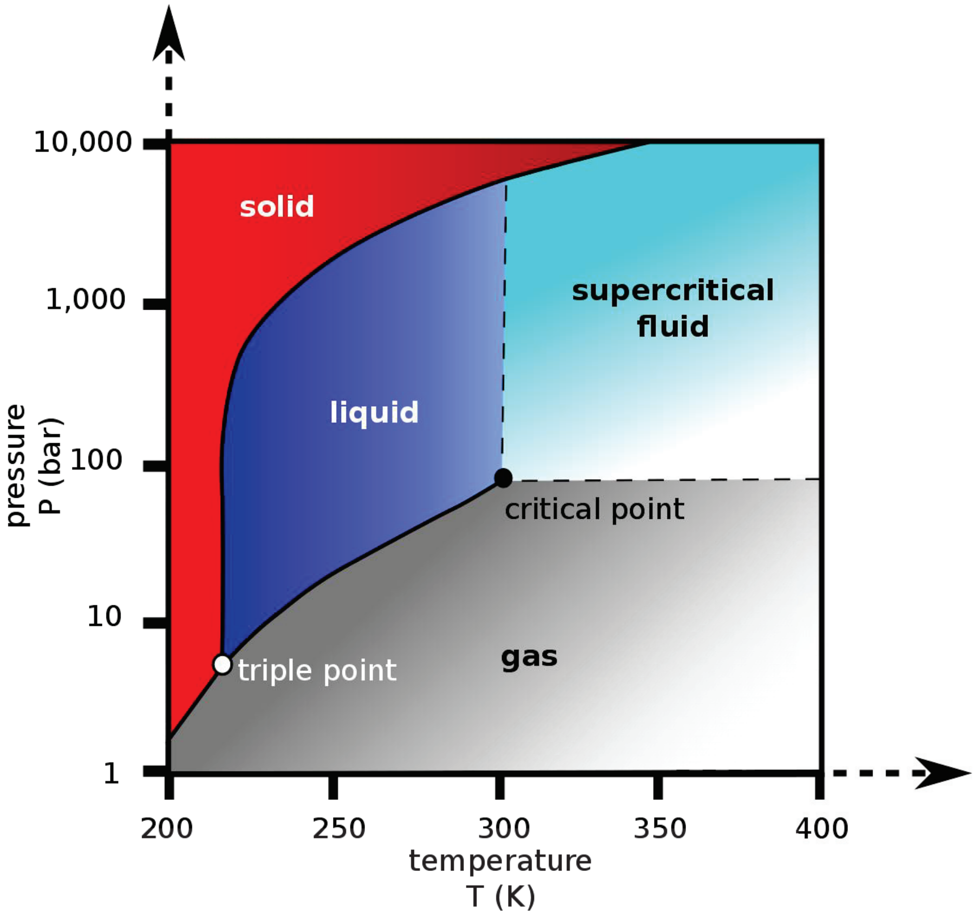

*Figure 3: Phase diagram of carbon dioxide displaying the pressure as a function of the temperature.*

Although carbon dioxide is used as a supercritical fluid, other substances could be also employed as shown in table 1 where the physical properties of some supercritical fluids are summarized.[5] Extraction under supercritical conditions is thus possible with a wide range of solvents. Nevertheless, some of them are discarded because of their toxicity or corrosion such as ammonia or for safety reasons (ethane being highly flammable). In most cases, carbon dioxide is employed because it is non-toxic, non-flammable, chemically inert, inexpensive and available at high purity. In addition, its relatively low critical temperature (31.1 °C) and pressure (73.8 bar) are easily achievable. These characteristics are interesting in order to extract and purify organic compounds with low decomposition temperature.

*Table 1: Physical properties of some supercritical fluids.*

| Fluids | Critical temperature | Critical pressure | | |
|---|---|---|---|---|
| | (°C) | Bar | Atm | psi |
| **Carbon dioxide** | 31.1 | 73.8 | 74.8 | 1070.4 |
| **Ethane** | 32.4 | 48.8 | 49.5 | 707.8 |
| **Methanol** | 240.1 | 80.9 | 82.0 | 1173.4 |
| **Ammonia** | 132.4 | 113.5 | 115.0 | 1646.2 |
| **Nitrous oxide** | 36.6 | 72.4 | 73.4 | 1050.1 |
| **Xenon** | 16.7 | 58.4 | 59.2 | 847.0 |
| **Water** | 374.4 | 221.2 | 224.1 | 3208.2 |

Supercritical drying using alcohols such as methanol deserves also to be mentioned. The critical temperature and pressure are relatively high which implies the deployment of a heavier safety device. It is also worth noting that methanol is not chemically inert. The hydroxyl groups present on the surface of the silica materials can react with methanol to form surface methoxy species. More hydrophobic materials are thus generated and present usually a higher mechanical resistance than materials dried *via* supercritical $CO_2$.

## B. Synthesis of the hybrid aerogels

For this preparation, anhydrous methanol was first inserted in a 50 mL round bottom flask previously placed in an ice bath along with tetramethyl orthosilicate (TMOS). Then, a solution of oxalic acid with a concentration of 1 mmol.L$^{-1}$ was prepared and added dropwise to the previous mixture. Finally, the resulting viscous solution was vigorously stirred at 0°C for 30 minutes prior to remove the ice bath for additional stirring at room temperature (24h). Following the number of aerogels needed, the proportions of the chemicals can be adjusted.

In order to avoid any cracks on the aerogels during the drying process, hydrophobic Teflon vials were used in the next step. For one aerogel, a Teflon vial was placed in an ice bath and a portion of the previous mixture was introduced. Then water and methanol were added before preparing a 1M solution of ammoniac. Finally, the ammoniac solution was added dropwise and the sample was stirred 90 s prior to remove the stirring magnet and placed it inside the fridge for 2h. The sample was further placed at room temperature for 2h and dried 48h at 50 °C.

Because the water is not miscible with the supercritical $CO_2$,[6] the water contained in the sample was exchanged with acetone which is miscible. Therefore, all eventual capillary constraints arising from a liquid-liquid interaction were removed. As shown in Figure 4, the samples were immersed in acetone to remove the water before being dried by supercritical $CO_2$.

*Figure 4: Aerogels immersed in acetone to remove water before being dried by supercritical $CO_2$.*

After this exchange process, the autoclave (Fig. 5) used to prepare the aerogels was cooled down to 10°C to be able to transfer the liquid $CO_2$ from the bottle to the autoclave. Then, the gel was placed in a crucible filled with acetone and placed in the autoclave. The system was tightly closed and completely filled with liquid $CO_2$. The next step consisted in closing the filling valve and opening the draining valve to purge out the solvent of the autoclave (procedure repeated 6 times). Once all the traces of the solvent were removed, the autoclave was again filled with the liquid adjusted above the gel and all the valves were closed. The temperature was set to 45°C and pressure to 95 bar for 1h before slowly releasing the pressure (ca. 1 bar/min) while keeping the same temperature. This slow depressurization avoids to crack the final material and the retention of the temperature avoids the condensation of $CO_2$. Indeed, as shown in figure 3, above the supercritical point and for a given pressure, the decrease of the temperature could lead to cross the boundary between the supercritical state and the liquid state. A picture of the supercritical device used for the preparation of our aerogels is presented in figure 5.

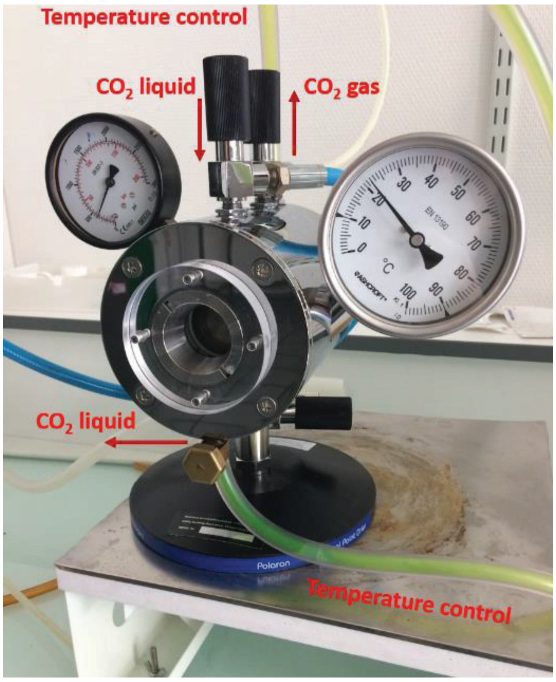

*Figure 5: Autoclave connected to a $CO_2$ bottle allowing to prepare the aerogels.*

Unfortunately, after many attempts based on the same reaction scheme already detailed for HYPSO 5, the aerogels were prepared but they exhibited a poor mechanical strength leading to a fine silica powder. This issue is also discussed in a recent review published by A. Lamy-Mendes.[7] Their application in d-DNP which uses harsh conditions was thus discarded and we focused our investigations on silica xerogel materials.

## IV. Xerogel

As mentioned above, the solvent in xerogel materials can be removed under ambient pressure drying. This technique which is less drastic than the use of supercritical carbon dioxide is also presented as an industrial and safer alternative to produce silica materials. However, using such drying technique, the characteristics of the silica xerogels are quite different. In comparison to aerogels, their porosity is lower (25 % vs 85 – 99 % for aerogels) albeit still high. In addition, these silica materials display high surface area and a pore size which can be tuned from 1 to 10 nm. A considerable shrinkage of the porosity, from 90 % to 95 % depending on the system, is observed during the drying process.[8]

## A. Preparation of hybrid silica xerogels

Hybrid silica xerogels were prepared either by direct incorporation of TEMPO radicals during the preparation of the materials or by post-functionalization of xerogels containing azidopropyl-fragments. As shown in Figure 6, these two strategies led to two types of samples: i) an orange silica xerogel molded in a cylindrical shape (direct incorporation of the TEMPO groups) and ii) an orange silica xerogel made of beads of different sizes (post-functionalization of azido-containing solids).

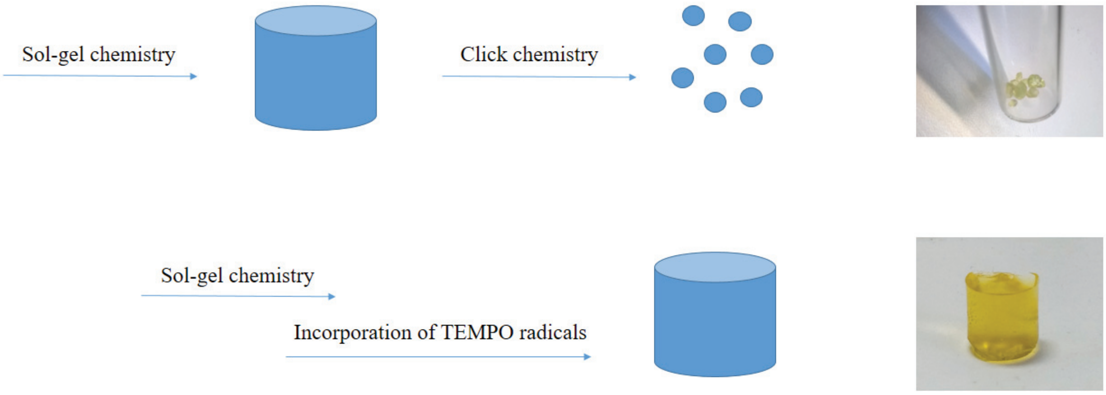

*Figure 6: Schematic representation of the two synthetic routes leading to the hybrid xerogels containing TEMPO radicals.*

The synthesis of both materials is explained in the following paragraph but more details can be found in the supporting information at the end of this chapter.

## 1. Hybrid silica xerogels obtained through post-functionalization

### a) Synthesis of the xerogels

Hybrid silica xerogels were obtained using a straightforward method based on sol-gel process in two steps. The first step consists in preparing a sol at 0°C by mixing methanol, TMOS and a portion of an oxalic acid solution [C] = 0.001 M. Then, the reaction mixture was maintained at 0°C for 30 minutes and finally left 24h at room temperature. The next day, the second step was performed by mixing an aliquot of the previous sol with milli-Q water, 3-azidopropyltriethoxysilane and a freshly prepared ammonia solution [C] = 1M at 0°C in a Teflon vial (this container was used for the same reason as before). Subsequently, the reaction mixture was kept 90 seconds at 0°C and the stirring magnet was removed before introducing the Teflon vial in the fridge for 2h. As shown in Figure 7, materials with various dilutions were prepared in cylindrical Teflon vials by incorporating different amounts of the 3-azidopropyltriethoxylsilane precursor.

Finally, all the closed Teflon vials containing the sols were aged at 50°C for 2 days in an oven. Then, the solvent was slowly removed by increasing the temperature up to 110 °C in 24 h with the Teflon vial caps slightly opened (1/4 of a turn). Transparent silica xerogels bearing azidopropyl-groups were thus obtained.

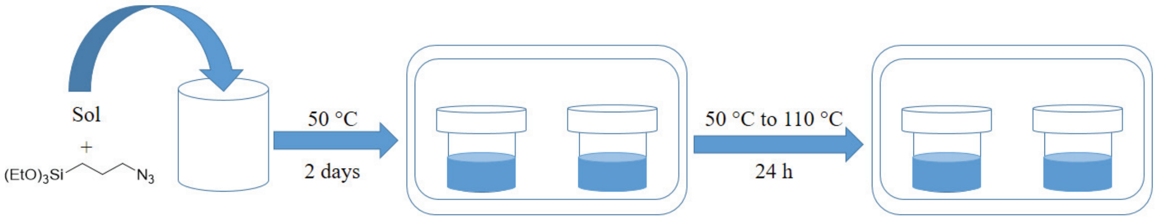

*Figure 7: Schematic representation of the synthesis of hybrid silica xerogels.*

Copper-catalyzed alkyne-azide cycloaddition was then performed to introduce the TEMPO radicals using the same protocol than the one used in the previous chapters. However, the speed of the stirring magnet was slowed down to avoid as much as possible to damage the monoliths and to avoid to create fine xerogel particles. A schematic representation of the synthesis along with a picture of the final materials are depicted in Figure 8.

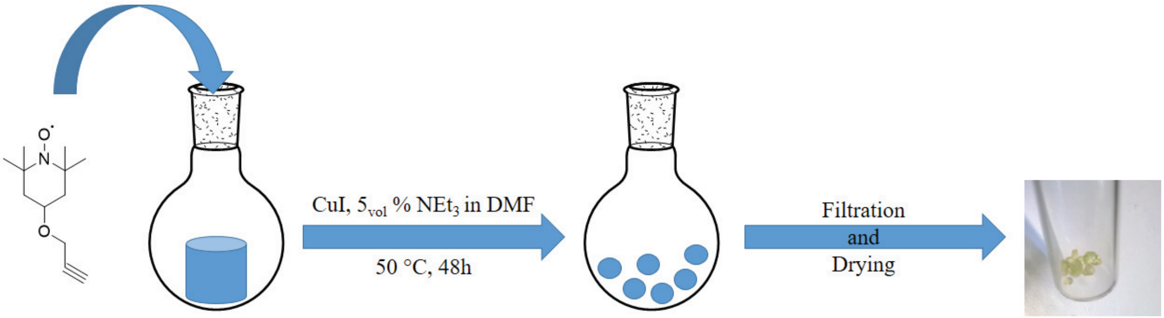

*Figure 8: Schematic representation of the TEMPO incorporation using CuAAC in the silica xerogels bearing azido groups.*

Materials with different radical concentrations were prepared and analyzed (vide infra) before impregnation with liquids and subsequent polarization.

### b) Characterization: $N_2$ adsorption/desorption experiments and EPR

After drying the samples for 12h at 50 °C under high vacuum, surface area, pore size and porous volume were obtained from $N_2$ adsorption/desorption measurements. The results are summarized in Table 2 with the radical concentration arising from electron spin counting using EPR. Moreover, EPR spectra for each samples are presented in Figure 11.

Surface areas ranging from 355 to 586 $m^2.g^{-1}$ were found with a pore size ranging from 3 to 6 nm. The samples display high porous volumes from 0.4 to 0.7 $cm^3.g^{-1}$ allowing to impregnate a large quantity of liquid. Nevertheless, small fluctuations can be observed and could be explained by inhomogeneous heating of the samples in the oven or a different solvent extraction rate when opening the Teflon vial caps.

*Tableau 2: $N_2$ adsoprtion/desorption analysis and electron paramagnetic resonance of the final xerogels with different radical concentrations.*

| Entry | [R]<br>(µmol.cm$^{-3}$) | $S_{BET}$<br>(m$^2$.g$^{-1}$) | Dp$^a$<br>(nm) | $V_p$(tot.)$^b$<br>(cm$^3$.g$^{-1}$) |
|---|---|---|---|---|
| 1 | 2 | 381 | 5 | 0.46 |
| 2 | 5 | 418 | 4 | 0.4 |
| 3 | 10 | 407 | 3 | 0.33 |
| 4 | 14 | 355 | 6 | 0.51 |
| 5 | 15 | 429 | 3 | 0.36 |
| 6 | 34 | 430 | 3 | 0.36 |
| 7 | 44 | 586 | 5 | 0.77 |

a: Mesopore mean diameter calculated using the BJH model (adsorption branch).b: total pore volume corresponding to the quantity of $N_2$ adsorbed at $P/P_0 = 0.99$.

As an example the adsorption/desorption isotherm along with the BJH plot allowing to determine the mean pore diameter for one of the xerogel post-functionalized with TEMPO radicals are presented in Figure 9 and 10.

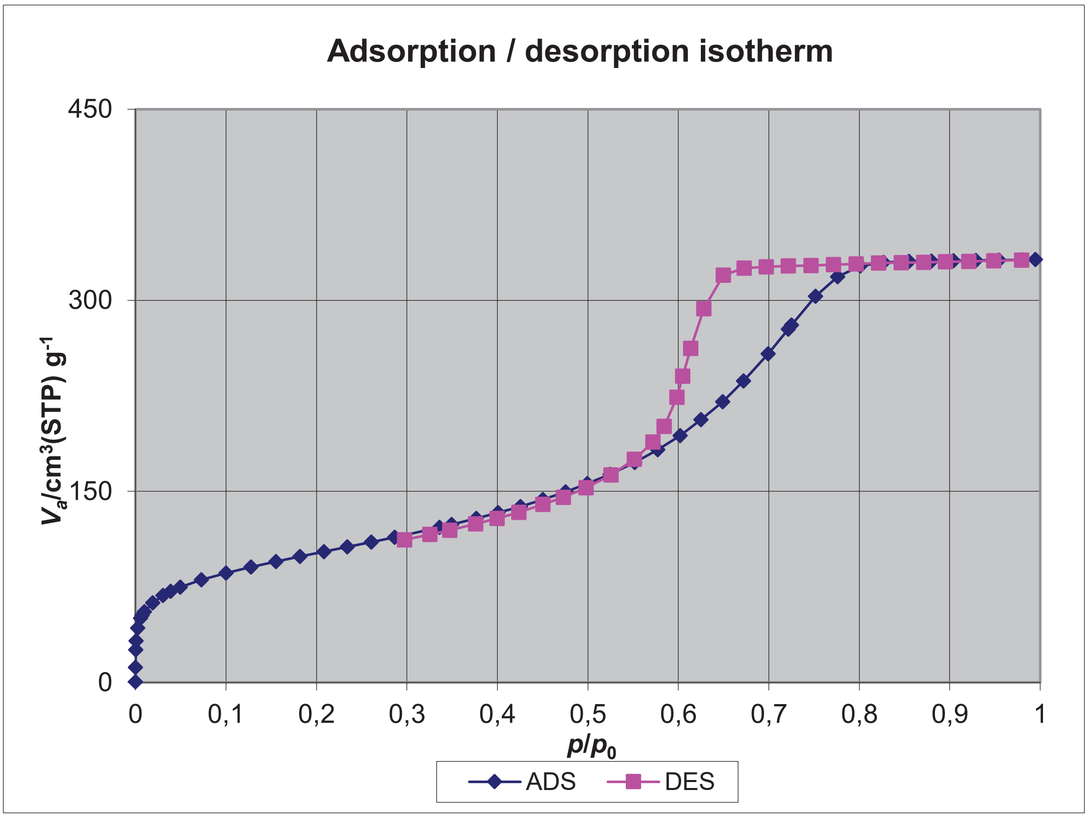

*Figure 9: Adsorption/desorption isotherm for one of the xerogel post-functionalized with TEMPO radicals ([R]= 14 µmol.cm$^{-3}$).*

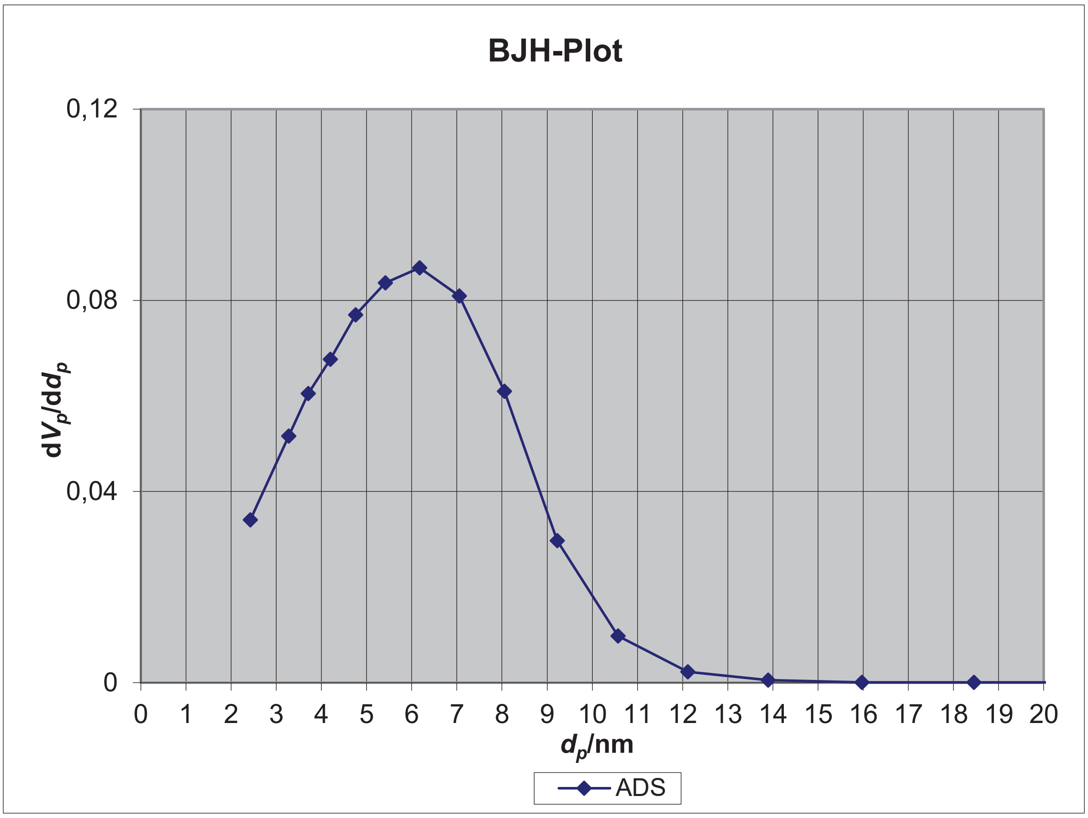

*Figure 10: Mesopore mean diameter for one of the xerogel post-functionalized with TEMPO radicals ([R]= 14 µmol.cm$^{-3}$).*

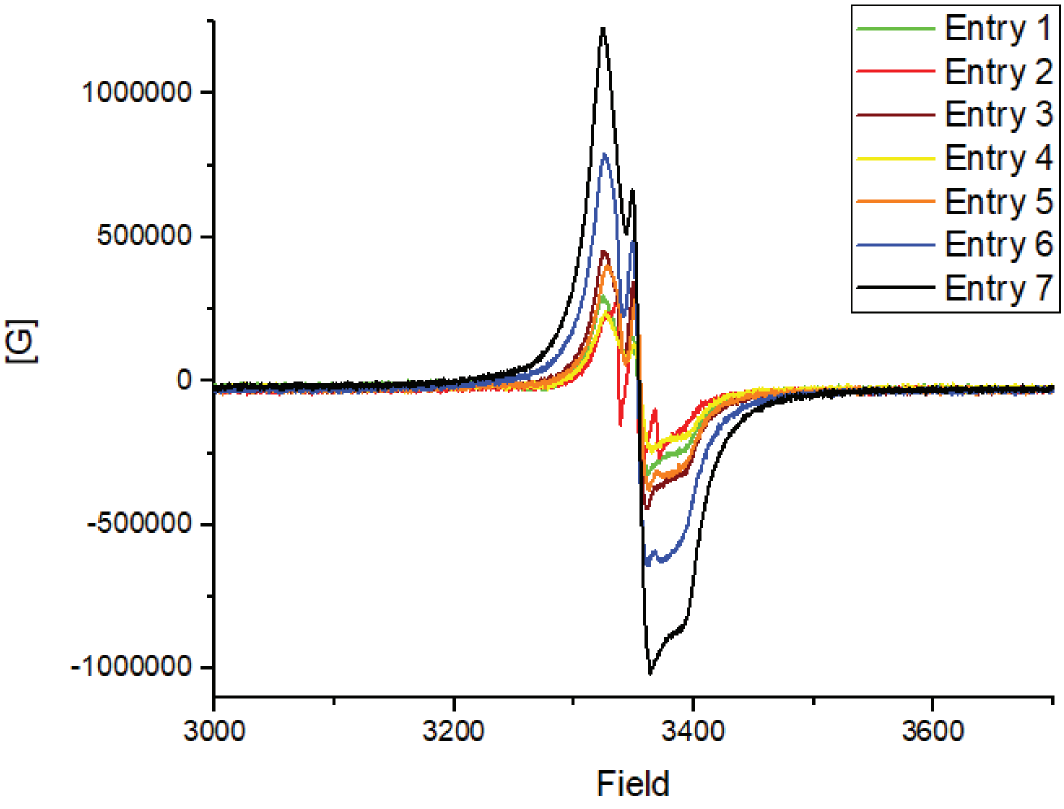

*Figure 11: EPR signal for xerogels obtained by direct incorporation of TEMPO radicals.*

## 2. Preparation of hybrid xerogels by direct incorporation of TEMPO radicals

### a) Synthesis of the xerogels

The second strategy consisted in preparing hybrid silica-based xerogels containing TEMPO radicals in one step. The synthetic process is more straightforward and may lead to the physical entrapment of some TEMPO radicals within the silica. This entrapment could be an advantage when polarizing pyruvic acid which can react with TEMPO radicals onto the matrix surface if it is not diluted in an aqueous solution. With respect to the aforementioned procedure which needs temperatures ranging from 50 °C to 110 °C, the protocol may need adjustments because such temperatures may be too extreme for the TEMPO radicals. A preliminary study therefore consisted in monitoring by EPR the stability of the TEMPO in THF at 70 °C as a function of the time.

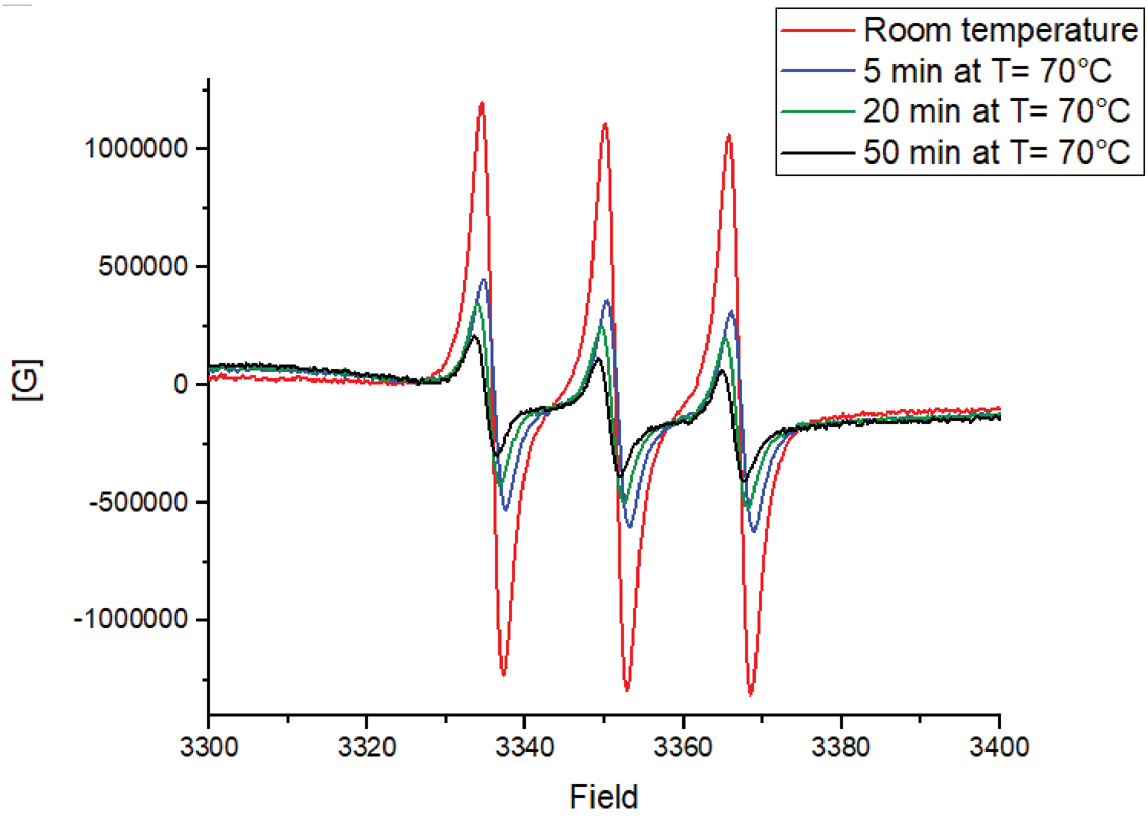

*Figure 12: EPR signal for TEMPO radicals in THF at room temperature (red line) and heated at T=70°C for 5 minutes (blue line) 20 minutes (green line) and 50 minutes (black line).*

As shown in Figure 12, after heating 5 minutes at T= 70 °C the intensity of the EPR signal started to decrease showing that the amount of paramagnetic species rapidly decreased at this temperature. We therefore decided to prepare the xerogels at a lower temperature (T= 50 °C) both for the aging time and the drying.

For their synthesis, the same sol containing TMOS, MeOH, water and oxalic acid was prepared. Compared to the previous preparation allowing to obtain hybrid silica xerogels through post-functionalization, the second step was performed by introducing different amounts of TEMPO radicals instead of the 3-azidopropyltriethoxysilane. As previously, samples were placed for 2h in the fridge and few hours at room temperature. Then, they were directly introduced in the oven and heated at 50°C for 2 days. Finally, they were dried 24h in the Teflon vials with the caps slightly opened (1/4 of a turn). A schematic representation of the synthesis is depicted in Figure 13.

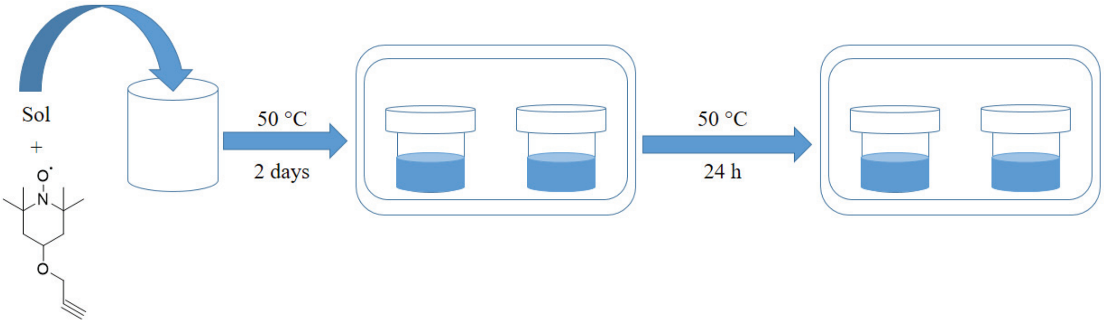

*Figure 13: Schematic representation of the preparation of the xerogels by direct incorporation of TEMPO radicals.*

Since TEMPO radicals were already entrapped in the silica framework, the resulting samples were simply dried under high vacuum at T= 50 °C and stored in a glovebox prior to be used for DNP. The silica xerogels with various concentrations in TEMPO radicals are shown in Figure 14 before and after the drying process.

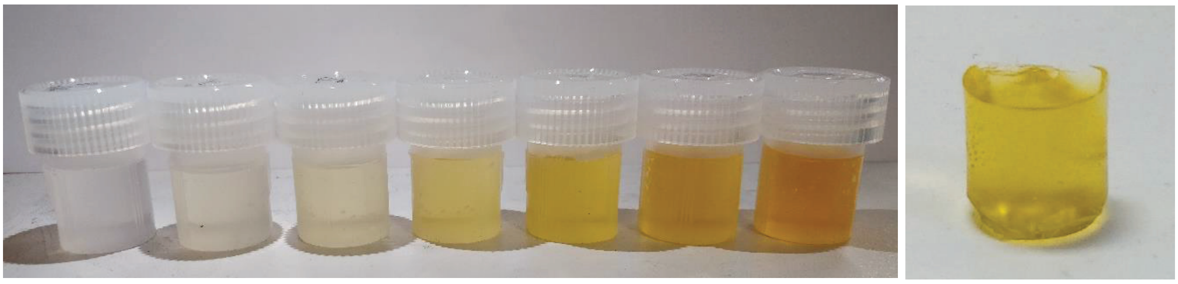

*Figure 14: Silica xerogels with different radical concentrations before drying (left) and after drying (right).*

### b) Characterization: $N_2$ adsorption/desorption experiments and EPR

Hybrid silica xerogels containing TEMPO were first dried under high vacuum at 50 °C for 12h. Then, they were analyzed using $N_2$ adsorption/desorption and EPR as shown in the table 3. Surface areas ranging from 389 to 587 $m^2.g^{-1}$, pore volumes ranging from 0.5 to 0.9 $cm^3.g^{-1}$ and pore-size from 4 to 6 nm were measured. In this case, we observed also small fluctuations which could be due, in most samples, to the very low quantity of TEMPO used. Overall, increasing the amount of radical led to the decrease of the surface area. Regarding the pore size, they were not very different (4 to 6 nm) and the pore volume was found to decrease while increasing the amount of TEMPO (exception for entry 3 and 4).

*Table 3: $N_2$ adsorption/desorption experiments and electron spin resonance for hybrid silica xerogels*

| Entry | [R] ($\mu$mol.$cm^{-3}$) | $S_{BET}$ ($m^2.g^{-1}$) | $Dp^a$ (nm) | $V_p(tot.)^b$ ($cm^3.g^{-1}$) |
|---|---|---|---|---|
| 1 | 17 | 587 | 6 | 0.90 |
| 2 | 51 | 531 | 5 | 0.78 |
| 3 | 76 | 525 | 4 | 0.55 |
| 4 | 90 | 449 | 5 | 0.70 |
| 5 | 91 | 476 | 6 | 0.76 |
| 6 | 113 | 420 | 6 | 0.64 |
| 7 | 226 | 389 | 5 | 0.58 |
| 8 | 304 | 427 | 4 | 0.47 |

a: Mesopore mean diameter calculated using the BJH model (adsorption branch).b: total pore volume corresponding to the quantity of $N_2$ adsorbed at $P/P_0 = 0.99$.

As an example the adsorption/desorption isotherm along with the BJH plot allowing to determine the mean pore diameter for one of the xerogel obtained by direct incorporation of TEMPO radicals are presented in Figure 15 and 16. Moreover, EPR spectra for each samples are presented in Figure 17.

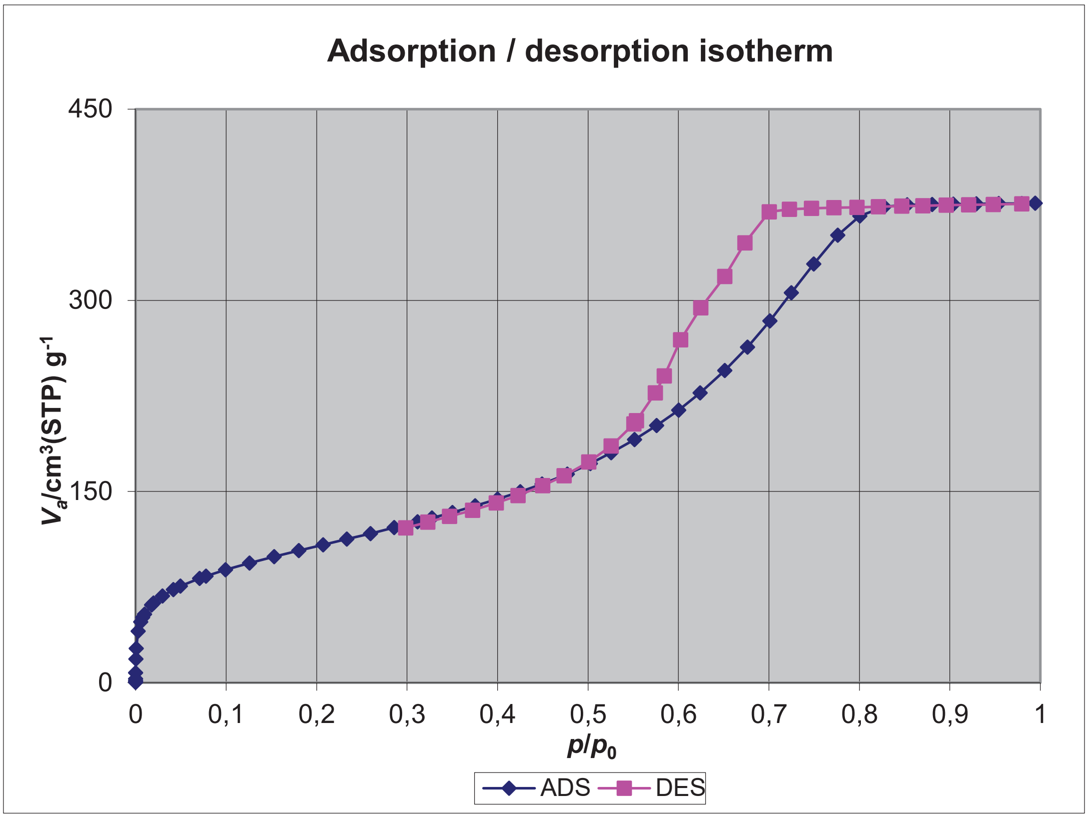

*Figure 15: Adsorption/desorption isotherm for one of the xerogel obtained by direct incorporation of TEMPO radicals ([R]= 226 µmol.cm$^{-3}$).*

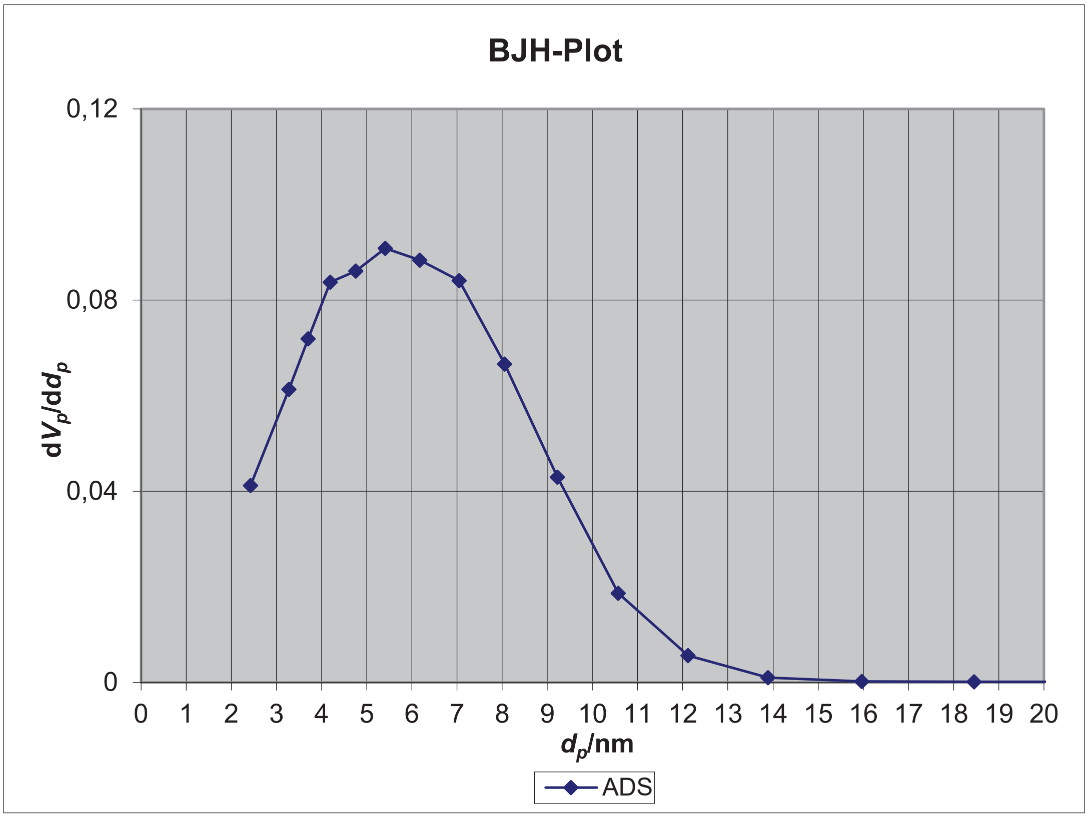

*Figure 16: Mesopore mean diameter for one of the xerogel obtained by direct incorporation of TEMPO radicals ([R]= 226 µmol.cm$^{-3}$).*

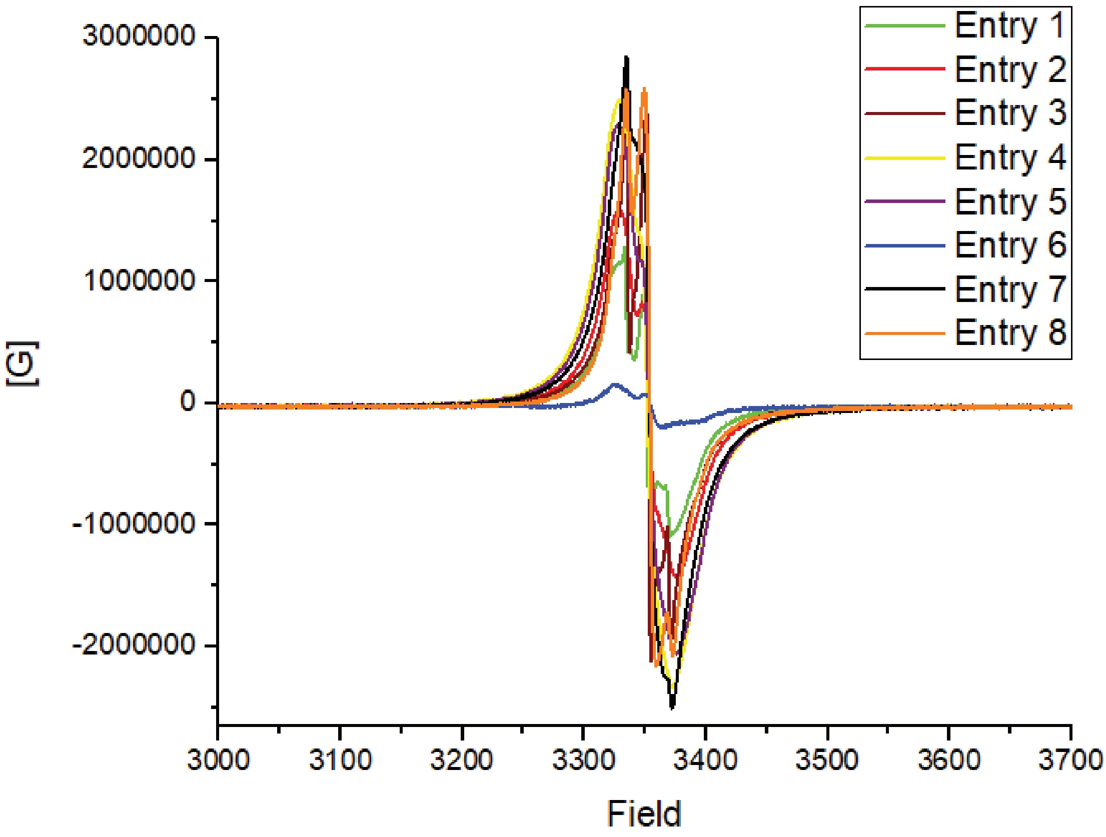

*Figure 17: EPR signal for xerogels prepared by direct incorporation of TEMPO radicals.*

# V. Dynamic nuclear polarization experiments

The aforementioned hybrid xerogel-materials were impregnated with a solution of $H_2O$:$D_2O$ (2:8) using the IWI technique as presented in chapter 2. The volume of $H_2O$:$D_2O$ solution corresponds to 90-100 % of the xerogel pore-volume. The wetted samples were further introduced in the DNP polarizer operating at $B_0 = 6.7$ T and T = 1.2 K. Proton polarization values were measured by using frequency-modulation since higher performances can be reached. Details procedures can be found in the supporting information at the end of this chapter.

## A. Polarization of the xerogels obtained via a post-grafting strategy

The polarization performances of the first bench of xerogels (post-introduction of TEMPO units) as a function of the radical concentrations (ranging from 2 to 44 µmol.cm$^{-3}$) are shown in Figure 18. For the lower radical concentration (0 to 15 µmol.cm$^{-3}$), the proton polarization levels are low (P($^1$H) < 10%) because an insufficient amount of radicals is present to efficiently polarize the surrounding protons. From 15 µmol.cm$^{-3}$ to 35 µmol.cm$^{-3}$, one can observe a slight increase of the polarization levels up to 15%. This result is in sharp contrast to what was observed for the HYPSO 5 materials which exhibited the maximum proton polarization of P($^1$H) = 99 % for a radical concentration of 34 µmol.cm$^{-3}$. Here, the maximum of polarization (P($^1$H) = 41 %) is observed for a radical concentration of 44 µmol.cm$^{-3}$.

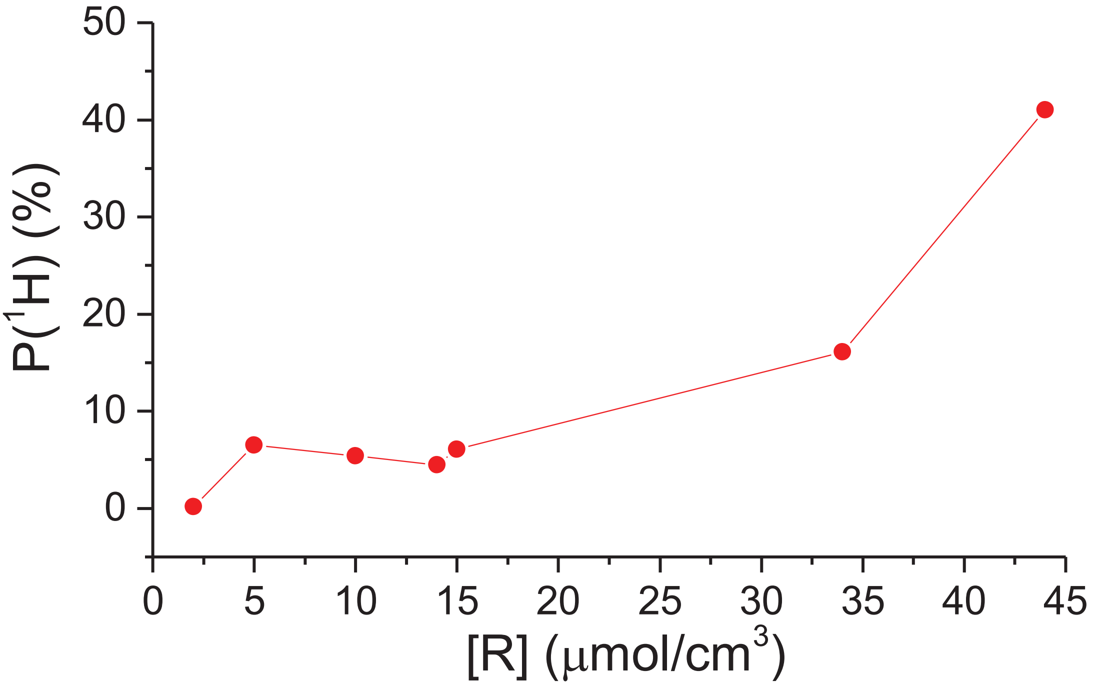

*Figure 18: Proton polarization values as a function of the radical concentration for hybrid silica xerogels prepared through post-functionalization.*

## B. Polarization of the xerogels obtained via the one-pot synthesis

The second preparation of xerogels (direct incorporation of TEMPO units) was also impregnated with a mixture of $H_2O$:$D_2O$ (8:2). As shown in Figure 19, proton polarization values were measured as a function of the radical concentration. In comparison to the previous curve, a different behavior is observed. Indeed, really small amount of TEMPO radicals allows to reach proton polarization values up to P($^1$H) = 46 % for a radical concentration of 17 µmol.cm$^{-3}$. Since these xerogel materials were prepared by direct incorporation of the TEMPO radical, the increase of the polarization for a low radical concentration could be attributed to a better radical distribution into the new matrix. Following this reasoning, a lower radical loading could afford higher performances but this preparation is challenging since only 5 mg of TEMPO radicals have been used to achieve the maximum proton polarization of this curve.

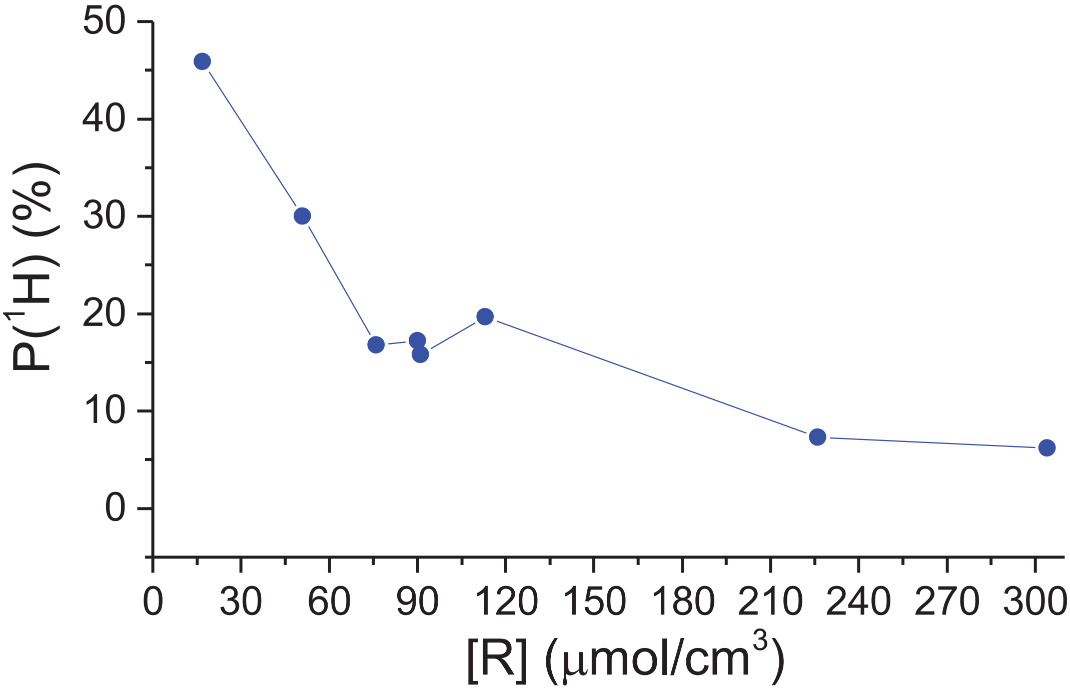

*Figure 19: Proton polarization values against the radical concentration for hybrid xerogels obtained with the one-pot synthesis.*

### 1. Measurement of the build-up times at 4.2 K

In addition, proton build-up times were recorded at 4.2 K for samples prepared *via* the one-pot synthesis. Relatively fast build-up times ranging from 26 s to 291 s were recorded. One can notice a moderate increase of the build-up time (from 26 s to 75 s when decreasing the radical concentration from 304 to 51 µmol.cm$^{-3}$) followed by a sharp increase of the build-up time (291 s) when the radical concentration is decreased to 17 µmol.cm$^{-3}$. These results show that a compromise between high proton polarization and fast build-up time has to be done.

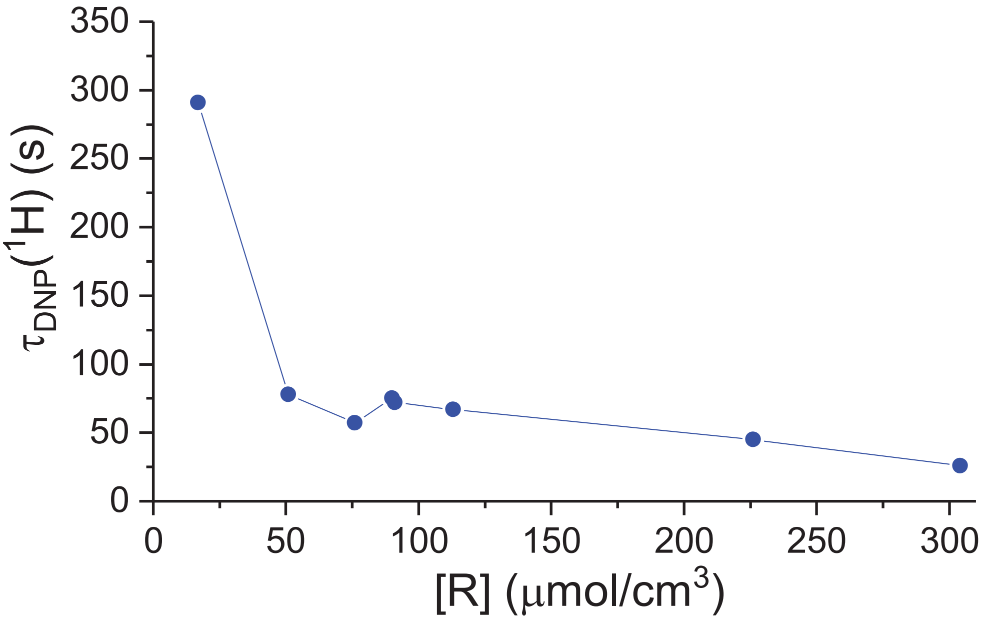

*Figure 20: Proton build-up times as a function of the radical concentration for the xerogels obtained through the one-pot synthesis.*

### 2. Measurement of the $T_1$ relaxation times at 4.2 K

The proton $T_1$ relaxation times were also measured at 4.2 K. The $T_1$ relaxation is the spin-lattice relaxation also called thermal relaxation or longitudinal relaxation. It corresponds to the energy transfer from the spins to the environment. The nuclei spins relax to their thermal equilibrium by dissipating the accumulate energy in the lattice. As shown in Figure 21, the general trend of the curve is similar to that measured for the proton build-up times. The $T_1(^1H)$ relaxation times are really fast for almost all the samples but longer for a radical concentration of 17 µmol.cm$^{-3}$ which gave a $P(^1H) = 46$ % and $\tau_{DNP}$ $(^1H)$= 291 s.

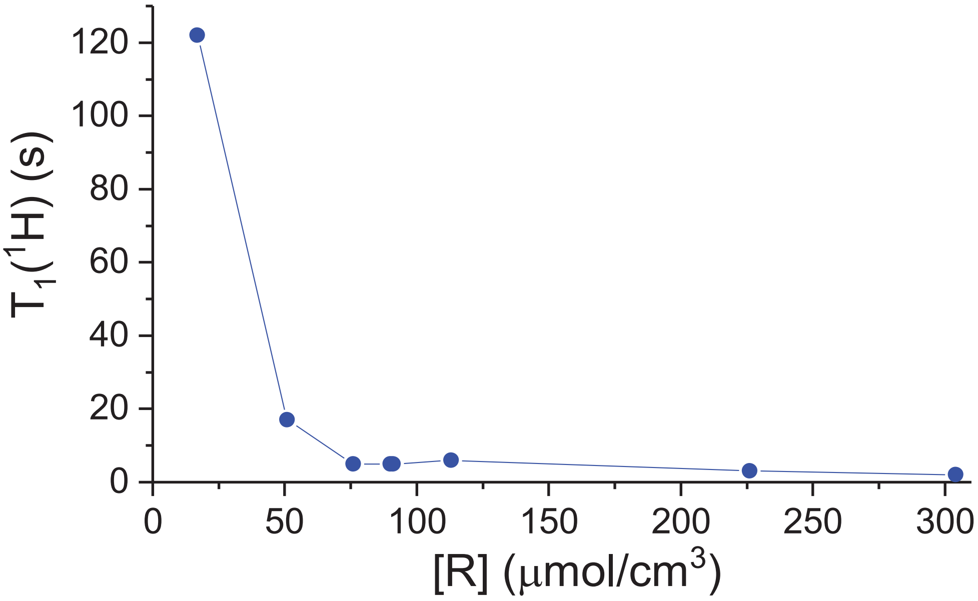

*Figure 21: T1-relaxation times as a function of the radical concentration for hybrid xerogel materials obtained via a one-pot synthesis.*

### 3. Paramagnetic impurities and $^1H$ NMR quantification

Paramagnetic species are essential for DNP experiments but their concentrations have to be precisely controlled. As explained before, the presence of radicals after dissolution would be detrimental for *in-vivo* or *in-vitro* applications but not only. Out of the magnetic field and at room temperature the presence of radicals will induce the fast depolarization of the surrounding polarized nuclei. The signal enhancement gained at low temperature is thus completely lost. To monitor the presence of TEMPO in the recovered sample after the dissolution step, a post-functionalized hybrid silica xerogel was used to polarize a 3M solution of [1-$^{13}$C] sodium acetate in $H_2O$:$D_2O$ (2:8).

The tests were performed on the hybrid xerogel beads with a radical concentration of [R] = 24 μmol.cm$^{-3}$. Each 3 minutes, cross-polarization experiments were performed with a contact times of 4 ms. The resulting experiment is plotted in Figure 22 and shows the proton polarization transfer to the carbon which is normalized and plotted as a function of the time. A fast build-up time was observed and one could dissolve the sample after only 6 minutes.

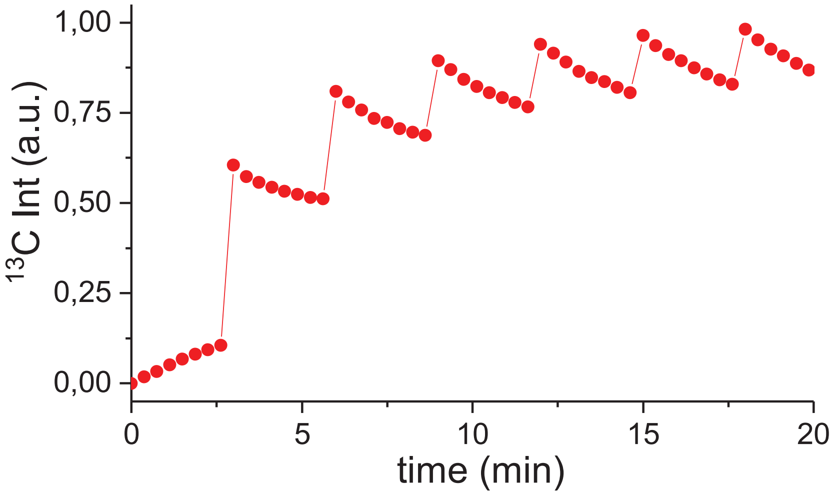

*Figure 22: Cross-polarization experiment for a hybrid silica xerogel with a radical concentration of [R]= 24 µmol.cm$^{-3}$ and impregnated with a 3M solution of [1-$^{13}$C] sodium acetate.*

Then, the dissolution stick was equipped with a small cellulose filter and installed on the top of the polarizer to dissolve the mixture trapped into the polarizing matrix in 10 s with 5 mL of $D_2O$ (120°C, 10 bar). This cellulose filter allowed to retain the beads while the hyperpolarized liquid was transferred to the NMR spectrometer. Relative long $T_1$ were measured showing that no radical species were present in solution: $T_1(^{13}C) = 68$ s for the sodium acetate solution and $T_1(^1H) = 36$ s for HDO.

In addition, the concentration of the acetate solution expelled from the solid was quantified by $^1$H NMR. After dissolution, the concentration of the hyperpolarized liquid was compared to a solution of sodium acetate with a known concentration used as standard. However, a concentration of 1.1 mM was measured after dissolution for the hyperpolarized solution which is far from the expected concentration of 9mM for a total recovery of the solution. In conclusion, the sodium acetate solution previously impregnated into the polarizing matrix was not completely expelled since the concentration before impregnation and after dissolution is different. The increase of the pore size of the polarizing matrices could probably improve this issue.

## 4. Polarization of different solutions using the same polarizing matrix

The design of these new porous polarizing matrices allowed to ease the filtration process. Each polarization experiment was performed with a different aliquot but it would be really attractive to be able to re-use such polarizing solids several times. We therefore tried to polarize twice a sodium acetate solution using a unique polarizing matrix.

For this experiment, hybrid xerogel beads with a radical concentration of 24 µmol.cm$^{-3}$ were selected and impregnated with a 3M solution of [1-$^{13}$C] sodium acetate in $H_2O$:$D_2O$ (2:8). Prior to be used in DNP, a cellulose filter was installed in the dissolution stick for recovering the polarizing beads to be further used in a second polarization run. The solution impregnated into the solid matrix was first polarized at T= 1.2 K (Figure 23) and cross-polarization experiments were performed to transfer the proton polarization to the carbon nuclei (Figure 24). After these first experiments, the polarizing beads were dissolved to expel the solution from the DNP polarizer to the NMR spectrometer. Then, the polarizing beads were recovered in the cellulose filter and soaked overnight in a 3M solution of [1-$^{13}$C] sodium acetate in $H_2O$:$D_2O$ (2:8) to exchange the $D_2O$ used to dissolve the sample. The day after, the same polarizing beads were introduced in the DNP polarizer to perform the second cycle of polarization/cross-polarization. The experiments were conducted at T= 1.2 K and the dissolution stick was again equipped with a new cellulose filter.

The recorded results are presented in Figure 23 for the $^{13}$C DNP build-up times and in Figure 24 for the cross-polarization experiments. In both cases, the blue curve corresponds to the first cycle of polarization/cross-polarization whereas the red curve corresponds to the second cycle of polarization/cross-polarization. In addition, the results were normalized and superimposed to be compared.

As shown in Figure 23, the $^{13}$C DNP build-up curves after the first and second cycle achieved were found very similar with only a small slight shift of the red curve toward lower values compared to the blue one. In addition, Figure 24 showing the cross-polarization experiments displays comparable results, indicating again the possibility to re-use this polarizing matrix for these experiments. Moreover, long $T_1$ were measured showing that no radical was present in the NMR spectrometer after the dissolution step ($T_1$($^{13}$C)= 74 s and $T_1$($^{1}$HDO)= 36 s).

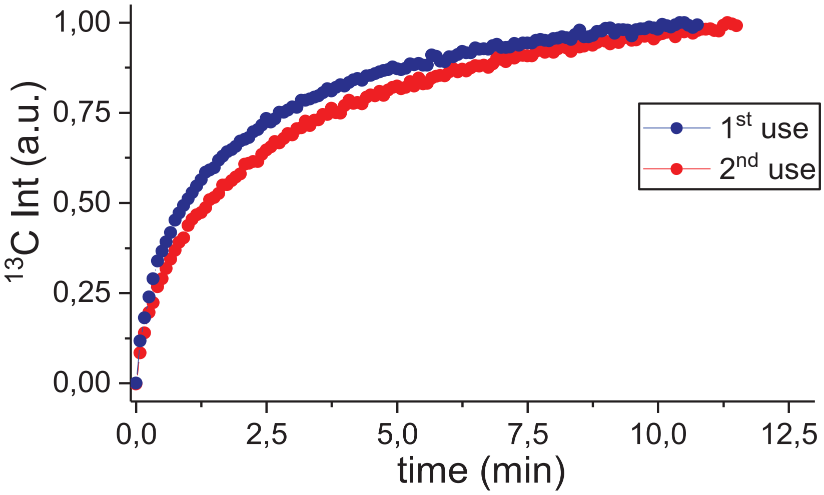

*Figure 23: $^{13}$C DNP build-up times after a first (blue) and second (red) polarization experiment using the same polarizing matrix.*

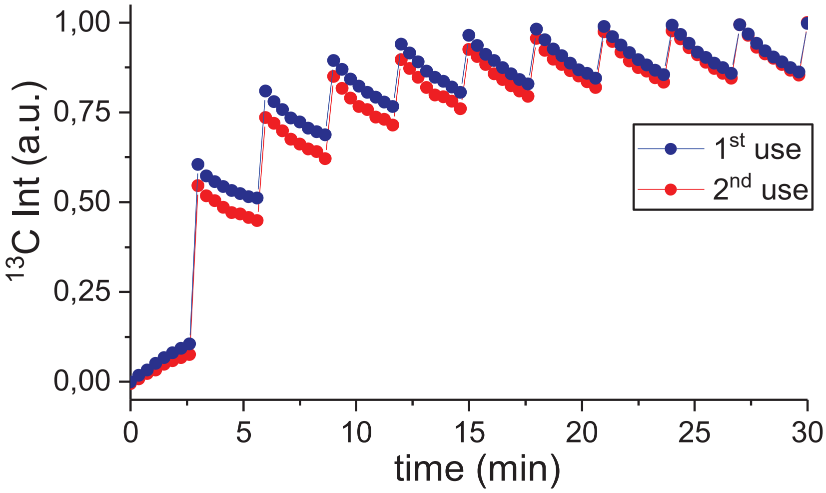

*Figure 24: Cross-polarization experiments after a first (blue) and (second) hyperpolarization using the same polarizing matrix.*

In conclusion, the xerogels functionalized with TEMPO radicals were found to improve the filtration process by providing polarizing matrices in the form of silica beads or monolithic cylinders. In this case, any silica particles were found in the NMR spectrometer after the dissolution step. At low temperature, the proton polarization as well as the carbon polarization measured were quite good and relatively short build-up times were obtained. For the first time, it was even possible to polarize twice a liquid with the same polarizing matrix. Both strategies could be used depending on the system which is studied. For example, the one-pot synthesis which can trap TEMPO radicals into the wall of the matrix could be used after a treatment with ascorbic acid to polarize acidic compounds. Nevertheless, these systems which are promising should be optimized.

# CONCLUSIONS
# AND
# PERSPECTIVES

The goal of this PhD project was to prepare solid matrices containing paramagnetic species (TEMPO radicals) covalently attached to their surface for d-DNP applications. These systems allowed to polarize various solutions of analytes without adding any additives such as glass forming agents. Different silica materials were successfully prepared and the introduction of the TEMPO radicals was adjusted. Modifying the physical and chemical features of the solids allowed to identify the main parameters impacting the polarization values. Their granulometry was tailored to ease the filtration step and the experimental protocols were modified to make the synthesis potentially easily scalable.

Initially, polarizing matrices, HYPSO 2 and HYPSO 3 based respectively on SBA-15 and SBA-16 architectures, were prepared by co-hydrolysis and co-condensation of the 3-azidopropyltriethoxysilane precursor and TEOS in the presence of structure directing agents. Such structure directing agents were removed before coupling the surface azido fragments with the TEMPO radicals through a copper(I)-catalyzed alkyne azide cycloaddition (Figure 25). The as-obtained materials displaying various radical concentrations were fully characterized by $N_2$ adsorption/desorption, EPR, SAXS, DRIFT and TEM further polarization. A maximum proton polarization of $P(^1H)= 50\ \%$ was recorded for HYPSO 2 materials whereas HYPSO 3 materials showed higher performances with a proton polarization of $P(^1H)= 63\ \%$. This improvement was explained by a better pore interconnectivity of HYPSO 3 promoting the diffusion of the polarization in the whole sample. In addition, cross-polarization experiments were also conducted on the optimal HYPSO 3 impregnated with a solution of sodium [1-$^{13}$C] acetate. As a result, a carbon polarization of $P(^{13}C)= 36\ \%$ was recorded but small traces of TEMPO radicals were found after dissolution, probably due to small silica particles in the hyperpolarized solution.

Independently of the pore network architecture, longer build-up times were recorded at 1.2 K than at 4.2 K. When applying frequency-modulation no impact on the build-up times were found at 4.2K. However, the use of the same modulation at 1.2 K decreased the build-up times. In general, a compromise between high polarization values and short build-up time was needed.

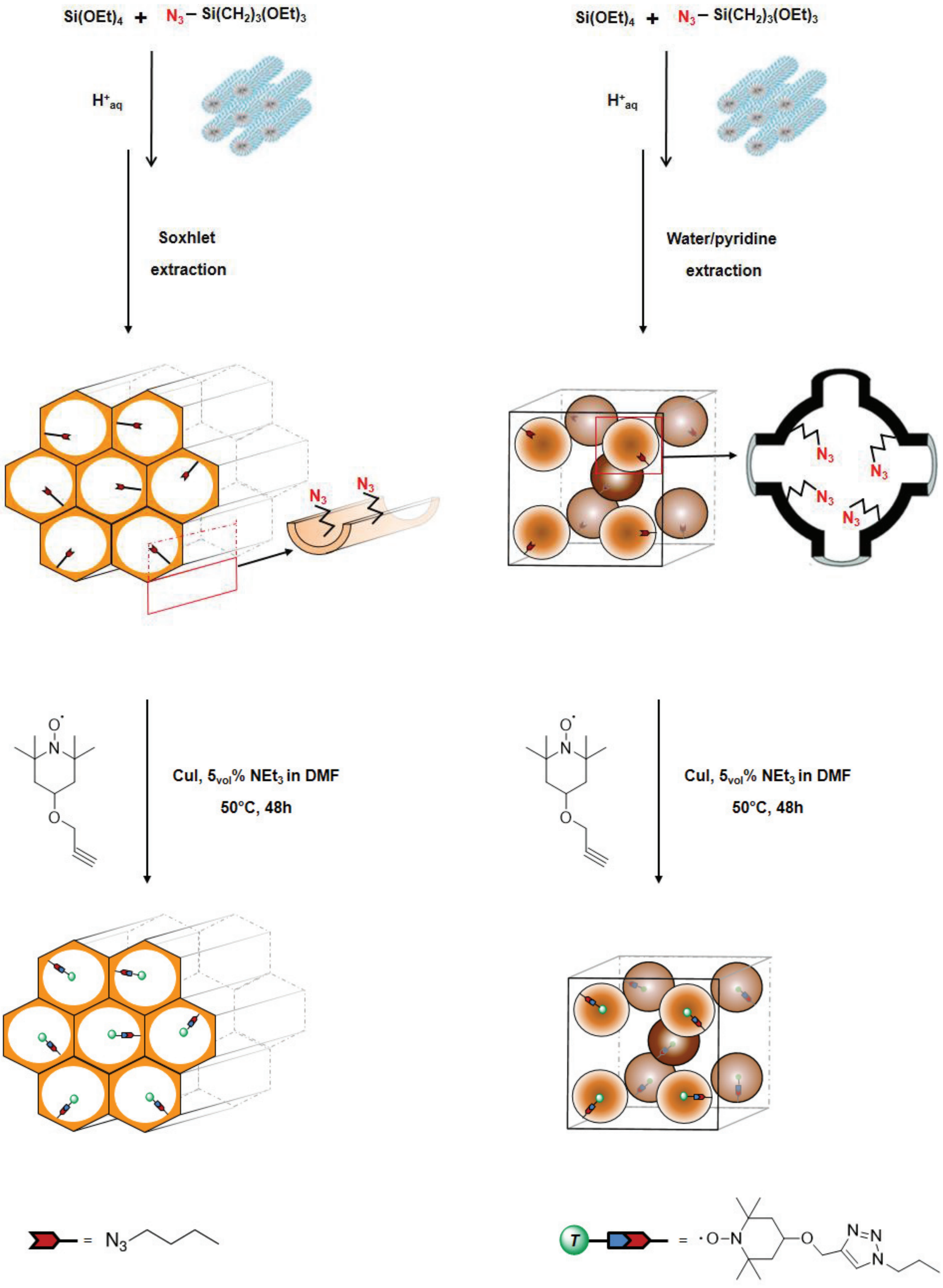

*Figure 25: Preparation of HYPSO 2 and HYPSO 3 from the silicon precursor to the final material bearing TEMPO radicals.*

The results observed for HYPSO 3 prompted us to develop non-structured silica materials exhibiting highly interconnected pores. For this purpose, robust commercially available mesoporous silica spheres were selected. A methodology was developed to post-functionalize these silica spheres by creating a silica layer containing the azido fragments which were further transformed into TEMPO radicals *via* a click reaction. These polarizing matrices were denoted HYPSO 5 and different starting materials displaying a pore size ranging from 6 nm to 28 nm and a constant particle size were coated. In a second time, porous silica spheres with a particle size ranging from 20 to 500 µm and exhibiting a constant pore size were also coated (Figure 26). These studies showed that the proton polarization values for this type of porous silica spheres were found slightly different depending on the particle size. Moreover, by increasing the particle size up to 500 µm, the filtration process was improved. Arising from the peculiar architecture of the HYPSO 5, high proton and carbon polarization values were recorded: P($^1$H)= 99% and P($^{13}$C)= 51%. Interestingly, this proton polarization value exceeds that obtained with state-of-the art DNP formulations reflecting thus the advantage of using these polarizing matrices.

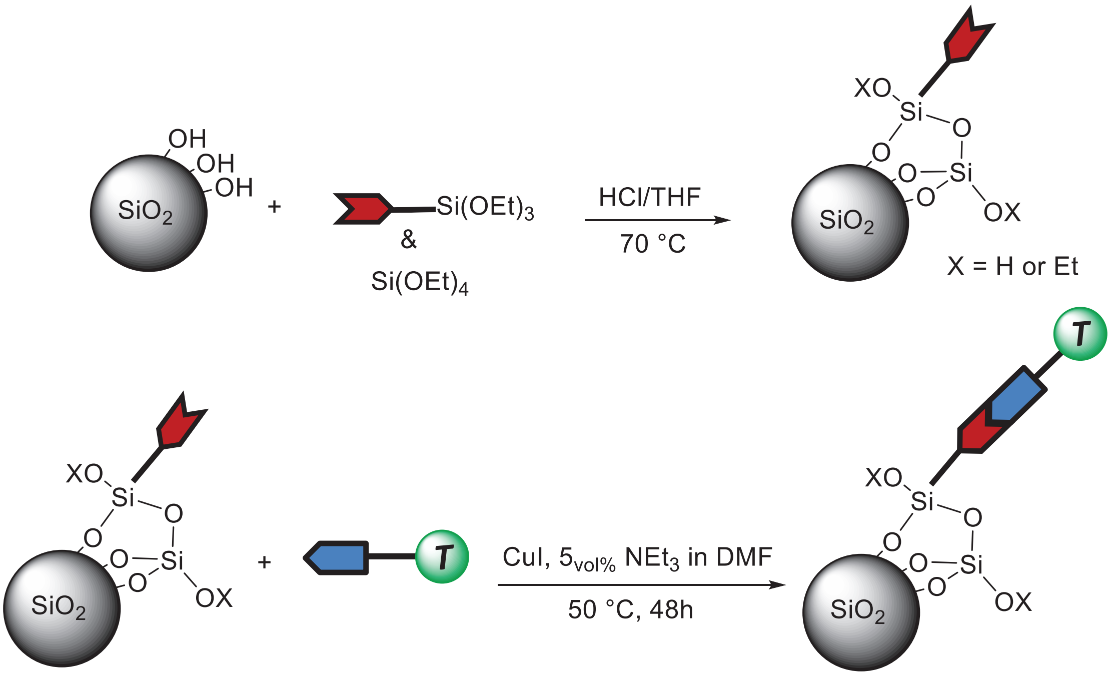

*Figure 26: Formation of the layer containing the azido moieties which are then coupled with TEMPO radicals through a copper-catalyzed alkyne-azide cycloaddition at the surface of the porous silica spheres.*

In addition, HYPSO 5 allowed for the first time to perform the filtration step out of the DNP polarizer. This is an important point since a simple PTFE filter could be added before the magnetic tunnel facilitating thus the conception of the dissolution set-up. Last, but not least, the first $^{13}$C MRI pictures were recorded using HYPSO 5 as polarizing matrix. The $^{13}$C pictures are presented in figure 20 and highlight the potential of these polarizing matrices for MRI in vivo applications.

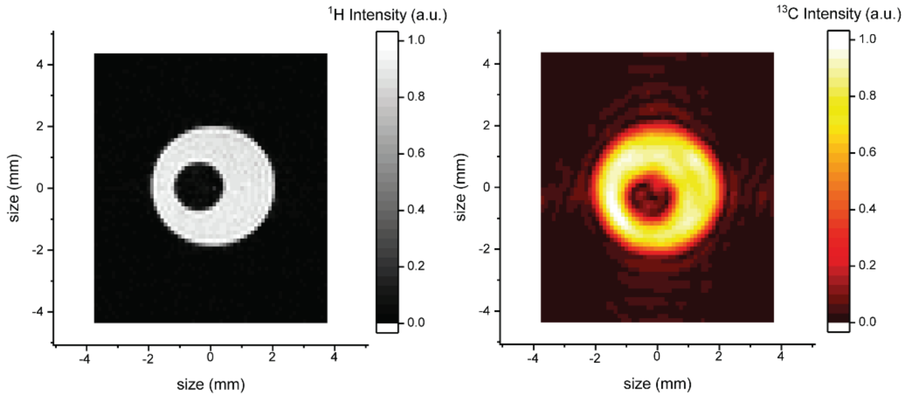

*Figure 27: $^1$H (left) and $^{13}$C pictures (right) acquired after hyperpolarization and dissolution of a solution of 3M sodium [1-$^{13}$C]acetate in $H_2O$:$D_2O$ (2:8) impregnated into HYPSO 5.*

As a summary, the following scheme displays the polarization values recorded depending on the pore network architecture of the polarizing matrices as observed by electron tomography.

| **HYPSO 2** | **HYPSO 3** | **HYPSO 5** |
|---|---|---|
| 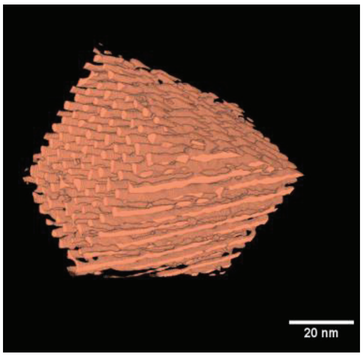 | 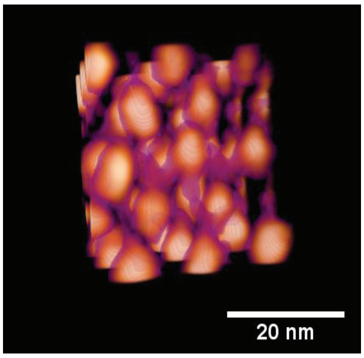 | 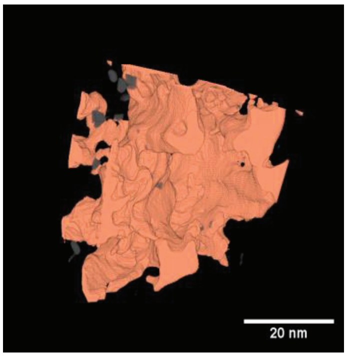 |
| P($^1$H)= 50 %<br>P($^{13}$C)= 33 % | P($^1$H)= 63 %<br>P($^{13}$C)= 36 % | P($^1$H)= 99 %<br>P($^{13}$C)= 51 % |
| D. Gajan et al.<br>Proc. Natl. Acad. Sci.,<br>2014 | D. Baudouin et al.<br>Chem. Sci.,<br>2016 | M. Cavaillès et al.<br>Angew. Chem.,<br>2018 |

Finally, another approach based on the synthesis of hybrid silica xerogels was developed to produce two distinct families of polarizing matrices. A first one obtained by the direct incorporation of the TEMPO radicals during the sol-gel process and the second one by post-functionalization of the azido-containing silica xerogels with TEMPO radicals. The first formulation led to samples with a monolithic shape whereas the second route led to large silica beads of different sizes. Preliminary results showed that proton polarization values up to $P(^1H)= 46$ % were found for samples prepared *via* a direct introduction of the TEMPO units with a TEMPO concentration of 17 $\mu mol.cm^{-3}$. Moreover, a comparable proton polarization value of $P(^1H)= 41$ % was recorded at $[R]= 44$ $\mu mol.cm^{-3}$ for the other family. This difference could be explained by a better radical distribution through the one-pot synthesis compared to the previous preparation. To confirm that, additional experiments consisting in measuring the EPR linewidths could be performed. These results highlight again the importance of the sample formulation and the importance of the localization of the paramagnetic species for optimized polarization performances. These polarizing matrices were also found useful to polarize different liquids with a unique monolith.

A perspective of our work could be the implementation of the strategy recently developed by D. Silverio and al.[9], allowing to hide the TEMPO radicals within the silica walls. This approach could be valuable to efficiently polarize pure pyruvic acid or biological solutions without any direct contact with the radicals. In this work, a tris-silylated precursor containing a nitroxide-based radical (Figure 28) was used to prepare through a sol-gel process two types of materials: i) an ordered mesoporous silica materials containing TEMPO radicals within the silica walls (HYPSO-W1) and ii) an ordered mesoporous silica materials doped with a bis(triethoxysilyl)ethane and containing TEMPO radicals within the silica walls (HYPSO-W2). The different routes to prepare these materials are presented in figure 28.

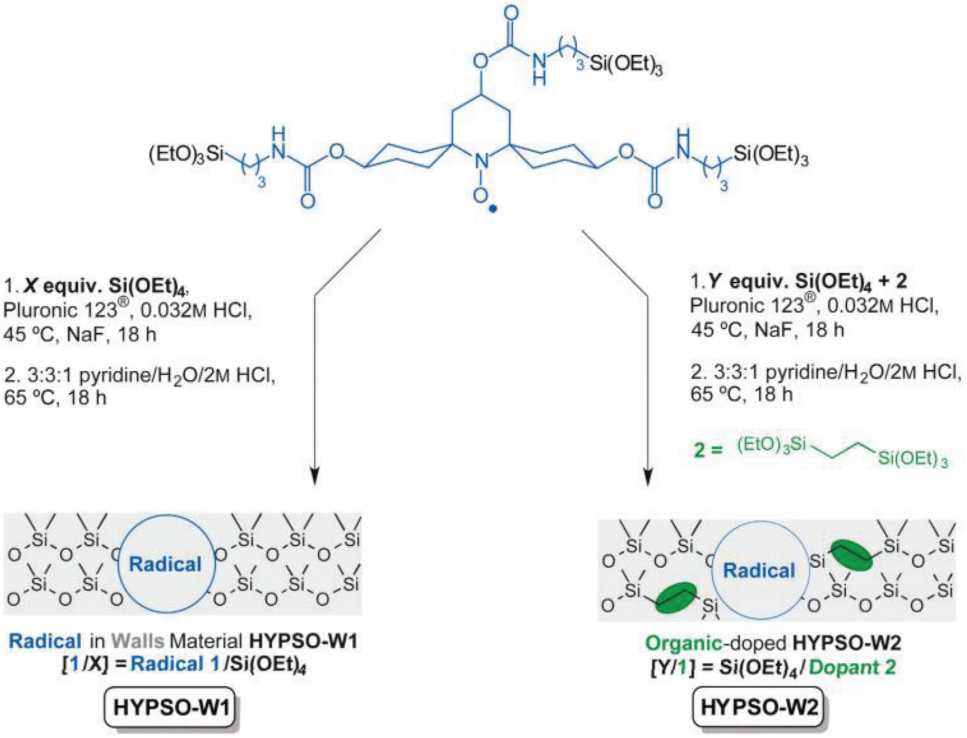

*Figure 28: Synthetic pathways leading to HYPSO-W1 and HYPSO-W2 containing the TEMPO radicals within the silica walls.*

Subsequently, samples were treated with an ascorbic acid solution to remove the radicals from the surface and keep only those in the walls. A decrease of 22 % and 36 % in radical content was recorded for HYPSO-W2 and HYPSO-W1 respectively. Finally, both samples were polarized at 1.2 K and 6.7 T using cross polarization experiments. After impregnation with neat pyruvic acid, proton polarization of P($^1$H)= 40 % and a carbon polarization of P($^{13}$C)= 17 % were recorded for the optimal polarizing matrix HYPSO-W2 with a dilution of [25/1]. Similarly, optimal HYPSO-W1 with a dilution of [1/200] was impregnated with neat pyruvic acid to yield to a proton polarization of P($^1$H)= 22 %. These results show that the introduction of TEMPO radicals within the silica walls is possible and that the organic-doped HYPSO-W2 gives higher performances than HYPSO-W1.

Another potential research project could be the use of these new polarizing matrices (HYPSO 5) to transport a sample hyperpolarized from one laboratory to another one without losing the freshly acquired signal enhancement. As shown recently by X. Ji et al.[10], samples such as [1-$^{13}$C]glucose, [$^{13}$C$_3$, $^{15}$N]alanine, [$^{13}$C$_2$, $^{15}$N]glycine and [1-$^{13}$C]sodium pyruvate prepared in the form of a micro-particulate powder were polarized through the use of a physically separated solution containing 80 mM TEMPOL-benzoate in toluene/THF (8:2) called the radical-rich phase (RRP) (Figure 29).

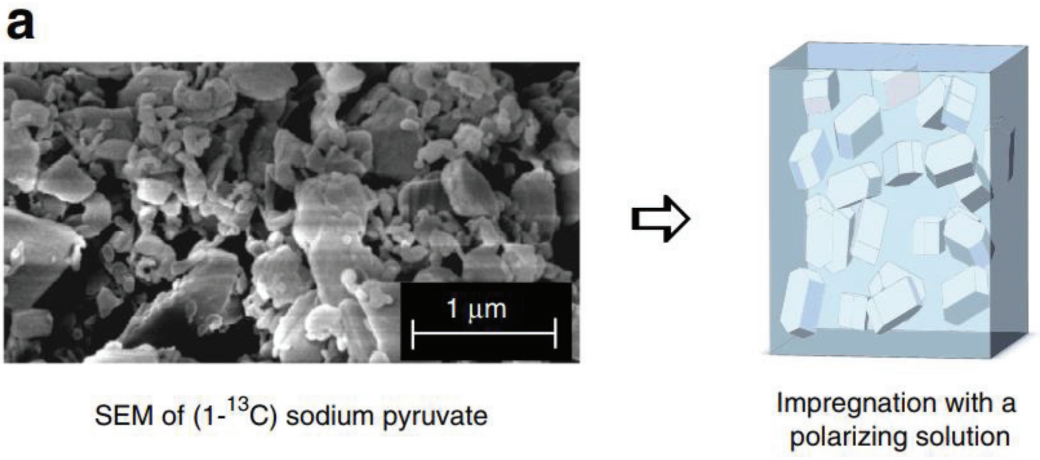

*Figure 29: SEM picture of a micro-powder of [1-$^{13}$C] sodium pyruvate and its impregnation with a polarizing solution.*

In contrast to the common DNP juice where the liquid to hyperpolarize is in close contact with the surrounding nuclei, in this type of formulation (Figure 29), the proton nuclei are in the RRP whereas the carbon nuclei are in the radical-free phase (RFP). Therefore, by mean of cross-polarization experiments the proton polarization can be transferred to the carbon nuclei of the target metabolite without suffering from depolarization since the paramagnetic species are physically separated in the RRP. It is important to mention that this phenomenon is due to the $^{13}$C-$^{13}$C spin diffusion which is two orders of magnitude slower than $^{1}$H-$^{1}$H spin diffusion in the RFP. Therefore, the carbon polarization is trapped in the RFP and the relaxation through the RRP is impossible since this phase is not enriched in $^{13}$C. Increase of the $^{13}$C spin-lattice relaxation times $T_1(^{13}C)$ was recorded with for example $T_1(^{13}C)$= 37h for the [1-$^{13}$C]sodium pyruvate with a micro-particulate formulation whereas $T_1(^{13}C)$= 20 min was recorded for the same sample in solution. To conclude, samples with long $T_1(^{13}C)$ could be polarized in one laboratory and used few hours after in another one. However, in this proof of concept system, the use of a glass-forming agent and free radicals remained an issue which could be tackled by the use of new polarizing matrices.

A last perspective could also be to use the hybrid xerogels obtained through the one-pot synthesis in continuous flow DNP. These polarizing matrices could act as chromatography columns containing paramagnetic species to polarize a liquid flow.

As suggested, numerous perspectives are possible with these polarizing matrices. However, to the best of our knowledge, systems implementing a DNP polarizer coupled with a MRI system *via* a tunnel magnetic allowing to preserve the polarization at room temperature are not available even in research laboratories. Few hardware combining a DNP polarizer at proximity of a MRI machine are available and the possibility to probe *in-vivo* systems with this machine is even lower. Although this technique is revolutionary and could be improved by using our polarizing matrices, the skills of chemists, biologists and physicists are essential to be able to widely develop a DNP polarizer coupled to a MRI machine.

# SUPPORTING INFORMATION

# VI. Preparation of the xerogels

## A. Hybrid silica xerogels

Hybrid silica xerogels obtained *via* post-functionalization or one-pot synthesis were prepared using the same sol part described below.

In a 50 mL round bottom flask equipped with a stirring magnet, tetramethylorthosilicate (TMOS) and anhydrous methanol were introduced at 0 °C. Then, an oxalic acid solution ([C]= 0.001 M) was added dropwise (around 1 drop each 2 seconds) and the reaction mixture was stirred for 30 minutes at 0 °C and 24h at room temperature (TMOS: MeOH: $H_2O$ ; 1:6:4). Following this quantity around 8 different samples can be prepared.

### 1. Hybrid silica xerogels obtained through post-functionalization

In a small Teflon vial placed in an ice bath, 3.76 mL of the previous solution and 779 µl of milli-Q water were inserted. Then the 3-azidopropyltriethoxysilane previously prepared was inserted in different amount depending on the chosen concentration. A fresh ammonia solution was prepared with a concentration of [C]= 1 M and 0.1 mL was added. Before removing the stirring magnet, the reaction mixture was mixed for 90 seconds. The Teflon vial was closed and placed in the fridge for 2h (Gelation time 4-5 minutes) and few hours at room temperature. The sample was aging in an oven at 50 °C for 48h and dried by applying a ramp from 50 °C to 110 °C in 24 h. Finally, the sample is naturally cooled down to room temperature and ready for the next step.

Under argon, the as-obtained material was coupled with TEMPO radicals in presence of CuI and DMF. The reaction mixture was heated up for 48h and washed with a solution of EDTA (3 x 50 mL), ethanol (3 x 50 mL) and diethyl ether (3 x 50 mL). The orange silica beads obtained were dried under high vacuum for 12h at 50 °C and stored in a glovebox.

### 2. Hybrid silica xerogels obtained through a one-pot synthesis

In a small Teflon vial placed in an ice bath, 3.76 mL of the previous solution and 779 µl of milli-Q water were inserted. Then TEMPO radicals previously prepared was inserted in different amounts depending on the chosen concentration. A fresh ammonia solution was prepared with a concentration of [C]= 1 M and 0.1 mL was added. Before removing the stirring magnet, the reaction mixture was mixed for 90 seconds. The Teflon vial was closed and placed in the fridge for 2h (Gelation time 4-5 minutes) and few hours at room temperature. The sample was dried 50 °C for 72h and left at room temperature to cool down. The final orange xerogel was dried under high vacuum for 12h at 50 °C and stored in a glovebox.

## B. Characterization

### 1. $N_2$ adsorption/desorption experiments

Xerogel beads were directly inserted in the tubes whereas the orange cylindrical monoliths were crashed and a small part inserted in the tubes. As usually, experiments were performed at 77 K using a BELSORB-Max from BEL-JAPAN. The pore diameter distribution and the mean pore diameter ($d_p$) were calculated using Barrett–Joyner–Halenda (BJH) method. The specific surface area ($S_{BET}$) was calculated using the Brunauer–Emmett–Teller (BET) equation.

### 2. Continuous wave electron paramagnetic resonance (CW EPR) parameters and sample preparation

CW EPR spectra were recorded on a Bruker EMX X Band spectrometer (9.5 GHz microwave frequency). Conversion time was set to 40.96 ms, time constant to 5.12 ms and 1024 data points were recorded. The modulation frequency was 100 kHz and the modulation amplitude 1 Gauss. In all measurements, attenuation was varied such that no saturation was observed.

### a) Determination of the radical concentration

The samples were filled in a 3.0 mm quartz tube with a maximum sample height of 3 mm. The sample position in the cavity was carefully optimized. The spectra were recorded at room temperature and with a sweep width of 600 Gauss and attenuation between 26 and 14 dB. The amount of radical was determined by double integration of the CW spectra and referencing to calibration curve of TEMPO in toluene solutions measured for the concentration range between 0.4 and 80 mM. An additional correction for the difference in the incident microwave power has been taken into account. Data was processed with OriginLab.

### b) Stability of the TEMPO radicals over the temperature

A first aqueous solution of HCl was prepared with a concentration of 2.3 M. Then 1.5 mL of this solution was poured in a second solution containing 10 mg of TEMPO radicals and 20 mL of THF. Finally, a capillary was filled with 0.05 mL of this latter solution and inserted in an EPR tube. Then, the system comprising the filled capillary in an EPR tube was immersed in an oil bath and heated. An EPR spectrum was acquired after 5, 20 and 50 minutes.

# VII. References

1. Shimizu, T.; Kanamori, K.; Nakanishi, K., Silicone-Based Organic–Inorganic Hybrid Aerogels and Xerogels. *Chemistry – A European Journal* **2017,** *23* (22), 5176-5187.
2. Kistler, S. S., Coherent Expanded Aerogels and Jellies. *Nature* **1931,** *127*, 741.
3. Bheekhun, N.; Abu Talib, A. R.; Hassan, M. R., Aerogels in Aerospace: An Overview. *Advances in Materials Science and Engineering* **2013,** *2013*, 18.
4. Maleki, H.; Durães, L.; García-González, C. A.; del Gaudio, P.; Portugal, A.; Mahmoudi, M., Synthesis and biomedical applications of aerogels: Possibilities and challenges. *Advances in Colloid and Interface Science* **2016,** *236*, 1-27.
5. Hitchen, S. M.; Dean, J. R., Properties of supercritical fluids. In *Applications of Supercritical Fluids in Industrial Analysis*, Dean, J. R., Ed. Springer Netherlands: Dordrecht, 1993; pp 1-11.
6. Francis, A. W., Ternary Systems of Liquid Carbon Dioxide. *The Journal of Physical Chemistry* **1954,** *58* (12), 1099-1114.
7. Lamy-Mendes, A.; Silva, R. F.; Durães, L., Advances in carbon nanostructure–silica aerogel composites: a review. *Journal of Materials Chemistry A* **2018,** *6* (4), 1340-1369.
8. Delia, L. B., Silicon Based Materials for Drug Delivery Devices and Implants. *Recent Patents on Nanotechnology* **2007,** *1* (3), 186-192.
9. L., S. D.; A., K. H.; Ta-Chung, O.; Mathieu, B.; Maxim, Y.; Laurent, V.; Pierrick, B.; Sachin, C.; David, G.; David, B.; Matthieu, C.; Basile, V.; Aurélien, B.; Gunnar, J.; Geoffrey, B.; Anne, L.; Lyndon, E.; Sami, J.; Chloé, T.; Christophe, C., Tailored Polarizing Hybrid Solids with Nitroxide Radicals Localized in Mesostructured Silica Walls. *Helvetica Chimica Acta* **2017,** *100* (6), e1700101.
10. Ji, X.; Bornet, A.; Vuichoud, B.; Milani, J.; Gajan, D.; Rossini, A. J.; Emsley, L.; Bodenhausen, G.; Jannin, S., Transportable hyperpolarized metabolites. *Nature Communications* **2017,** *8*, 13975.